Oil & Natural Gas Technology

DOE Award No.: DE-FC26-06NT15520

Final Report

pH SENSITIVE POLYMERS FOR IMPROVING RESERVOIR SWEEP AND CONFORMANCE CONTROL IN CHEMICAL FLOODING

Submitted by:
University of Texas, Austin
P.O. Box 7726
Austin, TX 78713

Prepared for:
United States Department of Energy
National Energy Technology Laboratory

September 30, 2008

Office of Fossil Energy

pH SENSITIVE POLYMERS FOR IMPROVING RESERVOIR SWEEP AND CONFORMANCE CONTROL IN CHEMICAL FLOODING

Final Report

September 16, 2004 – March 31, 2008

By

Mukul M. Sharma
Steven L. Bryant
Chun Huh

September 15, 2008

Work Performed under Contract No. DE-FC26-04NT15520

Traci Rodosta
Project Manager
U. S. Department of Energy
National Energy Technology Laboratory
Morgantown, WV

Prepared by
The University of Texas at Austin

DISCLAIMER

ABSTRACT

There is an increasing opportunity to recover bypassed oil from depleted, mature oilfields in the US. The recovery factor in many reservoirs is low due to inefficient displacement of the oil by injected fluids (typically water). The use of chemical flooding methods to increase recovery efficiencies is severely constrained by the inability of the injected chemicals to contact the bypassed oil. Low sweep efficiencies are the primary cause of low oil recoveries observed in the field in chemical flooding operations even when lab studies indicate high oil recovery efficiency. Any technology that increases the ability of chemical flooding agents to better contact the remaining oil and reduce the amount of water produced in conjunction with the produced oil will have a significant impact on the cost of producing oil domestically in the US. This translates directly into additional economically recoverable reserves, which extends the economic lives of marginal and mature wells.

The objective of this research project was to develop a low-cost, pH-triggered polymer for use in IOR processes to improve reservoir sweep efficiency and reservoir conformance in chemical flooding. Rheological measurements made on the polymer solution, clearly show that it has a low viscosity at low pH and exhibits a sudden increase in viscosity (by 2 orders of magnitude or more) at a pH of 3.5 to 4. This implies that the polymer would preferentially flow into zones containing water since the effective permeability to water is highest in these zones. As the pH of the zone increases due to the buffering capacity of the reservoir rock, the polymer solution undergoes a liquid to gel transition causing a sharp increase in the viscosity of the polymer solution in these zones. This allows operationally robust, in-depth conformance treatment of such water bearing zones and better mobility control.

The rheological properties of HPAM solutions were measured. These include: steady-shear viscosity and viscoelastic behavior as functions of pH; shear rate; polymer concentration; salinity, including divalent ion effects; polymer molecular weight; and degree of hydrolysis.

A comprehensive rheological model was developed for HPAM solution rheology in terms of: shear rate; pH; polymer concentration; and salinity, so that the spatial and

temporal changes in viscosity during the polymer flow in the reservoir can be accurately modeled.

A series of acid coreflood experiments were conducted to understand the geochemical reactions relevant for both the near-wellbore injection profile control and for conformance control applications. These experiments showed that the use hydrochloric acid as a pre-flush is not viable because of the high reaction rate with the rock. The use of citric acid as a pre-flush was found to be quite effective. This weak acid has a slow rate of reaction with the rock and can buffer the pH to below 3.5 for extended periods of time. With the citric acid pre-flush the polymer could be efficiently propagated through the core in a low pH environment i.e. at a low viscosity.

The transport of various HPAM solutions was studied in sandstones, in terms of permeability reduction, mobility reduction, adsorption and inaccessible pore volume with different process variables: injection pH, polymer concentration, polymer molecular weight, salinity, degree of hydrolysis, and flow rate. Measurements of polymer effluent profiles and tracer tests show that the polymer retention increases at the lower pH.

A new simulation capability to model the deep-penetrating mobility control or conformance control using pH-sensitive polymer was developed. The core flood acid injection experiments were history matched to estimate geochemical reaction rates. Preliminary scale-up simulations employing linear and radial geometry floods in 2-layer reservoir models were conducted.

It is clearly shown that the injection rate of pH-sensitive polymer solutions can be significantly increased by injecting it at a pH below 3.5 (at a fixed bottom-hole pressure). This improvement in injectivity by a factor of 2 to 10 can have a significant impact on the economics of chemical flooding and conformance control applications. Simulation tools and experimental data presented in this report help to design and implement such polymer injection projects.

Table of Contents

ABSTRACT iv

EXECUTIVE SUMMARY x

1. Rheological Properties of HPAM Solutions 1
    1.1 Introduction 1
    1.2 Theory 3
    1.3 Materials and Tool 4
        1.3.1 Materials 4
        1.3.2 Rheometer 5
    1.4 Test Descriptions 5
        1.4.1 Dynamic Strain Sweep Test 6
        1.4.2 Dynamic Frequency Sweep Test 6
        1.4.3 Strain-Controlled Transient Test 6
        1.4.4 Steady-Rate Test 7
    1.5 Measurement Plan 7
    1.6 Rheometer Verification 8
    1.7 pH Sensitivity of HPAM 8
    1.8 Sensitivity Analysis 10
        1.8.1 Effect of Polymer Concentration 10
        1.8.2 Effect of Salinity 11
        1.8.3 Effect of Degree of Hydrolysis 12
        1.8.4 Effect of Molecular Weight 13
        1.8.5 Effect of Divalent Ions 14
    1.9 Conclusion 15
    1.10 Appendix 1-A: Viscosity Data for Various HPAM Solutions 16

2. Rheological Modeling Procedure for HPAM Solutions 61
    2.1 Introduction 61
    2.2 Derivation of A Rheological Model 63
        2.2.1 Equilibrium Chain-Extension Ratio by the Brannon-Peppas model 64
        2.2.2 Intrinsic Viscosity by Modified Mark-Houwink Equation 66
        2.2.3 A Correlation for Low Shear-Limit Viscosity 67

2.2.4 Carreau Equation 67
2.3 Determination of Viscosity Model Parameters 68
2.3.1 Determination of Definable and Calculable Parameters 69
2.3.2 Determination of Fitting Parameters 70
2.4 Matching Results with Laboratory Data 72
2.5 Conclusions 73

3. Citric Acid Coreflood Experiments 93
3.1 Introduction 93
3.2 Acid Evaluation 94
3.3 Theory and Experimental Setup 95
3.3.1 Theory 95
3.3.2 Experimental Setup 96
3.4 Experimental Procedure 97
3.4.1 Solution Preparation 97
3.4.2 Coreflood Procedure 98
3.4.3 Cation Analysis in the Effluent Samples 98
3.5 Measurement Plan 99
3.6 Berea Mineralogy 99
3.7 Experimental Results 101
3.7.1 Acid Coreflood Experiments 101
3.7.2 Cation Analysis 102
3.8 Experimental Damköhler Number 103
3.9 Conclusions 104

4. Preliminary Reactive Flow and Transport Reservoir Simulations to History-Match the Acid Coreflood Results 120
4.1 Introduction 120
4.2 Description of GEM-GHG 120
4.3 Simulation Input 122
4.4 First Trial for History Matching 123
4.5 Second Trial for Matching the Initial pH 124
4.6 Third Trial for Matching the Initial pH 124
4.7 Final Match 125
4.8 Conclusions 126

4.9 Appendix 4-A: Simulation Code for CMG-GHG....127

5. Transport Evaluation of HPAM Solutions....145
5.1 Introduction....145
5.2 Theory....149
5.2.1 Solution Properties....149
5.2.2 Petrophysical Properties....150
5.2.3 Flow Efficiency....151
5.2.4 Polymer Adsorption....152
5.2.5 Inaccessible Pore Volume and Surface Exclusion Layer Phenomenon....153
5.2.6 Polymer Effluent Concentration and Tracer Test....154
5.3 Coreflood Experimental Setup....155
5.4 Experimental Procedure....156
5.4.1 Solution Preparation....156
5.4.2 Calibration Curve for a Capillary Viscometer....157
5.4.3 Polymer Coreflood Experiment....158
5.4.4 Tracer Tests....159
5.5 Measurement Plan....160
5.6 Analysis of Coreflood Experiments....160
5.6.1 Injection Polymer Preparation....160
5.6.2 Base Case....160
5.6.3 Effect of pH....162
5.6.4 Effect of Polymer Concentration....163
5.6.5 Effect of Molecular Weight....164
5.6.6 Effect of Salinity....165
5.6.7 Effect of Degree of Hydrolysis (DH)....166
5.6.8 Effect of Flow Rate....166
5.6.9 Desorption....167
5.7 Conclusions....167

6. Development and Use of a Simulation Model for Mobility/Conformance Control Using a pH-Sensitive Polymer....201
6.1 Introduction....201
6.2 Simulation Model Description....202

6.3 Core Flood History Macthing 203
6.3.1 Simulated Mineral Interaction Effects 205
6.3.2 Sensitivity to One-Mineral Model with First-Order Mineral Reaction Rate 206
6.3.3 Sensitivity to Weak Acid Injection 207
6.4 Conformance Control Using pH-Sensitive Polymer: Linear Geometry Model 207
6.5 Conformance Control Using pH-Sensitive Polymer: Radial Geometry Model 209
6.6 Improved Injectivity Using pH-Sensitive Polymer....211
6.7 Conclusion 211
6.8 Appendix 6-A: Mineral Reaction Rate Equation Used in GEM-GHG Simulator....212
6.9 Appendix 6-B: Calculation of Damköhler Number....212

7. Application of pH-Triggered Polymers in Fractured Reservoirs to Increase Sweep Efficiency....225
7.1 Introduction....225
7.2 Experimental Method....227
7.2.1 Preparation of fractured cores....227
7.2.2 Polymer preparation....228
7.2.3 Coreflood Set up 228
7.2.4 Batch experiments....229
7.3 Results and Discussion 229
7.3.1 Geochemical reactions – batch experiments....229
7.3.2 Reduction in permeability of fractured sandstone cores....230
7.3.3 Reduction in permeability of fractured carbonate cores 231
7.3.4 Constant pressure injection 232
7.3.5 Depth of polymer propagation into fractured reservoirs....232
7.4 Conclusion 233

List of Tables 245

List of Figures 252

Bibliography 268

Abbreviations and Nomenclature 277

EXECUTIVE SUMMARY

1. PROBLEM STATEMENT

This report proposes the use of Partially Hydrolyzed Polyacrylamide (HPAM) in low pH conditions for in-depth conformance control applications, as well as for near-wellbore injection profile control in polymer flooding applications. HPAM is a water-soluble polymer most commonly used for polymer flooding applications due to its low cost and good viscosifying ability. Further, it has a molecular structure that allows for better injectivity into porous media than microgels, even in neutral pH conditions. The presence of anionic carboxyl groups on the HPAM chain again results in the pH dependence on viscosity, created by the coiling and uncoiling mechanism of polymer chains. As described later in more detail, the HPAM polymer is also attractive due to the ability to adjust its "degree of hydrolysis," which affects the degree of viscosity change according to pH.

This research intends to exploit the pH sensitivity of HPAM in order to develop a more efficient polymer flood process. The low-pH polymer flood process is intended to inject HPAM solution, at low pH conditions, into the reservoir. Because polymer molecules are in a tightly-coiled state and the viscosity is low, the polymer solution can pass through the near wellbore region with a relatively low pressure drop. This can save a significant amount of electrical power during injection, and also enables the use of large-molecular-weight polymers without the danger of their mechanical degradation. The low-pH polymer injection can also avoid the generation of unwanted fractures near the wellbore. Away from the near wellbore region, the polymer solution becomes thickened by a spontaneous reaction between the injected acid solution and the resident rock mineral components – thus lowering the brine mobility and increasing oil-displacement efficiency, as intended.

Another possible application of low-pH polymer injection is conformance control in a highly heterogeneous reservoir. During the secondary recovery stage, water flooding can sweep most oil from the high permeability zones, but leave oil in the low permeability zones. The polymer solution, under low pH condition, can be placed deep into such high permeability sands with a relatively low injection pressure. The use of a high polymer concentration, and/or a polymer high in molecular weight, will allow

effective blocking of the high-permeability zones. With the generation of very high viscosity, induced by pH increase, the thickened polymer solution in the high-permeability sands can divert the subsequently injected water to the low-permeability zone, so that the oil trapped in that zone can be efficiently recovered.

For both applications, a proper acid solution is necessary to buffer the polymer solution at a low pH condition during the propagation of the polymer slug some distance into the reservoir. Both applications are restricted to sandstone reservoirs, because the acid consumption in carbonate reservoirs is expected to be too rapid.

In addition, the use of microgels is evaluated either for conformance control application in high permeability reservoirs or for water / gas shut-off application in fractured reservoirs. Microgels show much more pronounced viscosity sensitivity to pH than HPAM polymers and, however, they have the problems of high retention and mechanical filtration in low- to mid- permeability rocks in low pH conditions (Choi, 2005; Choi *et al.*, 2006). Therefore, it is attractive to use microgels in reservoirs where good transport is guaranteed (such as high permeability or fractured reservoirs) because microgels can be used as effective blocking agents with economic advantages.

2. PROJECT OBJECTIVE

The overall objective of this project is to develop a low-cost, pH triggered polymer for use in polymer flooding to improve reservoir sweep efficiency and reservoir conformance in chemical flooding.

The specific objectives of this research project are to:

- Quantify the rheological properties of HPAM solutions, such as: steady-shear viscosity and viscoelastic behavior as functions of pH; shear rate; polymer concentration; salinity, including divalent ion effects; polymer molecular weight; and degree of hydrolysis.
- Develop comprehensive rheological correlations for HPAM solutions in terms of: shear rate; pH; polymer concentration; and salinity, so that the spatial and temporal changes in viscosity during the polymer flow in the reservoir can be accurately modeled.
- Select a proper acid and its performance for optimal gellation in the desired reservoir location. This is done with a series of acid coreflood experiments to understand the

geochemical reactions relevant for both the near-wellbore injection profile control and for conformance control applications.

- Quantify transport of various HPAM solutions in sandstones, in terms of permeability reduction, mobility reduction, adsorption and inaccessible pore volume with different process variables: injection pH, polymer concentration, polymer molecular weight, salinity, degree of hydrolysis, and flow rate. This is done with a series of laboratory coreflood experiments.
- Evaluate the use of microgels in the application of conformance control in high permeability reservoirs. The new simulation capability to model the deep-penetrating mobility control or conformance control using pH-sensitive polymer is developed. History matching of coreflood acid injection experiments to estimate geochemical reactions and reaction rates occurring in Berea cores is then performed. Preliminary scale-up simulations employing linear and radial geometry floods in 2-layer reservoir models are done.
- Evaluate the use of microgels for water / gas shut-off application in fractured reservoirs. Extensive laboratory works are done using outcrop cores with artificial fractures for both sandstone and carbonate rocks.

3. PROJECT TASKS

The proposal originally presented six Tasks to meet the objectives stated above. In the process of conducting the research it was determined that the project objectives could best be met with the five Tasks listed below. The use of CO_2 as a pH control chemical was found to be of low priority based on early geochemical simulations and was not pursued as one of the Tasks due to time and resource constraints. The project was conducted in accordance with the Tasks that are summarized below.

Task 1: Polymer characterization for subsurface application

Task 2: Core flow tests for polymer propagation

Task 3: Conformance control and sweep in heterogeneous formations

Task 4: Core flood experiments for pH and polymer propagation on porous media

Task 5: Simulation of potential sweep improvement with pH triggered polymer

4. APPROACH AND METHODOLGY

The approach and methodology of this project are discussed below.

4.1 Polymer Characterization for Subsurface Application

The effects of the following variables were investigated: pH; shear rate; polymer concentrations; salinity; molecular weight; and the degree of hydrolysis on rheological properties of HPAM. The goal is to understand how the HPAM rheology changes with the above variables, and to select the optimal rheological conditions to satisfy the variety of process conditions required for field applications. Along with a wide range of pH (2 to 10), which is a major variable in this research, the additional six variables affecting the HPAM rheology were systematically studied: (a) shear rate from 0.1 to 1000 s^{-1}; (b) polymer concentration from 2000 to 8000 ppm; (c) molecular weight from 8 to 20 million; (d) degree of hydrolysis from 0 to 100%; (e) salinity from 0.5 to 10%; and (f) the presence of divalent ions of calcium. The ARES LS-1 rheometer (from TA Instruments), suitable to low viscosity solutions, was used to measure the rheological properties of HPAM, including viscoelastic behaviors at various oscillatory strains, as well as steady-shear viscosities.

A comprehensive rheological model for HPAM solutions was developed to describe the spatial and temporal viscosity changes during polymer flow in the reservoirs. It is a modification of the rheological model for microgels (Huh *et al.* 2005), because the viscosifying mechanism of HPAM solutions is quite similar to that of the polyacrylate microgels. The procedure of fitting the laboratory-measured data to obtain the empirical parameters of the viscosity model is also developed and described.

4.2 Coreflood Experiments: pH Propagation

The selection of a proper acid as a pH control agent was evaluated to ensure a low-pH environment near the injection wellbore, and thereby prevent viscosification of the injected HPAM polymer solution. Both strong acid (hydrochloric acid) and weak acid (citric acid) were evaluated to find the proper acid for this application. A 1" diameter Berea core plug was prepared by epoxy molding to avoid contact between acid and the steel if a core-holder is used. Various variables were chosen to quantify geochemical reactions between rock mineral components and acid solution: (a) pH = 2.5

and 3.5; (b) flowrate = 1 and 2 ml/min; (c) core length = 5 and 8"; and (d) shut-In effects. The pH of the effluents from corefloods was measured, and the effluent samples were also collected at the end of the core in order to analyze the cation components in the effluents. Mineralogy of Berea sandstone before and after acidizing was identified by petrographic analysis method in order to provide information regarding minerals that participate in the reactions.

Preliminary reactive flow and transport reservoir simulations were also carried out to characterize geochemical reactions; this was achieved by history-matching the results from the laboratory acid coreflood experiments. A commercial GEM simulator with additional Green House Gas geochemical reaction capabilities (from Computer Modeling Group) was used in this study. Following up on the recent simulation work by Benson (2007), effluent pH and cation concentration histories for the five coreflood cases were history-matched in order to identify the reaction parameters.

4.3 Transport of HPAM Solutions: Coreflood Experiments

This task consists of polymer flow corefloods, with the aim of understanding and quantifying the transport mechanisms of HPAM solution in a Berea core, specifically in terms of: transport efficiency; retention; and inaccessible pore volume. The same variables investigated for the rheological measurements were again studied: (a) pH = 2.5, 3.5, and 6.0; (b) degree of hydrolysis = 0, 25, and 30%; (c) molecular weight = 8 and 20 million; (d) polymer concentration = 0.5 and 0.8%; and (e) salinity = 2.0 and 3.0%. A Hassler core-holder with two pressure taps was set up and two pressure transducers, 100 and 1000 psi for each tap, were connected to cover a wide range of pressure drop measurements during brine flow and the polymer flow. A long capillary tube was installed at the effluent side serving as a capillary viscometer, while measuring pressure drop; the pressure drop can be converted to the polymer effluent concentration. This can be done for each core experiment by empirical correlations obtained from separate capillary tube tests with different polymer concentrations. The reagent-grade sodium bromide was added to the injection solution for the tracer test. After passing through the pH meter, the effluent fractions were collected by a fraction collector, in order to measure the effluent bromide (tracer) concentration profile with bromide-selective electrode.

4.4 Simulation Model for Mobility/Conformance Control Using a pH-Sensitive Polymer

Polymer-bank placement design and process scale-up requires simulation of transport of microgel, acid-mineral geochemical reactions, pH changes, and the coupling between aqueous phase composition and viscosity. Such a capability was implemented in a commercial reservoir simulator and preliminary simulations verify the operation and effectiveness of the complex new features, which can describe both the mobility and conformance control applications. Determination of reservoir mineralogy and mineral reaction rates is critical to modeling *in-situ* pH changes accurately. History matching of coreflood acid injection experiments was used to estimate geochemical reactions and reaction rates occurring in Berea cores. Linear and radial geometry floods in 2-layer reservoir models were carried out as preliminary scale-up simulations. Acidic fluids can be propagated farther into a reservoir in a low-pH state, using high injection velocity, an acid preflush, or weak acids. The Damkohler number was found to be a useful dimensionless quantity for characterizing acid floods with pH-sensitive polymer. Slugs of pH-sensitive polymer improve oil recovery better than continuous polymer flooding or waterflooding.

4.5 Application of pH-Triggered Polymers in Fractured Reservoirs to Increase Sweep Efficiency

We used commercially available polymers which exhibit low viscosity at a pH below 3 but transform to gels at pH > 4. Polymer solutions were injected through artificial fractures in outcrop cores. Both sandstone and carbonate rocks raise the polymer solution pH. The presence of acid-soluble minerals containing cations such as calcium can independently trigger viscosification by precipitating the polymer. After polymer injection, a shut-in time allows further reaction to increase the pH and thus affects the Permeability Reduction Factor (PRF), the ratio of original fractured core permeability to treated core permeability. The PRF was measured to be in the range of 200 to 5 during the various experiments. The gelation is faster and PRF is higher in carbonates than in sandstones. Because the neutralization capacity of a core is large, it is possible to approximate reactive transport in a reservoir by continuously re-circulating

the polymer effluent. Experiments showed gel-like characteristics after 30 pore volumes of recirculation in Berea sandstone.

Overall Benefits of the Research

The use of chemical flooding methods to increase recovery efficiencies is severely constrained by the inability of the injected chemicals to contact the bypassed oil. Low sweep efficiencies are the primary cause of low oil recoveries observed in the field in chemical flooding operations even when lab studies indicate high oil recovery efficiency.

This research project presents a widely used, low-cost, pH-triggered polymer for use in IOR processes to improve reservoir sweep efficiency and reservoir conformance in chemical flooding. Rheological measurements made on the polymer solution, clearly show that it has a low viscosity at low pH and exhibits a sudden increase in viscosity (by 2 orders of magnitude or more) at a pH of 3.5 to 4. This implies that the polymer would preferentially flow into zones containing water since the effective permeability to water is highest in these zones. As the pH of the zone increases due to the buffering capacity of the reservoir rock, the polymer solution undergoes a liquid to gel transition causing a sharp increase in the viscosity of the polymer solution in these zones. This allows operationally robust, in-depth conformance treatment of such water bearing zones and better mobility control.

The rheological properties of HPAM solutions were measured. These include: steady-shear viscosity and viscoelastic behavior as functions of pH; shear rate; polymer concentration; salinity, including divalent ion effects; polymer molecular weight; and degree of hydrolysis. A comprehensive rheological model was developed for HPAM solution rheology in terms of: shear rate; pH; polymer concentration; and salinity, so that the spatial and temporal changes in viscosity during the polymer flow in the reservoir can be accurately modeled.

A series of acid coreflood experiments were conducted to understand the geochemical reactions relevant for both the near-wellbore injection profile control and for conformance control applications. These experiments showed that the use hydrochloric acid as a pre-flush is not viable because of the high reaction rate with the rock. The use of citric acid as a pre-flush was found to be quite effective. This weak acid has a slow rate

of reaction with the rock and can buffer the pH to below 3.5 for extended periods of time. With the citric acid pre-flush the polymer could be efficiently propagated through the core in a low pH environment i.e. at a low viscosity.

The transport of various HPAM solutions was studied in sandstones, in terms of permeability reduction, mobility reduction, adsorption and inaccessible pore volume with different process variables: injection pH, polymer concentration, polymer molecular weight, salinity, degree of hydrolysis, and flow rate. Measurements of polymer effluent profiles and tracer tests show that the polymer retention increases at the lower pH.

A new simulation capability to model the deep-penetrating mobility control or conformance control using pH-sensitive polymer was developed. The core flood acid injection experiments were history matched to estimate geochemical reaction rates. Preliminary scale-up simulations employing linear and radial geometry floods in 2-layer reservoir models were conducted.

It is clearly shown that the injectivity of pH-sensitive polymer solutions can be significantly increased by injecting it at a pH below 3.5 (at a fixed bottom-hole pressure). This improvement in injectivity (by a factor of 2 to 10) can have a significant impact on the economics of chemical flooding and conformance control applications. Simulation tools and experimental data presented in this report help to design and implement such polymer injection projects.

1. Rheological Properties of HPAM Solutions

1.1 INTRODUCTION

High-injectant viscosity is a key requirement to ensure good volumetric sweep efficiency for secondary or tertiary recovery of oil. Typically, polymers are used to increase the viscosity of the displacing fluid, thereby reducing its mobility, and effectively suppressing viscous channeling in heterogeneous oil reservoirs. One of the most widely used polymers for mobility control is partially-hydrolyzed polyacrylamide (HPAM). It is a water-soluble polyelectrolyte with negative charges along its chain; the repulsion between the negative charges contributes to the chain extension, thereby resulting in high viscosity. Due to this feature, HPAM can be used in lower quantities, as compared to non-ionic polymers, while still yielding the desired viscosity levels. Further, the ready availability and low cost of HPAM promotes its wide use in the oil recovery business.

The viscosity of HPAM in solution depends on: its molecular weight; its degree of hydrolysis; its concentration; the brine salinity; and reservoir conditions (pH, temperature, and pressure). The polymer property and concentration are manageable in the preparation stage on the surface, while the reservoir conditions are not. Salinity and pH are two major factors that influence the viscosity of HPAM solutions. Due to the shielding of negatives charges, the presence of electrolytes or protons drastically reduces viscosity (the concentrations of electrolytes and protons are increased in high salinity or low pH, respectively). Divalent ions have considerably more effect on viscosity than do monovalent ions. Temperature is another significant cause of viscosity reduction. As the designs of EOR processes are developed and improved, (i.e., the addition of alkali or acid, use of soft water, and high-temperature applications), it will be critical to understand the effects of the above variables on polymer viscosity.

In the 1970s, a number of researchers attempted to quantify the influence of the above variables on the HPAM viscosity through laboratory measurements (Mungan, 1969; Mungan, 1972; Nouri *et al*., 1971; Ferrer, 1972; Martin *et al*., 1975; Szabo, 1979). They investigated viscosity dependence on polymer concentration, salinity, molecular weight, degree of hydrolysis, and temperature. However, pH effects have not been systematically investigated with a few exceptions (Ferrer, 1972; Szabo, 1979). Since the

1980s, the primary research focus for viscosity behavior has been to study the effects of divalent ions (Ward *et al*., 1981; Nashawi, 1991). It was reported that calcium ions cause greater viscosity reduction than magnesium ions, and the mixture of divalent and monovalent ions results in greater (thus more detrimental) viscosity reduction than individual ions. Key studies are summarized chronologically in **Table 1.1**.

Recently, there has been increased interest in the non-Newtonian rheology of the polymer solution, such as the effects of viscoelasticity on oil recovery (Wang *et al*., 2001). Of HPAM's used in oil field applications, those very high in molecular weight exhibit viscoelasticity, making the elastic (storage) component as important as the viscous (dissipate) component. It has been shown that viscoelastic behavior is associated with shear degradation in porous media (Hill *et al*., 1974; Maerker, 1975; Tinker *et al*., 1976; Seright, 1983). The high elongational viscosities and stresses caused by the elasticity of the polymer tear the polymer chain at a high shear rate. Such shear degradation has an important implication for high-rate polymer flow at near wellbore region. Another potential contribution of elastic property is shear thickening of the polymer solution in porous media (Delshad *et al*., 2008). When polymer flows through consecutive pore throats and bodies in porous media at a very high shear rate, the apparent viscosity rapidly increases (Maerker, 1984; Delshad *et al*., 2008). In several recent papers which discuss the influence of polymer viscoelastic property on polymer flooding, enhancement of displacement efficiency is attributed to polymer viscoelastic properties (Wang *et al*., 2001; Wu *et al*., 2007).

Our low pH application of HPAM requires developing detailed rheological property correlations for a wide range of pH in order to characterize flow behavior at such pH conditions. Thus, we carried out extensive bulk rheological measurements of HPAM solutions for a wide pH range (2 ~ 10), including steady shear tests and oscillatory tests. We also performed sensitivity studies of polymer rheology on the following: polymer concentration; molecular weight; degree of hydrolysis; salinity; and divalent ion. Note that pH is used as a major variable for all the sensitivity studies. All measurements were carried out by the ARES LS-1 rheometer, with double-wall cup couette geometry, suitable for low-viscosity samples. These bulk rheology measurements will provide viscosity data required for a rheological model, described in **Chapter 2**, and polymer flooding evaluation, described in **Chapter 5**.

1.2 THEORY

To aid in the interpretation of our oscillatory measurements, a brief introduction to "viscoelasticity" is provided here. Elastic property is defined as the ability of the material to recover its original configuration after being deformed. Hooke's law describes a linear elastic relationship for an ideal solid, where the shear stress (τ) is proportional to the applied shear strain (γ):

$$\tau = G\gamma \tag{1.1}$$

The constant of proportionality is the elastic modulus, which is a measure of its stiffness or the ability to resist deformation. Similarly, viscosity represents the ability of the material to dissipate deformational energy through flow. A linear viscous relationship for an ideal viscous fluid obeys Newton's law. The shear stress (τ) is proportional to the rate of shear strain ($d\gamma/dt$):

$$\tau = \eta \frac{d\gamma}{dt} \tag{1.2}$$

The combined behavior that the material exhibits is called 'viscoelasticity.' The simplest constitutive relationship for viscoelastic fluids is the Maxwell model, which combines the above linear models (2.1 and 2.2), and is only applicable to small deformations. The Maxwell model does not realistically represent the rheology of HPAM solutions; however, it can provide qualitative insight regarding the viscoelasticity of the fluid. Two important quantities need to be addressed to interpret viscoelasticity. The first is elastic or storage modulus, *G'*, which represents the solid-like elastic component in the response of sinusoidal strain or stress; this property is exactly in phase with applied frequency, ω, and gives information on the elasticity of the fluid. The second quantity which must be addressed is viscous or loss modulus, *G"*, which describes liquid-like response, out of phase with the frequency by $\pi/2$. It provides viscous or dissipative information of the fluid. The unit for both moduli is force per unit area. Other dynamic quantities that can be measured in oscillatory tests are summarized in **Table 1.2**. In this research, the simple Maxwell model with only two moduli, *G'* and *G"*, is used for the interpretation of viscoelasticity of HPAM solutions.

Figure 1.1 shows the typical Maxwell type behavior of two moduli in oscillatory testing. The loss modulus predominates in the range of very low frequencies, which means liquid-like response governs. As the frequency increases, the storage modulus increases at a faster rate than the loss modulus, and the solid-like response governs after a certain frequency. Such crossover frequency has an important meaning: the longest relaxation time can be approximated by taking the inverse of the numerical value in radians per second. Physically, the relaxation time indicates the time that it takes for the deformed material, e.g., a polymer chain, to regain its original configuration, and it is in direct relation to the degree of elasticity. If one sample shows higher relaxation time, then it has a higher degree of elastic property than does the other – thus, it will take longer for the deformed material to regain its original configuration.

1.3 MATERIALS AND TOOL

1.3.1 Materials

A series of partially-hydrolyzed polyacrylamide (HPAM), unhydrolyzed non-ionic polyacrylamide (PAM), and polyacrylic acid (PAA), provided from SNF Inc., were chosen for the comparison of the different variables. **Table 1.3** summarizes all the polymers used in these measurements with their important properties. Reagent-grade sodium chloride (NaCl) and calcium chloride ($CaCl_2$) were used as salts to prepare brine. High concentrations of acid and alkali solution (which minimize the dilution effect [10% hydrochloric acid (HCl) and 1.0M sodium hydroxide (NaOH)]) were used to generate the desired pH of the polymer solution.

The 200 ml sample for each measurement was prepared on a mass-balance base in a beaker. The required amount of salts were added in pre-weighed de-ionized water (with a resistivity of greater than 18 MΩ·cm), and the brine was mixed by using a magnetic stirrer for at least 30 minutes. The polymers were gently added on the 2/3 spot of a well-developed vortex shoulder, built up by the high-speed mixing, and the vinyl film was covered and sealed after purging the void space with non-reactive Argon gas to prevent contact with air. The speed was reduced to the medium speed and the polymer solution was further mixed for at least one day (but less than two days) to guarantee complete hydration. The solutions for high molecular weight polymers, such as Flopaam

3630S, were prepared with special care, by mixing for more than two days (but less than three days). In the interest of accurate measurements, polymer concentration change was avoided by not performing filtration.

Once the sample was ready, the pH was decreased to 2.0 by adding 10% hydrochloric acid. The pencil-thin pH electrode was used to minimize the solution lost by contact, and the pH value was read after more than 5 minutes of mixing in order to ensure the homogenous acidization or alkalization. 8.5ml of the solution, the required amount for the measurement in double-wall cup couette geometry, was sampled by a syringe and then the measurement was carefully performed in the sequence described in Section 2.4. The pH of the solution was stepped up as 3, 4, 5, 6, 8, and 10 by adding 1.0M sodium hydroxide; the samples were taken out at each step to perform the same series of measurements.

1.3.2 Rheometer

For the rheology measurements, ARES LS-1 (the Advanced Rheometric Expansion System Low Shear-1) from TA Instruments, which has independent strain and stress controls, was used as shown in **Figure 1.2**. This rheometer is suitable for low-viscosity fluid, as it has a High Performance LS air-bearing motor and patented Force Rebalance Transducer™ (FRT). It measures the torque generated by the sample in response to either an oscillatory or steady-shear strain deformation. Strain is applied by motor; torque is sensed by the transducer, and converted to time-varying or steady properties whose results are displayed in the rheometer software named TA Orchestrator. The double-wall Couette geometry was used because it can handle low-viscosity fluids and it enables the use of relatively small sample volumes.

1.4 TEST DESCRIPTIONS

Table 1.4 summarizes the test sequence performed for one sample with its input parameters. As dynamic-mode tests, strain and frequency sweeps were performed to investigate viscoelastic property, while two steady-mode tests, including transient and steady shear measurements, were done to quantify accurate steady shear viscosities of various HPAM solutions. The details for each test are described in the following sub-sections.

1.4.1 Dynamic Strain Sweep Test

Dynamic strain sweep performs successive measurements at logarithmic step increases in strain, while holding frequency and temperature constant, to determine the limits of linear viscoelasticity and torque levels. In our measurements, the sweeps were conducted over the range of strain between 1 and 200% at a frequency of 10 rad/s. As an example, **Figure 1.3** shows the result plot of dynamic strain sweep test for 0.5% Flopaam 3330S, prepared in 0.5% sodium chloride brine at pH = 10.2. The viscoelasticity represented by two moduli (*G'* and *G"*) remain constant up to about 40% strain input, after which it starts to decrease, indicating the measurement being out of linear viscoelastic regime. In this case, 5% strain was chosen for the next dynamic frequency sweep test.

1.4.2 Dynamic Frequency Sweep Test

The dynamic frequency sweep test was performed to investigate viscoelastic behavior of samples in the specified range of oscillatory frequencies. Similar to strain sweep, successive measurements at logarithmic step increases in frequency were conducted at constant strain and temperature. At the strain chosen within the linear viscoelastic region in the previous dynamic sweep test, the sweeps were performed over the frequency range between 0.1 and 100 rad/s. **Figure 1.4** shows the result of the dynamic frequency sweep tests for 0.5% Flopaam 3330S, prepared in 0.5% sodium chloride brine at pH = 10.2. The result plot closely follows the typical Maxwell-type behavior, with the crossover point indicated.

1.4.3 Strain-Controlled Transient Test

The transient test accurately measures the steady-state properties at a constant shear rate during the selected time duration. Four separate zones (where the user defines a shear rate and its time duration) can be programmed to investigate stress growth; time required to reach steady-state flow behavior; and relaxation before and after steady shear. The major purpose of our measurements is to obtain an accurate viscosity at a specific shear rate. The tests for four shear rates (1, 10, 100, 1000 s^{-1}) were separately run for

each sample, with a time-zone schedule of 20 sec pause (zero shear rate), 100 sec measurement, and 50 sec pause. The example for 0.5% Flopaam 3330S, prepared in 0.5% sodium chloride brine, at pH = 10.2 at 1000 s^{-1} shear rate, is shown in **Figure 1.5**. It is observed that the stress response is overshot at the beginning of the measurement and also has "tails" at the end (*i.e.*, symptoms of the viscoelasticity of the polymer solution). The shear steady viscosity at a specific shear rate is obtained by taking an average of the values in plateau region.

1.4.4 Steady-Rate Test

As the last step, the steady-rate test was performed to generate flow curves for the fluid sample. This test is conducted by varying magnitudes of steady shear rate, at constant temperature to measure steady viscosities. The shear deformation varies from 0.1 to 1000 s^{-1}, with a 20 sec delay before and after measurement, and a 30 sec measurement duration set for each measurement to obtain accurate properties. **Figure 1.6** shows the measurement result of 0.5% Flopaam 3330S, prepared in 0.5% sodium chloride brine, at pH = 10.2, which shows typical non-Newtonian behavior of the polymer solution. In the very low shear deformation, Newtonian behavior (which is independent of shear rate) is identified, and after about 0.2 s^{-1}, the shear thinning behavior is clearly observed.

1.5 MEASUREMENT PLAN

Figure 1.7 shows the plan for the rheological measurements of HPAM solutions. As a base case, 0.5% Flopaam 3330S (which has 8M molecular weight and 25 – 30% degree of hydrolysis), prepared in 0.5% sodium chloride brine, was chosen. Although 0.5% polymer concentration is relatively high for EOR applications, it was selected to investigate clear rheological dependence on the variables. The effects of various variables on the polymer rheology were systematically investigated and compared. These were variables such as: (a) degree of hydrolysis; (b) salinity; (c) polymer concentration; (d) molecular weight; and (e) divalent ion. Note that temperature was maintained at 25 degree C for all measurements.

1.6 RHEOMETER VERIFICATION

Prior to the measurements for case studies, the performance of ARES LS-1 rheometer was verified in two ways: reproducibility and consistency with another instrument. Reproducibility was confirmed by repeating the measurements for the base case polymer sample. In the measurements, the solution preparations were also repeated. Therefore, this test includes the reproducibility of solution preparations as well as the functioning of the rheometer. **Figure 1.8** shows the comparison results of the viscosities between the first and second measurements and **Figure 1.9** compares the results of dynamic frequency sweep tests between the first and second measurements at pH = 2.0 and 10.0. Both results are in perfect match.

A rotational viscometer Fann-35A was used to check the consistency with the rheometer. This viscometer is designed to measure only the viscosity of the solutions at different rotational speeds: 3, 6, 100, 200, and 600 rpm. It simply consists of bob and rotor sleeve. The rotation of the rotor sleeve causes fluid flow, which exerts a torque on the stationary bob attached to the torsion spring. The torque is expressed as the dial-reading, which can be converted to the viscosity by simple power law theory. **Figure 1.10** compares the results between the ARES LS-1 rheometer and the Fann 35A viscometer and confirms quite good matches for both results. Note that this plot was prepared as viscosity versus shear rate at specific pH. It is difficult to meet specific shear rates in the measurements of the Fann 35A viscometer because only rotational speed can be controlled, and the speed is converted to shear rate by several parameters, such as consistency and flow-behavior index.

1.7 PH SENSITIVITY OF HPAM

HPAM has two functional groups (amino and carboxyl) along its ethylene back-bone chain, as shown in **Figure 1.11**. The carboxyl groups mainly control its pH-sensitive rheological properties. The carboxyl groups can exchange protons with dissolved salts in water, depending on pH conditions. At a high pH, the carboxyl groups dissociate and are negatively charged, thereby developing a strong electrostatic repulsion between them. This repulsion makes the polymer chains stretch, resulting in the increased solution viscosity. On the other hand, low pH causes all carboxyl groups to be protonated with hydrogen ions, resulting in no charges on the polymer chain. The

polymer molecules are now in a tightly coiled state which decreases viscosity. This mechanism is clearly demonstrated in **Figure 1.12,** which shows one example of viscosity behavior of HPAM solution as a function of pH. This behavior is reversible and physical, caused by the change of proton concentrations.

The pH dependence of HPAM solution is characterized by transition zones where the viscosity suddenly changes. As shown in **Figure 1.12**, the transition occurs between two critical pH's, 3 and 6, with the lower and higher pH regions showing almost plateau viscosity behavior. It can be concluded that all carboxyl functional groups on HPAM are saturated with protons at pH = 3; below this level, excessive protons only contribute to decreasing pH. On the other hand, the carboxyl groups are totally dissociated with protons at pH = 6, where the polymer molecules reach their maximum extension, resulting in the maximum viscosity. The shear rate dependency of HPAM solution is shown in **Figure 1.13,** plotted as the measured viscosity against the shear rate. As the shear rate increases, the pH sensitivity on the viscosity becomes smaller. The reason can be found in that HPAM shows a shear thinning behavior – as the shear rate increases, the viscosity decreases. Because high shear causes polymer chains to be highly deformed and lined up in flow direction, the size of polymer chains (triggered by pH) will only slightly affect the change in viscosity.

Figures 1.14 and 1.15 show the response of storage and loss moduli as a function of frequency for different pH's. The results show that both moduli increase as the pH increases, and the transition zone between 3 and 6 is clearly observed from modulus curve shift (*i.e.*, broader space between curves at pH 3 and 6). **Figure 1.16** illustrates the pH sensitivity of relaxation time that can be estimated by taking reciprocal of frequency at the cross-over point between two moduli. As pH increases, relaxation time increases, which means that the elasticity of HPAM polymer solution increases. It is also interesting to see that the approximate shape of this curve similarly corresponds to that of the viscosity curve, as shown in **Figure 1.12**. **Figure 1.17** shows another demonstration of dynamic behavior where loss modulus is plotted against elastic modulus. It forms a circular shape, which indicates that two moduli increase together at a certain point, after which the viscous modulus decreases as the elastic modulus increases; this corresponds to the typical Maxwell-type behavior shown in **Figure 1.1**.

1.8 SENSITIVITY ANALYSIS

Described below are the results for pH sensitivity studies of HPAM on the following variables: polymer concentration; salinity; degree of hydrolysis; molecular weight; and divalent ions. For an effective comparison, the figures for each study are arranged as the following sequences and details of measurements in sensitivity studies are given in Section 1.10.

Plots for shear steady viscosity

(a) Viscosity curves measured at four shear rates (1, 10, 100, 1000 s^{-1}) as a function of pH for the variable change.

(b) Viscosity curves measured at one shear rate of 10 s^{-1} as a function of pH for the variable change (this plot is prepared by selecting the curves at shear rate of 10 s^{-1} from plot (a) for clear comparison).

(c) Viscosity curves as a function of the variable for different pH's.

(d) Flow curves (viscosity as a function of shear rate) for the variable change at two different pH's: 2 and 10.

Plots for time-varying properties

(e) Elastic modulus curves as a function of frequency for the variable change at two different pH's: 2 and 10.

(f) Storage modulus curves as a function of frequency for the variable change at two different pH's: 2 and 10.

(g) Elastic modulus curves as a function of storage modulus for the variable change at two different pH's: 2 and 10.

(h) Relaxation time curves as a function of pH for the variable change.

1.8.1 Effect of Polymer Concentration

The polymer concentration was varied from 0.2, to 0.5, to 0.8%, while all other variables were kept constant. As shown in **Figures 1.18(a)** and **(b)**, the viscosity increases as the polymer concentration increases for all pH regions; the curves are shifted upwards as the concentration increases. The increased numbers of polymer molecules result in more interactions between polymer chains, which cause more frictional effects

to increase the viscosity. Exponential proportionality of viscosity on polymer concentration is shown in **Figure 1.18(c)**. This is because the polymer chains overlap extensively, behaving almost like weak gels. **Figure 1.18(d)** shows the flow curves for different polymer concentration at two pH's; 2 and 10. The results show that the solution at lower pH and lower polymer concentration tends to exhibit more Newtonian behavior. In the case of 0.2% polymer concentration at pH = 2.0, the polymer solution shows a perfect Newtonian behavior. Some viscosities of higher concentration at low pH are less than those of low concentration at high pH, indicating that the pH influence on the viscosity is considerably more pronounced than that of the polymer concentration. Note that viscosities of 0.2% polymer at low pH and 1000 s^{-1} shear rate exceed those at lower shear rates with the same concentration; this is marked with a circle in **Figure 1.18(a)**. This measurement artifact is due to the flow inertia normally occurring in a concentric-cylinder geometry at high-speed for low-viscosity fluid flow. Secondary flow (Taylor vortices) leads to extra dissipation, which superficially increases viscosity (Barnes, 2000).

Figures 1.18 (e) and (f) respectively compare the elastic and loss moduli as functions of frequency for two different pH's, *i.e.*, pH =2.0 and 10.0. **Figure 1.18(g)** displays the relationship between elastic and loss moduli for the same two pH's. It is shown that, similar to the viscosity behavior, the viscoelastic property of polymer solution remarkably increases for all pH regions as the polymer concentration increases. On the other hand, the relaxation time shows a slightly different behavior from the viscosity. As shown in **Figure 1.18(h)**, the approximate relaxation time hardly changes as a function of pH in the case of 0.2% polymer concentration, indicating that the elastic property remains constant irrespective of pH change. However, the response of relaxation time on pH in high polymer concentration is remarkably pronounced.

1.8.2 Effect of Salinity

A wide range of salinities – 0.5, 1.0, 3.0, and 10.0% – was chosen for its effect on solution rheology. As mentioned earlier, the presence of salts has a buffering effect, shielding the charges along the polymer chain with the salt cations, resulting in molecular shrinkage with the consequent viscosity reduction. This mechanism is quite similar to the pH effect on viscosity in which protons replace the role of salt cations. The inverse

proportionality of the viscosity to salinity is illustrated in **Figures 1.19(a)** and **(b)**. It is also observed that critical salinity (above which salinity no longer affects viscosity) exists because the numbers of polymer molecules to be shielded by salt cations are limited. In this case, the critical salinity is approximately 3.0% as shown in **Figure 1.19(c)**. In the region above the critical salinity, the viscosity is observed to increase very slightly as the salinity increases. This may be due to the solvent quality (Sorbie, 1991). Poor solvent quality for higher salinity causes the interaction between polymers to become more important, thus resulting in the viscosity increase (Sorbie, 1991). However, the effect is not as significant as the charge effect. Another observation is that the influence of salinity on the viscosity at high pH is significant, while the salinity only slightly affects the viscosity at low pH. Most molecules are already shrunk by high proton concentration at low pH and, therefore, there is no more influence by salinity. As demonstrated in **Figure 1.19(d),** three almost overlapping curves at low pH indicate that the above interpretation may be reasonable.

The dependence of dynamic property on salinity is shown in **Figures 1.19(e)** to **(h)**. At low pH regions, both moduli are in very narrow ranges, irrespective of salinity, as shown in **Figures 1.19(e)** to **(g)**. This indicates that dynamic property remains almost constant. This phenomenon can be explained with the same reasoning that explained viscosity behavior: the high proton concentration causes the polymer chains to shrink to a minimum size. On the other hand, the moduli have pronounced proportionality on salinity at high pH region. No dependence of approximate relaxation time on pH is found in cases of more than 3% salinity, as shown in **Figure 1.19(h)**, indicating that the elastic property remains almost constant with respect to pH. However, in case of low salinity, the dependence becomes more pronounced.

1.8.3 Effect of Degree of Hydrolysis

The degree of hydrolysis is an important variable that determines the pH sensitivity because it represents the percent of carboxyl groups that carry negative charges along the polymer chains, and thus rendering the pH sensitivity. Starting from polymers with 0% degree of hydrolysis, commercially available hydrolyzed polymers with degree of 25, 30, and 100% have been studied and the results compared. It is clearly observed that the pH sensitivity is more pronounced as the degree of hydrolysis increases,

as shown in **Figures 1.20(a)** and **(b)**. Pure polyacryamide (0% degree of hydrolysis) which has only amino functional groups along its backbone chain (non-ionic polymer) does not show any pH sensitivity (straight horizontal line). On the other hand, pure polyacrylic acid (100% degree of hydrolysis) shows the maximum pH sensitivity. However, the pH dependence of polymer viscosity, between 30% and 100% degree of hydrolysis, does not change in the expected progression, as shown in **Figure 1.20(c)**. **Figure 1.20(d)** shows the shear viscosity curves for polymers with different degrees of hydrolysis, at two different pH's: 2 and 10. The figure also shows the expected relationship between pH sensitivity and degree of hydrolysis. Although there is no pH sensitivity for the polymer with 0% degree of hydrolysis, it shows the shear thinning behavior due to its chain configuration change.

Similar to the dependence of shear viscosity on the degree of hydrolysis, both storage and loss moduli exactly overlap at 0% degree of hydrolysis, which means that there is no sensitivity of elasticity on pH. The difference between two moduli curves for different pH's is getting larger as the degree of hydrolysis increases, as observed in **Figures 1.20(e)** to **1.20(g)**. **Figure 1.20(h)** shows the approximate relaxation time (defined by the inverse of the cross-over frequency) as a function of pH for different degrees of hydrolysis. As expected, 0% degree of hydrolysis polymer shows no dependence on pH, while elastic property becomes more pronounced as degree of hydrolysis increases. However, 100% degree of hydrolysis has a smaller relaxation time than 20 and 25% degree of hydrolysis at high pH region, which differs from the viscosity trend. This may be due to the tight arrangement of negative charges on the backbone chain, in the case of 100% hydrolysis polymer.

1.8.4 Effect of Molecular Weight

Molecular weight affects hydrodynamic radius and charge density per molecule; a polymer higher in molecular weight shows larger hydrodynamic radius and higher charge density for polyelectrolyte. **Figures 1.21(a)** to **(d)** compare the pH dependence of the shear viscosity for 8M and 20M molecular weight polymers. When all other variables remain constant, it is observed that the 20M polymer has higher viscosity for all pH ranges. However, the pH sensitivity in the low pH region is more pronounced than that in the high pH region. This may be because the number of negative charges for the 8M

polymer (with 30% degree of hydrolysis in high pH region) is already enough to induce its maximum hydrodynamic radius of the polymer chains. Therefore, the only difference may come from the absolute molecular sizes of both HPAM's, resulting in relatively slight difference in high pH region. On the other hand, since the effects of charges as well as the absolute molecular sizes are significant at the low pH region, the viscosity difference becomes more pronounced.

Approximate relaxation time as well as dynamic moduli, as shown in **Figures 1.21(e)** to **(h),** proves that the polymer higher in molecular weight exhibits more pronounced viscoelastic behavior than the polymer lower in molecular weight, which closely follows the trend in the viscosity behavior. However, the trend of relaxation time is opposite to the viscosity trend: at the low pH region, both polymers show the similar tendency of less relaxation time. However, the relaxation time of the 20M polymer becomes greater (more elastic behavior) compared to that of the 8M polymer in high pH region.

1.8.5 Effect of Divalent Ions

The effect of divalent ions on rheological properties has been investigated by employing calcium chloride as a divalent salt. Since HPAM polymers are incompatible with brine prepared with only calcium chloride (in this case, precipitation occurs), sodium chloride has been also added. **Figures 1.22(a)** and **(d)** compare the pH sensitivity of two different brines: 0.5% sodium chloride only, and a combination of 0.2% sodium chloride and 0.3% calcium chloride. The effect of divalent ions is thus determined to be quite significant to reducing the viscosity of the HPAM polymer solution at high pH region to a value even less than that of the same polymer solution prepared in 10% sodium chloride brine, as shown in **Figure 1.22(b)**. The divalent ions (Ca^{2+} or Mg^{2+}) are known to tightly bind to anions along the polyelectrolyte chain because it has higher charge and polarisability, causing the polymer chain to contract to its minimum size. However, at low pH region, both solutions show quite similar viscosity behavior.

The HPAM solution prepared in divalent ions does not show any pH sensitivity on dynamic properties because of its compressed size. As shown in **Figures 1.22(e)** to **(g)**, the two moduli curves at different pH's almost overlap each other, and the relaxation time remains constant as a straight line, as shown in **Figure 1.22(h)**. This observation

seems reasonable because the viscosity of this solution is much lower than that of the HPAM solution prepared in 10% sodium chloride brine, which does not show any pH sensitivity on viscoelasticity.

1.9 CONCLUSION

The following conclusions are made:

1. The viscosity of partially hydrolyzed polyacrylamide (HPAM) shows pH sensitivity due to the anionic carboxyl groups along its molecular chain. The negatively charged carboxyl groups in high-pH conditions induce extension of the molecules through electrostatic repulsion among the groups, thereby increasing viscosity; conversely, low-pH conditions cause the molecules to become coiled, resulting in low-viscosity.
2. The salinity change does not affect viscosity at low-pH, because protons already shield the negative ions of HPAM polymers. As the pH increases, however, the effect of salinity becomes more pronounced, up to the critical salinity, above which the pH no longer affects viscosity. Divalent ions have a much more pronounced effect on viscosity than do the monovalent ions, but again, the viscosity changes only slightly at low-pH.
3. There are two factors that can affect the viscosity of HPAM at low-pH region: polymer concentration and molecular weight. This is because the polymer concentration changes the interactions among polymer molecules, and the molecular weight directly affects the chain size.
4. The degree of hydrolysis (percent of carboxyl groups among all side groups along the polymer chain) is a significant variable that affects the pH dependence of the viscosity. As the degree of hydrolysis is increased, the influence of pH on the viscosity becomes more pronounced. However, after 30% degree of hydrolysis, its influence lessens, especially in the high-pH region.
5. HPAM molecules with high molecular weight show viscoelastic properties. The relaxation time-scan shows a dependence that is similar to that discussed above. There are two exceptions: a) the relaxation time shows no sensitivity to pH in the salinity above 3%, or the presence of divalent ions; and b) the

relaxation time of a 100% hydrolyzed polymer is much less than that of even a 20 to 25% hydrolysis polymer.

1.10 APPENDIX 1-A: VISCOSITY DATA FOR VARIOUS HPAM SOLUTIONS

Tables 1.5 through **1.15** provide all rheological data for various HPAM solutions, including their steady-shear viscosities and viscoelastic behaviors, which were measured by the ARES LS-1 rheometer. **Figures 1.18** to **1.22** were prepared based upon these data.

Table 1.1: Examples of rheological properties of HPAM polymers (continued on next page)

Reference	Viscometer	Polymers	Shear Rate	Variables	Range
Mungan (1969)	• Cannon-Fenske (Modified Oswald Type) viscometer	3 HPAM's	• 7 to 2000 s^{-1}	• Molecular Weight • Polymer Concentration • NaCl Salinity • pH • Temperature • Degree of Hydrolysis	• 2-10 million • 0.005-0.25% • 0-2% • 4-10 • 150-350 degF • 25% and more
Nouri *et al*. (1971)	• Cone and plate viscometer	11 polyacryl-amide out of 14 polymers	• 0.3 to 60 rpm	• Polymer Concentration • Molecular Weight • NaCl Salinity • Temperature	• 0.025-0.35 % • 1-14 million • 0-10% • 70-200 degF
Ferrer (1972)	• Cannon-Fenske viscometer	4 HPAM's out of 14 polymers		• Polymer Concentration • Molecular Weight • NaCl Salinity • pH	• 1 to 1000 ppm • 0 to 5% • 2 to 12
Mungan (1972)	• Weissenberg Rheogoniometer • Cannon-Fenske Viscometer • Capillary Tubes	3 HPAM's	• 10^{-3} to 10^{5} s^{-1}	• Polymer Concentration • NaCl Salinity • Divalent Ion • Molecular Weight • Degree of Hydrolysis	• 500 to 2,500 ppm • 0 to 20,000 ppm • $MgCl_2$ and $CaCl_2$ • 2 ~ • 25% and more

Table 1.1: Examples of rheological properties of HPAM polymers

Reference	Viscometer	Polymers	Shear Rate	Variables	Range
Martin *et al*. (1975)	• Brookfield LVT Viscometer	3 HPAM's	• 7.3 s^{-1}	• Degree of Hydrolysis • NaCl Salinity • Divalent Ions	• 0, 15, 25, 35% • 0 to 100000 ppm • $CaCl_2$
Szabo (1979)	• Brookfield LVT Viscometer	10 HPAM's out of 28 polymers	• 12.5 and 70.0 s^{-1}	• Polymer Concentration • NaCl Salinity • pH	• 300 to 1200 ppm • 0.1 to 10% • 7 to 12
Ward *et al*. (1981)	• Brookfield LVT • Cannon-Ubbelohde four-bulb capillary viscometer • Contraves LS-30 viscometer	3 HPAM's	• 10 to 1000 s^{-1} for CU viscometer • 0.02 to 129 s^{-1} for LS-30	• Divalent Ions	• $MgCl_2$ and $CaCl_2$
Nasr-El-Din *et al*. (1991)	• Co-axial rotational viscometer (Contraves LS-30)	1 HPAM	• 0.01 to 130 s^{-1}	• Polymer Concentration • NaCl Salinity • Divalent Ions • Alkali (NaOH) and Surfactant	• 125 to 5000 ppm • 0 to 16% • $CaCl_2$ • 0 to 10%
Nashawi (1991)	• Screen viscometer	1 HPAM		• Polymer Concentration • Divalent Ions • Mixing divalent ions	• 500-2500 ppm • Mg^{2+}, Ca^{2+}, Fe^{2+}

Table 1.2: Dynamic quantities that can be measured in oscillatory test at shear geometry

Symbol	Variable
τ^*	Complex Stress Amplitude
γ^*	Complex Strain Amplitude
δ	Phase Shift
G^*	Complex Modulus
G'	Elastic (Storage) Modulus
G''	Viscous (Loss) Modulus
J^*	Complex Compliance
J'	Elastic (Storage) Compliance
J''	Viscous (Loss) Compliance
η^*	Complex Viscosity
η'	In phase Viscosity
η''	Out of phase Viscosity

Table 1.3: SNF polymers used in rheological measurements with specifications

Brand Name	Chemical Name	MW	DH
Flopaam 3330S	Partially Hydrolyzed Polyacrylamide	8M	25 – 30 %
Flopaam 3630S	Partially Hydrolyzed Polyacrylamide	20M	25 – 30 %
FA920SH	Pure Polyacrylamide	8M	0 %
Flopaam 2330S	Partially Hydrolyzed Polyacrylamide	8M	20 – 25 %
ALP 99 VHM	Pure Polyacrylic Acid	8M	100 %

Table 1.4: Test sequence for rheological measurements

Dynamic Tests	Frequency	Strain
I. Dynamic Strain Sweep	10.0 (rad/s)	1.0 ~ 100 (%)
II. Dynamic Frequency Sweep	0.1 ~ 100 (rad/s)	5 ~ 20 (%)
Steady Tests	Shear Rate	
III. Step Rate (Transient)	1, 10, 100, 1000 (s-1)	
IV. Steady Shear	0.1 ~ 1000	

Table 1.5(a): Viscosity and relaxation time as a function of pH for 0.5% Flopaam 3330S (8M molecular weight and 25~30 % degree of hydrolysis), prepared in 0.5% sodium chloride brine

pH	Viscosity (cP)				Relaxation Time (s/rad)
	Shear Rate (s^{-1})				
	1	10	100	1000	
2.1	17.64	14.85	9.63	6.88	0.0450
3.1	12.59	12.47	9.23	5.53	0.0336
4.1	40.39	35.30	19.06	9.74	0.0324
5.2	227.18	112.41	37.06	14.52	0.0645
6.1	373.58	149.47	44.37	16.18	0.1196
8.2	409.17	158.85	46.51	16.77	0.1424
10.2	406.40	157.74	46.21	16.73	0.1298

Table 1.5(b): Elastic and loss moduli for 0.5% Flopaam 3330S (8M molecular weight and 25~30 % degree of hydrolysis), prepared in 0.5% sodium chloride brine

Frequency (rad/s)	Modulus ($dyne/cm^2$)			
	pH = 2.1		pH = 10.2	
	Elastic (G')	Loss (G")	Elastic (G')	Loss (G")
0.100	0.004	0.015	0.049	0.537
0.158	0.003	0.028	0.116	0.804
0.251	0.003	0.046	0.274	1.234
0.398	0.003	0.077	0.531	1.790
0.631	0.010	0.107	0.990	2.477
1.000	0.020	0.170	1.677	3.352
1.585	0.039	0.264	2.657	4.320
2.512	0.073	0.405	3.965	5.457
3.981	0.155	0.598	5.614	6.645
6.310	0.302	0.870	7.628	7.984
10.000	0.602	1.218	10.060	9.500
15.849	1.137	1.599	13.064	11.153
25.119	2.051	1.840	16.902	13.124
39.811	3.562	1.639	22.474	15.230
63.096	5.419	-0.542	31.395	15.950
100.000	4.314	-5.240	44.301	11.748

Table 1.6(a): Viscosity and relaxation time as a function of pH for 0.2% Flopaam 3330S (8M molecular weight and 25~30 % degree of hydrolysis), prepared in 0.5% sodium chloride brine

pH	Viscosity (cP)				Relaxation Time (s/rad)
	Shear Rate (s^{-1})				
	1	10	100	1000	
2.1	3.58	3.00	2.55	3.61	0.0744
3.2	2.85	2.93	2.67	3.41	0.0722
4.1	6.91	6.72	5.33	4.35	0.0492
5.2	22.90	19.55	10.94	6.16	0.0426
6.5	35.25	27.10	13.15	6.72	0.0461
8.8	37.69	28.10	13.49	6.93	0.0439
10.4	38.03	28.25	13.65	7.09	0.0454

Table 1.6(b): Elastic and loss moduli for 0.2% Flopaam 3330S (8M molecular weight and 25~30 % degree of hydrolysis), prepared in 0.5% sodium chloride brine

Frequency (rad/s)	Modulus ($dyne/cm^2$)			
	pH = 2.1		pH = 10.4	
	Elastic (G')	Loss (G")	Elastic (G')	Loss (G")
0.100	0.003	0.007	0.014	0.037
0.158	0.005	0.013	0.002	-0.058
0.251	0.003	0.014	0.001	-0.097
0.398	0.004	0.022	0.002	0.153
0.631	0.010	0.036	0.024	0.228
1.000	0.011	0.049	0.041	0.364
1.585	0.014	0.066	0.111	0.549
2.512	0.024	0.092	0.234	0.818
3.981	0.042	0.129	0.448	1.151
6.310	0.077	0.179	0.771	1.595
10.000	0.153	0.230	1.289	2.102
15.849	0.298	0.245	2.135	2.684
25.119	0.493	0.126	3.478	3.218
39.811	0.532	-0.185	5.590	3.177
63.096	0.284	-0.499	9.103	1.480
100.000	0.249	-0.415	11.182	-6.188

Table 1.7(a): Viscosity and relaxation time as a function of pH for 0.8% Flopaam 3330S (8M molecular weight and 25~30 % degree of hydrolysis), prepared in 0.5% sodium chloride brine

pH	Viscosity (cP)				Relaxation Time (s/rad)
	Shear Rate (s^{-1})				
	1	10	100	1000	
2.1	108.87	63.93	26.73	11.95	0.0530
3.1	71.81	54.05	25.95	11.49	0.0344
4.1	176.83	108.26	40.33	16.90	0.0356
5.1	820.48	276.81	73.37	23.91	0.2104
6.2	1290.05	363.46	88.75	26.87	0.4650
8.8	1364.15	377.61	91.08	27.22	0.4653
10.1	1373.94	379.66	91.52	27.27	0.5057

Table 1.7(b): Elastic and loss moduli for 0.8% Flopaam 3330S (8M molecular weight and 25~30 % degree of hydrolysis), prepared in 0.5% sodium chloride brine

Frequency (rad/s)	Modulus ($dyne/cm^2$)			
	pH = 2.1		pH = 10.1	
	Elastic (G')	Loss (G")	Elastic (G')	Loss (G")
0.100	0.012	0.116	0.676	2.453
0.158	0.018	0.191	1.275	3.528
0.251	0.033	0.295	2.243	4.850
0.398	0.076	0.450	3.657	6.364
0.631	0.164	0.677	5.612	8.112
1.000	0.297	0.968	8.081	9.941
1.585	0.541	1.367	11.191	11.926
2.512	0.901	1.864	14.918	13.990
3.981	1.428	2.476	19.241	16.135
6.310	2.166	3.184	24.216	18.379
10.000	3.178	4.024	29.843	20.801
15.849	4.582	4.962	36.243	23.479
25.119	6.737	5.878	43.688	26.639
39.811	10.050	6.392	53.123	30.143
63.096	15.000	5.286	66.779	34.070
100.000	24.112	-1.886	89.466	33.700

Table 1.8(a): Viscosity and relaxation time as a function of pH for 0.5% Flopaam 3330S (8M molecular weight and 25~30 % degree of hydrolysis), prepared in 1.0% sodium chloride brine

pH	Viscosity (cP)				Relaxation Time (s/rad)
	Shear Rate (s^{-1})				
	1	10	100	1000	
2.2	16.42	15.62	9.97	6.84	0.0425
3.2	15.73	14.58	10.08	6.15	0.0339
4.2	45.02	36.67	18.95	9.90	0.0330
5.2	179.40	93.78	33.20	13.91	0.0517
6.4	279.75	123.41	39.55	15.76	0.0789
8.8	298.38	128.60	40.89	15.97	0.0905
10.2	297.05	127.87	40.62	16.11	0.0832

Table 1.8(b): Elastic and loss moduli for 0.5% Flopaam 3330S (8M molecular weight and 25~30 % degree of hydrolysis), prepared in 1.0% sodium chloride brine

Frequency (rad/s)	Modulus ($dyne/cm^2$)			
	pH = 2.2		pH = 10.2	
	Elastic (G')	Loss (G")	Elastic (G')	Loss (G")
0.100	0.000	0.018	0.036	0.370
0.158	0.008	0.023	0.073	0.582
0.251	0.004	0.031	0.146	0.868
0.398	0.009	0.059	0.323	1.292
0.631	0.013	0.108	0.662	1.854
1.000	0.013	0.162	1.120	2.489
1.585	0.035	0.250	1.815	3.294
2.512	0.058	0.378	2.833	4.264
3.981	0.149	0.595	4.057	5.322
6.310	0.296	0.864	5.634	6.523
10.000	0.591	1.228	7.598	7.921
15.849	1.114	1.633	10.094	9.486
25.119	2.033	1.987	13.465	11.388
39.811	3.669	1.728	18.597	13.104
63.096	5.766	-0.320	26.534	13.356
100.000	4.747	-5.407	38.569	9.860

Table 1.9(a): Viscosity and relaxation time as a function of pH for 0.5% Flopaam 3330S (8M molecular weight and 25~30 % degree of hydrolysis), prepared in 3.0% sodium chloride brine

pH	Viscosity (cP)				Relaxation Time (s/rad)
	Shear Rate (s^{-1})				
	1	10	100	1000	
2.4	18.50	15.93	10.09	7.04	0.0438
3.3	16.09	15.14	10.43	6.49	0.0342
4.4	25.51	24.19	15.82	8.59	0.0297
5.4	65.79	53.64	25.52	11.50	0.0325
6.8	86.92	65.72	28.65	12.40	0.0328
8.6	88.73	66.52	28.92	12.48	0.0325
10.6	88.21	66.41	28.84	12.43	0.0334

Table 1.9(b): Elastic and loss moduli for 0.5% Flopaam 3330S (8M molecular weight and 25~30 % degree of hydrolysis), prepared in 3.0% sodium chloride brine

Frequency (rad/s)	Modulus ($dyne/cm^2$)			
	pH = 2.4		pH = 10.6	
	Elastic (G')	Loss (G")	Elastic (G')	Loss (G")
0.100	0.006	0.016	0.000	-0.089
0.158	0.006	0.028	0.009	-0.120
0.251	0.003	0.045	0.020	0.229
0.398	0.005	0.076	0.020	0.346
0.631	0.008	0.116	0.035	0.546
1.000	0.018	0.182	0.090	0.882
1.585	0.038	0.277	0.236	1.320
2.512	0.080	0.420	0.505	1.943
3.981	0.176	0.629	0.983	2.832
6.310	0.338	0.911	1.768	3.885
10.000	0.649	1.275	2.963	5.139
15.849	1.193	1.677	4.672	6.579
25.119	2.143	2.010	7.250	8.095
39.811	3.784	1.833	11.267	9.345
63.096	5.861	-0.391	17.145	9.164
100.000	5.018	-5.548	27.566	4.387

Table 1.10(a): Viscosity and relaxation time as a function of pH for 0.5% Flopaam 3330S (8M molecular weight and 25~30 % degree of hydrolysis), prepared in 10.0% sodium chloride brine

pH	Viscosity (cP)				Relaxation Time (s/rad)
	Shear Rate (s^{-1})				
	1	10	100	1000	
2.7	23.33	17.78	10.46	7.75	0.0488
3.7	22.49	19.87	12.59	7.34	0.0352
4.7	47.45	39.16	20.68	11.01	0.0324
5.8	94.72	65.12	28.05	13.46	0.0351
8.0	110.58	72.52	30.00	14.14	0.0364
9.6	108.67	71.61	29.67	13.93	0.0371
11.1	109.57	71.90	29.81	13.98	0.0375

Table 1.10(b): Elastic and loss moduli for 0.5% Flopaam 3330S (8M molecular weight and 25~30 % degree of hydrolysis), prepared in 10.0% sodium chloride brine

Frequency (rad/s)	Modulus ($dyne/cm^2$)			
	pH = 2.7		pH = 11.1	
	Elastic (G')	Loss (G")	Elastic (G')	Loss (G")
0.100	0.016	0.031	0.014	0.115
0.158	0.016	0.047	0.011	0.184
0.251	0.021	0.073	0.027	0.293
0.398	0.026	0.101	0.056	0.440
0.631	0.032	0.155	0.111	0.676
1.000	0.038	0.226	0.225	1.025
1.585	0.071	0.337	0.432	1.504
2.512	0.145	0.493	0.797	2.143
3.981	0.253	0.715	1.383	2.946
6.310	0.453	0.998	2.221	3.909
10.000	0.793	1.353	3.418	5.044
15.849	1.382	1.742	5.125	6.389
25.119	2.372	1.987	7.667	7.857
39.811	4.004	1.687	11.740	8.998
63.096	5.948	-0.796	17.885	8.568
100.000	4.496	-5.660	28.529	3.687

Table 1.11(a): Viscosity and relaxation time as a function of pH for 0.5% FA920SH (8M molecular weight and 0 % degree of hydrolysis), prepared in 0.5% sodium chloride brine

pH	Viscosity (cP)				Relaxation Time (s/rad)
	Shear Rate (s^{-1})				
	1	10	100	1000	
2.1	44.38	39.09	21.63	10.31	0.0286
3.2	42.91	38.24	21.35	10.21	0.0276
4.2	43.36	38.47	21.48	10.29	0.0285
7.3	47.04	38.96	21.62	10.30	0.0278
10.3	42.57	37.69	21.33	10.29	0.0276

Table 1.11(b): Elastic and loss moduli for 0.5% FA920SH (8M molecular weight and 0 % degree of hydrolysis), prepared in 0.5% sodium chloride brine

Frequency (rad/s)	Modulus ($dyne/cm^2$)			
	pH = 2.1		pH = 10.3	
	Elastic (G')	Loss (G")	Elastic (G')	Loss (G")
0.100	0.025	0.043	0.004	0.045
0.158	0.017	0.076	0.020	0.076
0.251	0.022	0.112	0.003	0.116
0.398	0.026	0.171	0.033	0.170
0.631	0.034	0.275	0.031	0.265
1.000	0.047	0.421	0.038	0.409
1.585	0.073	0.665	0.062	0.644
2.512	0.162	1.043	0.156	0.992
3.981	0.348	1.575	0.316	1.535
6.310	0.707	2.326	0.637	2.275
10.000	1.369	3.305	1.282	3.265
15.849	2.506	4.521	2.380	4.493
25.119	4.382	5.819	4.215	5.836
39.811	7.594	6.882	7.413	6.890
63.096	12.793	6.477	12.571	6.685
100.000	20.959	0.885	20.891	1.052

Table 1.12(a): Viscosity and relaxation time as a function of pH for 0.5% Flopaam 2330S (8M molecular weight and 20~25 % degree of hydrolysis), prepared in 0.5% sodium chloride brine

pH	Viscosity (cP)				Relaxation Time (s/rad)
	Shear Rate (s^{-1})				
	1	10	100	1000	
2.1	21.63	19.16	12.25	7.22	0.0366
3.2	21.10	20.15	12.79	7.29	0.0343
4.2	46.80	37.81	19.15	9.84	0.0327
5.2	157.15	86.15	31.78	13.30	0.0450
6.2	261.47	119.15	39.25	15.24	0.0627
8.7	282.80	125.01	40.38	15.51	0.0762
10.6	281.01	124.11	40.18	15.35	0.0671

Table 1.12(b): Elastic and loss moduli for 0.5% Flopaam 2330S (8M molecular weight and 20~25 % degree of hydrolysis), prepared in 0.5% sodium chloride brine

Frequency (rad/s)	Modulus ($dyne/cm^2$)			
	pH = 2.1		pH = 10.6	
	Elastic (G')	Loss (G")	Elastic (G')	Loss (G")
0.100	0.037	0.020	0.036	0.371
0.158	0.037	0.037	0.080	0.555
0.251	0.036	0.052	0.188	0.819
0.398	0.050	0.075	0.313	1.197
0.631	0.044	0.132	0.618	1.717
1.000	0.049	0.208	1.042	2.391
1.585	0.069	0.323	1.690	3.167
2.512	0.108	0.490	2.589	4.105
3.981	0.202	0.762	3.758	5.203
6.310	0.376	1.107	5.259	6.462
10.000	0.717	1.591	7.158	7.916
15.849	1.336	2.178	9.672	9.527
25.119	2.465	2.733	12.977	11.454
39.811	4.370	2.838	17.931	13.426
63.096	7.388	1.250	25.868	14.305
100.000	8.718	-4.973	38.151	10.813

Table 1.13(a): Viscosity and relaxation time as a function of pH for 0.5% ALP99VHM (8M molecular weight and 100 % degree of hydrolysis), prepared in 0.5% sodium chloride brine

pH	Viscosity (cP)				Relaxation Time (s/rad)
	Shear Rate (s^{-1})				
	1	10	100	1000	
2.1	4.29	3.73	3.78	4.39	0.0569
3.1	3.63	3.81	3.57	3.68	0.0522
4.1	22.01	20.84	14.80	8.42	0.0271
5.1	134.55	89.31	35.56	14.43	0.0327
6.2	262.14	136.97	45.61	16.96	0.0499
8.4	305.94	150.05	48.08	17.64	0.0612
10.1	280.91	141.78	46.28	17.15	0.0556

Table 1.13(b): Elastic and loss moduli for 0.5% ALP99VHM (8M molecular weight and 100 % degree of hydrolysis), prepared in 0.5% sodium chloride brine

Frequency (rad/s)	Modulus ($dyne/cm^2$)			
	pH = 2.1		pH = 10.1	
	Elastic (G')	Loss (G")	Elastic (G')	Loss (G")
0.100	0.011	0.001	0.008	0.320
0.158	0.003	0.007	0.049	0.503
0.251	0.002	0.009	0.108	0.773
0.398	0.004	0.018	0.211	1.156
0.631	0.005	0.030	0.421	1.725
1.000	0.006	0.041	0.803	2.488
1.585	0.010	0.066	1.434	3.476
2.512	0.022	0.107	2.406	4.683
3.981	0.034	0.164	3.734	6.084
6.310	0.079	0.243	5.598	7.629
10.000	0.179	0.342	7.928	9.376
15.849	0.380	0.444	10.925	11.325
25.119	0.711	0.432	14.916	13.512
39.811	1.115	0.042	20.617	15.718
63.096	1.084	-0.714	29.351	16.598
100.000	0.563	-1.317	42.629	12.830

Table 1.14(a): Viscosity and relaxation time as a function of pH for 0.5% Flopaam 3630S (20M molecular weight and 25~30 % degree of hydrolysis), prepared in 0.5% sodium chloride brine

pH	Viscosity (cP)				Relaxation Time (s/rad)
	Shear Rate (s^{-1})				
	1	10	100	1000	
2.1	110.84	50.34	19.72	8.37	0.1020
3.2	92.65	49.02	19.43	9.84	0.0705
4.1	145.86	74.52	25.80	12.77	0.0699
5.1	543.75	157.48	42.46	16.38	0.4636
6.2	796.81	196.74	49.65	17.79	0.8373
9.3	822.57	202.81	50.75	18.01	0.9641
10.5	823.98	204.28	50.81	17.88	0.8745

Table 1.14(b): Elastic and loss moduli for 0.5% Flopaam 3630S (20M molecular weight and 25~30 % degree of hydrolysis), prepared in 0.5% sodium chloride brine

Frequency (rad/s)	Modulus ($dyne/cm^2$)			
	pH = 2.1		pH = 10.5	
	Elastic (G')	Loss (G")	Elastic (G')	Loss (G")
0.100	0.014	0.140	0.556	1.717
0.158	0.030	0.213	1.062	2.373
0.251	0.074	0.322	1.780	3.142
0.398	0.146	0.467	2.742	3.969
0.631	0.266	0.653	3.988	4.853
1.000	0.437	0.876	5.485	5.726
1.585	0.680	1.151	7.280	6.609
2.512	1.023	1.456	9.305	7.541
3.981	1.444	1.816	11.562	8.487
6.310	2.004	2.244	14.090	9.502
10.000	2.745	2.730	16.938	10.668
15.849	3.798	3.266	20.143	12.025
25.119	5.386	3.745	24.183	13.706
39.811	7.843	3.632	29.825	15.635
63.096	12.039	2.077	38.769	16.117
100.000	16.395	-8.514	52.167	11.693

Table 1.15(a): Viscosity and relaxation time as a function of pH for 0.5% Flopaam 3330S (8M molecular weight and 25~30 % degree of hydrolysis), prepared in 0.2% sodium chloride and 0.3% calcium chloride brine

pH	Viscosity (cP)				Relaxation Time (s/rad)
	Shear Rate (s^{-1})				
	1	10	100	1000	
2.1	16.16	14.79	9.73	6.28	0.0423
3.1	13.53	13.42	9.69	5.81	0.0338
4.1	24.81	23.77	15.34	8.33	0.0299
5.1	53.49	45.14	22.65	10.61	0.0302
6.1	62.38	50.70	24.26	11.08	0.0321
8.8	62.49	50.96	24.29	11.08	0.0319
10.1	62.52	50.83	24.24	11.02	0.0321

Table 1.15(b): Elastic and loss moduli for 0.5% Flopaam 3330S (8M molecular weight and 25~30 % degree of hydrolysis), prepared in 0.2% sodium chloride and 0.3% calcium chloride brine

Frequency (rad/s)	Modulus ($dyne/cm^2$)			
	pH = 2.1		pH = 10.1	
	Elastic (G')	Loss (G")	Elastic (G')	Loss (G")
0.100	0.019	0.021	0.006	-0.062
0.158	0.021	0.031	0.007	-0.113
0.251	0.003	0.042	0.003	0.147
0.398	0.006	0.068	0.017	0.239
0.631	0.005	0.101	0.010	0.391
1.000	0.012	0.163	0.053	0.607
1.585	0.028	0.252	0.135	0.924
2.512	0.060	0.385	0.274	1.446
3.981	0.135	0.590	0.604	2.143
6.310	0.283	0.868	1.158	3.033
10.000	0.568	1.230	2.087	4.105
15.849	1.096	1.655	3.487	5.333
25.119	2.038	1.953	5.683	6.624
39.811	3.625	1.786	9.182	7.692
63.096	5.731	-0.316	14.559	7.349
100.000	5.006	-5.135	23.733	2.025

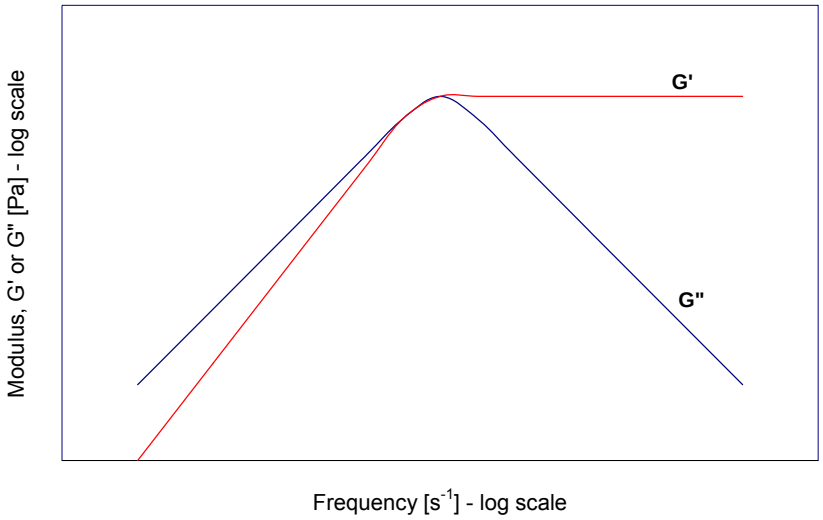

Figure 1.1: Typical Maxwell type behavior of elastic and viscous moduli in oscillatory testing (Barnes, 2000)

Figure 1.2: ARES LS-1 Rheometer

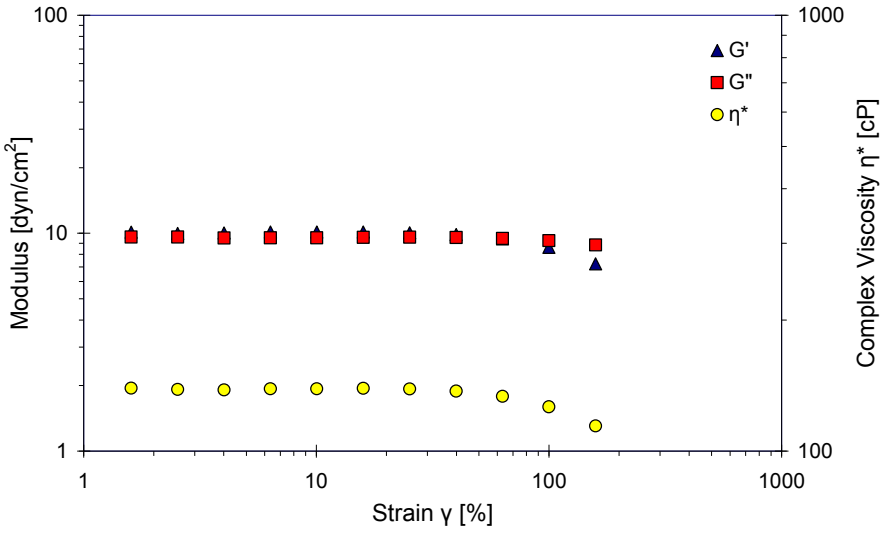

Figure 1.3: Dynamic strain sweep test for 0.5% Flopaam 3330S prepared in 0.5% sodium chloride brine at pH = 10.2

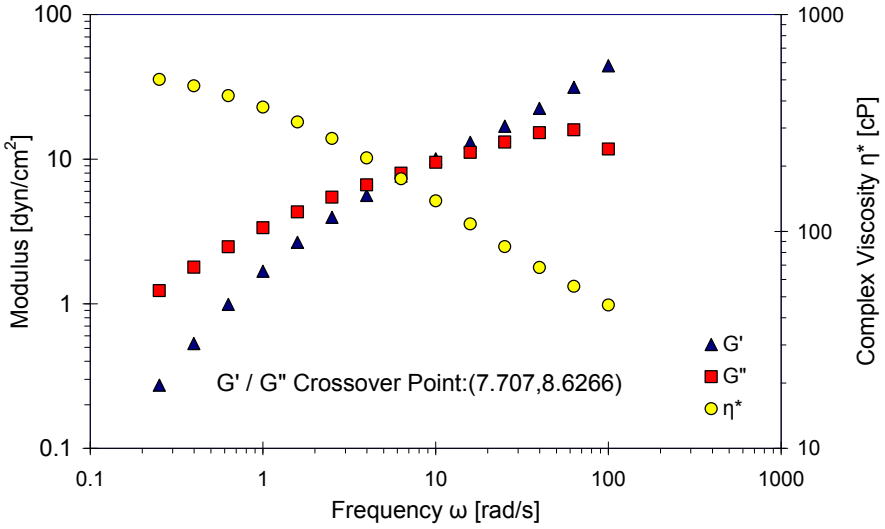

Figure 1.4: Dynamic frequency sweep test for 0.5% Flopaam 3330S prepared in 0.5% sodium chloride brine at pH = 10.2

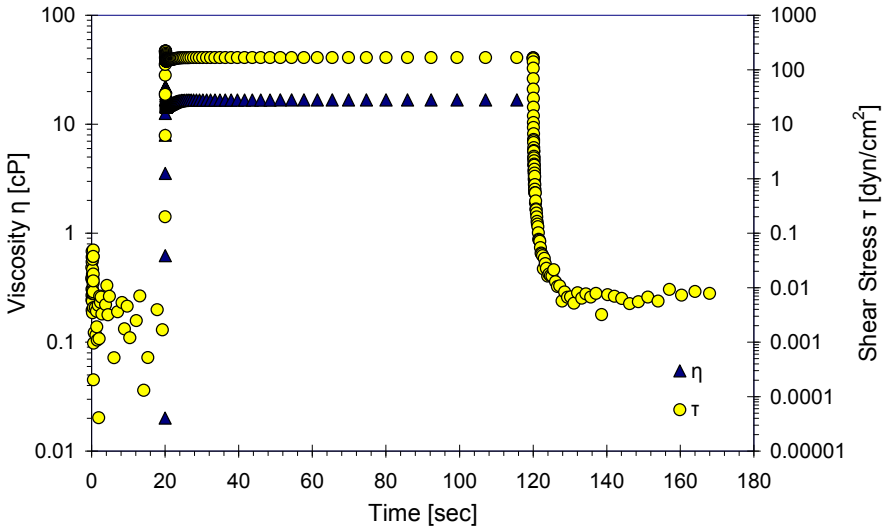

Figure 1.5: Strain-controlled transient test for 0.5% Flopaam 3330S prepared in 0.5% sodium chloride brine at pH = 10.2 at 1000 s^{-1} shear rate

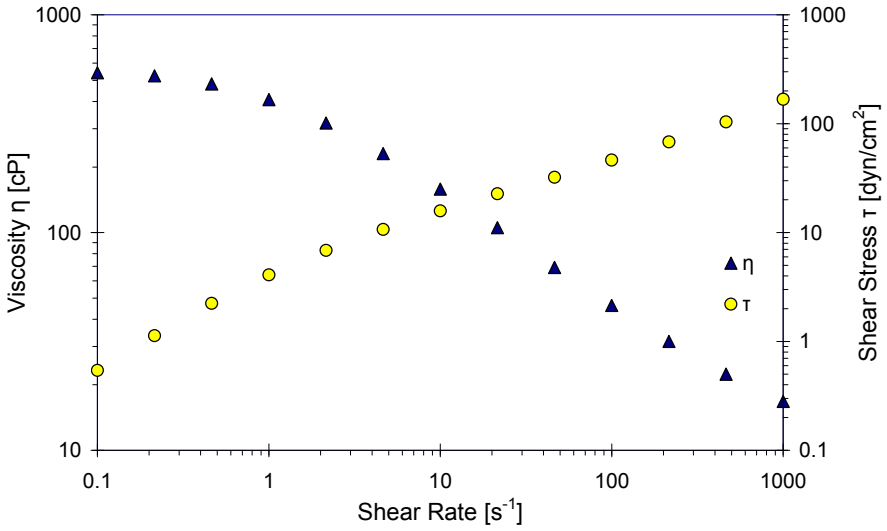

Figure 1.6: Steady rate test for 0.5% Flopaam 3330S prepared in 0.5% sodium chloride brine at pH = 10.2

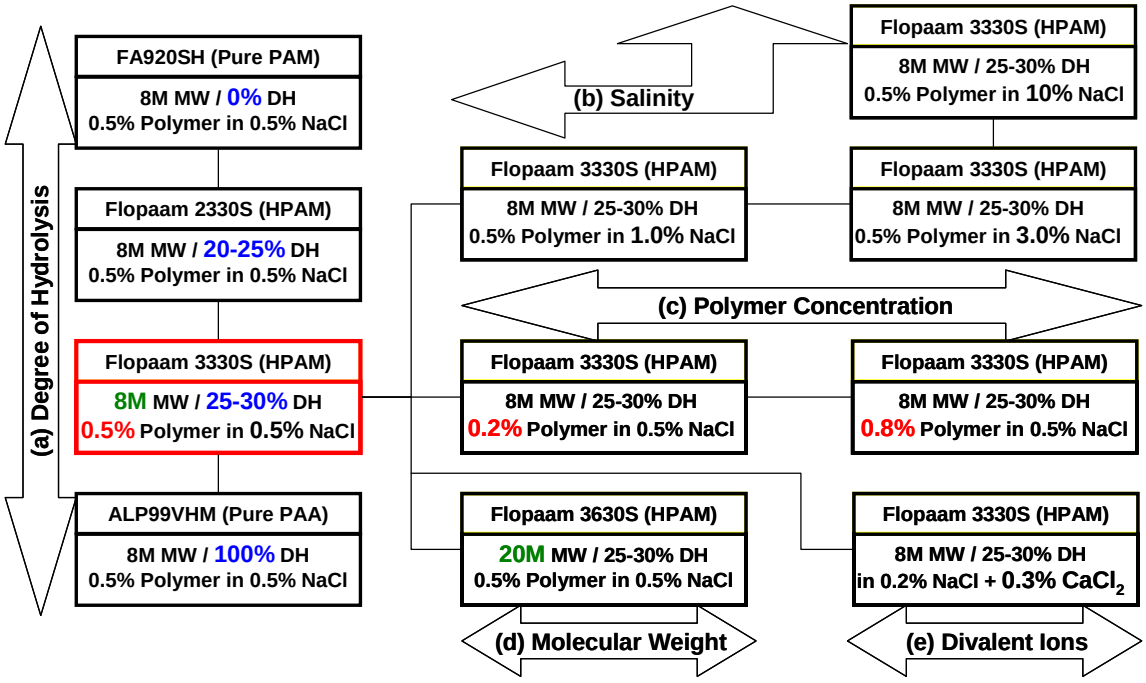

Figure 1.7: Plan for the rheological measurements of HPAM solutions

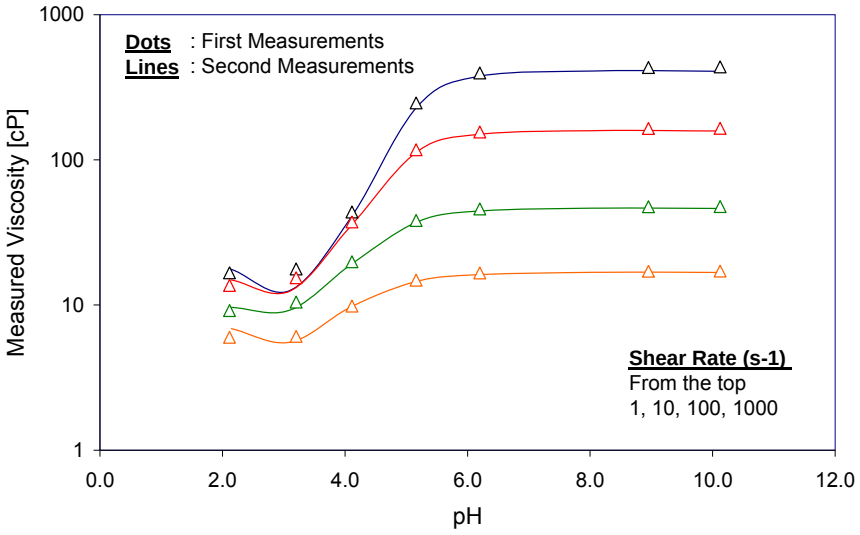

Figure 1.8: Comparison results of viscosities between the first and second measurements for 0.5% Flopaam 3330S prepared in 0.5% sodium chloride brine as a function of pH

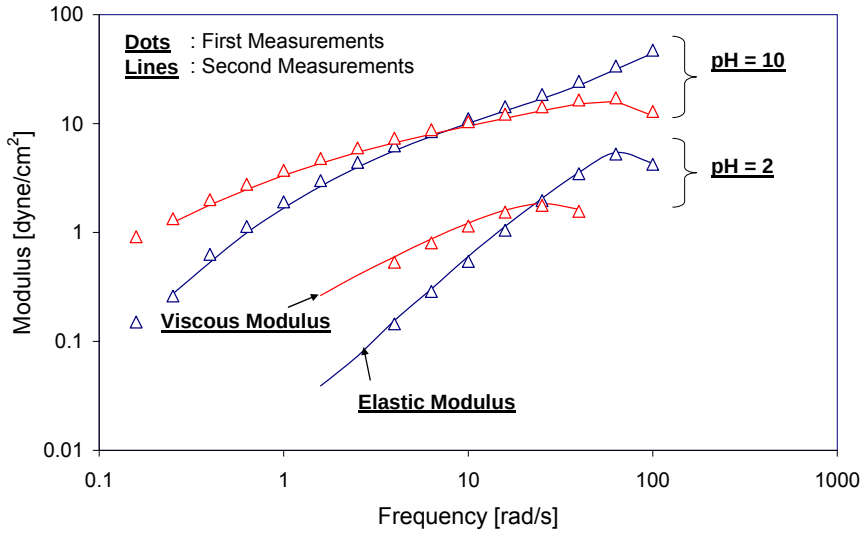

Figure 1.9: Comparison results of dynamic frequencies between the first and second measurements for 0.5% Flopaam 3330S prepared in 0.5% sodium chloride brine at pH = 2 and 10 as a function of frequency

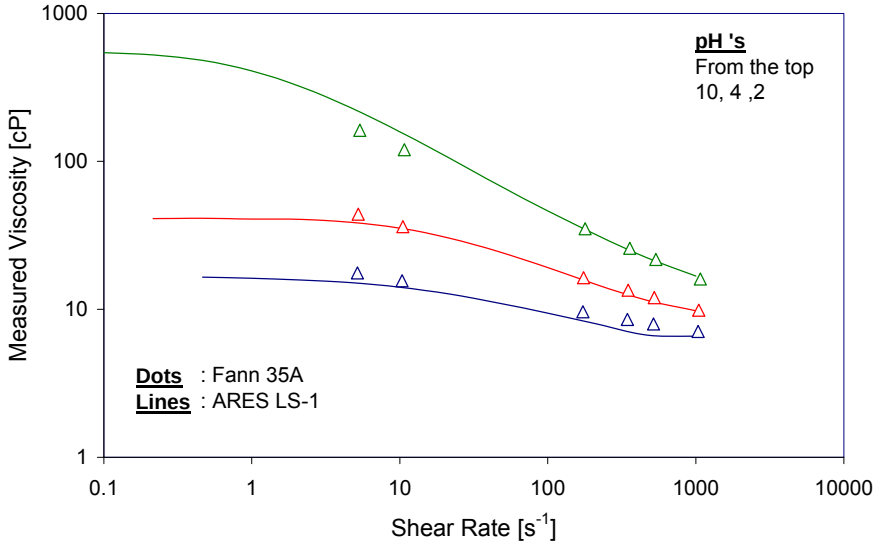

Figure 1.10: Comparison results of measured viscosities between ARES LS-1 rheometer and Fann 35A viscometer for 0.5% Flopaam 3330S prepared in 0.5% sodium chloride brine as a function of shear rate

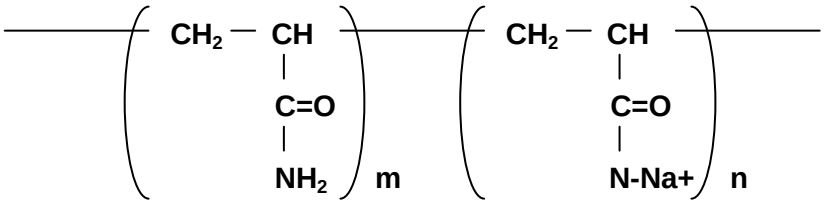

Figure 1.11: Chemical Structure of Partially Hydrolyzed Polyacrylamide. The left molecule represents amino groups and the right molecule indicates carboxyl functional groups. Hydrolysis level is defined by the mole % of carboxyl functional groups amongst the total functional groups

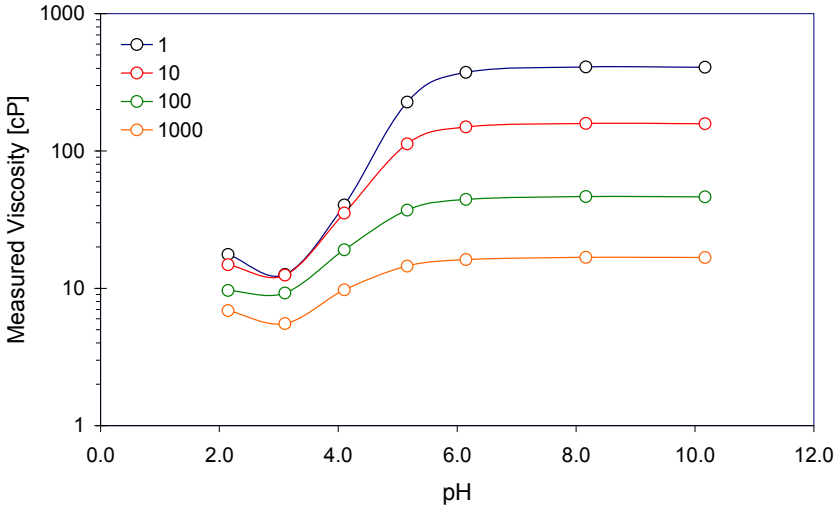

Figure 1.12: Viscosity measurements for 0.5% Flopaam 3330S prepared in 0.5% sodium chloride brine as a function of pH

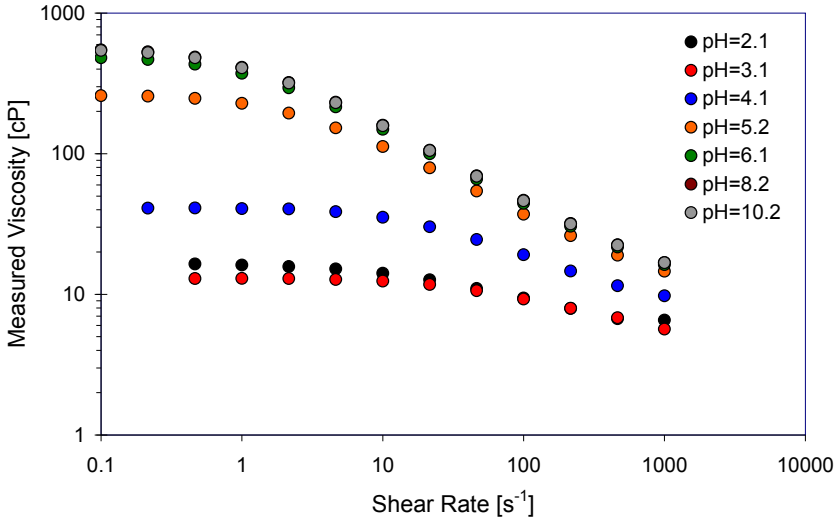

Figure 1.13: Viscosity measurements for 0.5% Flopaam 3330S prepared in 0.5% sodium chloride brine as a function of shear rate

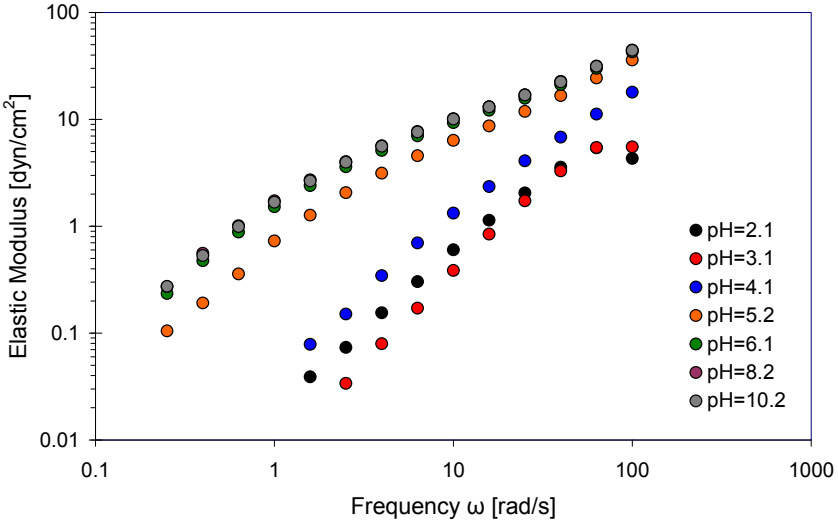

Figure 1.14: Elastic modulus measurements for 0.5% Flopaam 3330S prepared in 0.5% sodium chloride brine as a function of frequency

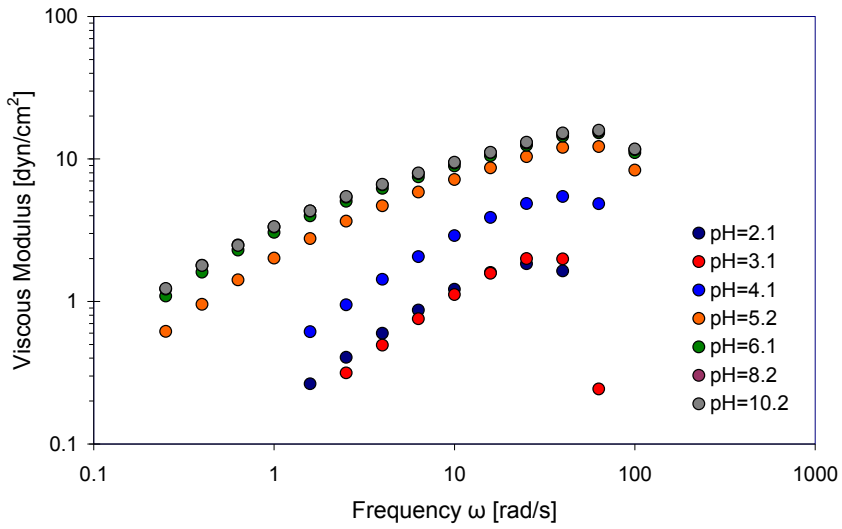

Figure 1.15: Viscous modulus measurements for 0.5% Flopaam 3330S prepared in 0.5% sodium chloride brine as a function of frequency

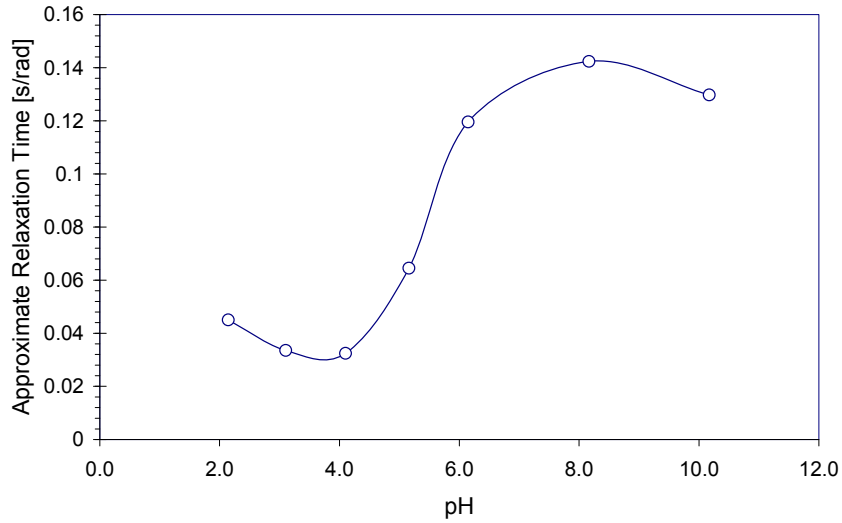

Figure 1.16: pH sensitivity of relaxation time for 0.5% Flopaam 3330S prepared in 0.5% sodium chloride brine

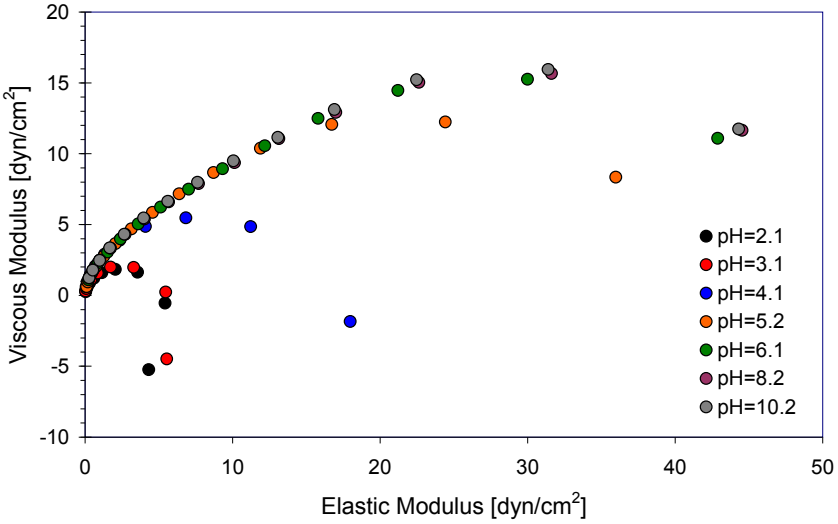

Figure 1.17: Loss modulus versus elastic modulus for 0.5% Flopaam 3330S prepared in 0.5% sodium chloride brine

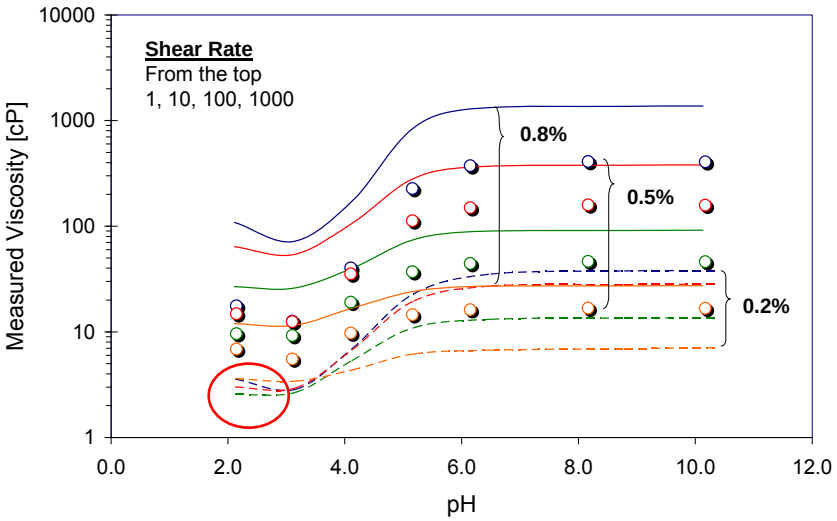

Figure 1.18(a): Influence of polymer concentration on measured viscosity as a function of pH for Flopaam 3330S prepared in 0.5% sodium chloride brine

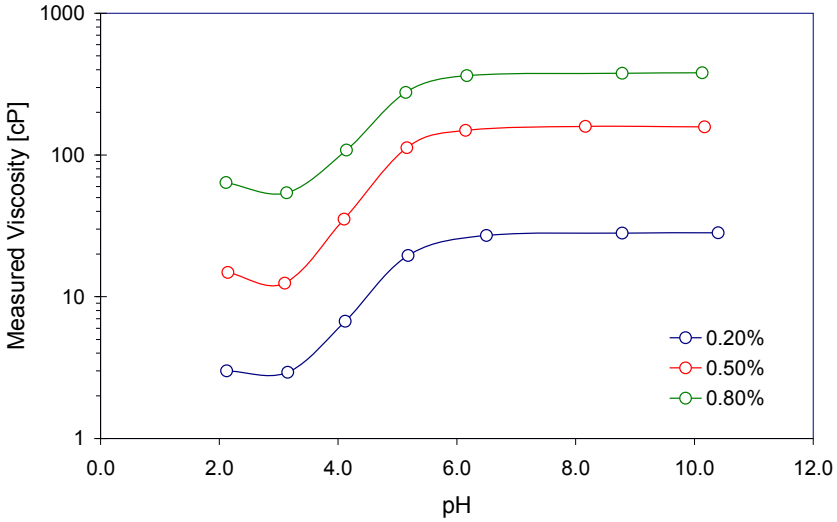

Figure 1.18(b): Influence of polymer concentration on measured viscosity as a function of pH for Flopaam 3330S prepared in 0.5% sodium chloride brine at shear rate of 10^{-1}

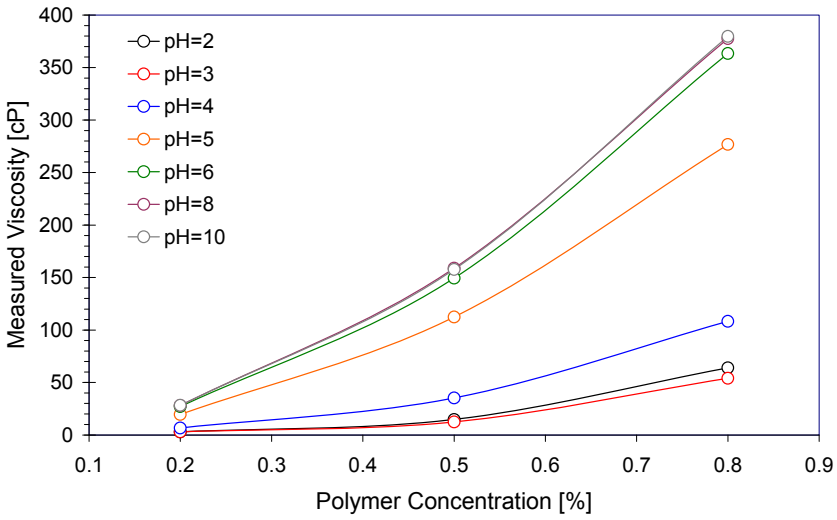

Figure 1.18(c): Measured viscosity as a function of polymer concentration at specific pH's for Flopaam 3330S prepared in 0.5% sodium chloride brine

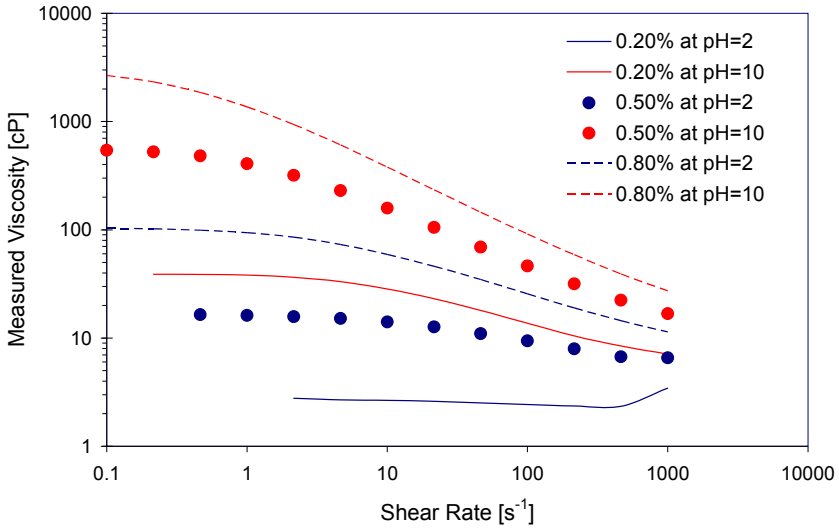

Figure 1.18(d): Influence of polymer concentration on measured viscosity as a function of shear rate at two specific pH's (pH = 2 and 10) for Flopaam 3330S prepared in 0.5% sodium chloride brine

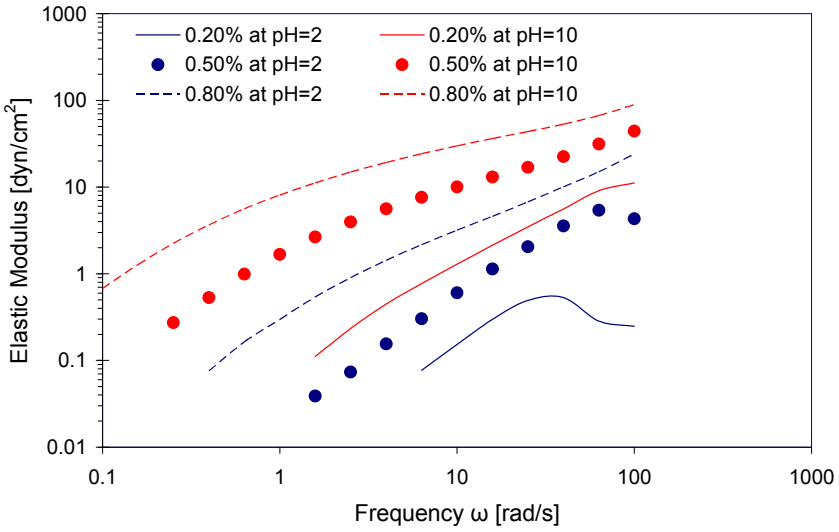

Figure 1.18(e): Influence of polymer concentration on elastic modulus (G') change at two specific pH's (pH = 2 and 10) for Flopaam 3330S prepared in 0.5% sodium chloride brine

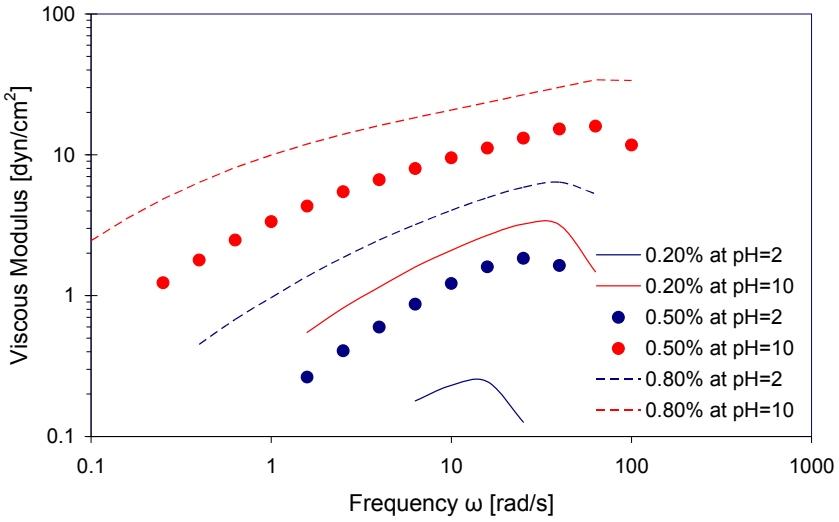

Figure 1.18(f): Influence of polymer concentration on viscous modulus (G") change at two specific pH's (pH = 2 and 10) for Flopaam 3330S prepared in 0.5% sodium chloride brine

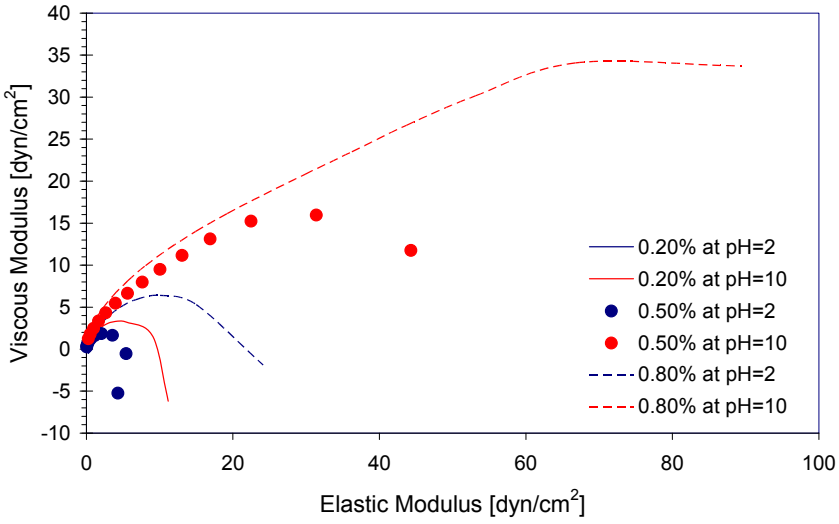

Figure 1.18(g): Influence of polymer concentration on elastic and viscous modulus Change at two specific pH's (pH = 2 and 10) for Flopaam 3330S prepared in 0.5% sodium chloride brine

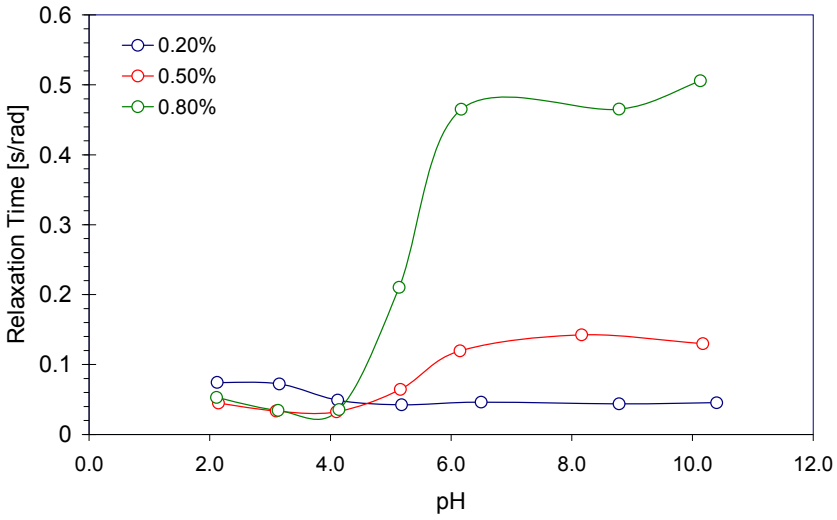

Figure 1.18(h): Influence of polymer concentration on approximate relaxation time as a function of pH for Flopaam 3330S prepared in 0.5% sodium chloride brine

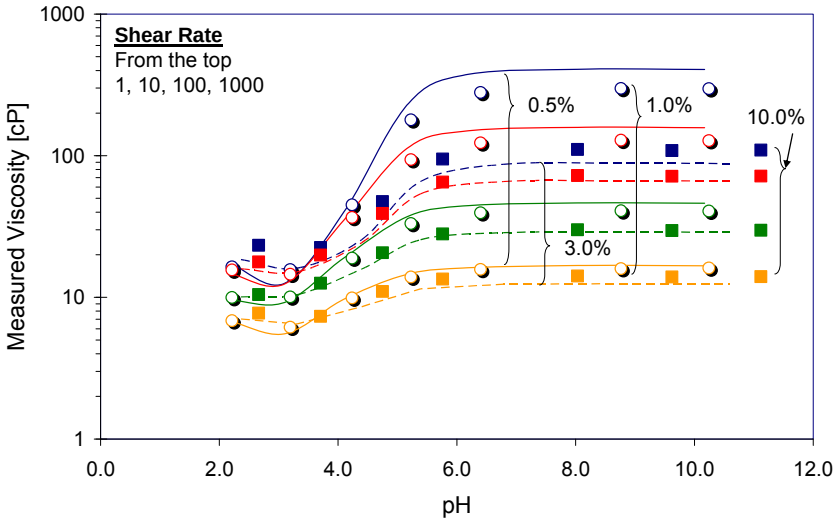

Figure 1.19(a): Influence of salinity on measured viscosity as a function of pH for 0.5% Flopaam 3330S prepared in sodium chloride brine

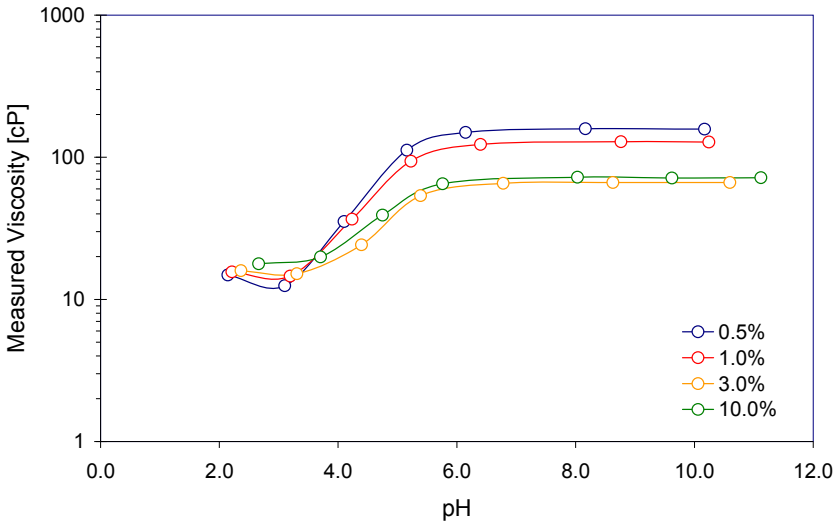

Figure 1.19(b): Influence of salinity on measured viscosity as a function of pH for 0.5% Flopaam 3330S prepared in sodium chloride brine at shear rate of 10^{-1}

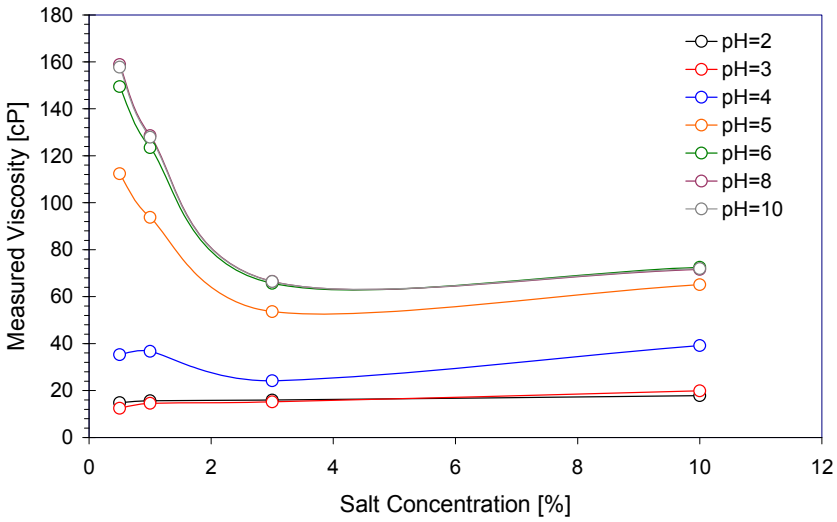

Figure 1.19(c): Measured viscosity as a function of salinity at specific pH's for 0.5% Flopaam 3330S prepared in sodium chloride brine

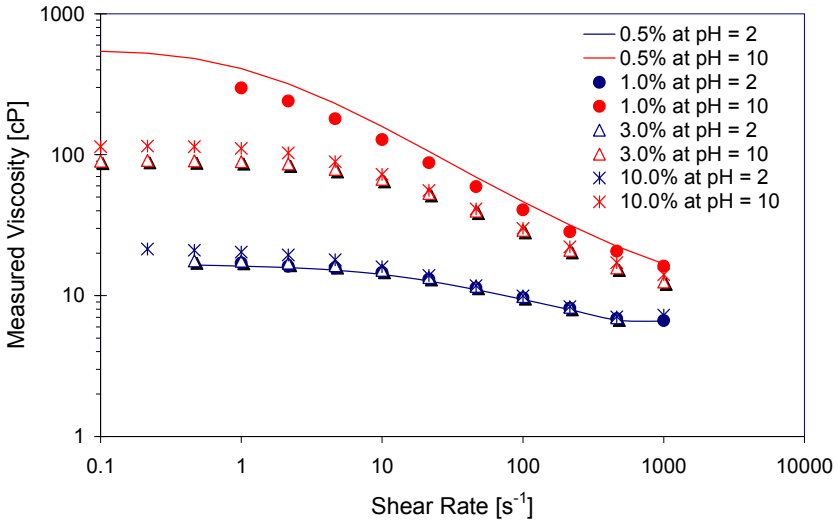

Figure 1.19(d): Influence of salinity on measured viscosity as a function of shear rate at two specific pH's (pH = 2 and 10) for 0.5% Flopaam 3330S prepared in sodium chloride brine

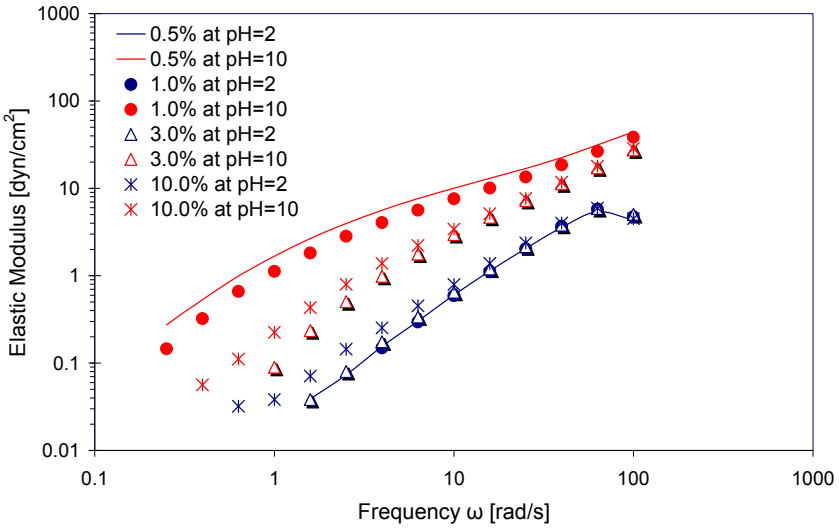

Figure 1.19(e): Influence of salinity on elastic modulus (G') change at two specific pH's (pH = 2 and 10) for 0.5% Flopaam 3330S prepared in sodium chloride brine

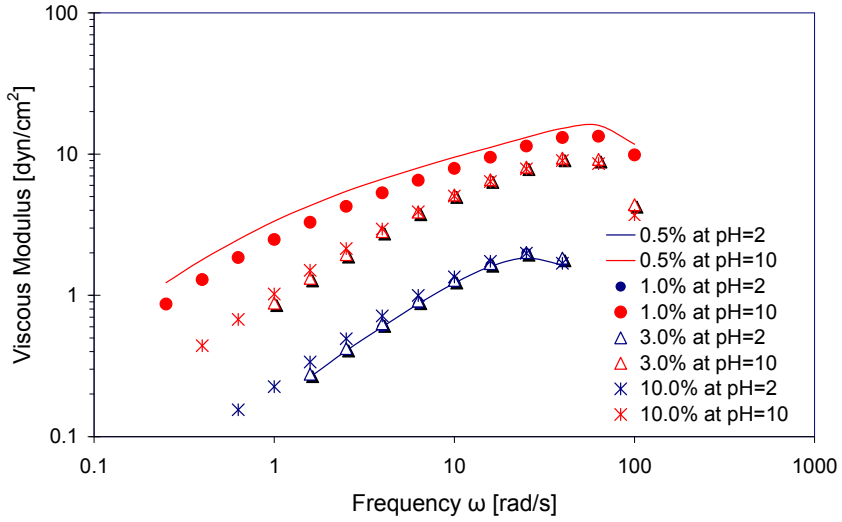

Figure 1.19(f): Influence of salinity on viscous modulus (G") change at two specific pH's (pH = 2 and 10) for 0.5% Flopaam 3330S prepared in sodium chloride brine

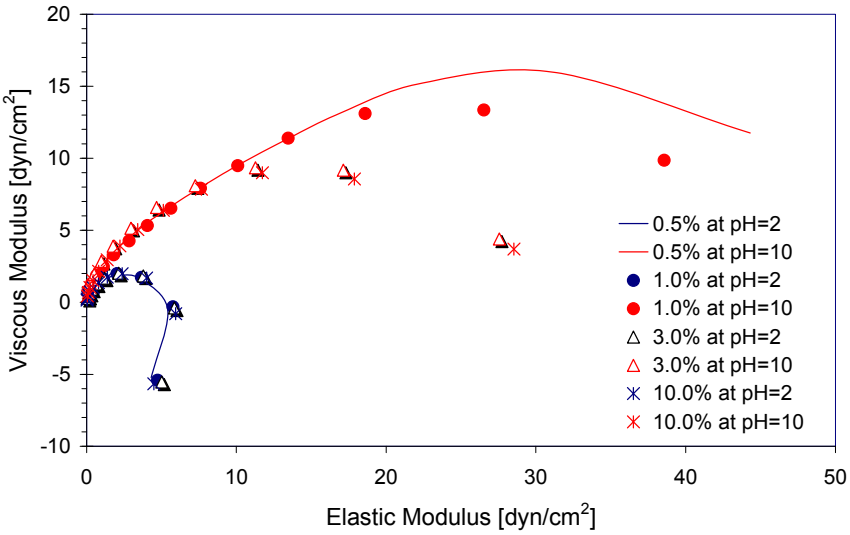

Figure 1.19(g): Influence of salinity on elastic and viscous modulus change at two specific pH's (pH = 2 and 10) for 0.5% Flopaam 3330S prepared in sodium chloride brine

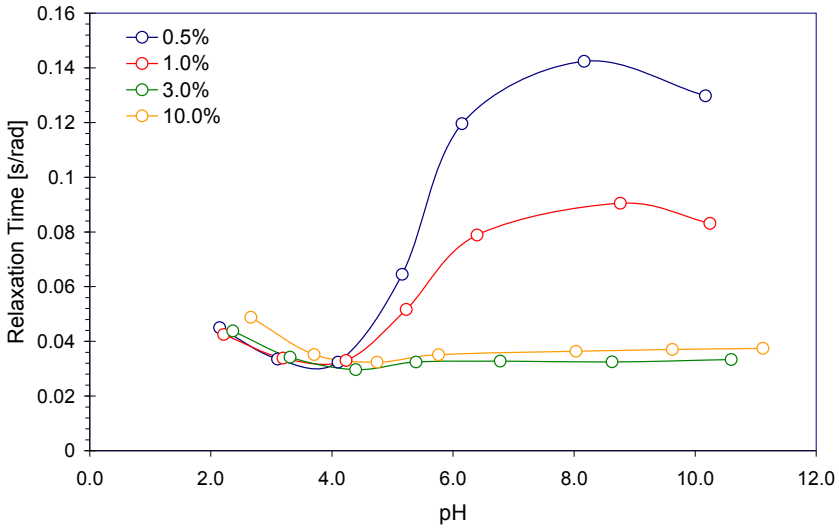

Figure 1.19(h): Influence of salinity on approximate relaxation time as a function of pH for 0.5% Flopaam 3330S prepared in sodium chloride brine

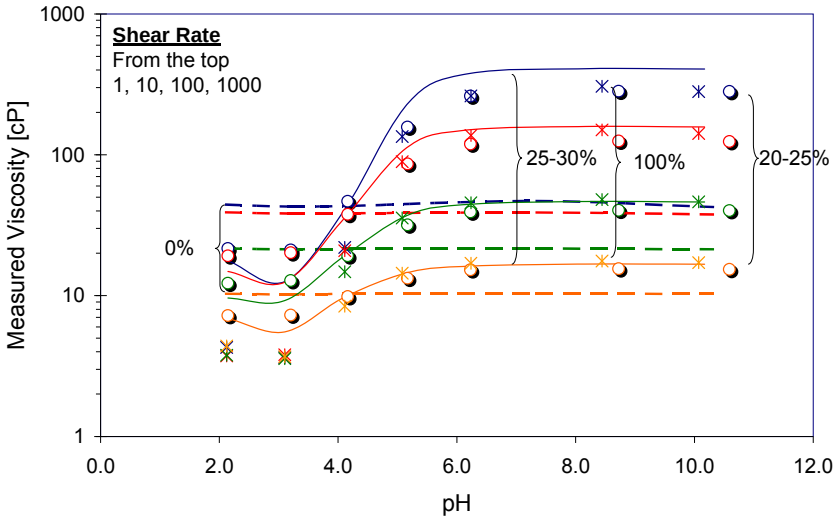

Figure 1.20(a): Influence of degree of hydrolysis on measured viscosity as a function of pH for 0.5% polymer prepared in 0.5% sodium chloride brine

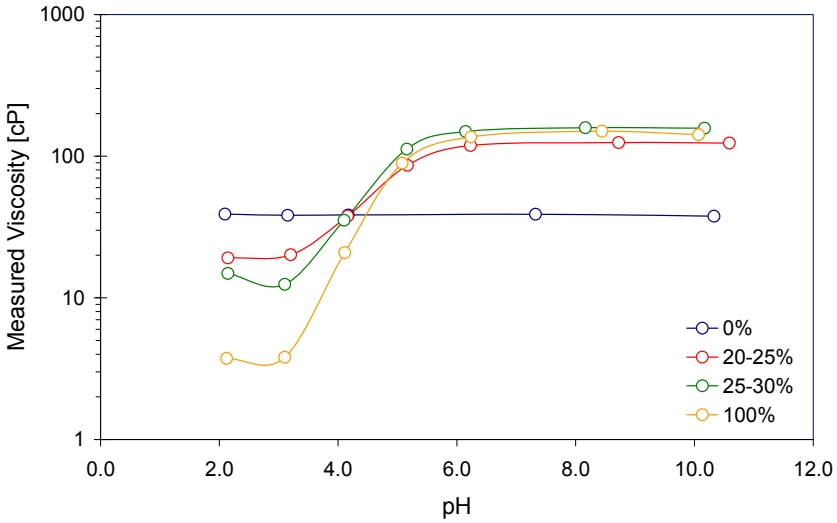

Figure 1.20(b): Influence of degree of hydrolysis on measured viscosity as a function of pH for 0.5% polymer prepared in 0.5% sodium chloride brine at shear rate of 10^{-1}

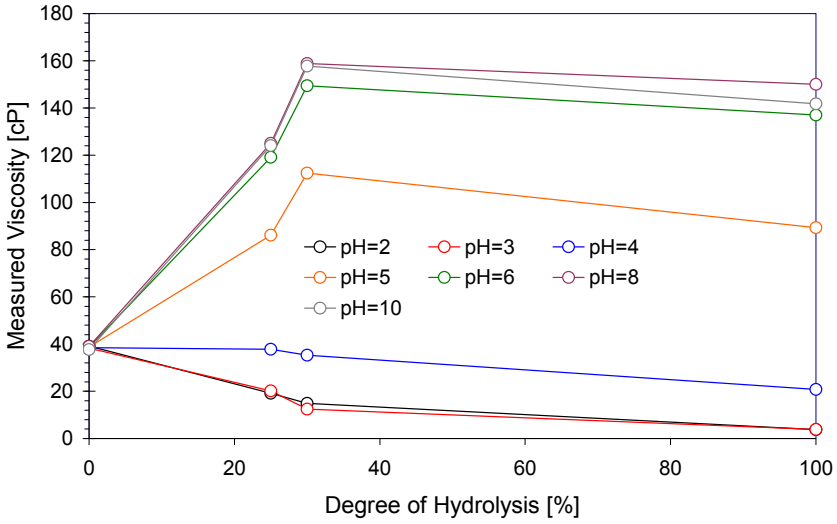

Figure 1.20(c): Measured viscosity as a function of degree of hydrolysis at specific pH's for 0.5% polymer prepared in 0.5% sodium chloride brine

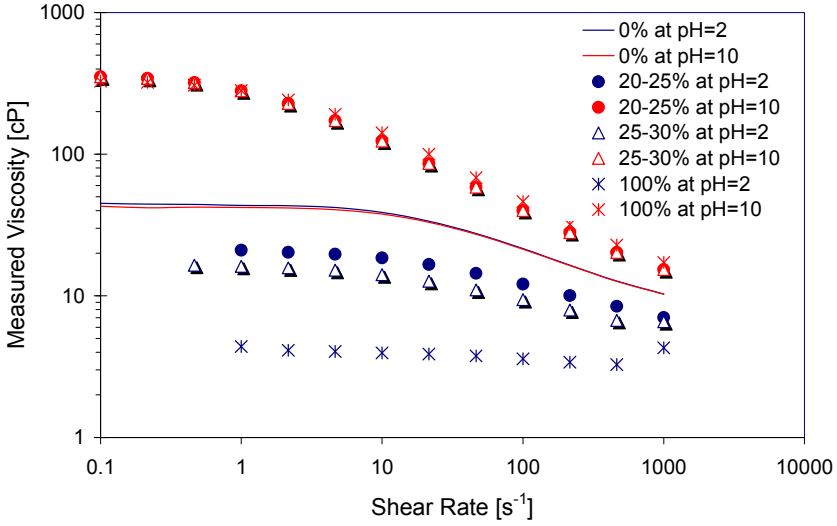

Figure 1.20(d): Influence of degree of hydrolysis on measured viscosity as a function of shear rate at two specific pH's (pH = 2 and 10) for 0.5% polymer prepared in 0.5% sodium chloride brine

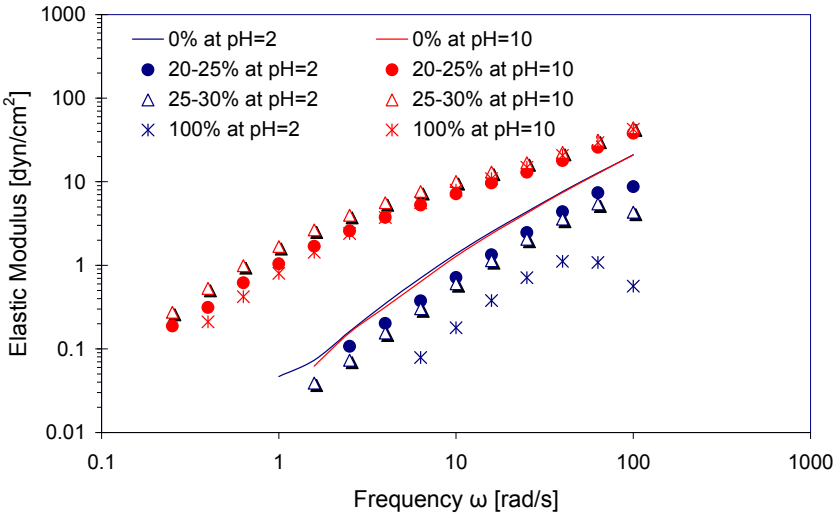

Figure 1.20(e): Influence of degree of hydrolysis on elastic modulus (G') change at two specific pH's (pH = 2 and 10) for 0.5% polymer prepared in 0.5% sodium chloride brine

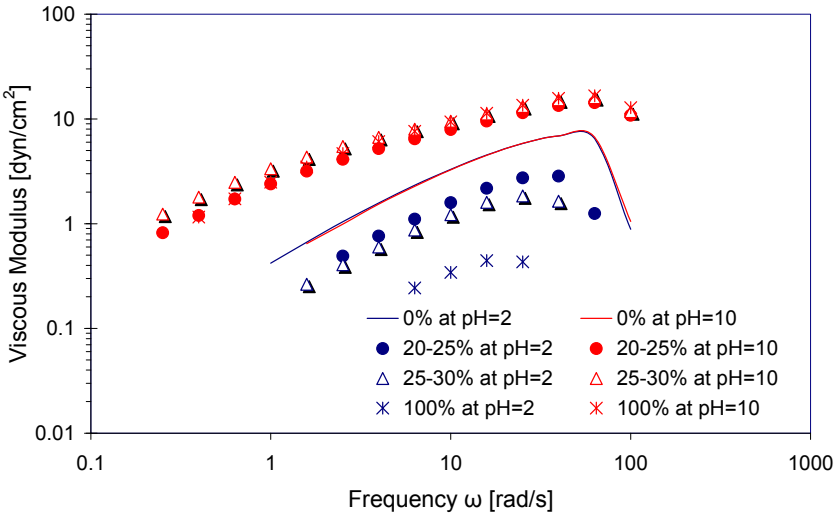

Figure 1.20(f): Influence of degree of hydrolysis on viscous modulus (G") change at two specific pH's (pH = 2 and 10) for 0.5% polymer prepared in 0.5% sodium chloride brine

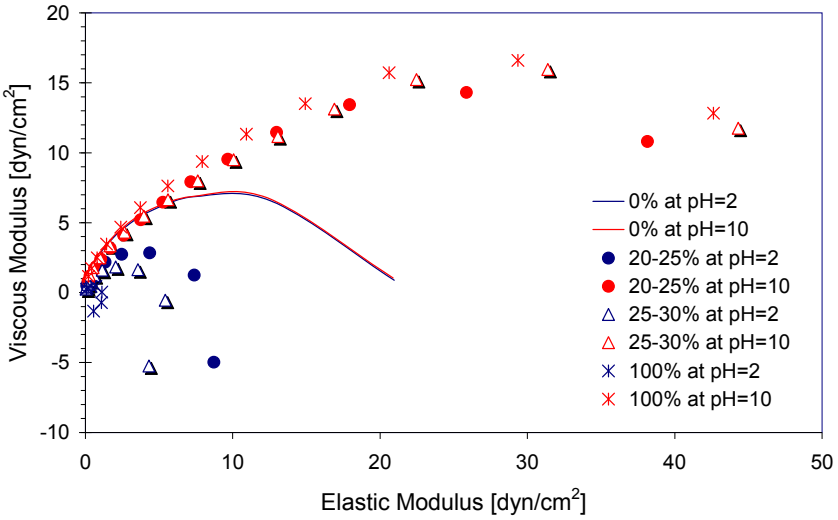

Figure 1.20(g): Influence of degree of hydrolysis on elastic and viscous modulus Change at two specific pH's (pH = 2 and 10) for 0.5% polymer prepared in 0.5% sodium chloride brine

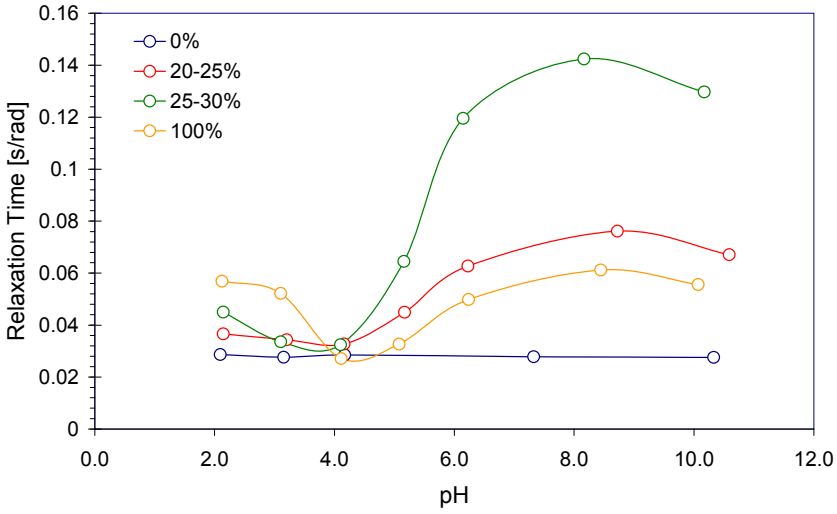

Figure 1.20(h): Influence of degree of hydrolysis on approximate relaxation time as a function of pH for 0.5% polymer prepared in 0.5% sodium chloride brine

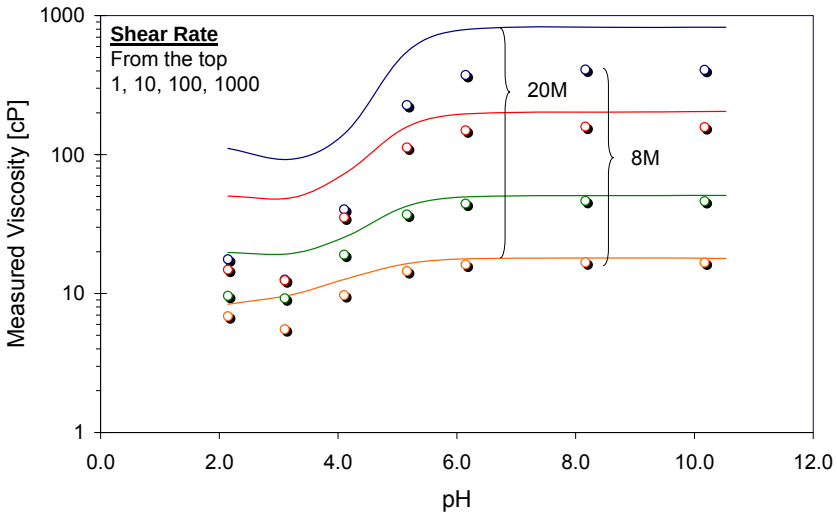

Figure 1.21(a): Influence of molecular weight on measured viscosity as a function of pH for 0.5% polymer prepared in 0.5% sodium chloride brine

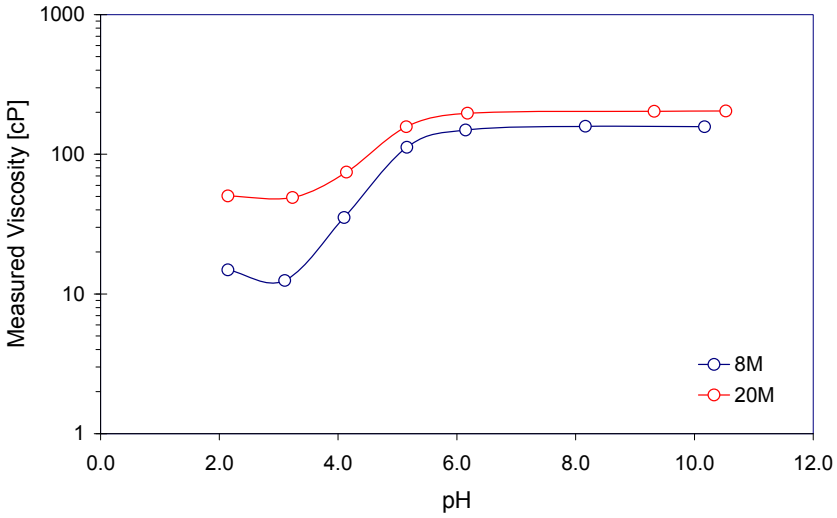

Figure 1.21(b): Influence of molecular weight on measured viscosity as a function of pH for 0.5% polymer prepared in 0.5% sodium chloride brine at shear rate of 10^{-1}

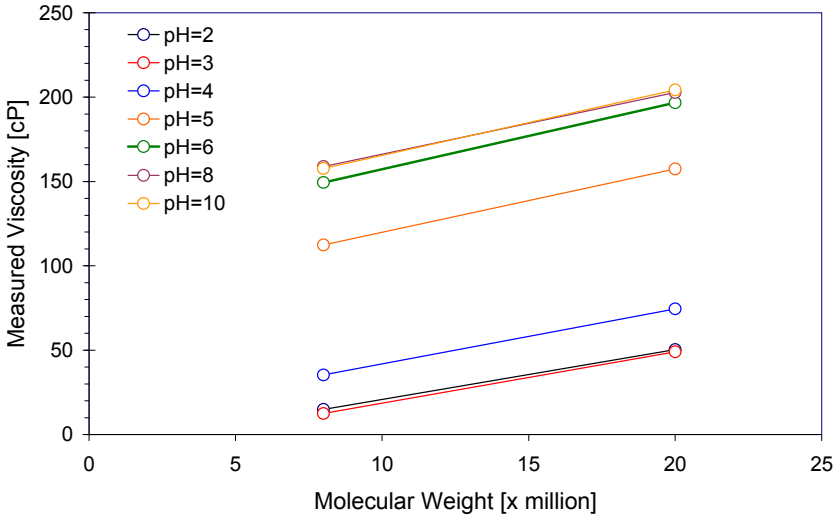

Figure 1.21(c): Measured viscosity as a function of molecular weight at specific pH's for 0.5% polymer prepared in 0.5% sodium chloride brine

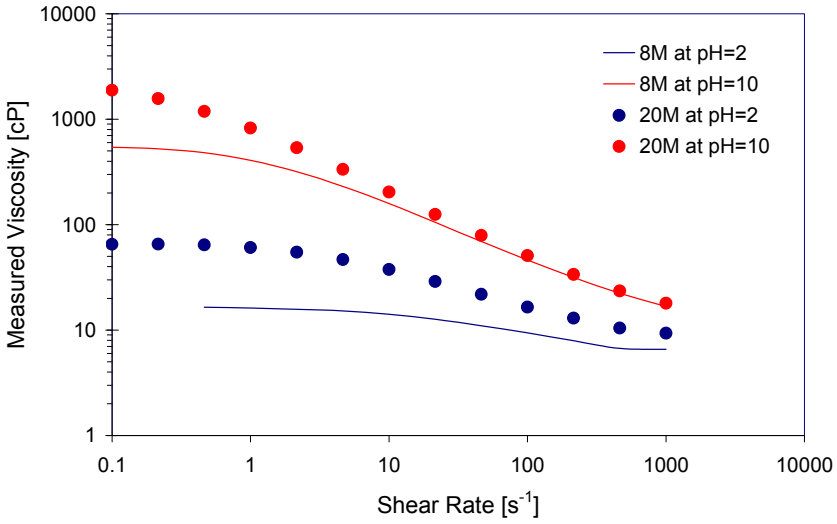

Figure 1.21(d): Influence of molecular weight on measured viscosity as a function of shear rate at two specific pH's (pH = 2 and 10) for 0.5% polymer prepared in 0.5% sodium chloride brine

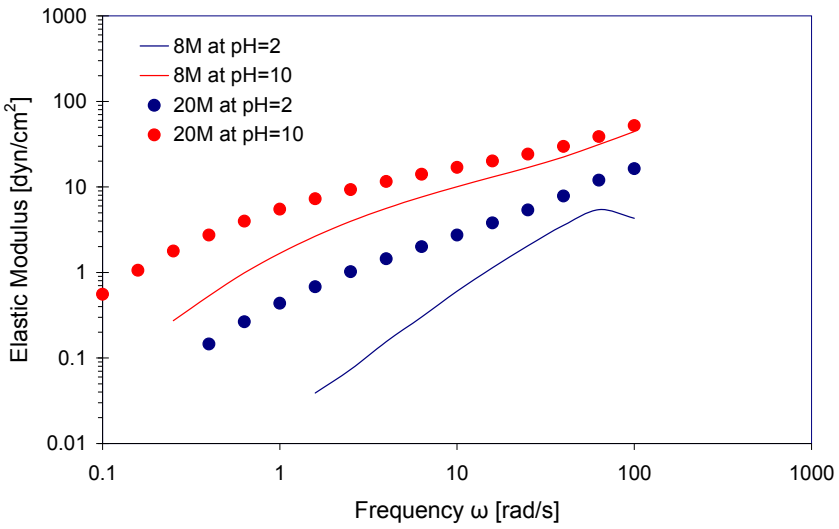

Figure 1.21(e): Influence of molecular weight on elastic modulus (G') change at two specific pH's (pH = 2 and 10) for 0.5% polymer prepared in 0.5% sodium chloride brine

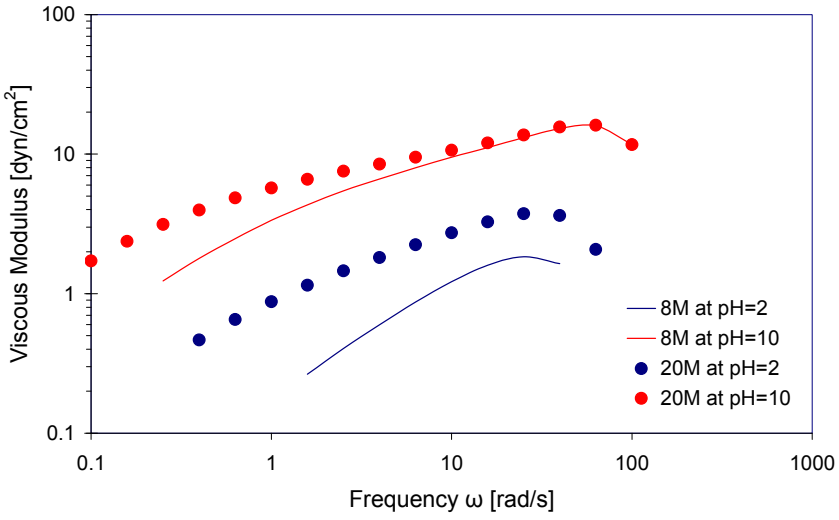

Figure 1.21(f): Influence of molecular weight on viscous modulus (G") change at two specific pH's (pH = 2 and 10) for 0.5% polymer prepared in 0.5% sodium chloride brine

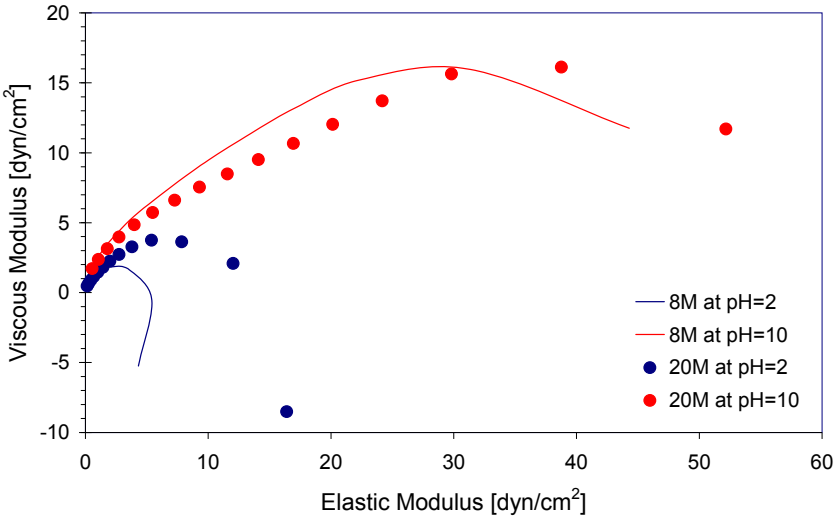

Figure 1.21(g): Influence of molecular weight on elastic and viscous modulus change at two specific pH's (pH = 2 and 10) for 0.5% polymer prepared in 0.5% sodium chloride brine

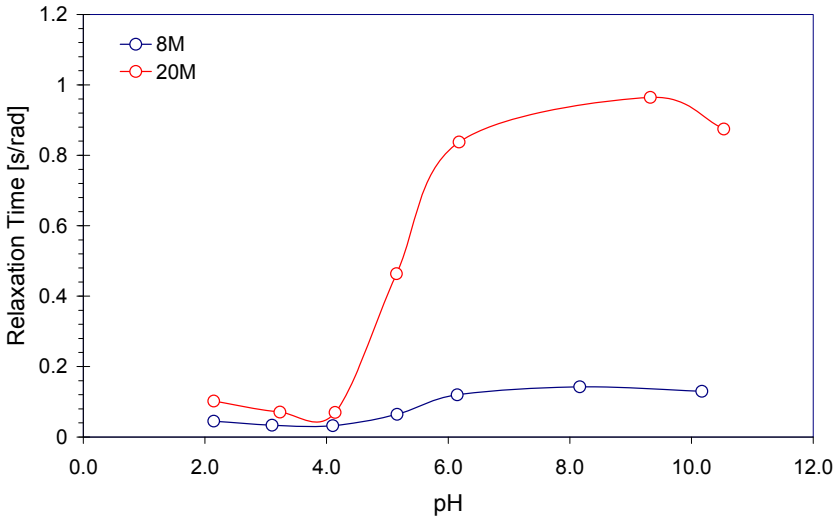

Figure 1.21(h): Influence of molecular weight on approximate relaxation time as a function of pH for 0.5% polymer prepared in 0.5% sodium chloride brine

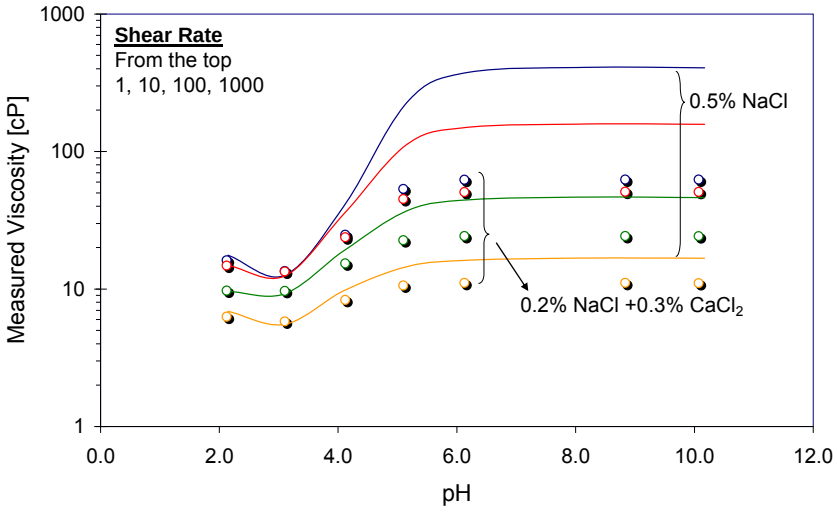

Figure 1.22(a): Influence of divalent ion on measured viscosity as a function of pH for 0.5% Flopaam 3330S prepared in 0.5% brine

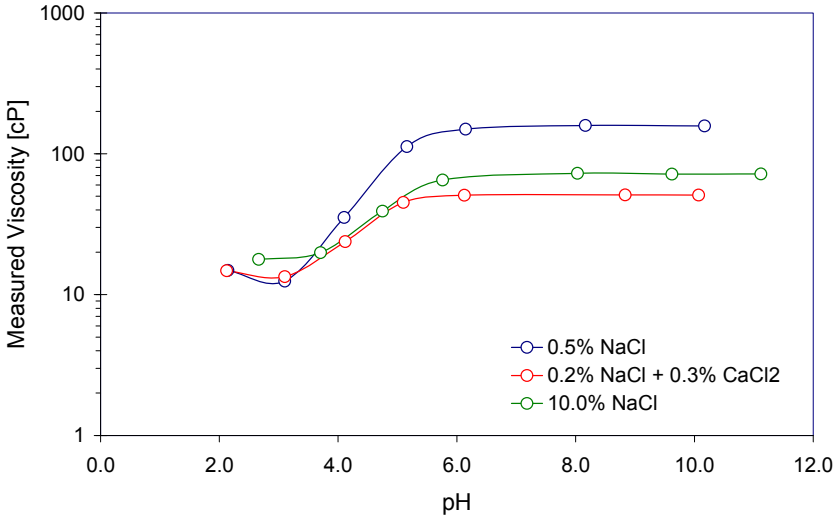

Figure 1.22(b): Influence of divalent ion on measured viscosity as a function of pH for 0.5% Flopaam 3330S prepared in 0.5% brine at shear rate of 10^{-1}

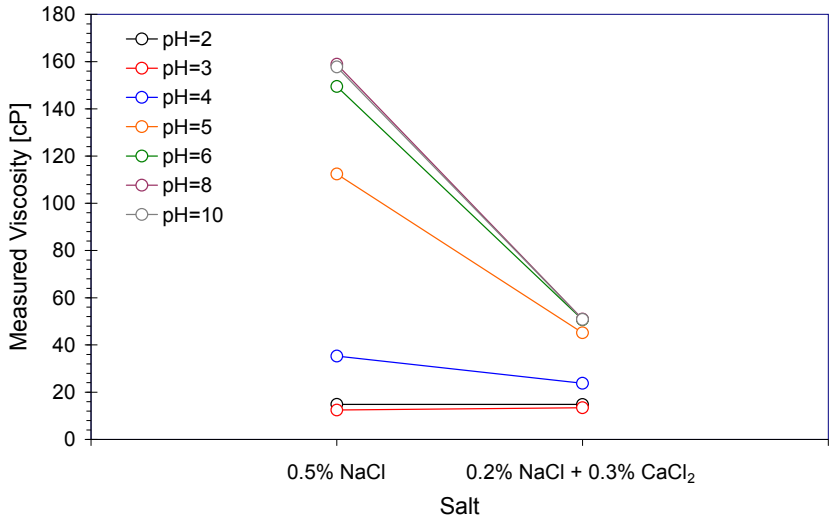

Figure 1.22(c): Measured viscosity as a function of divalent ion at specific pH's for 0.5% Flopaam 3330S prepared in 0.5% brine

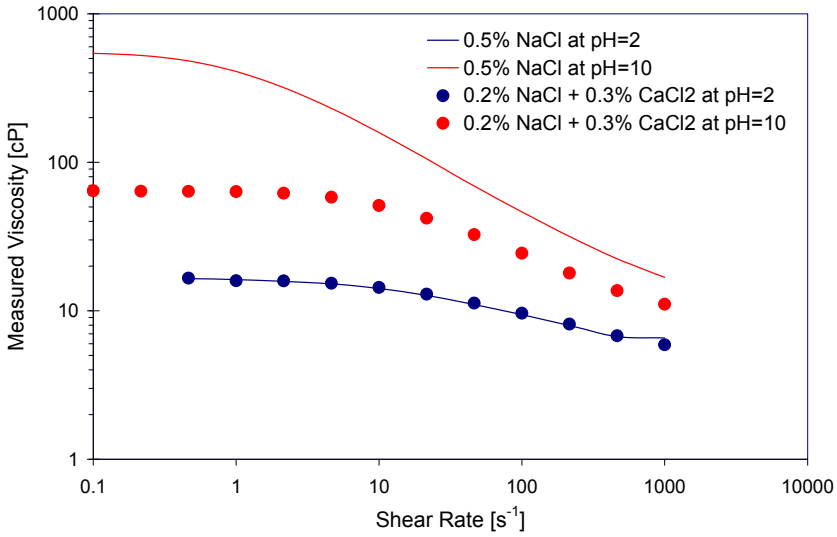

Figure 1.22(d): Influence of divalent ion on measured viscosity as a function of shear rate at two specific pH's (pH = 2 and 10) for 0.5% Flopaam 3330S prepared in 0.5% brine

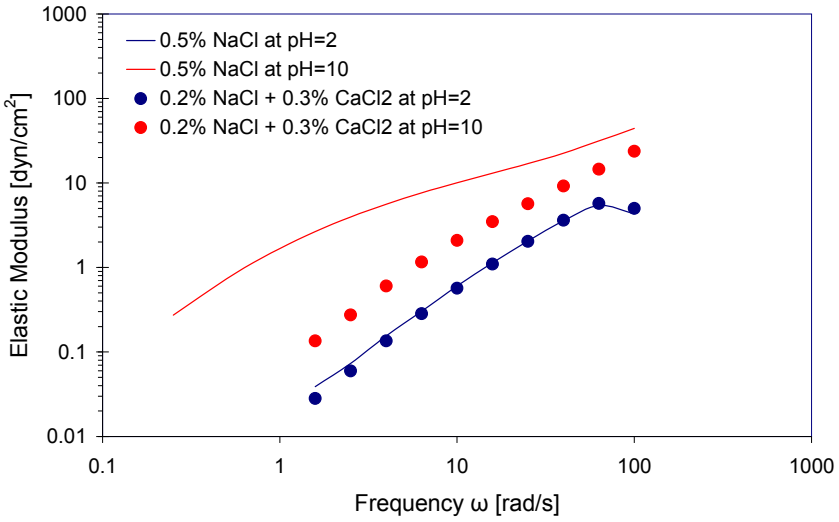

Figure 1.22(e): Influence of divalent ion on elastic modulus (G') change at two specific pH's (pH = 2 and 10) for 0.5% Flopaam 3330S prepared in 0.5% brine

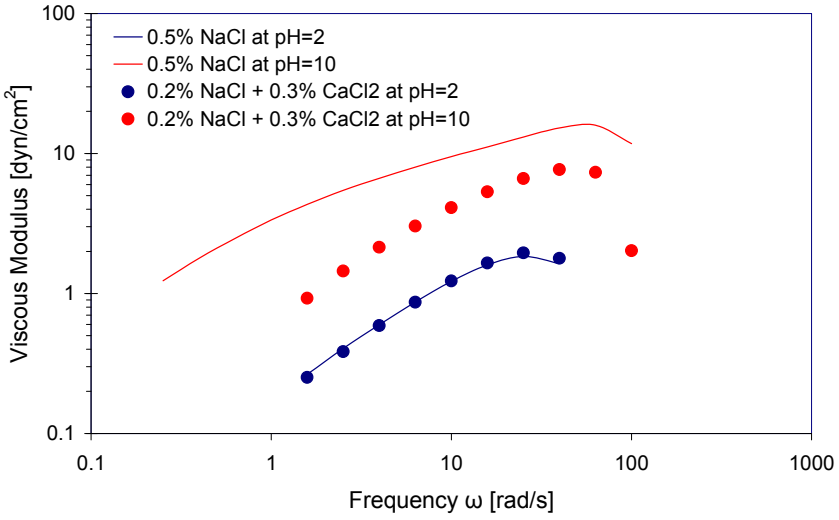

Figure 1.22(f): Influence of divalent ion on viscous modulus (G") change at two specific pH's (pH = 2 and 10) for 0.5% Flopaam 3330S prepared in 0.5% brine

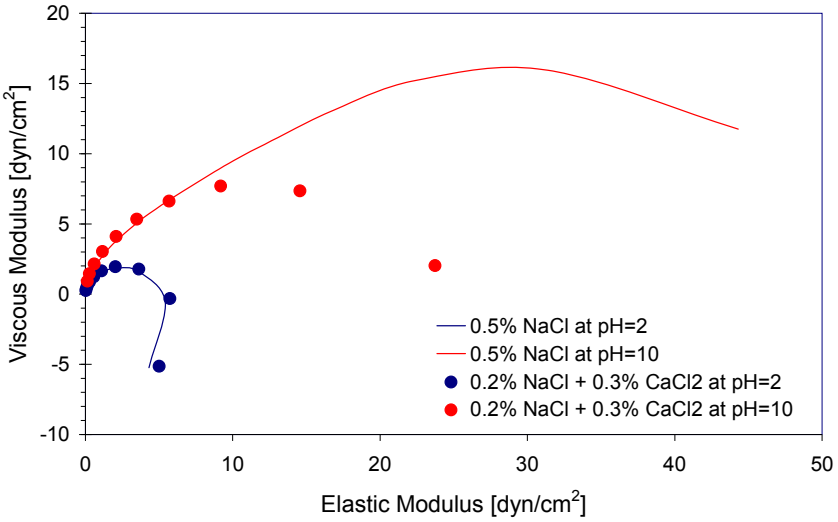

Figure 1.22(g): Influence of divalent ion on elastic and viscous modulus change at two specific pH's (pH = 2 and 10) for 0.5% Flopaam 3330S prepared in 0.5% brine

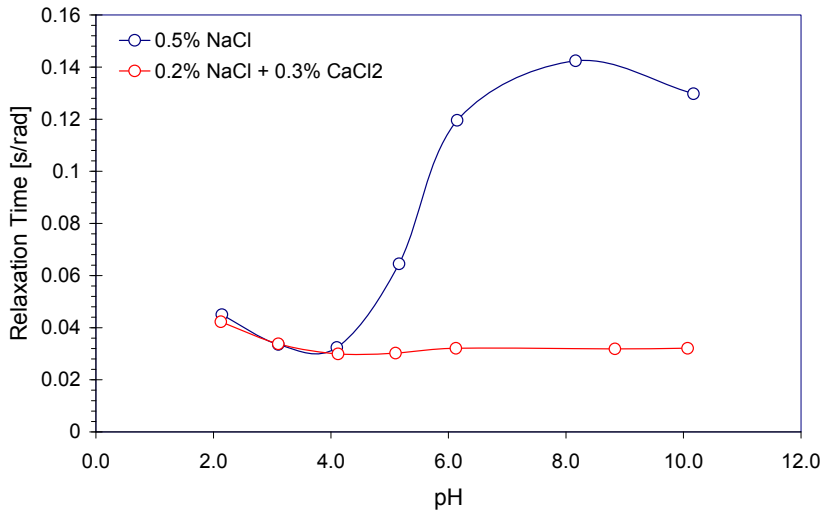

Figure 1.22(h): Influence of divalent ion on approximate relaxation time as a function of pH for 0.5% Flopaam 3330S prepared in 0.5% brine

2. Rheological Modeling Procedure for HPAM Solutions

2.1 INTRODUCTION

Viscosity is an important parameter to characterize the flow of polymer solution that is injected into porous media to improve displacement efficiency and to preserve the integrity of chemical banks for various EOR processes. An accurate viscosity prediction is, therefore, required in modeling to estimate the production performance of polymer-related applications for successful reservoir treatment. In simple laminar flow, most of EOR polymers show shear thinning non-Newtonian behavior: the viscosity decreases as the shear rate increases. This phenomenon is related to the structural characteristics of polymer chains, which are aligned up along the flow streamline in proportion to the shear rate. **Figure 2.1** schematically shows the typical shear dependence of the viscosity in a diluted polymer solution for EOR processes. The shear-thinning behavior occurs in the specific range of the shear rates, and the solution shows Newtonian behavior at sufficiently low or high shear rates, where the structural characteristics of polymer chains no longer affect the viscosity. HPAM, the polymer of our interest, is one of the common shear-thinning polymers and has random-coil macromolecular structure, which is susceptible to the reservoir conditions (such as salinity, pH, and temperature).

The most common viscosity model describing the non-Newtonian relationship between viscosity and the shear rate is the power-law model (Bird *et al*., 1960). This model is valid only for the shear-thinning region:

$$\eta = K\dot{\gamma}^{n-1} \tag{2.1}$$

where $\dot{\gamma}$ is the shear rate, K is the consistency index and n is the power-law exponent. For Newtonian fluid, n = 1 and K is the constant viscosity. n decreases as the viscosity deviates from the Newtonian behavior. It is widely used because of its simplicity, which requires only two parameters. Another common correlation is the Carreau model which has four parameters (Sorbie, 1991):

$$\eta = \eta_\infty + \left(\eta_\infty - \eta_o\right)\left[1+\left(\lambda\dot{\gamma}\right)^2\right]^{(n-1)/2} \tag{2.2}$$

where η_∞ and η_o are the infinite and zero shear-limit viscosities, respectively, and λ is the time constant. This model accounts for the full range of shear rates, including plateau

regions (Newtonian regions) at low and high shear rates. However, it has the disadvantage of requiring two more parameters than does the power-law model. Several well-known models suited for specific conditions have been proposed: the Bingham plastic model (Bingham, 1962); the Ellis model (Bird *et al.*, 1960); the Eyring model (Kincaid *et al.*, 1941); and others.

The power-law and Carreau viscosity models are useful, in that they can reasonably describe a shear-dependent viscosity behavior in simple analytic form. However, they need to be extended to model viscosity variations during the flow of polymer solution in porous media. Along with the shear rate variation, polymer concentration (which directly affects the viscosity) varies due to retention (adsorption and mechanical filtration), dispersion, and diffusion in the reservoir flow of polymer solution. The variations of salinity and temperature between injection fluid and reservoir brine also contribute to the change in the polymer viscosity. Commercial reservoir simulators, such as CMG (Computational Modeling Group) and Eclipse, have only a limited capability to predict such viscosity variations. This limited capability may cause severe errors in polymer flooding designs, and therefore, it is necessary to develop viscosity correlations applicable to such variations in reservoir conditions.

In this chapter, we propose a versatile modeling procedure to compute the viscosity of HPAM solution in terms of: shear rate; salinity; polymer concentration; and pH. The development of this procedure is necessary 1) as a pre-requisite for our low pH process, in which pH causes a drastic viscosity change, and 2) for accurate EOR process simulations for HPAM-related applications. This modeling procedure is empirical in nature, but combines several well-established correlations. The starting point is a modeling procedure for microgel systems proposed earlier by Huh *et al.* (2005). Some equations were modified in order to better describe the viscosity behavior of HPAM solutions in terms of the above variables. The detailed procedures for model derivation and the determination of model parameters are reported in this chapter. The matching results with laboratory measurements are also presented to show the accuracy of the model predictions.

2.2 DERIVATION OF A RHEOLOGICAL MODEL

Our viscosity model is based on the assumption that the mechanism of viscosity change of HPAM solution, triggered by salinity or pH, is quite similar to that of soft polyelectrolyte microgels. If salinity decreases or pH increases, microgel absorbs water into its molecular-network structure, thereby swelling the microgel and, subsequently, sharply increasing viscosity. Similarly, HPAM is an anionic polyelectrolyte whose chain extension is triggered by the same electrostatic repulsion, resulting in a sharp increase of viscosity. Although there is a considerable difference between the degree of extension (of HPAM) and the degree of swelling (of microgels), the viscosity change is mostly due to the charge-induced size effect of macromolecules in both cases. As shown in **Figure 2.2,** this fact can be supported by the observation that HPAM and microgels show the same form of viscosity curves as a function of pH. The recent development of a microgel modeling procedure (Huh *et al.*, 2005) that is capable of computing the viscosity as a function of shear rate, salinity, polymer concentration, and pH was used as a basic modeling scheme. Some modifications were made in order to develop a viscosity model for HPAM solution.

The modeling procedure takes the following steps to compute the viscosity of HPAM solutions:

- Compute the equilibrium chain-extension ratio (Q) from the modified Brannon-Peppas model (1988, 1990, 1991) in terms of salinity and pH.
- Relate the equilibrium chain-extension ratio (Q) to the intrinsic viscosity ($|\eta|$) by employing the modified Mark-Houwink equation.
- Relate the intrinsic viscosity ($|\eta|$) to the zero-shear-limit viscosity (η_o) by a new correlation in the form of power-law.
- Calculate the viscosity (η) at a specific shear rate by the Carreau equation. The power-law exponent (n) and the time constant (λ) are predicted by the modified Lange and Huh equation.

A flowchart for the modeling procedure is shown in **Figure 2.3**. This procedure was programmed with both Microsoft® Excel VBA (Visual Basic Application) and FORTRAN. The Newtonian-Ralph method was used to solve non-linear form of the

modified Brannon-Peppas model to obtain equilibrium chain-extension ratio (*Q*). The description of each step is introduced in the following sections.

..2.2.1 Equilibrium Chain-Extension Ratio by the Brannon-Peppas model

The original equilibrium swelling model by Brannon-Peppas and Peppas (1988, 1990, 1991) was derived from the chemical potential balance of the system at swelling equilibrium state by three contributions: mixing, elastic-retractive, and ionic energies:

$$\left(\Delta\mu_1^*\right)_{ion} - \left(\Delta\mu_1\right)_{ion} = \left(\Delta\mu_1\right)_{mix} + \left(\Delta\mu_1\right)_{el} \tag{2.3}$$

Equation (2.3) states that the difference between the ionic contributions from the chemical potential of the swelling agent, inside and outside of the gel network, is equal to the sum of the contributions to the chemical potential of the mixing and elastic forces due to polymer-swelling agent interactions. The evaluation of each term in equation (2.3) (based on the Flory-Huggins thermodynamic theory, the rubber elasticity theory, and ionic interaction theories, respectively) leads to the following equilibrium swelling model:

$$\frac{V_1}{4I}\left(\frac{\upsilon_{2,s}}{\bar{\upsilon}}\right)^2\left(\frac{K_a}{10^{-pH}+K_a}\right)^2 = \ln(1-\upsilon_{2,s}) + \upsilon_{2,s} + \chi_1\upsilon^2{}_{2,s}$$
$$+\left(\frac{V_1}{\bar{\upsilon}\overline{M}_c}\right)\left(1-\frac{2\overline{M}_c}{\overline{M}_n}\right)\upsilon_{2,s}\left[\left(\frac{\upsilon_{2,s}}{\upsilon_{2,r}}\right)^{1/3} - \frac{1}{2}\left(\frac{\upsilon_{2,s}}{\upsilon_{2,r}}\right)\right] \tag{2.4}$$

where V_1 is the molar volume of solvent; I is the ionic strength of solvent; $\upsilon_{2,s}$ is the polymer volume fraction in the swollen network; $\bar{\upsilon}$ is the specific molar volume of dry polymer; K_a is the dissociation constant of ionizable groups on polymer; χ_1 is the polymer-solvent interaction parameter; $\overline{M}_c$ is the average molecular weight between crosslinks; $\overline{M}_n$ is the average molecular weight of polymer before crosslinking; and $\upsilon_{2,r}$ is the polymer volume fraction in the relaxed state.

In the case of HPAM solutions, we simply adopted equation (2.4) and empirically corresponded the two parameters ($\overline{M}_c$ and $\overline{M}_n$) to the new concepts suitable for HPAM solutions: average molecular weight of polymer before crosslinking ($\overline{M}_n$) corresponded to average molecular weight of HPAM polymer; and average molecular weight between

crosslinks ($\bar{M}_c$) corresponded to average molecular weight between repeating chain units. These modifications bring the equilibrium swelling ratios to the values that are reasonable for HPAM solutions, showing that the degree of chain extension for HPAM is much smaller than the swelling of microgel. **Figure 2.4** compares the calculated swelling ratio of microgel (with $\bar{M}_n$ = 75,000 and $\bar{M}_c$ = 12,000) to that of HPAM (with $\bar{M}_n$ = 8,000,000 and $\bar{M}_c$ = 71), clearly showing the difference of the equilibrium swelling ratio of microgel from the chain-extension ratio for HPAM. All other parameters remain the same as described in **Figure 2.4**. Hereafter, the equilibrium swelling ratio, Q will be named "Equilibrium Chain-Extension Ratio." As before, the equilibrium chain-extension ratio is given by:

$$Q = 1/\upsilon_{2,s} \tag{2.5}$$

It is important to understand the effect of the parameters on the equilibrium chain-extension ratio. Although these screening studies for microgels were already done by Brannon-Peppas and Peppas (1988, 1990, 1991), similar studies for HPAM polymers have been performed in this research to confirm whether the trends correspond to those of microgels, and to streamline the procedure for the determination of unknown parameters in this model. The parameters for the 0.5% Flopaam 3330 solution, prepared in 0.5% sodium chloride brine, were used: V_1 = 18 cm^3/mol; I = 0.09; pK_a = 4.9; χ_1 = 0.8; $\bar{M}_c$ = 8,000,000; $\bar{M}_n$ = 71.3; $\upsilon_{2,r}$ = 0.5, and the effects of four parameters – pK_a, I, $\upsilon_{2,r}$, and χ_1 – are investigated. **Figure 2.5** shows the effect of pK_a on the equilibrium chain-extension ratio (Q). First, it is noted that the equilibrium chain-extension ratio shows a drastic increase as pH increases, which is quite similar to the shape of the viscosity curve. The role of pK_a is to shift the equilibrium chain-extension ratio curve to the right or left direction. If pK_a is decreased, the pH region where the equilibrium chain-extension ratio drastically increases is decreased. **Figure 2.6** illustrates how ionic strength (I) affects the extension ratio. I represents mainly the salinity and, as expected, the increase of ionic strength reduces the equilibrium chain-extension ratio in the high pH region. The effects of $\upsilon_{2,r}$, and χ_1 are to control the equilibrium chain-extension ratio of high and low pH regions, respectively, as shown in **Figures 2.7** and **2.8**. In both cases, the lower the value

is, the higher the equilibrium chain-extension ratio is. These observations conform exactly to those of Brannon-Peppas and Peppas (1988, 1990, 1991).

2.2.2 Intrinsic Viscosity by Modified Mark-Houwink Equation

The intrinsic viscosity is a property related to molecular size and polymer chain extension in solution; it is therefore a pertinent parameter to connect the hydrodynamic molecular size (equilibrium chain-extension ratio) with the viscosity. The intrinsic viscosity is defined as the limit of the reduced viscosity or inherent viscosity as the solution concentration goes to zero:

$$|\eta| = \lim_{c \to 0} \frac{\eta_o - \eta_s}{c\eta_s} = \lim_{c \to 0} \eta_R \tag{2.6}$$

or

$$|\eta| = \lim_{c \to 0} \frac{\ln(\eta_o / \eta_s)}{c} = \lim_{c \to 0} \frac{\ln(\eta_r)}{c} \tag{2.7}$$

where η_o is the limiting Newtonian viscosity at the zero shear limit; η_s is the solvent viscosity; and C is the polymer concentration.

A modified Mark-Houwink equation was adopted as a correlation between intrinsic viscosity and equilibrium chain-extension ratio, as was done for microgels. The Mark-Houwink equation is a simple and useful correlation to relate molecular weight of polymer to the intrinsic viscosity:

$$|\eta| = aM^b \tag{2.8}$$

where a and b are constants for a given polymer; M is the molecular weight of the polymer. As Huh *et al*. (2005) did, we modified this correlation by replacing the molecular weight with the equilibrium chain-extension ratio:

$$|\eta| = aQ^b \tag{2.9}$$

Values of a and b will be empirically determined from the laboratory viscosity data, as shown in Section 2.5.

2.2.3 A Correlation for Low Shear-Limit Viscosity

As the next step, the intrinsic viscosity is related to the zero-shear limit viscosity. In the original gel model, the Martin equation was used for this purpose to provide good model prediction with laboratory data:

$$\eta_o = \eta_s + \eta_s C|\eta| \exp(k'' C|\eta|) \tag{2.10}$$

where *k''* is the empirical constant. However, it was found through matching attempts with laboratory-measured data that this correlation could not satisfactorily describe the low shear-limit viscosity of HPAM. Other formulations have also been tested for the matching: the Huggins (1942) and Kraemer (1938) models that are applicable to low polymer concentrations; and the model by Lyons *et al.* (1970) for relatively high polymer concentrations. None of them could fit the laboratory-measured data satisfactorily. Unlike biopolymers such as Xanthan with stiff backbones, HPAM has very flexible random coils with complicated interactions among molecules, which makes it difficult to match the laboratory-measured data to the above well-known correlations.

Based on extensive screening studies, a new empirically-derived correlation is proposed to relate the intrinsic viscosity to the zero-shear limit viscosity. It was found that good data fits could be achieved when the product of polymer concentration and intrinsic viscosity is proportional to specific viscosity in a power-law form:

$$\eta_r = \frac{\eta_o - \eta_s}{\eta_s} = \left[C|\eta|\right]^{k''} \tag{2.11}$$

where η_r is the relative viscosity. This correlation provides good fits with measurements, which will be explained in Section 2.4.

2.2.4 Carreau Equation

The well-known Carreau equation was chosen to account for the shear dependence of the viscosity:

$$\eta = \eta_\infty + \left[\eta_o - \eta_\infty\right]\left[1 + \left(\lambda\dot{\gamma}\right)^2\right]^{(n-1)/2} \tag{2.12}$$

where η_o and η_∞ are the limiting Newtonian viscosities at the low and high shear limits, respectively; and $\dot{\gamma}$ is the shear rate; λ is the time constant; and n is the power-law exponent.

Lange and Huh (1994) proposed the following empirical equations to relate the two constants (λ and n) in the Carreau equation to the product of polymer concentration and intrinsic viscosity. They provided good prediction for Xanthan biopolymer and were adopted in the earlier gel model (Huh *et al.*, 2005):

$$(n-1)=e_1+e_2\,C|\eta| \tag{2.13}$$

$$\lambda=e_3+e_4\left[C|\eta|\right]^{e_5} \tag{2.14}$$

where e_1 to e_5 are the empirical parameters specific to each polymer. In case of HPAM, an equation for (n-1) was modified to be proportional to the natural logarithm of the product of polymer concentration and intrinsic viscosity, which gives the best fit for the laboratory-measured data:

$$(n-1)=e_1+e_2\ln\left[C|\eta|\right] \tag{2.15}$$

With the above equations, the bulk viscosity for HPAM can be calculated as a function of shear rate, salinity, polymer concentration, and pH.

2.3 DETERMINATION OF VISCOSITY MODEL PARAMETERS

In the viscosity model for HPAM, there are 19 parameters to describe the dependence on: shear rate; salinity; polymer concentration; and pH. Some can be easily obtained from literature sources, or by simple calculations, while others should be determined by fitting the laboratory-measured data. **Table 2.1** lists all the parameters necessary for the viscosity calculation of HPAM. This section describes: 1) the procedure by which those parameters can be determined through laboratory-measured data; and 2) the resultant values of procedure execution. A set of parameters for each polymer employed in rheological measurements (in **Chapter 1**) is determined: Flopaam 3330S (8M MW, 25~30% degree of hydrolysis); Flopaam 3630S (20M MW); Flopaam 2330S (20~25% degree of hydrolysis); and ALP99VHM (100% degree of hydrolysis, pure polyacrylic acid). However, no values of parameters for FA920SH (0% degree of hydrolysis, pure polyacrylamide) are given because the polymer has no dependence on pH, making the application of the Brannon-Peppas model unnecessary. The following is a summary of the steps to determine the model parameters:

- Determine the values of parameters available from literature sources, as well as those parameters that are easily calculable.
- Obtain three variables (η_o, λ and n) in the Carreau equation for each pH by using the viscosity data measured at four shear rates (1, 10, 100, 1000 s^{-1}).
- Repeat the same calculations for at least two different polymer concentrations.
- Obtain the intrinsic viscosities ($[\eta]$) at pH = 3 and 10 and k'' by evaluating the measured η_o values with the new power-law correlation obtained in the previous step.
- Calculate the values of the equilibrium extension ratio (Q) from the modified Brannon-Peppas model at pH = 3 and 10.
- Obtain the parameters, a and b, in the modified Mark-Houwink equation by evaluating two sets of equilibrium extension ratios and intrinsic viscosities at pH = 3 and 10.
- Evaluate e_1 to e_5 by fitting the curve for all the laboratory data (λ and n) at two different polymer concentrations with equation (2.14) and (2.15).
- Adjust pK_a value to match the transition pH between the model and laboratory-measured data.
- Evaluate e_1 to e_5 again to find more accurate values.

The procedure is described below with a concrete example of Flopaam 3330S, which has a 25-30% degree of hydrolysis and a molecular weight of approximately 8,000,000. The laboratory data at three different polymer concentrations (0.2, 0.5, and 0.8%) were used for this evaluation.

2.3.1 Determination of Definable and Calculable Parameters

Table 2.2 summarizes the values of 9 model parameters for Flopaam 3330S. These values were obtained from literature sources, or by simple calculations. Three parameters that are typical of carboxylated polyacrylates, polymethacrylates, or related

copolymers (Brannon-Peppas *et al.*, 1991) were adopted for our model: 1) the specific volume of the dry polymer ($\bar{\upsilon}$) = 0.8 cm3/g; 2) the polymer volume fraction in the relaxed state ($\upsilon_{2,r}$) = 0.5; and 3) the polymer-solvent interaction parameter (χ_1) = 0.8. An initial pK_a of 4.5 was assumed, which was then adjusted during the parameter determination procedure. An average molecular weight of $\bar{M}_n$ = 8,000,000 was used with the repeating unit of $\bar{M}_c$ = 71.3. The value of $\bar{M}_c$ was obtained by averaging the molecular weights of carboxyl- and amino- groups on the basis of degree of hydrolysis. As solvent (brine) properties, molar volume V_1 = 18 cm^3/mol was used with ionic strength I = 0.09 for 0.5% NaCl brine. The ionic strength for the dissociation of an electrolyte M_xX_m can be calculated by:

$$I = \frac{1}{2}\sum z_i^2 m_i \qquad (2.16)$$

where z_i and m_i are the valence factor and the concentration of i-th ion, respectively. Solvent viscosity of η_s = 1 cP was assumed, and polymer concentrations of C = 0.002, 0.005, 0.008 g/cm^3 were used. All calculations were performed on the assumption that the viscosity at high-shear limit (η_∞) reaches to its solvent viscosity of 1 cP.

2.3.2 Determination of Fitting Parameters

As preliminary calculations to determine the parameters by data fitting, the viscosity data shown in **Tables 1.5(a)** to **1.7(a)** in **Chapter 1** were used to determine three parameters in the Carreau equation (η_o, λ and n). These calculations were done at pH's (2, 3, 4, 5, 6, 8, 10) for all three polymer concentrations (C = 0.002, 0.005, 0.008 g/cm^3). The least square method was used to obtain the best fit between the calculated and measured data; the resultant parameters are tabulated in **Table 2.3**. The next step is to determine intrinsic viscosities, $[\eta]$ at pH = 3.0 and 10.0, and an empirical constant, *k"* in a new power-law correlation. Since the intrinsic viscosity is independent of the polymer concentration, two values should be available at low and high pH, respectively. On the other hand, the value of *k"* should be one value because it is a constant specific to the type of polymer. Two sets of η_o values at pH = 3.0 and 10.0 for polymer

concentrations, 0.2 and 0.8%, were used to find those parameters; and the data for 0.5% polymer concentration was used to verify the fit. The intrinsic viscosities of $[\eta]$ = 561 and 1788 cm^3/g at pH = 3.0 and 10.0, respectively, and the polymer-specific constant of k'' = 2.84 were obtained. **Table 2.4** compares the computed and measured zero-shear limit viscosities, η_o, for three different concentrations, which show good matches.

The parameters a and b, in the modified Mark-Houwink equation, are the next to be determined. They were easily calculated by employing two sets of intrinsic viscosities (obtained in the above step) and the equilibrium chain-extension ratios at pH = 3.0 and 10.0. The equilibrium chain-extension ratio can be obtained with the modified Brannon-Peppas model and the required input parameters were as described in Section 2.3.1. The results show equilibrium extension ratios of Q =1.52 and 38.7 at pH = 3.0 and 10.0, respectively; the results also show the parameters in the modified Mark-Houwink equation as a = 481.46 and b = 0.359. The empirical parameters, e_1 to e_5 were then obtained as the final step. As shown in **Table 2.3,** the values of $C[\eta]$ corresponding to each pH were first calculated for all three polymer concentrations: with C as a fixed value, $[\eta]$ can be obtained from the modified Brannon-Peppas model. The values of (n-1) and λ were plotted and curve fitted against $C[\eta]$ by employing equation (2.14) and (2.15) to determine the values of e_1 to e_5. **Figure 2.9** and **2.10** show the curve-fitting results for (n-1) and λ, with good fitting results. The assumed value of pK_a was then adjusted to match the location of transition pH between the calculated and measured viscosities, because it shifts the viscosity curve to the left or right direction, as mentioned in Section 2.2.1. Finally, the curve fittings of (n-1) and λ were repeated for the accurate values of e_1 to e_5. **Table 2.5** summarizes all 19 parameters for Flopaam 3330S.

For polymers with different molecular weights and degrees of hydrolysis (different types of polymers), new sets of parameters have been prepared and are also listed in **Table 2.5**: Flopaam 3630S (20M MW); Flopaam 2330S (20~25% degree of hydrolysis); and ALP99VHM (100% degree of hydrolysis, pure polyacrylic acid). The laboratory-measured data for two polymer concentrations (0.2 and 0.5%) were used to determine the parameters, and the same procedure as that of Flopaam 3330S was taken.

2.4 MATCHING RESULTS WITH LABORATORY DATA

This section describes the validity of model predictions, as determined by their comparison with laboratory measurement data. **Figures 2.11** to **2.13** show the comparisons between laboratory data and model predictions for different concentrations (0.2, 0.5, 0.8%) of Flopaam 3330S, prepared in 0.5% sodium chloride brine. It is observed that the model provides excellent matches with laboratory data for a wide range of pH. The model also fits very well with the transition pH, where the viscosity changes by one or two orders of magnitude. **Figures 2.14** to **2.16** show the same plots in terms of shear rate for the different pH's, in order to confirm good prediction capability of this model. Basically, the Brannon-Peppas model accounts for the pH and salinity sensitivity of the viscosity, in terms of the equilibrium chain-extension ratio (Q), as shown in **Figure 2.4**. The Carreau model then describes the shear rate dependence of the viscosity. Two additional models – the Mark-Houwink and new power-law models – convey the HPAM molecular size information to the Carreau equation in terms of polymer concentration, by way of zero-shear limit viscosity and intrinsic viscosity. Although this modeling procedure was empirically derived, it shows good capability of predicting the viscosity.

The predictive capability of this model was extended and verified for a wide range of salinity. **Figures 2.17** to **19** show comparisons between the laboratory data and model predictions for 0.5% Flopaam 3330S, prepared in different concentrations of sodium chloride brine – 1, 3, and 10%. The model provides a good match for 1% brine; however, it deviates from laboratory data for 3% sodium chloride salinity. It then gives better predictions in case of 10% brine, as shown in **Figure 2.19**. The answer could be found in **Figure 1.19(c)** in **Chapter 1**. The salinity of 3% represents the critical value above which the viscosity does not change significantly (and is even slightly increasing). The model is not able to describe the region above the critical salinity. The term of I in the Brannon-Peppas model is the only parameter to control the salinity change. **Figure 2.20** compares an equilibrium chain-extension ratio response with the measured viscosity as a function of salinity, ranging from 0 to 10% sodium chloride brine for 0.5% Flopaam 3330S, at pH = 10.0. It is shown that as the ionic strength I increases, the equilibrium extension ratio decreases continuously and does not show similar a trend in the region above the critical salinity. The validity of the model, in terms of the effect of divalent ions, was also checked as shown in **Figure 2.21**. The calculated viscosities are much higher than the measured values, showing that divalent ions have more pronounced

effects on the viscosity reduction than do monovalent ions. In other words, the effect of divalent ions on the viscosity reduction is much more severe than the effect of increasing ionic strength. Therefore, it can be concluded that this model is valid only in the presence of monovalent ions below critical salinity.

Figures 2.22 and **2.23** show comparisons between laboratory data and the model prediction for Flopaam 3630, which has molecular weight of 20 million. The polymer concentrations are 0.2 (shown in **Figure 2.22**) and 0.5% (shown in **Figure 2.23**), prepared in 0.5% sodium chloride brine. **Figures 2.24** and **2.25** show comparisons between laboratory data and the model predictions for 0.2 and 0.5% Flopaam 2330 (20~25% degree of hydrolysis), prepared in 0.5% sodium chloride brine, respectively. **Figures 2.26** and **2.27** show comparisons between laboratory data and the model predictions for 0.2 and 0.5% ALP99VHM (100% degree of hydrolysis), prepared in 0.5% sodium chloride brine, respectively. These graphs all demonstrate the excellent predictive capability of the viscosity model for different types of polymers. Once the parameters for one type of polymer have been determined, this modeling procedure is both versatile and useful because the viscosity can be predicted in terms of: shear rate; salinity; polymer concentration; and pH. The laboratory measurements for at least two polymer concentrations are necessary to obtain the unknown model parameters. The implementation of this model in reservoir simulators will therefore allow more accurate performance prediction of polymer-related EOR applications in the field by providing the temporal and spatial viscosity changes during flow in the reservoir.

2.5 CONCLUSIONS

A new empirical model for HPAM solution viscosity, which combines four well-established equations, is proposed for a wide range of pH, salinity, polymer concentration, and shear rate. The good match with experimental results shows that the model can successfully predict the measured viscosity. However, the model has difficulty predicting viscosity above a critical salinity and in the presence of divalent ions.

Table 2.1: Parameters necessary in the viscosity model of HPAM

No.	Symbols	Descriptions	Unit
Modified Brannon-Peppas Model			
1	$\bar{\upsilon}$	Specific volume of dry polymer	cm^3/g
2	K_a	Dissociation constant of ionizable groups on polymer	
3	$\bar{M}_n$	Average molecular weight of polymer	
4	$\bar{M}_c$	Average molecular weight between repeating unit	
5	$\upsilon_{2,r}$	Polymer volume fraction in the relaxed state	
6	χ_1	Polymer-solvent interaction parameter	
7	V_1	Molar volume of solvent	cm^3/mol
8	I	Ionic strength of solvent	
Modified Mark-Houwink Equation			
9	a	Polymer specific empirical constant	
10	b	Polymer specific empirical constant	
Power-Law Correlation			
11	η_s	Solvent viscosity	mPa s (cP)
12	C	Polymer concentration	g/cm^3
13	k''	Polymer-specific constant	
Carreau Equation			
14	η_∞	Limiting Newtonian viscosity at the high shear limits	mPa s (cP)
15-19	$e_1 \sim e_5$	Empirical parameters	

Table 2.2: 9 model parameters for Flopaam 3330S obtained from literature sources or by simple calculations

No.	Symbols	Values	Unit
Modified Brannon-Peppas Model			
1	$\bar{\upsilon}$	0.80	cm^3/g
2	$\bar{M}_n$	8,000,000	
3	$\bar{M}_c$	71.3	
4	$\upsilon_{2,r}$	0.5	
5	χ_1	0.8	
6	V_1	18	cm^3/mol
7	I	0.09	
Power-Law Correlation			
8	η_s	1	mPa s (cP)
Carreau Equation			
9	η_∞	1	mPa s (cP)

Table 2.3: Data sets of zero-shear limit viscosity (η_o), time constant (λ), and flow behavior index (n) in the Carreau model evaluated at each pH for three polymer concentrations (0.2, 0.5, and 0.8%) of Flopaam 3330S polymer

pH	η_o	λ	n	$C\|\eta\|$
0.2% Flopaam 3330S				
1.99	2.697	0.096	0.955	1.12
3.02	2.880	0.075	0.963	1.13
3.99	6.937	0.107	0.875	1.70
5.05	22.977	0.149	0.709	3.06
6.37	35.497	0.204	0.657	3.54
8.66	38.020	0.229	0.658	3.58
10.28	38.381	0.236	0.662	3.58
0.5% Flopaam 3330S				
2.01	17.756	0.257	0.805	2.81
2.97	12.623	0.035	0.736	2.83
3.97	40.477	0.120	0.685	4.18
5.03	238.337	0.470	0.517	7.61
6.02	414.523	0.698	0.475	8.77
8.04	459.452	0.741	0.470	8.94
10.05	456.555	0.744	0.470	8.94
0.8% Flopaam 3330S				
1.98	112.404	0.425	0.612	4.49
3.00	72.320	0.208	0.648	4.52
4.01	180.440	0.312	0.565	6.89
5.01	971.042	0.896	0.428	12.11
6.04	1773.813	1.362	0.393	14.04
8.66	1904.555	1.405	0.387	14.30
10.01	1921.846	1.411	0.387	14.30

Table 2.4: Computed and measured zero-shear limit viscosities, η_o, for three different concentrations of Flopaam 3330S polymer

Polymer Conc.	0.2%	0.5%	0.8%
Measured			
η_o for pH = 2.0	2.87	12.62	72.32
η_o for pH = 10.0	38.38	456.56	1921.88
Calculated			
η_o for pH = 2.0	2.39	19.76	72.32
η_o for pH = 10.0	38.38	506.20	1921.88

Table 2.5: Summary of the best-fit parameters

No.	Symbols	Unit	3330S	3630S	2330S	ALP99VHM
Modified Brannon-Peppas Model						
1	$\bar{\upsilon}$	cm^3/g	0.8	0.8	0.8	0.8
2	pK_a		4.9	5.5	4.9	4.7
3	$\bar{M}_n$		8,000,000	20,000,000	8,000,000	8,000,000
4	$\bar{M}_c$		71.35	71.35	71.30	72.06
5	$\upsilon_{2,s}$		0.5	0.5	0.5	0.5
6	χ_1		0.8	0.8	0.8	0.8
7	V_1	cm^3/mol	18	18	18	18
8	I		-	-	-	-
Modified Mark-Houwink Equation						
9	a		481.46	692.26	592.79	371.19
10	b		0.36	0.19	0.26	0.57
New Power-Law Correlation						
11	η_s	mPa s (cP)	1	1	1	1
12	C	g/cm^3	-	-	-	-
13	k''		1.84	3.09	1.79	1.11
Carreau Equation						
14	η_∞	mPa s (cP)	1	1	1	1
15	e_1		-0.226	-0.262	-0.223	-0.189
16	e_2		-0.024	-0.118	-0.026	0.009
17	e_3		0.070	0.033	0.063	-0.087
18	e_4		1.52×10^{-2}	1.48×10^{-2}	2.36×10^{-2}	7.54×10^{-2}
19	e_5		1.678	3.234	2.664	0.708

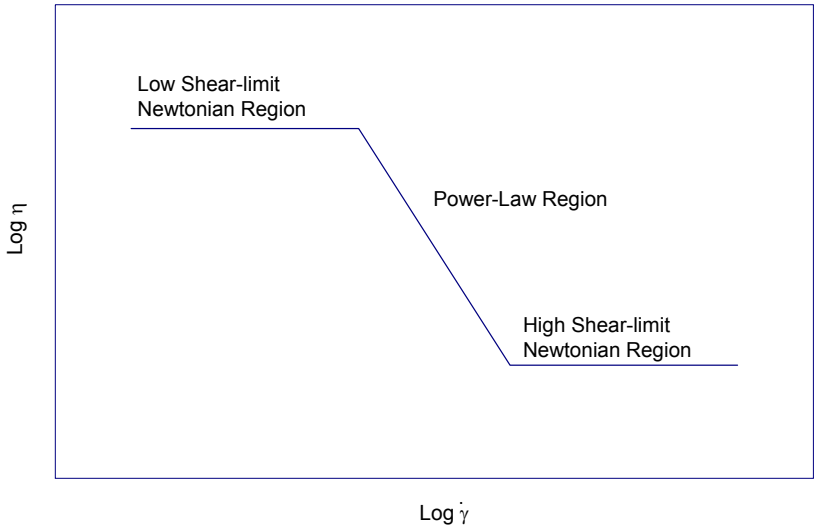

Figure 2.1: Typical non-Newtonian shear thinning behavior of polymer solution

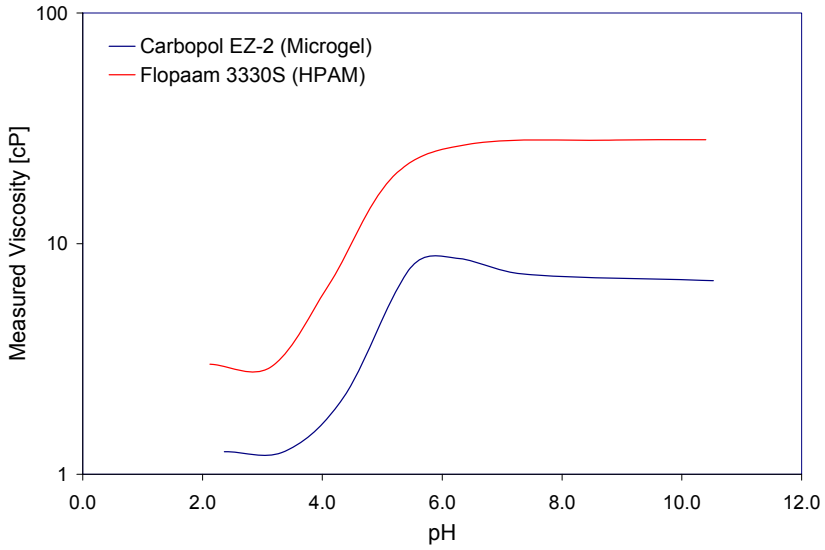

Figure 2.2: A comparison of viscosity curves between microgel (1.0% Carbopol EZ-2 in 3.0% sodium chloride brine) and HPAM (0.5% Flopaam 3330S in 0.5% sodium chloride brine) at shear rate = 10 s^{-1}

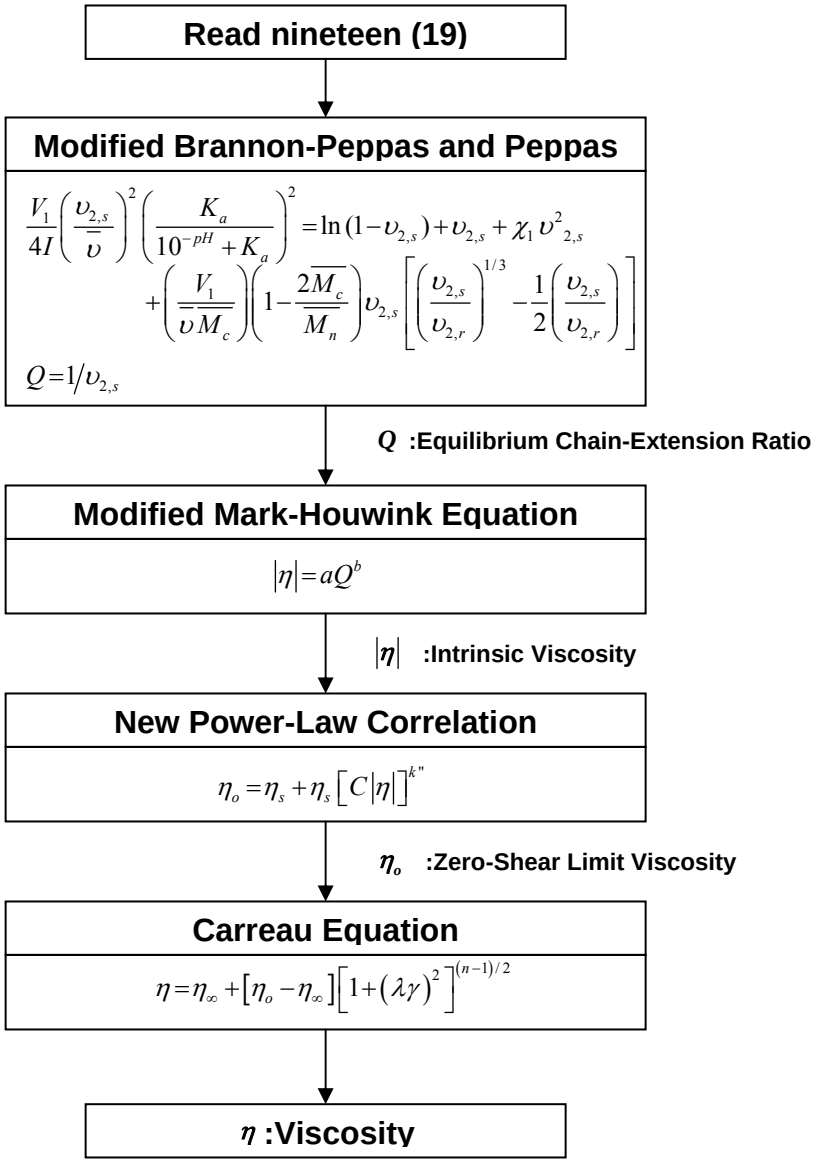

Figure 2.3: A flowchart for the viscosity modeling procedure of HPAM polymer

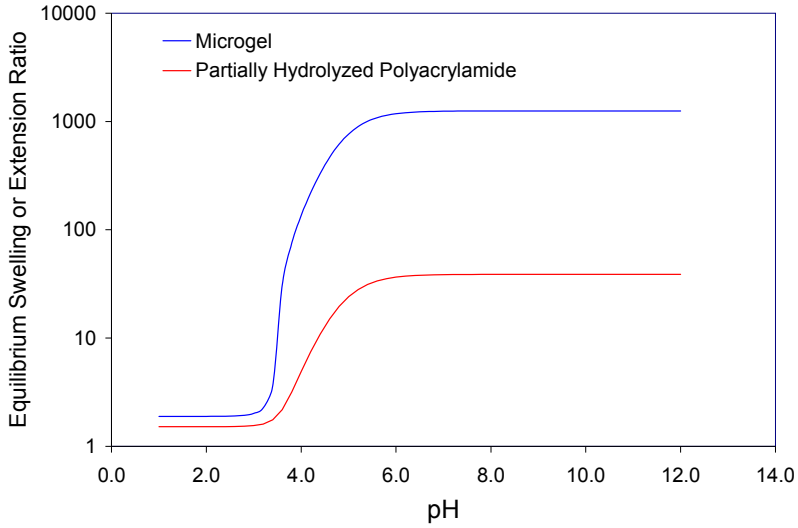

Figure 2.4: Calculated equilibrium swelling ratio of microgel with $\bar{M}_n$ = 75,000 and $\bar{M}_c$ = 12,000 to calculated equilibrium chain-extension ratio of HPAM with $\bar{M}_n$ = 8,000,000 and $\bar{M}_c$ = 71. Common parameters: $\bar{\upsilon}$ = 0.8 cm^3/g; pK_a = 4.7; $\upsilon_{2,r}$ = 0.5; χ_1 = 0.8; I = 0.09

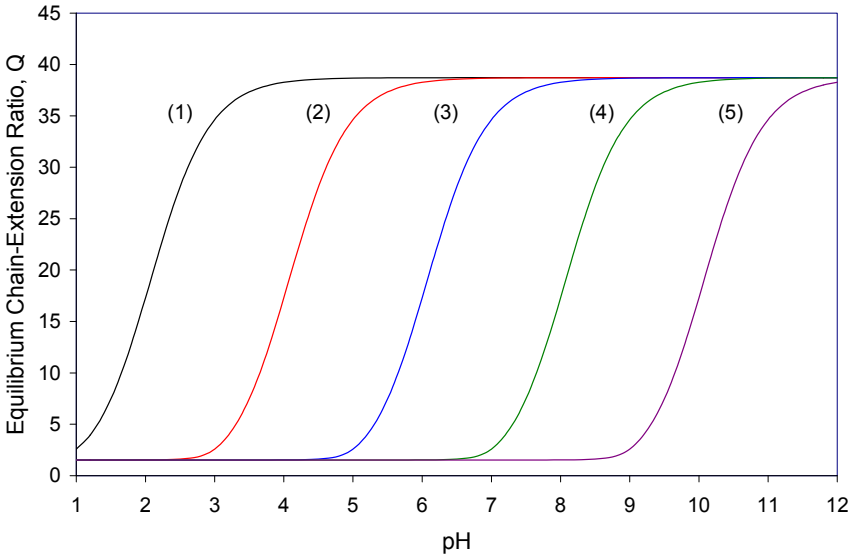

Figure 2.5: Effect of pK_a on the equilibrium chain-extension ratio (Q) with: (1) pK_a = 2.0; (2) pK_a = 4.0; (3) pK_a = 6.0; (4) pK_a = 8.0; (5) pK_a = 10.0

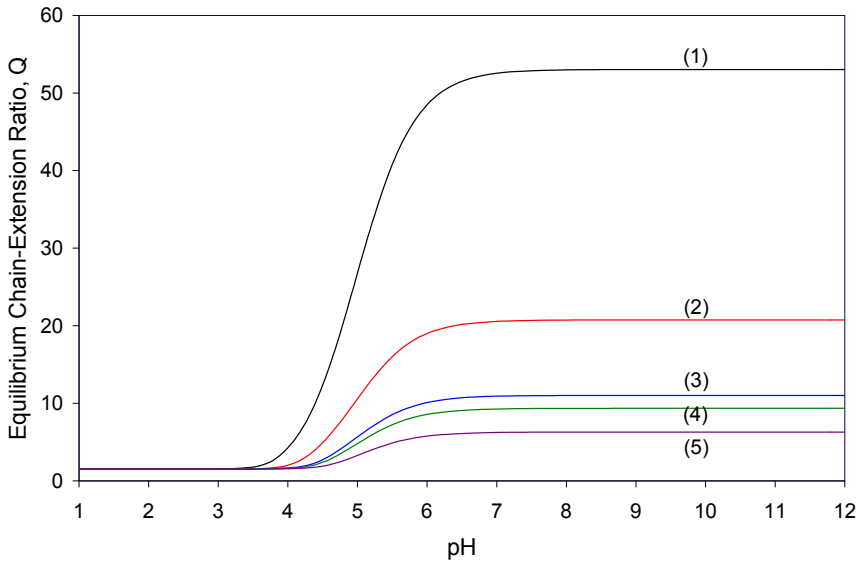

Figure 2.6: Effect of ionic strength (I) on the equilibrium chain-extension ratio (Q) with: (1) $I = 0.05$; (2) $I = 0.25$; (3) $I = 0.75$; (4) $I = 1.0$; (5) $I = 2.0$

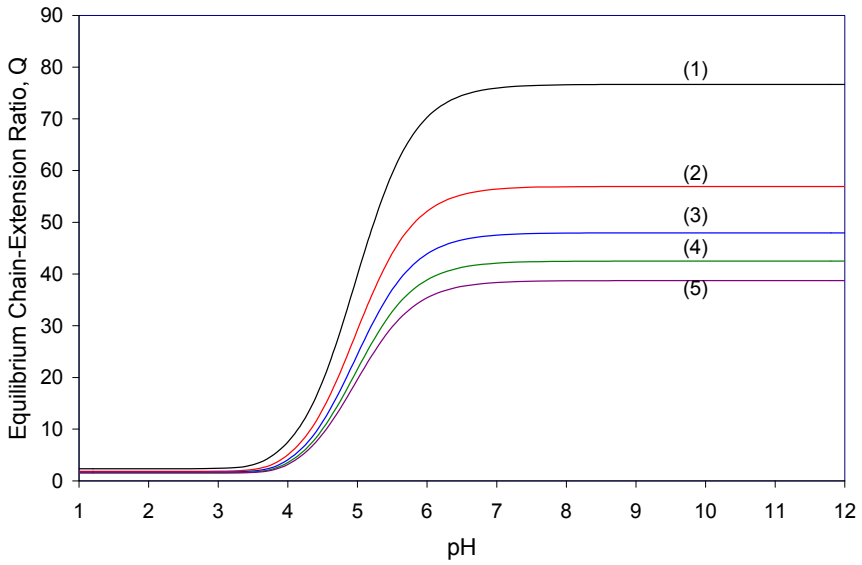

Figure 2.7: Effect of $\upsilon_{2,r}$ on the equilibrium chain-extension ratio (Q) with: (1) $\upsilon_{2,r} = 0.1$; (2) $\upsilon_{2,r} = 0.2$; (3) $\upsilon_{2,r} = 0.3$; (4) $\upsilon_{2,r} = 0.4$; (5) $\upsilon_{2,r} = 0.5$

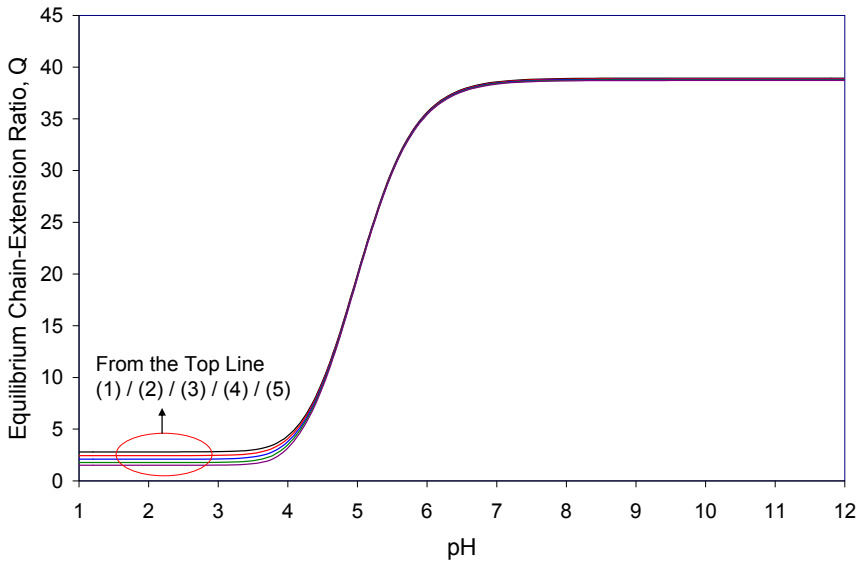

Figure 2.8: Effect of χ_1 on the equilibrium chain extension ratio (Q) with: (1) $\chi_1 = 0.0$; (2) $\chi_1 = 0.2$; (3) $\chi_1 = 0.4$; (4) $\chi_1 = 0.6$; (5) $\chi_1 = 0.8$

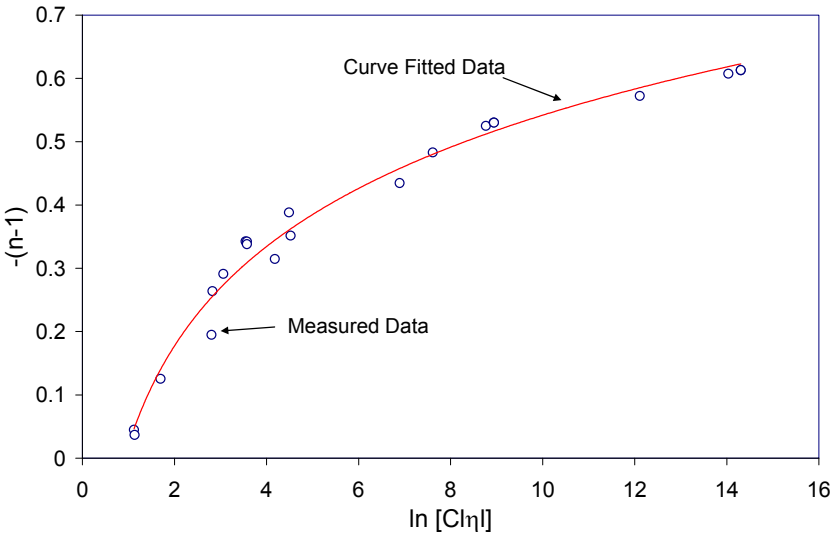

Figure 2.9: Curve-fitting graphs of measured (n-1) as a function of Clηl

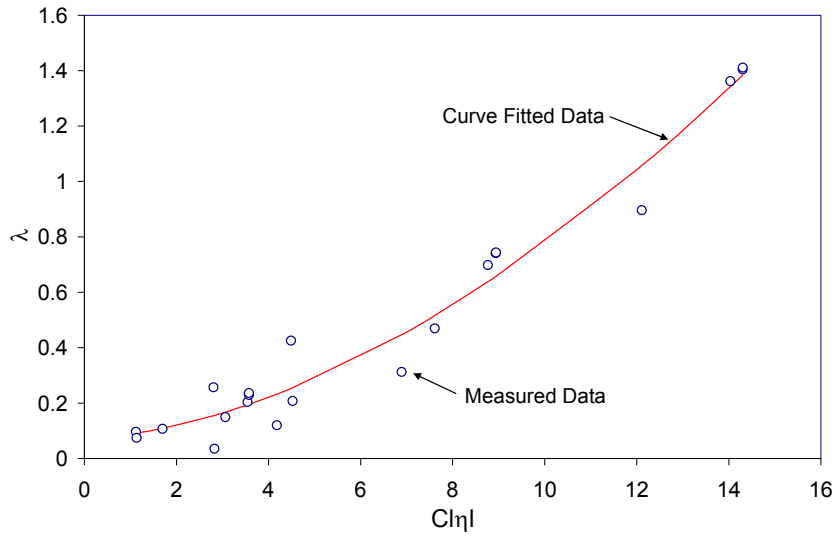

Figure 2.10: Curve-fitting graphs of measured λ as a function of Clηl

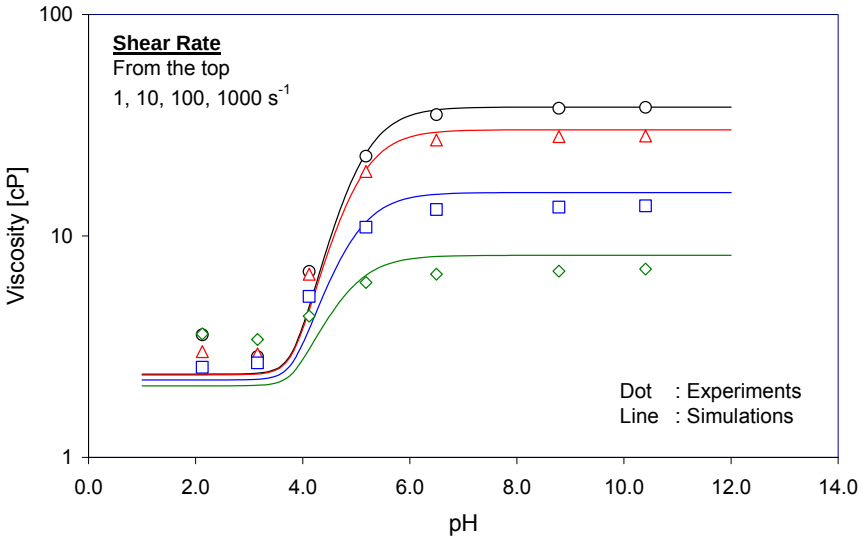

Figure 2.11: A comparison between laboratory data and model predictions for 0.2% of Flopaam 3330S prepared in 0.5% sodium chloride brine

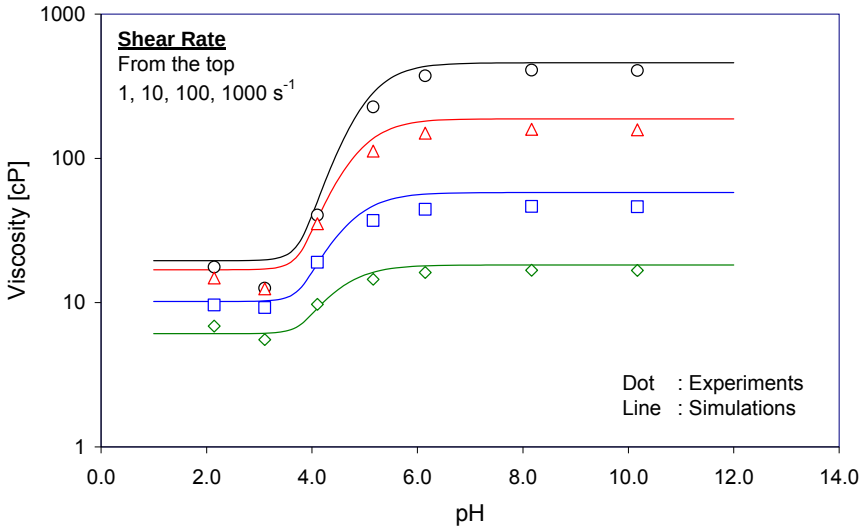

Figure 2.12: A comparison between laboratory data and model predictions for 0.5% of Flopaam 3330S prepared in 0.5% sodium chloride brine

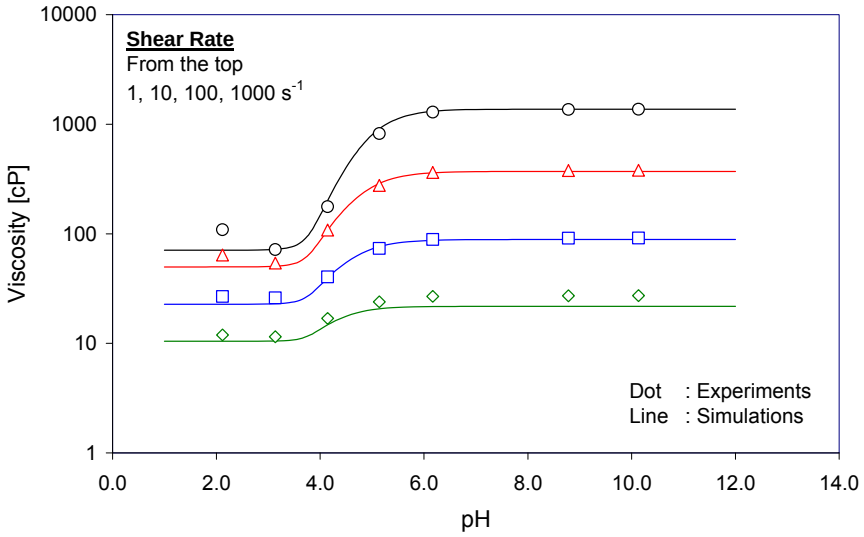

Figure 2.13: A comparison between laboratory data and model predictions for 0.8% of Flopaam 3330S prepared in 0.5% sodium chloride brine

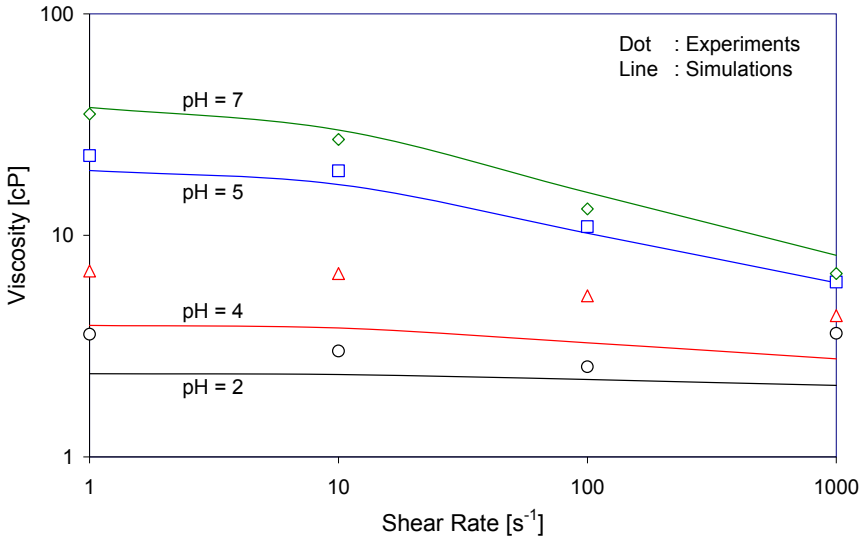

Figure 2.14: A comparison between laboratory data and model predictions in terms of shear rate for 0.2% of Flopaam 3330S prepared in 0.5% sodium chloride brine

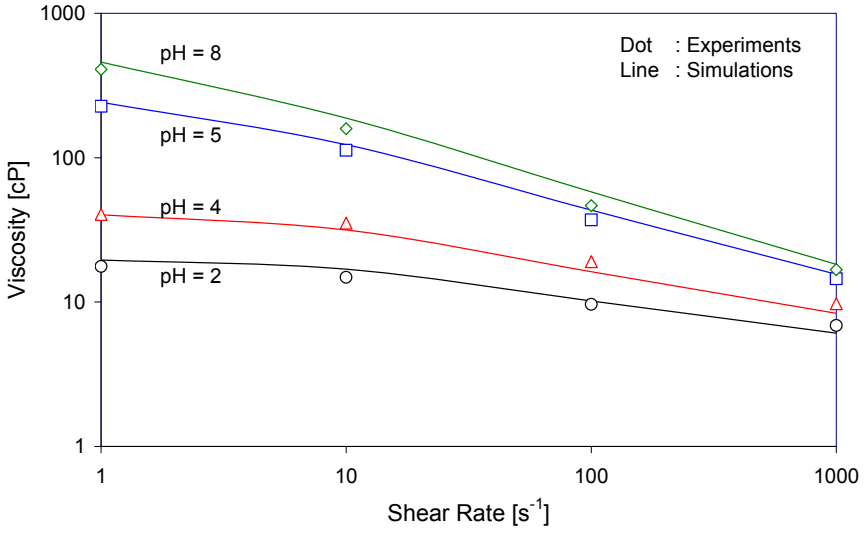

Figure 2.15: A comparison between laboratory data and model predictions in terms of shear rate for 0.5% of Flopaam 3330S prepared in 0.5% sodium chloride brine

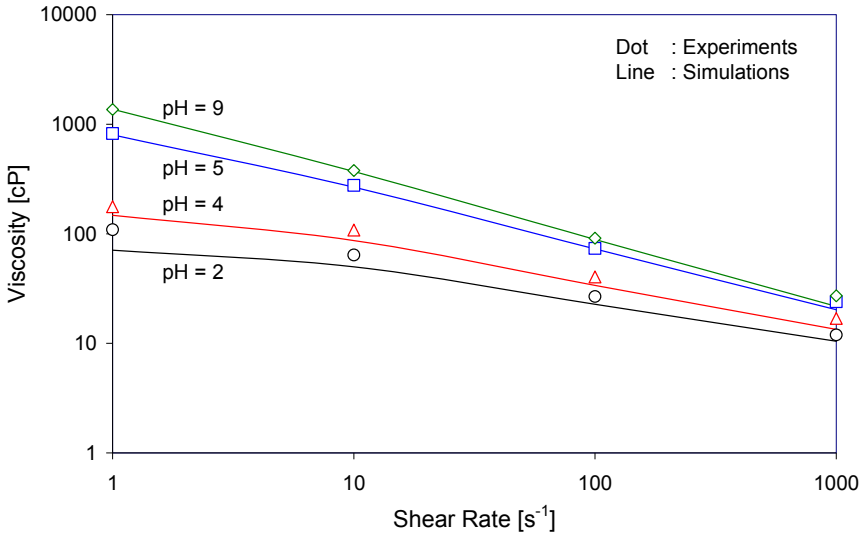

Figure 2.16: A comparison between laboratory data and model predictions in terms of shear rate for 0.8% of Flopaam 3330S prepared in 0.5% sodium chloride brine

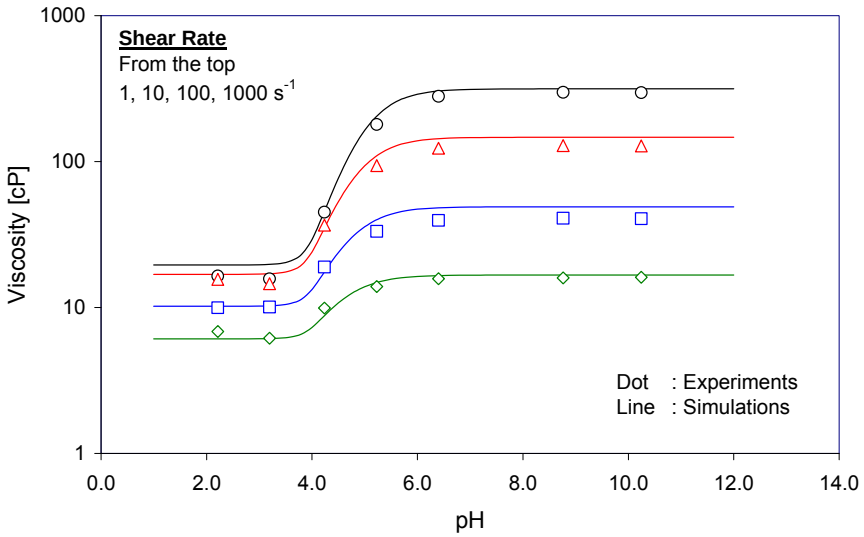

Figure 2.17: A comparison between laboratory data and model predictions for 0.5% of Flopaam 3330S prepared in 1.0% sodium chloride brine

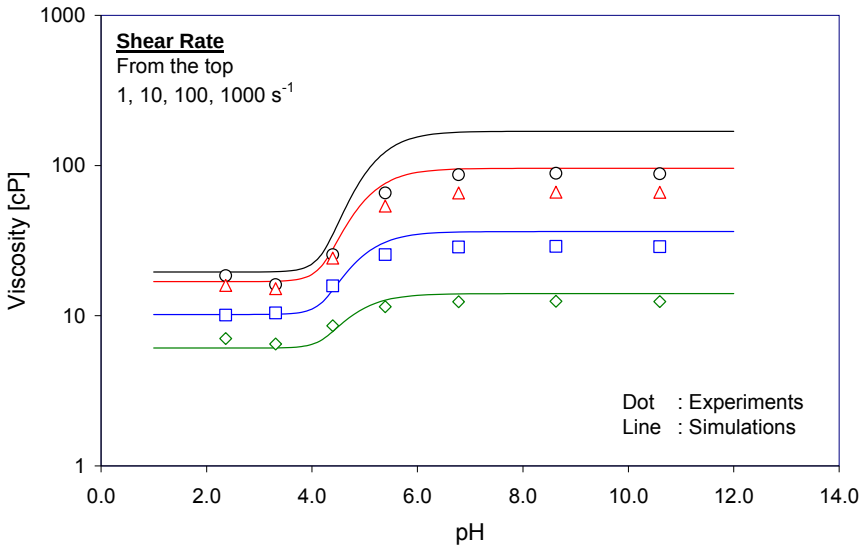

Figure 2.18: A comparison between laboratory data and model predictions for 0.5% of Flopaam 3330S prepared in 3.0% sodium chloride brine

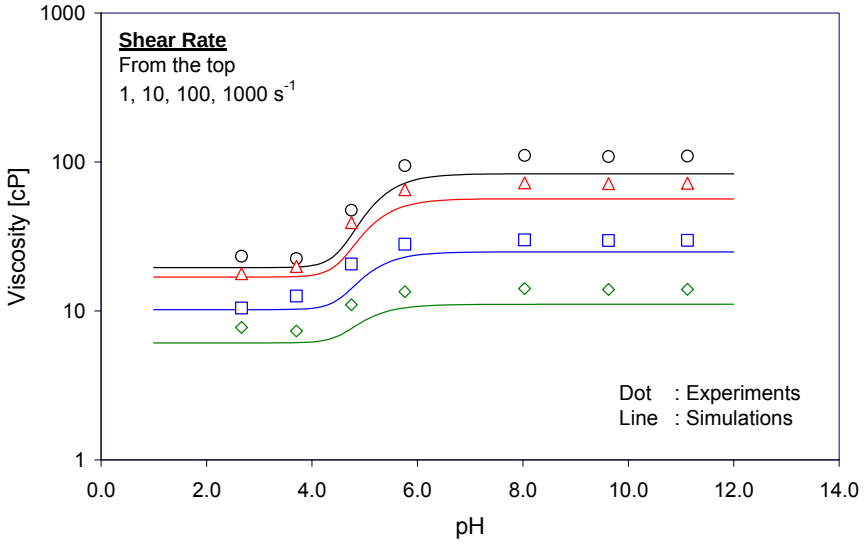

Figure 2.19: A comparison between laboratory data and model predictions for 0.5% of Flopaam 3330S prepared in 10.0% sodium chloride brine

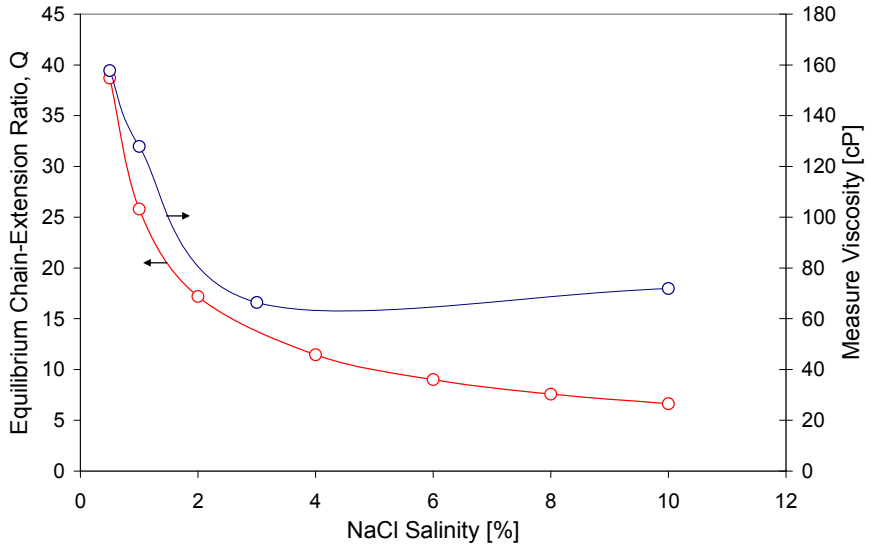

Figure 2.20: Equilibrium chain extension ratio and measured viscosity as a function of salinity ranging from 0 to 10% for 0.5% Flopaam 3330S in sodium chloride brine at pH = 10.0

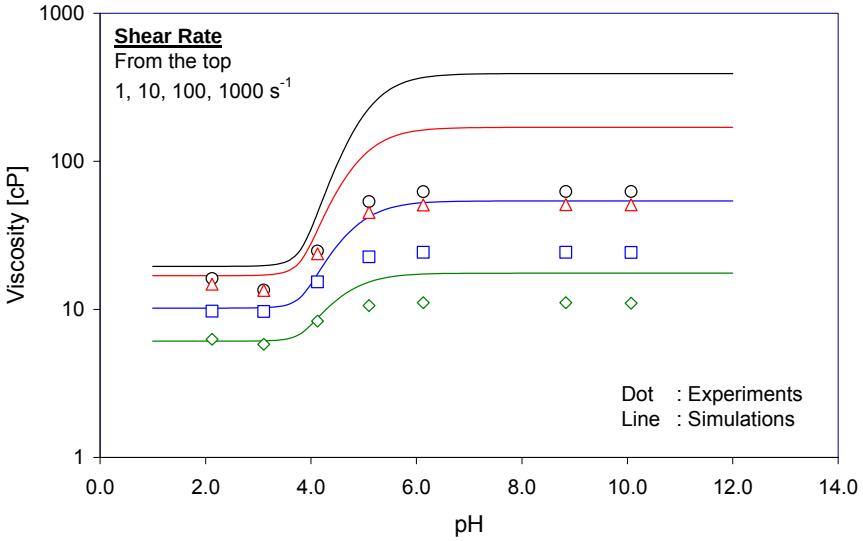

Figure 2.21: A comparison between laboratory data and model predictions for 0.5% Flopaam 3330S prepared in 0.2% sodium chloride and 0.3% calcium chloride brine

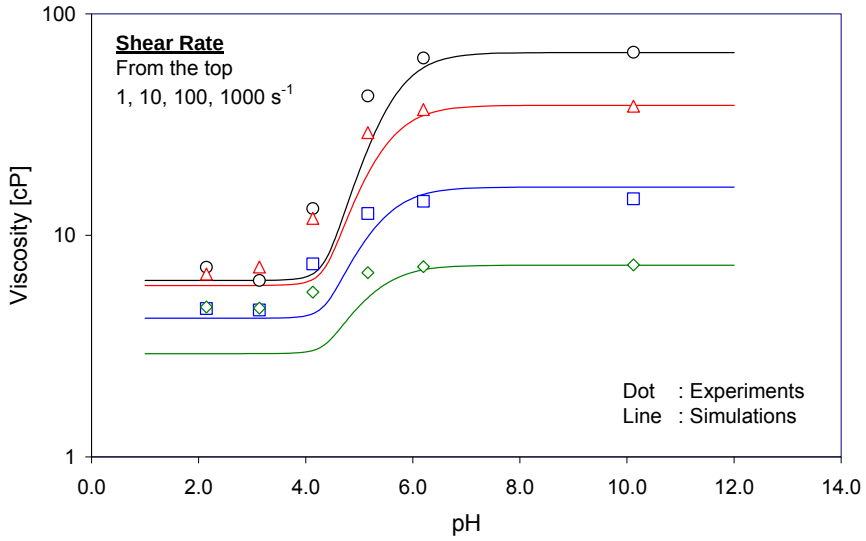

Figure 2.22: A comparison between laboratory data and model predictions for 0.2% of Flopaam 3630S prepared in 0.5% sodium chloride brine

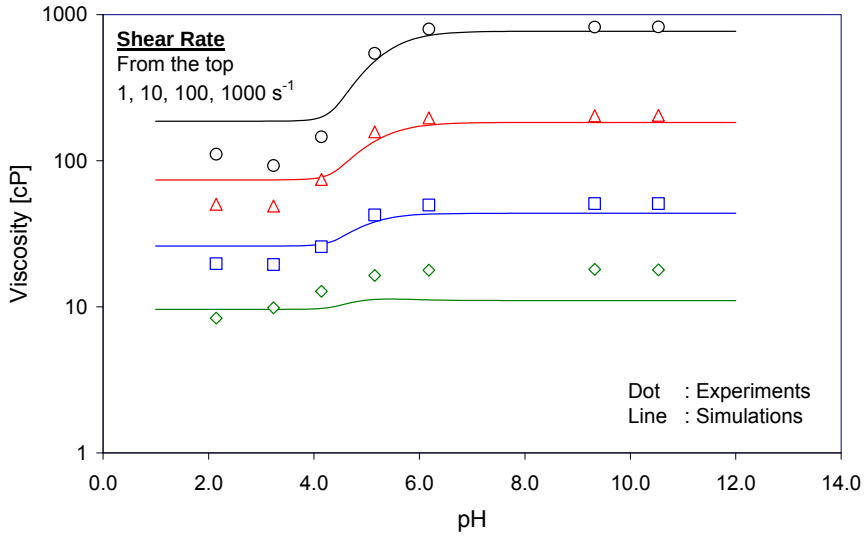

Figure 2.23: A comparison between laboratory data and model predictions for 0.5% of Flopaam 3630S prepared in 0.5% sodium chloride brine

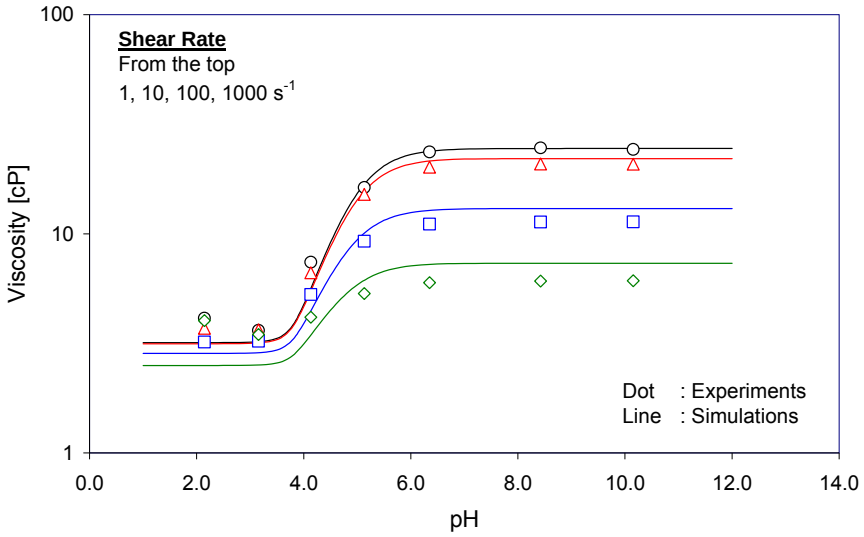

Figure 2.24: A comparison between laboratory data and model predictions for 0.2% of Flopaam 2330S prepared in 0.5% sodium chloride brine

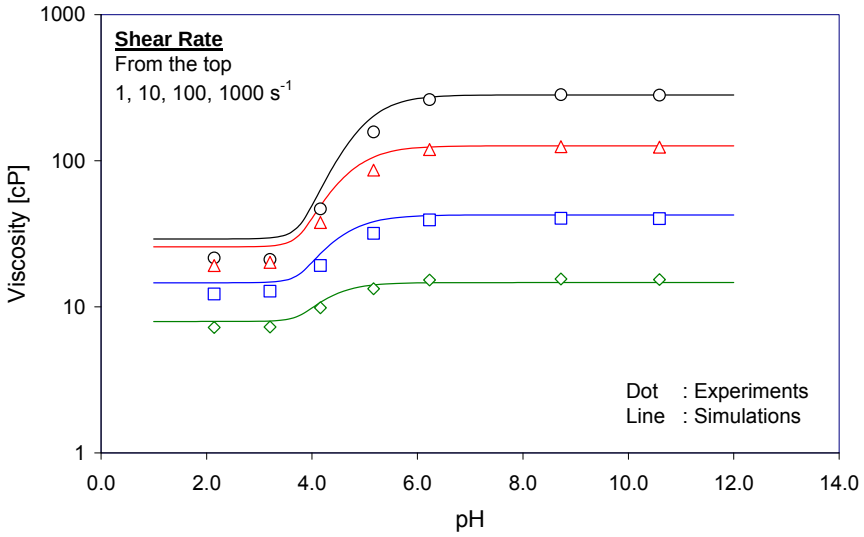

Figure 2.25: A comparison between laboratory data and model predictions for 0.5% of Flopaam 2330S prepared in 0.5% sodium chloride brine

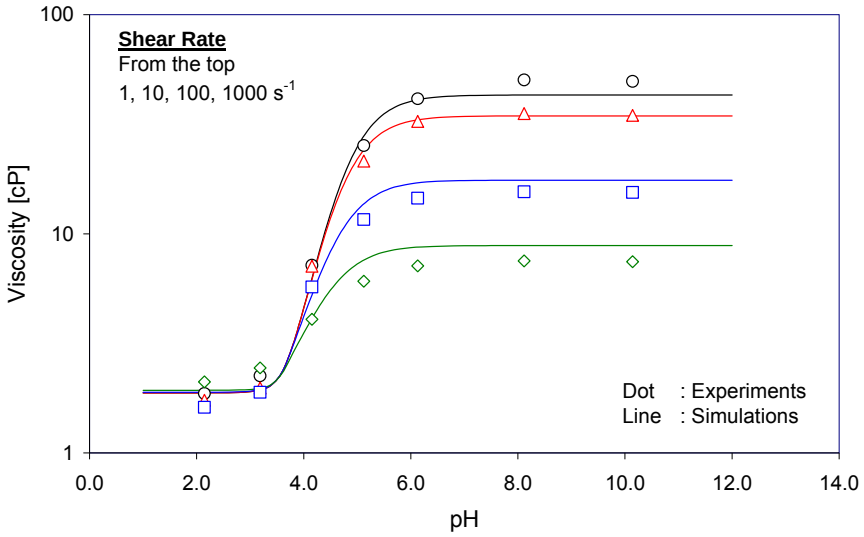

Figure 2.26: A comparison between laboratory data and model predictions for 0.2% of ALP99VHM prepared in 0.5% sodium chloride brine

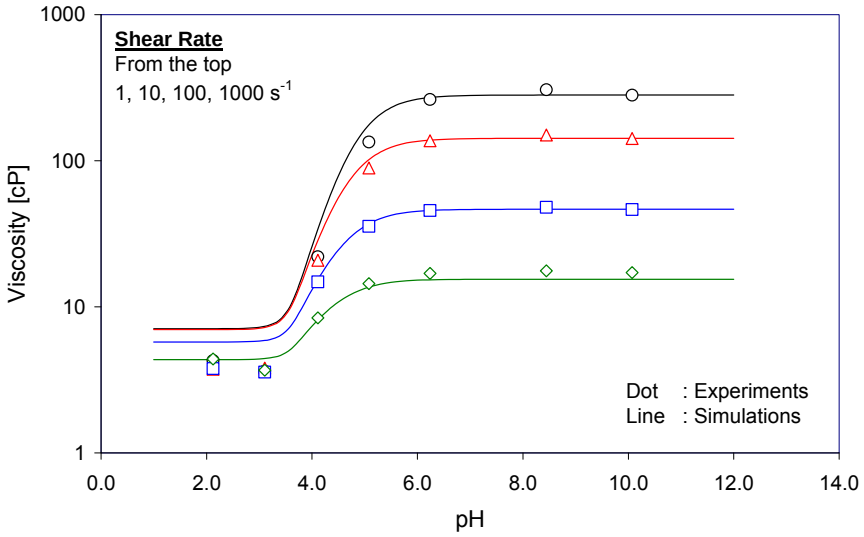

Figure 2.27: A comparison between laboratory data and model predictions for 0.5% of ALP99VHM prepared in 0.5% sodium chloride brine

3. Citric Acid Coreflood Experiments

3.1 INTRODUCTION

In our low-pH application to control the viscosity of HPAM solution, pH is a trigger that makes it possible to significantly improve the transport of the polymer bank in the reservoir. The objective is to minimize flow resistance (viscosity barrier) in the areas where the treatment is not needed, and to maximize sweep efficiency in the main hydrocarbon-bearing zone in the reservoir, by controlling the pH of the injected polymer bank. To keep the polymer viscosity low, the injected solution pH should remain low in the near wellbore region, or during placement deep in the reservoir. The pH would then be spontaneously increased at the proper location by in-situ geochemical reactions with rock minerals. Characterizing accurately geochemical reactions is the key for successful applications of our low-pH process.

The use of low-pH conditions can easily be found in the petroleum industry; matrix acidizing and acid fracturing are two such applications (Economides *et al.*, 1994). Matrix acidizing is a well stimulation technique to remove the damage in the near wellbore region, whereas acid fracturing is intended to treat the surfaces of fractured walls to ensure the communication between the rock matrix and high conductivity path (fracture). Both techniques intend to dissolve the mineral components hindering hydrocarbon production. Typically, hydrochloric acids (HCl) or hydrofluoric acids (HF) are preferred to attack the specific minerals in an economical and efficient manner. Another use of acid can be found in drilling applications (Huang *et al*., 2000; Al-Moajil *et al*., 2008; Al-Otaibi *et al*., 2008). Strong or organic acids are used as additives in various cleaning fluids to remove filter cake formed by drilling mud. Brine compatibility and reservoir temperature are important factors in determining the effectiveness of this application.

The use of acid in our application not only controls the viscosity of HPAM solutions, but also causes complicated reactions with rock minerals. The reactions depend on several factors: mineralogy and mineral compositions of the reservoir rocks; type and concentration of the acid solution, and; the reservoir environments, such as temperature and pressure. Among the above considerations, the most uncertainty is placed on mineralogy and mineral compositions of the reservoir rocks, because these

vary depending on the depositional environment and diagenetic processes. In particular, the acid-mineral reactions are heterogeneous reactions occurring only on the rock surfaces, which makes it difficult to quantify the geochemical reaction kinetics. The success of our application depends on accurate predictions of geochemical reactions so that the pH of polymer solution in the reservoir can be effectively controlled.

This chapter describes a series of acid coreflood experiments which analyze the effluent pH and cation history in order to understand geochemical reactions between acid and rock minerals. As a first acid-screening step, hydrochloric acid (HCl) and citric acid ($C_6H_8O_7$) are employed as strong and weak acids, respectively, and their effectiveness as pH control agents in our application is evaluated. Petrographic analysis is also carried out in order to identify Berea mineralogy and its compositions. In addition, energy-dispersive analysis by x-rays (EDAX) is used to analyze chemical elements of specific minerals. In the acid coreflood experiments, the effluent pH and cation histories are collected, compared, and analyzed for different injection pH's, flow-rates, core lengths, and shut-in conditions. These laboratory-measured data are used for preliminary history matching simulation in order to find the geochemical reaction kinetic parameters, as described in **Chapter 4**.

3.2 ACID EVALUATION

Hydrochloric acid (HCl) was first evaluated as a pH control agent because it can be used in relatively small amounts to effectively decrease the solution pH. Hydrochloric acid with pH = 1.0 was injected into a 1"-diameter, 9"-long Berea core at 25˚C, and the effluent pH was monitored. **Figure 3.1** shows the effluent pH history as a function of pore volume injected (PVI). The effluent pH is stabilized at around 5 and slowly decreases before the shock pH front is identified at 150 PVI. Hydrochloric acid is actively consumed by minerals to decrease proton concentrations in the effluent, *i.e.*, increase the effluent pH. This condition induces HPAM solutions to be thickened to their maximum viscosity at a given polymer concentration and salinity (See **Chapter 1**). Such strong acid is not desirable for our low-pH process, in that it cannot maintain the low-pH condition in the area where a good transport of polymer bank is required, until a very large volume has been injected.

Citric acid was employed as a weak acid in order to evaluate its effectiveness as a pH control agent. Citric acid is attractive for use here because it is environmentally safe, as proven by its wide use in the food industry. The injection condition of citric acid solution was pH = 2.78, and the test was carried out with a 1"-diameter, 5"-long Berea core at 25˚C. **Figure 3.2** compares the effluent pH histories of hydrochloric acid and citric acid as functions of PVI in the Berea core plug. Unlike the hydrochloric acid, citric acid successfully maintains the low-pH condition while it is slowly being consumed, due to its low reactivity. This low-pH condition causes the HPAM chains to remain coiled, thereby resulting in low-viscosity (because a high concentration of protons shields the negative charges of HPAM's). Citric acid is also desirable to use because it causes less cation dissociation from rock minerals which may cause a drastic viscosity drop in the polymer solution. In this research, citric acid was chosen as a pH control agent for our application, and its reactions with Berea sandstone were extensively studied and reported here.

3.3 THEORY AND EXPERIMENTAL SETUP

3.3.1 Theory

In both neutral and acid brine injections, the permeability (k) of the core was calculated with the Darcy equation for a linear single-phase flow:

$$k = \frac{q \mu L}{A \Delta P} \tag{3.1}$$

where q is the flow rate, μ is the fluid viscosity, L is the core length, A is the cross-sectional area, and ΔP is the pressure drop across the core.

The Damköhler number, which is the ratio of acid consumption rate and acid convection rate, is a dimensionless number that represents the relative importance of reaction kinetics, acid concentration, and injection rate. In general, a large Damköhler number greater than 10 indicates a fast reaction rate relative to convection rate, whereas a low number less than 1 represents a convection-dominant process with slow reaction rate. The quantitative definition of the Damköhler number may vary according to the system under consideration. In this research, the following equation was chosen and used to

obtain the Damköhler number from the results of the five coreflood experiments (Lake *et al*., 2002).

$$N_{Da} = \frac{residence\ time}{reaction\ time} = \frac{(L\phi A)/q}{(1/k_R)} \tag{3.2}$$

where ϕ is the porosity, and k_R is the reaction rate constant. All parameters needed to calculate the residence time can be easily obtained from the experimental data. However, the reaction rate constant must be estimated in a certain way because no direct measure of reaction kinetics is available in the experiments. The pH variation and time obtained during the shut-ins were used under the assumption of first order reaction between proton and reaction-participated minerals. Although Damköhler number is defined in the flowing condition, it is reasonable to use the shut-in data, a) because the reaction rate constant, as intrinsic kinetic property, is not affected by any factors such as acid concentration, mineral concentrations, and flow conditions, and b) because only the kinetic reaction during shut-ins is involved. The first order rate law can be expressed as:

$$k_R\left[H^+\right] = -\frac{d\left[H^+\right]}{dt} \tag{3.3}$$

This equation can be integrated (from initial shut-in to final shut-in) to obtain:

$$k_R = -\frac{\ln\dfrac{\left[H^+\right]}{\left[H^+\right]_o}}{t} \tag{3.4}$$

where $[H^+]_o$ is the initial hydrogen concentration, $[H^+]$ is the final hydrogen concentration, and t is the shut-in time.

3.3.2 Experimental Setup

Figure 3.3 shows a schematic diagram for the acid coreflood setup. 1”-diameter Berea cores were prepared by epoxy molding in order to avoid the acid solution contacting acid-reactive materials, such as steel. A standard epoxy resin (EPON™ Resin 828, Miller-Stephenson Chemical Co. Inc) was mixed with hardener (Versamid® 125, Miller-Stephenson Chemical Co. Inc) in a 2:1 ratio, on a mass basis. The mixed epoxy resin was well stirred with a glass rod and prepared. Separately the Berea core was glued with two 1”-diameter end-caps that have a small hole in the middle for fluid flow. A

hollow cylindrical plastic holder, 2.5" in diameter, was prepared and vertically placed on a flat desk, and the core was inserted at the middle point inside the plastic holder. The prepared epoxy resin was slowly poured into the space between the core and the plastic holder, and was then cured at a room temperature for 24 hours.

A dual piston pump (Model 1500 Digital HPLC pump, Scientific Systems Inc.) was used to maintain constant flow-rate of injected fluid. The pump is designed to inject the fluid on a continuous basis, without any shut-in for refilling. It is also suitable for acid handling, due to its self-flush feature. The core was set up vertically and the acid solution was injected from the bottom to top, in order to ensure even flow-distribution. The pump was connected at the inlet of the core and the outlet was routed to a back pressure regulator (Grove Valve & Regulator co.). The pressure regulator, controlled by compressed gas (nitrogen or air), is designed to apply back-pressure in the system, in the range of 0 to 100 psi. An 80-psi back-pressure was applied to operate above the bubble point pressure of the fluid system, in order to ensure that no CO_2 gas would be generated by acid-mineral reactions. A pressure transducer (Model DP15-30, Validyne Engineering Corp.) was installed across the core to measure the pressure drop. The outlet of the back-pressure regulator was connected to a fraction collector (Retriever II, ISCO Inc.) via an in-line pH indicator (Cole Parmer Inc.) The signals from the pressure transducer and pH indicator were collected and transformed in a data collector (Model MCI-20, Validyne Engineering Corp.) and the data were displayed in the LabVIEW version 8 (National Instrument Co.). The plastic tubing was used in all flow lines. All experiments were run at room temperature (25˚C). **Figure 3.4** shows a photograph of the acid coreflood setup.

3.4 EXPERIMENTAL PROCEDURE

3.4.1 Solution Preparation

Reagent-grade citric acid and sodium chloride were used to prepare the acid solution and brine, respectively. The sufficient amount of 3% sodium chloride brine was prepared on a mass basis in a beaker. Some of the brine was used for brine permeability measurements. A powder form of citric acid was directly added to the pre-prepared brine, using high-speed mixing, while the pH of the solution was simultaneously measured by a pencil-thin pH meter. Once the pH reached the target value, the void

space of the beaker was purged with non-reactive Argon gas, in order to prevent contact with air, and the beaker was covered with a vinyl film.

3.4.2 Coreflood Procedure

The closed system for the epoxy-molded core was prepared by blocking the valves, and the vacuum evacuation was performed by using a Vacuum Pump (Model 2AAR2, Marvac Scientific Manufacture Co.) for more than 10 hours. The core was twice saturated with pure CO_2 gas, at 30 minute intervals at the beginning of vacuum evacuation, in order to effectively remove air in the pores of the Berea core. The core was then saturated with 3% sodium chloride brine, and the porosity was calculated by the difference between the dead volume of the closed system and the brine saturation amount. After the back-pressure regulator was set at 80 psi, 3% sodium chloride brine was injected for approximately 5 pore volumes, in order to measure the brine permeability. Subsequently, the acid solution was injected into the core, while collecting the effluent samples in plastic tubes, in a fraction collector, and also measuring pH continuously with an in-line pH meter. The planned injection rate was maintained for each experiment. The injection of acid solution was stopped when the pH front was identified. The pH and the pressure drop were logged at 10 second intervals by the data collector.

3.4.3 Cation Analysis in the Effluent Samples

The collected effluent samples were stored after purging the void space with non-reactive Argon gas to prevent oxidation with air. After the coreflood experiments were completed, 20 samples were selected from each experiment in which the pH response showed meaningful changes; those samples were then sent to the outside lab (Test America Inc.) for cation analysis. This analysis provided the types of minerals which had participated in the acid-mineral reactions, and helped to determine the reaction kinetics. Five cations – Aluminum (*Al*), Calcium (*Ca*), Iron (*Fe*), Magnesium (*Mg*), and Potassium (*K*) were measured by Inductively Coupled Plasma – Atomic Emission Spectrometry (SW-846 method 6010B/C). The types of cations used for the analysis were determined on the basis of potential reactions between acid solution and minerals, as identified in

Section 3.6: Aluminum (*Al*) from kaolinite; Calcium (*Ca*) from calcite or dolomite; Iron (*Fe*) from siderite; Magnesium (*Mg*) from dolomite; and Potassium (*K*) from K-feldspar.

3.5 MEASUREMENT PLAN

Table 3.1 shows the plan for citric acid coreflood measurements. The chosen base case is here described as the injection of pH = 2.5 citric acid in 3% sodium chloride brine into a 5" long Berea core at 1 ml/min, without shut-in. The following effects were studied to investigate how the change of different variables affects the effluent pH and cation concentration response, as a function of PVI: (a) pH = 2.5 and 3.5; (b) flow rate = 1 and 2 ml/min; (c) core length = 5 and 8 inches, and; (d) the presence of shut-in (three shut-ins during 6 hours on high and low pH plateau, and pH front). The measurements were intended to characterize the geochemical reactions between citric acid solution and rock minerals, in terms of the variables.

3.6 BEREA MINERALOGY

The Berea sandstone is a well-sorted quartzose sandstone, consisting primarily of quartz and a small amount of rock fragments, carbonate, feldspars, kaolinite, and some clay minerals. Many analysis results for Berea sandstone have been reported in the literature (Flesch *et al*., 1977; Smith *et al.,* 1986; Cheung *et al.,* 1992; Churcher *et al.,* 1991; Carr *et al*., 1998). However, the published compositions and mineralogy of Berea sandstone differ from one another, and thus cannot be generalized. This is because depositional environments vary and the diagenetic alteration process causes additional overgrowths and cementation of minerals. In addition, the erosion process in geological-scale time causes more severe alteration.

In order to characterize geochemical reactions more accurately, thin section analyses of Berea sandstone, before and after acidizing, were carried out. Since all the cores involved in the coreflood experiments and these analyses were cut from the same quarry, their mineralogy and mineral compositions are assumed to be identical. The core which was used in Test [A2] (injection of pH = 2.5 citric acid in 3% sodium chloride brine into 8" long Berea core at 1 ml/min without shut-in) was selected as the thin-section analysis sample after the acidizing coreflood. Two thin sections were cut from each of the core plugs (once before and once after acidizing) and were examined with the

conventional petrographic microscope. Samples were impregnated with blue-dyed epoxy to help in estimating porosity. Petrographic analysis was conducted to determine changes in mineralogical, textural, and pore system properties after the acidizing process.

Figures 3.5 and **3.6** show the photomicrographs taken under a plane-polarizer for the thin section analysis of the Berea sandstone before acidizing. The porous nature of Berea sandstone is clearly observed, shown in blue color in both figures. The mineralogical analysis shows that the main framework grains consist of quartz, potassium-Feldspar (K-Feldspar), and Lithics fragments. Quartz is the primary mineral, occupying approximately 78% of the total (including the portion of quartz overgrowth); K-Feldspar is about 4% and Lithics fragments (mostly low-grade metamorphic, quartzite, and some highly altered volcanic rock fragments) are about 7%. The cementations and quartz overgrowths, normally formed at high temperatures (above 80 ˚C), are also identified and indicate a relatively deep burial depth for this Berea sandstone. The evidence of quartz growth is marked in both figures. The cements comprise approximately 5% quartz (by growths), 5% carbonate, 4% kaolinite, and 2% iron oxide. The rhombic shape of the carbonate cements in **Figure 3.6** signifies that they are likely to be siderite, dolomite, or ankerite, as calcite mostly forms in blocky shapes. The brownish color can be identified in carbonate minerals, which indicates that an oxidization reaction occurred. The mineralogy and its composition, estimated by this analysis, are summarized in **Table 3.2**.

Figures 3.7 and **3.8** show the photomicrographs taken under a plain-polarizer for the thin section analysis of the Berea sandstone after acidizing. It is observed that, after acidizing, secondary pores were formed by the dissolution of carbonate cements. The possible spot of such secondary pore is marked in **Figure 3.7**. The other minerals and cements most likely remained the same as before the acidizing. As expected, citric acid is so weak that only carbonate components were dissolved to form secondary porosity.

In order to identify the type of carbonate cements involved in the citric acid-mineral reactions, a microprobe equipped with an Energy-Dispersive Analysis by X-rays (EDAX) system was used. This is an analytical technique used for the elemental analysis, or chemical characterization, of a sample. A beam of X-rays is focused on the test-spot of the sample in order to make it release energy (in the form of an X-ray by electron movements) in discrete energy levels. The emitted X-ray depends on the atomic

structure of the elements, which enables the identification of the chemical elements of minerals. **Figure 3.9** show the results of the chemical elements analysis of the Berea sandstone. Three spots on the carbonate cement section were selected and analyzed. Iron (Fe) was detected as the most abundant element, followed by calcium (Ca) and magnesium (Mg), in that order. This suggests that the carbonate cement involved in the citric acid-mineral reactions is either Iron-rich dolomite, or mixed dolomite and siderite. Since the mixed dolomite-siderite is not commonly observed as cement composition in rocks, it can be concluded that the carbonate cement is an Iron-rich dolomite, and the high Iron peak is due to local oxidation (see brownish spots in **Figure 3.6**).

3.7 EXPERIMENTAL RESULTS

3.7.1 Acid Coreflood Experiments

Table 3.3 summarizes petrophysical properties (absolute permeability and porosity) and residence time for five coreflood experiments. The Berea sandstone cores used in these experiments have 500 to 600 md brine permeability, and 18 to 20% porosity, both in the range for typical Berea sandstone. **Figures 3.10** to **3.14** show the effluent pH and pressure drop as functions of PVI for each coreflood experiment. The pressure drop remains almost constant in all five corefloods, showing that the permeability remains constant. The dissolution of a trace amount of carbonate cement minerals probably did not change the size of the pore throats. The pH response from the citric acid acidizing the Berea sandstone can be characterized by two notable pH fronts. The pH drops very quickly from pH = 10 to the first stabilized pH when the acid solution breaks through the core. The first stabilized pH varies depending on the pH of the injected acid solution. The effluent pH then shows a very gentle hump across several decades of PVI (several hundreds in case of pH = 3.70), and deceases very slowly to return to the original pH of the injected fluid, as the carbonate minerals are slowly consumed.

Figure 3.15 compares all the effluent pH responses for the five coreflood experiments. Compared to the base case [A1] (Injection of pH = 2.5 citric acid in 3% sodium chloride brine into a 5" long Berea core at 1 ml/min, without shut-in), the Test [A2] (core length = 8") shows the earlier forms of the pH front. The lower pH of the

injection fluid (pH = 2.47), as compared to that of the [A1] base case (pH = 2.72), is a major contributor for this difference. Longer core, which increases the residence time, may be another reason, as the reactions would have more time to move towards the equilibrium. In the case of Test [A3], which is in the higher flow-rate (2 ml/min), the pH response has a milder slope than the [A1] base case, indicating that more PVI are needed to decrease the pH to its original value. The lower residence time created by the higher flow-rate slows down the reaction. The shut-in case of Test [A4] affects the pH response only slightly, as compared to the [A1] base case. Three shut-ins of 6 hours each generated the instantaneous pH peaks, indicating that the protons are consumed by reaction with carbonate rock minerals to reach the equilibrated pH at those points. The high pH = 3.7 case of Test [5] shows a quite different shape of pH curve from others. The low proton concentration by one order of magnitude causes the reaction to be severely retarded. Although approximately 600 pore volumes were injected, the effluent pH did not reach its original injection pH, as shown in **Figure 3.16** (which is the same plot as **Figure 3.15,** with the extended x-axis scale).

Unlike a strong acid, such as hydrochloric acid, the results show that citric acid can effectively control the pH of the injected solution, so that the pH remains low during propagation; this is due to the low reactivity of citric acid. This result satisfies the required pH conditions for the polymer solution (as defined by our low pH processes), because the low pH means low viscosity, which will result in better transport. The peak pH's observed during the several shut-ins guarantee that the pH of the polymer solution placed deep in the reservoir can be increased to return to the high viscosity of polymer. The pH of the injected fluid and the flow-rate are two main parameters with which to control the pH profile in the reservoirs.

3.7.2 Cation Analysis

The five cations in the effluents - Aluminum (*Al*), Calcium (*Ca*), Iron (*Fe*), Magnesium (*Mg*), and Potassium (*K*) – are shown in **Figures 3.17** to **3.21** as functions of PVI for each coreflood experiment. All the plots also include the corresponding pH history for reference. In all five figures, it is observed that the trends of cation concentrations conform to those of pH, because both parameters are indicators of the degree of geochemical reactions. Potassium (*K*) was not detected, indicating that K-Feldspar was not involved in the acid mineral reactions, which agrees with the

observation by thin section analysis. Additionally, aluminum (*Al*) was found in only small amounts, in a few ppm levels, showing that Kaolinte hardly reacted with citric acid.

A great deal of three cations - Calcium (*Ca*); Iron (*Fe*); and Magnesium (*Mg*) - were detected in four coreflood experiments- [A1] to [A4]- whose injected pH's are in the range between 2.5 and 2.8. Calcium (*Ca*) was the most dissociated cation, followed by Iron (*Fe*) and Magnesium (Mg), in that order. These results conform to those of EDAX analysis to confirm that the carbonate mineral is an Iron-rich dolomite, consisting of Calcium, Iron, and Magnesium. The only difference is that more Calcium (*Ca*) than Iron (*Fe*) was detected in this analysis. Considering that only three tiny spots were analyzed with EDAX, and the compositional distribution in mineral is highly heterogeneous, such difference may be regarded as an experimental scatter. In particular, magnesium (*Mg*) was not found in Test [A5], which is the high pH = 3.7 injection case. Low-reactivity dropped the magnesium concentration to a level lower than the detection limit.

Further, comparing the maximum ion concentration for each coreflood experiment can serve as a good indicator of the kinetic reactions. **Table 3.4** summarizes the comparison results. Test [A2], which has long core length (8"), shows the highest maximum ion concentrations, suggesting that the kinetic reactions have progressed further toward equilibrium. Tests [A1] and [A4] show similar maximum ion concentrations, indicating that the shut-ins affect the kinetic reactions only slightly. The high flow-rate case (Test [A3]) exhibits lower value than [A1] and [A4], showing that lower residence time slows down the reactions. For Test [A5], which is a high-pH injection case, the maximum cation concentrations are much lower than other cases by one order of magnitude, indicating that the high pH retards the kinetic reactions.

3.8 EXPERIMENTAL DAMKÖHLER NUMBER

The Damköhler number was estimated for the five corefloods to quantify the relative importance of citric acid-carbonate mineral reactions, at several different conditions, as compared to their convection rates. As the first step, the reaction rate constant (k_R) was estimated using Equation (3.4) from data of the three shut-ins in Test [A4] because this test was the only one involved in shut-ins (see **Figure 3.13**). **Table 3.5** summarizes the reaction rate constants calculated with the initial and peak pH values

during shut-ins and the corresponding shut-in times. The values for the first two shut-ins are in a similar range, while the last value shows relatively a big difference from the others. Since the last shut-in was done in the region where the effluent pH had reached the injected pH (which means that reaction-participated carbonate mineral had already been consumed), only the values for the first two shut-ins were averaged to use the reaction rate constant for all five coreflood experiments. Recall that the reaction rate constant does not change by the variables in these experiments (pH, core length, flow rate, and the presence of shut-ins) as discussed in Section 3.3.1.

Table 3.6 shows the Damköhler numbers for the five corefloods. All the numbers are less than 1, which indicates that the reaction is very slow, in comparison to the convection rates. Compared to the base case [A1] (injection of pH = 2.5 citric acid solution into a 5" long Berea core at 1 ml/min, without shut-in), Test [A2] with longer core length (8" case) shows a higher Damköhler number by 53%, indicating that higher residence time results in faster progress of kinetic reactions. A 53% increase comes from 8/5, which is the ratio of core lengths between two tests. Higher flow-rate, shown in Test [A3] (2 ml/min case), decreases the Damköhler number because of the reduced residence time (*i.e.*, less contact time between acid and minerals). The Damköhler numbers for Tests [A4] and [A5] are, however, similar to that of Test [A1], because all the parameters involved in equation (3.4) remain constant. Only the overall reaction rate was changed by the difference of the injection pH for Test [A5]. However, for Test [A4], the presence of shut-ins does not affect the overall reaction rate considerably, as shown in **Figures 3.15** or **3.16**.

3.9 CONCLUSIONS

The following conclusions are made:

1. Citric acid can successfully buffer the low-pH of the injected polymer solution, thereby allowing it to maintain low-viscosity and to propagate effectively in reservoir rock.
2. Petrographic analyses, by thin section and EDAX analysis, show that the Berea sandstone used in the coreflood experiments largely consists of framework grains and cements. The framework grains include: approximately 73% quartz (including the portion of quartz overgrowth), 4% K-feldspar, and

7% lithic fragments. The cements comprise approximately 5% quartz by growths, 5% carbonate, 4% kaolinite, and 2% iron oxide.

3. The petrographic analysis of thin section, before and after acidizing, shows that a carbonate mineral, likely to be iron-rich dolomite, is involved in the geochemical reaction between citric acid and rock minerals.
4. The changes of flow rate, core length, and the pH of injected acid solution all affect the reaction kinetics; the reactions become slower as flow rate or pH increases, or the core length becomes longer. The experimentally evaluated Damköhler number for each case supports these observations. The effect of pH change upon reaction kinetics is most pronounced.

Table 3.1: Plan for citric acid coreflood measurements

Test No.	Description	Flow Rate	Core Length	Shut-In
[A1]	pH = 2.5 Citric Acid	1 ml/min	5”	No
[A2]	pH = 2.5 Citric Acid	1 ml/min	8”	No
[A3]	pH = 2.5 Citric Acid	2 ml/min	5”	No
[A4]	pH = 2.5 Citric Acid	1 ml/min	5”	Yes*
[A5]	pH = 3.5 Citric Acid	1 ml/min	5”	No

* 3 shut-ins for 6 hours each

Table 3.2: Mineralogy and composition of Berea sandstone analyzed by Thin Section Method

Minerals	Formula	Estimated Volume Fraction (%)
Framework Grains		
Quartz	SiO_2	78
K-Feldspar	$KAlSi_3O_8$	4
Lithics Fragments		7
Cements		
Quartz	SiO_2	(5)
Carbonate	$Ca(Fe, Mg)(CO_3)_2$	5
Kaolinite	$Al_2Si_2O_5(OH)_4$	4
Fe-Oxide	Fe_2O_3	2

Table 3.3: Petrophysical properties (absolute permeability and porosity) and residence time for five coreflood experiments: Base case is the injection of pH = 2.5 citric acid prepared in 3% sodium chloride brine into a 5" long Berea core at 1 ml/min, without shut-in

Test No.	[A1]	[A2]	[A3]	[A4]	[A5]
Variable	Base	8" Long	2ml/min	Shut-In	pH=3.5
Injected pH	2.78	2.54	2.76	2.76	3.72
Porosity (%)	19.6	18.8	20.5	18.9	17.8
Permeability (md)	664	613	564	481	533
Residence Time (min)	12.4	19.0	6.6	12.0	11.2

Table 3.4: Comparison of maximum cation concentration in ppm for five coreflood experiments

Unit: ppm

Test No.	Calcium	Iron	Magnesium
[A1]	265	190	71.3
[A2]	328	184	88.7
[A3]	213	113	55.4
[A4]*	254 (459)	147 (418)	69.4 (132)
[A5]	20.5	10.0	0.00

* (maximum cation concentration at peak pH)

Table 3.5: Reaction rate constants calculated with the initial and peak pH values during shut-ins and the corresponding shut-in times in Test [A4]

No	Initial pH	Peak pH	Initial [H^+]	Peak [H^+]	Shut-in Time (s)	k (s^{-1})
1	3.7233	4.8896	1.89E-04	1.29E-05	21310	1.26E-04
2	3.4021	4.3266	3.96E-04	4.71E-05	21678	9.82E-05
3	2.7907	3.1783	1.62E-03	6.63E-04	21450	4.16E-05
					Average value of first two reaction rate constants	1.12E-04

Table 3.6: Experimental Damköhler number for five coreflood experiments

Test No	Length (cm)	Porosity	Area (cm^2)	Flow Rate (cm^3/s)	k (s^{-1})	N_{Da}
[A1]	12.72286	0.195808	4.976278	0.016667	1.12E-04	8.34E-02
[A2]	20.29	0.187647	4.986326	0.016667	1.12E-04	1.28E-01
[A3]	12.73048	0.205233	5.046827	0.033333	1.12E-04	4.43E-02
[A4]	12.73048	0.189178	4.976278	0.016667	1.12E-04	8.06E-02
[A5]	12.7127	0.177938	4.96624	0.016667	1.12E-04	7.56E-02

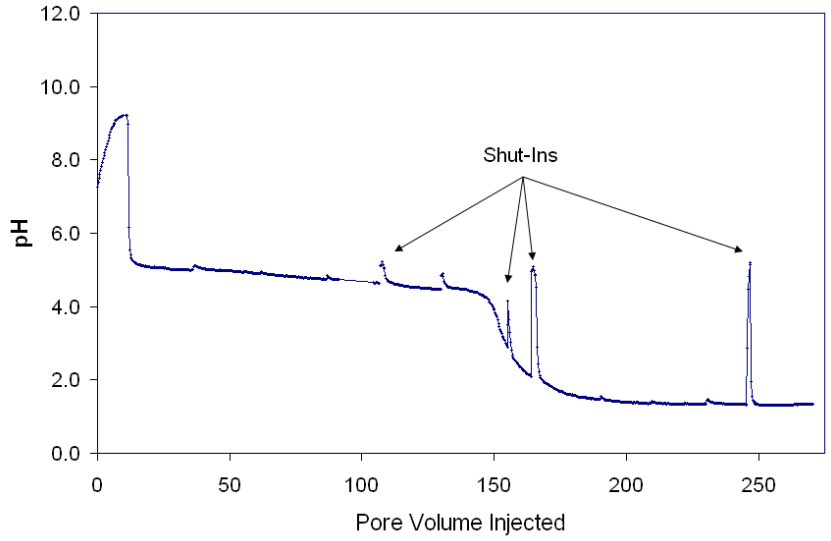

Figure 3.1: Effluent pH history as a function of pore volume injected (PVI) when hydrochloric acid with pH = 1.0 is injected into 1" diameter and 9" long Berea core

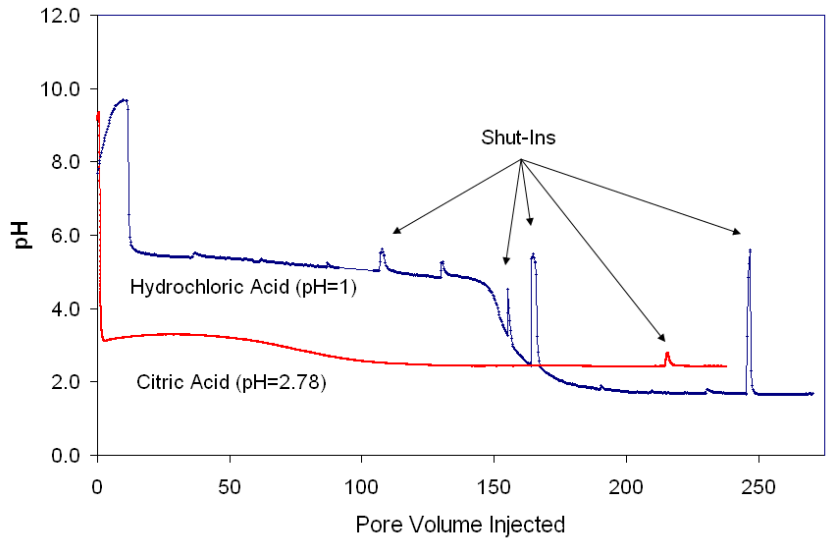

Figure 3.2: Comparison results of the effluent pH histories as a function of PVI between hydrochloric acid and citric acid in Berea core plug

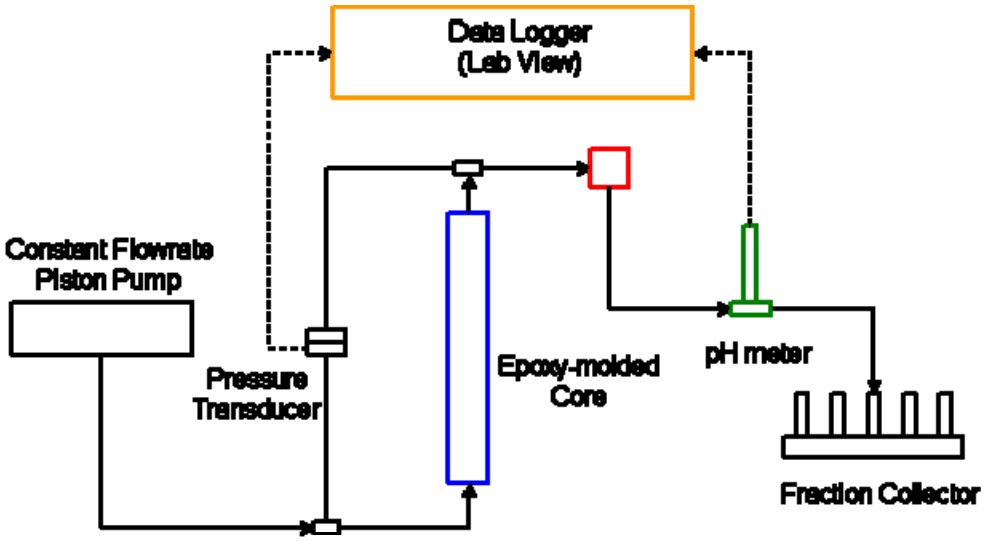

Figure 3.3: Schematic diagram for the acid coreflood setup

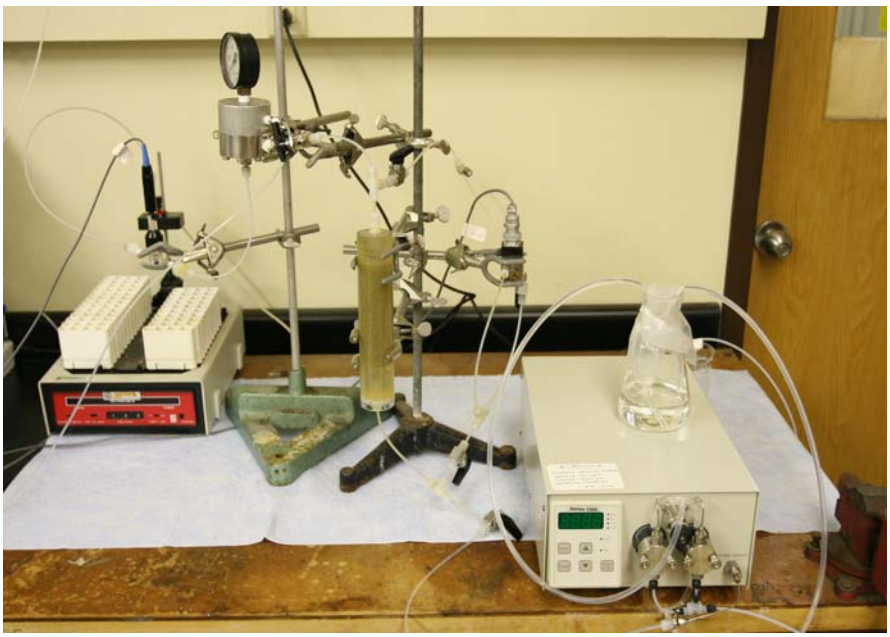

Figure 3.4: Photograph of the acid coreflood setup

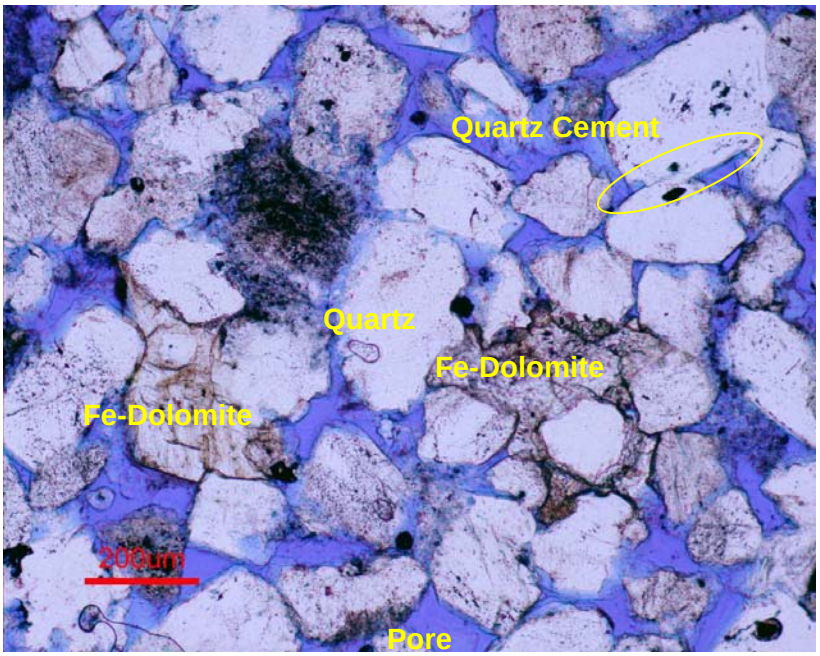

Figure 3.5: Photomicrograph taken under plain-polarizer for the thin section analysis of Berea sandstone before acidizing (1)

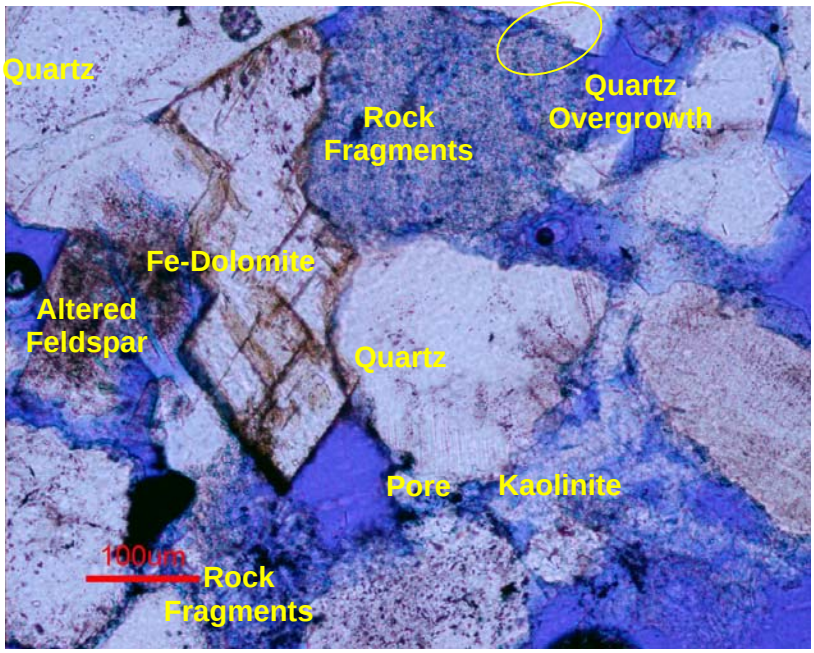

Figure 3.6: Photomicrograph taken under plain-polarizer for the thin section analysis of Berea sandstone before acidizing (2)

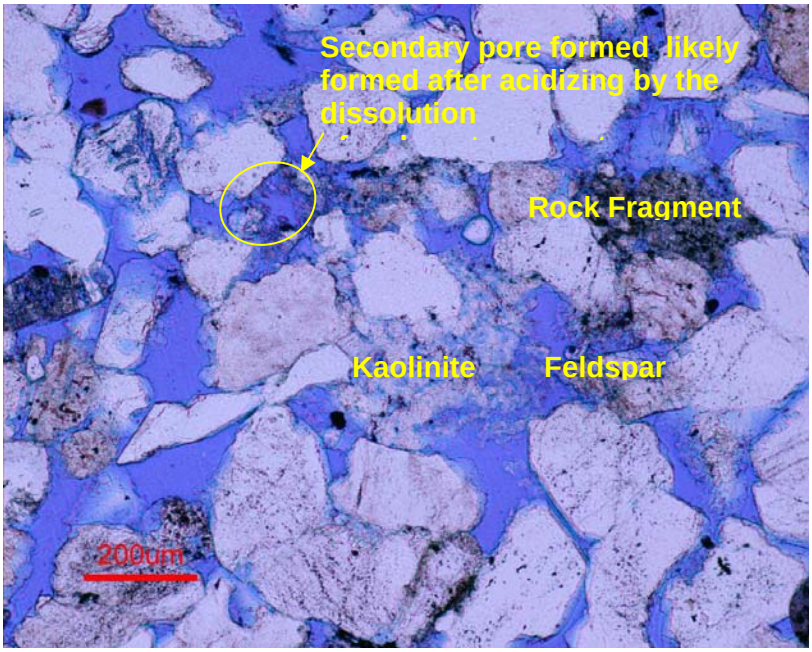

Figure 3.7: Photomicrograph taken under plain-polarizer for the thin section analysis of Berea sandstone after acidizing (1)

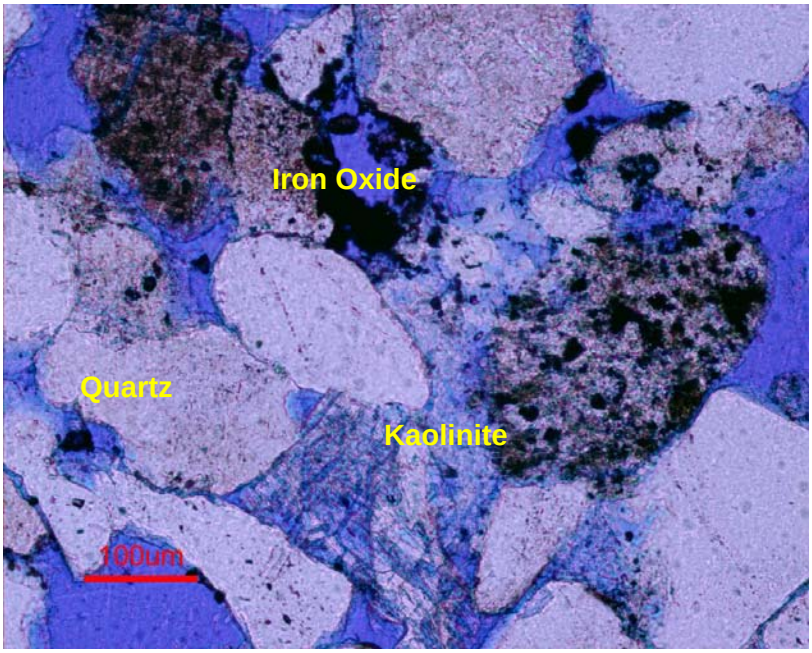

Figure 3.8: Photomicrograph taken under plain-polarizer for the thin section analysis of Berea sandstone after acidizing (2)

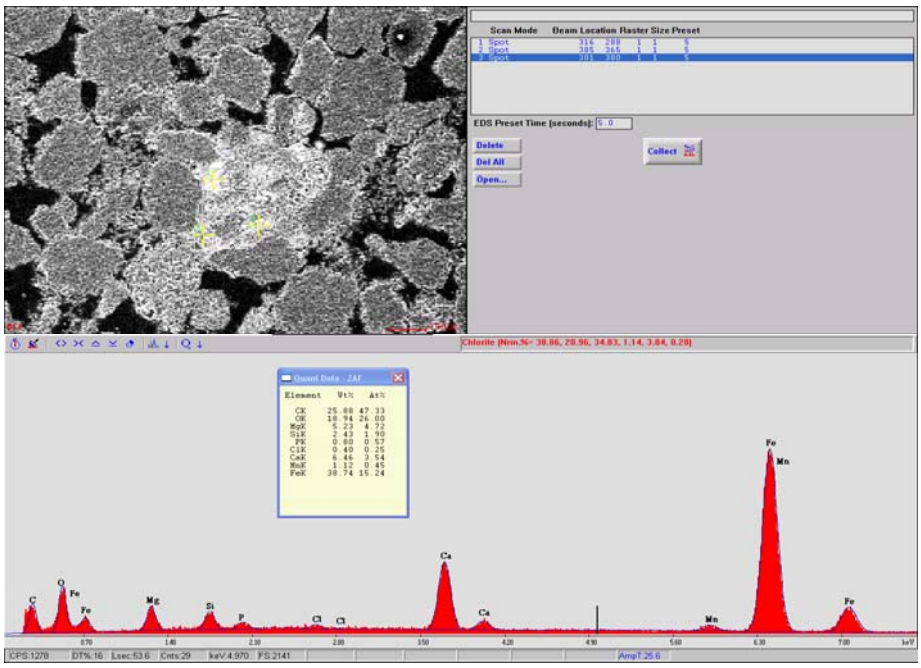

Figure 3.9: Results by microprobe equipped with energy-dispersive analysis by x-rays (EDAX) system

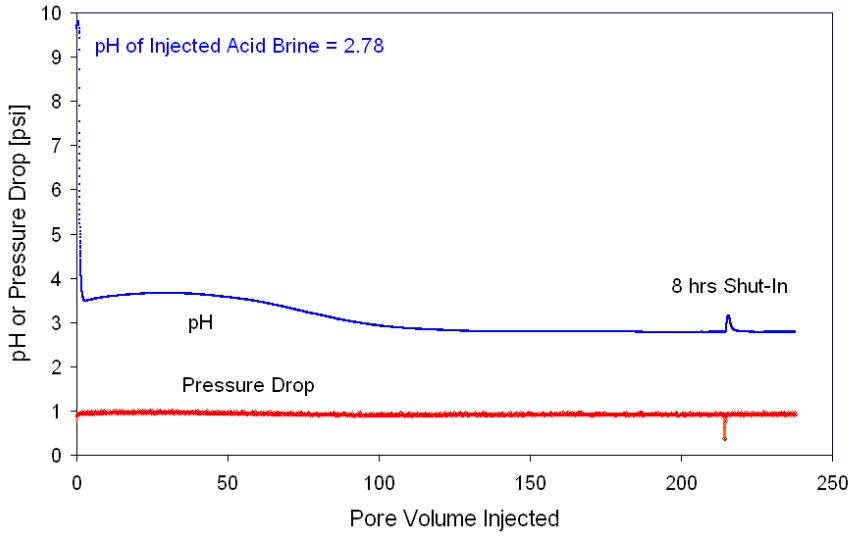

Figure 3.10: Effluent pH and pressure drop history as a function of pore volume injected for test number [A1]

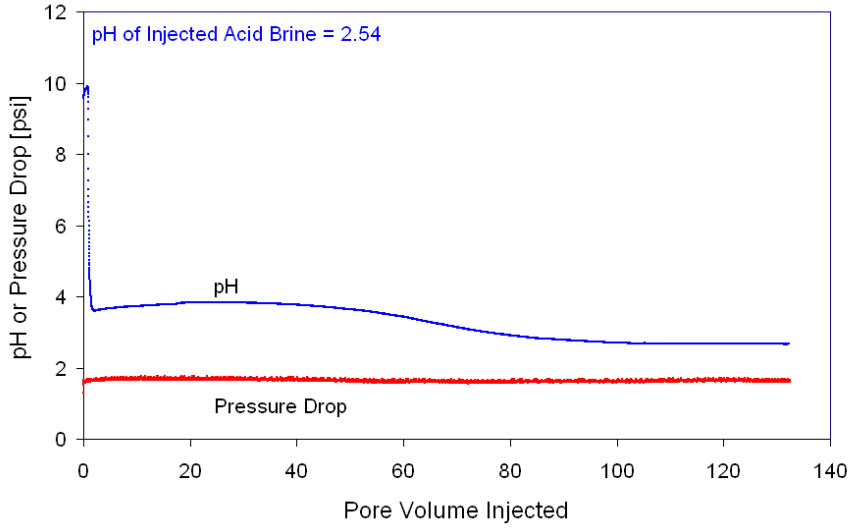

Figure 3.11: Effluent pH and pressure drop history as a function of pore volume injected for test number [A2]

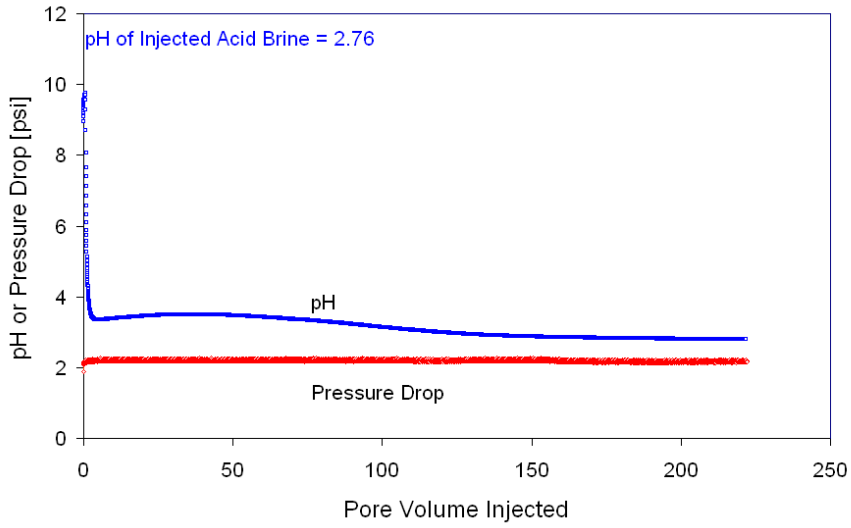

Figure 3.12: Effluent pH and pressure drop history as a function of pore volume injected for test number [A3]

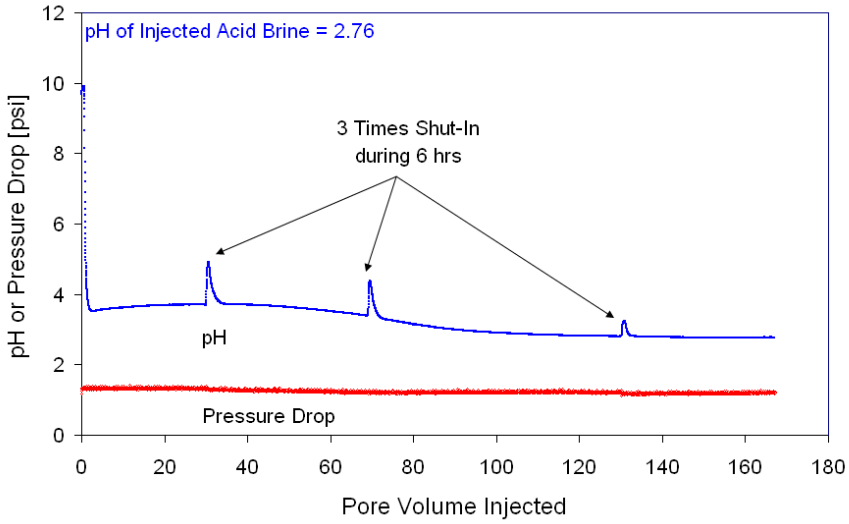

Figure 3.13: Effluent pH and pressure drop history as a function of pore volume injected for test number [A4]

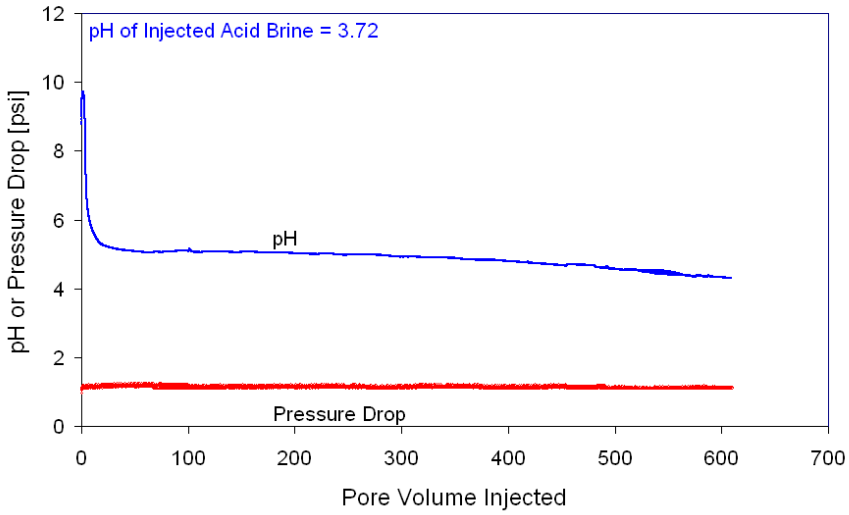

Figure 3.14: Effluent pH and pressure drop history as a function of pore volume injected for test number [A5]

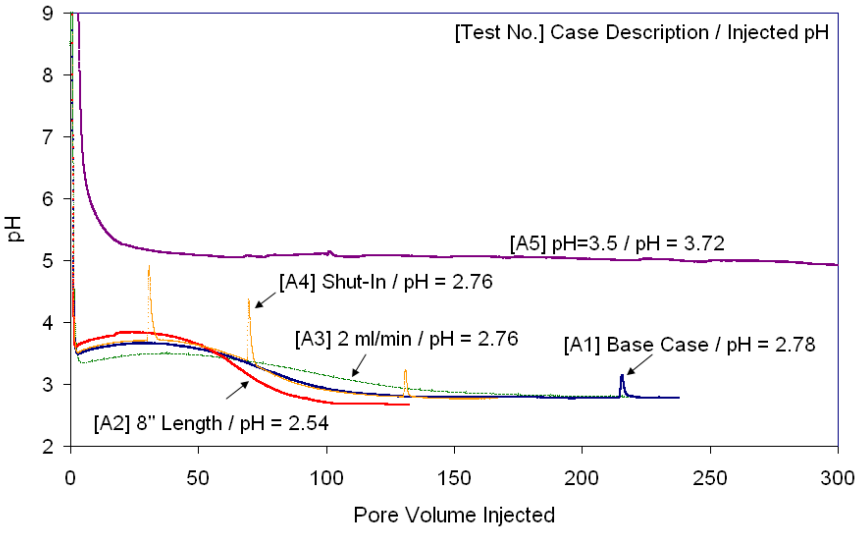

Figure 3.15: Comparison of all the effluent pH responses for the five coreflood experiments

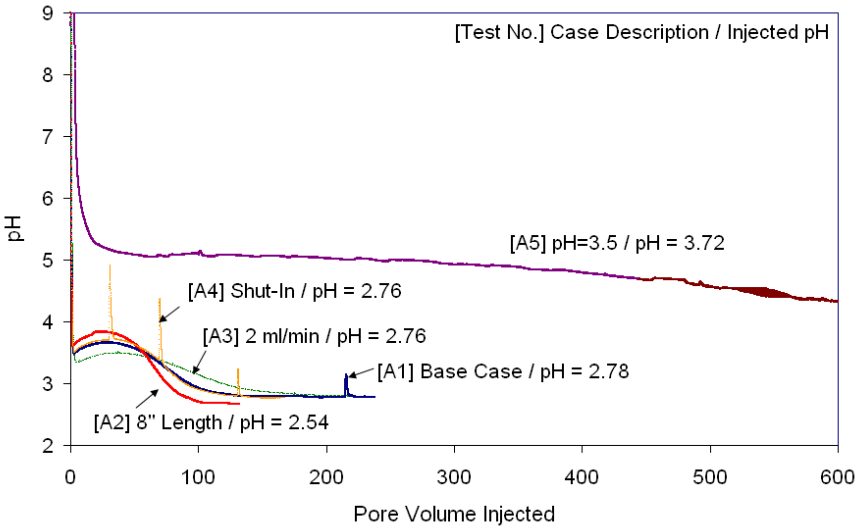

Figure 3.16: Comparison of all the effluent pH responses for the five coreflood experiments with the extended x-axis scale

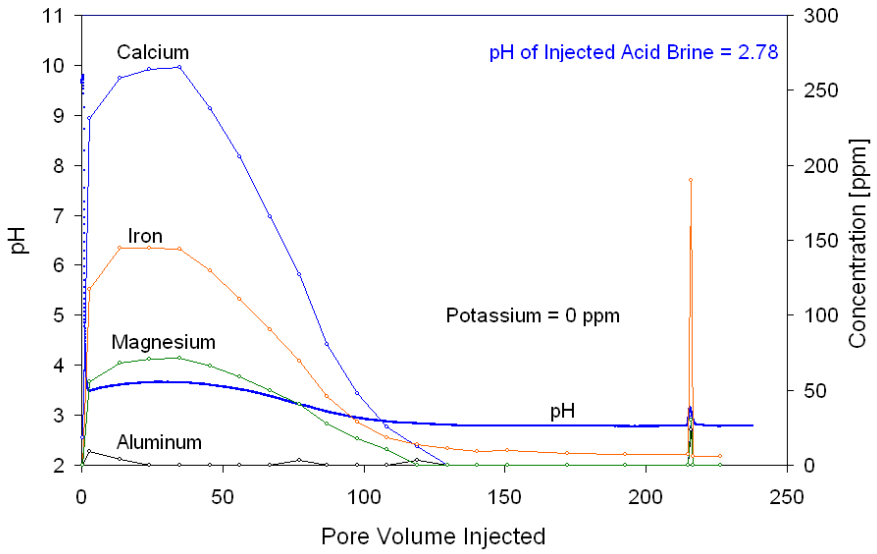

Figure 3.17: Five cations history - Aluminum (*Al*), Calcium (*Ca*), Iron (*Fe*), Magnesium (*Mg*), and Potassium (*K*) – as a function of pore volume injected for test number [A1]

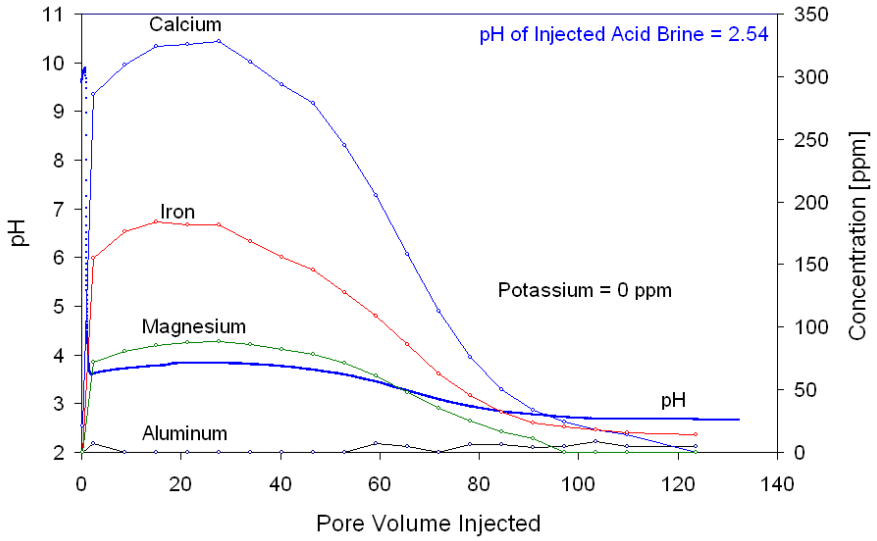

Figure 3.18: Five cations history - Aluminum (*Al*), Calcium (*Ca*), Iron (*Fe*), Magnesium (*Mg*), and Potassium (*K*) – as a function of pore volume injected for test number [A2]

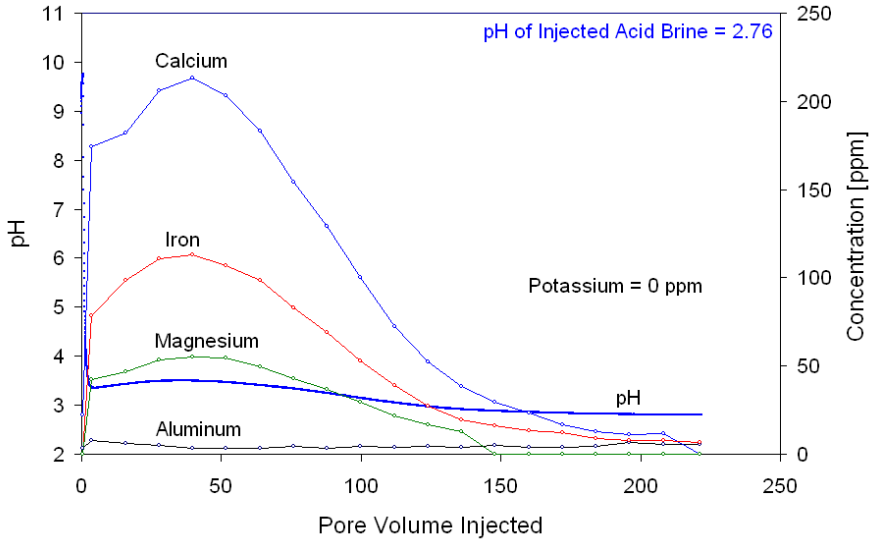

Figure 3.19: Five cations history - Aluminum (*Al*), Calcium (*Ca*), Iron (*Fe*), Magnesium (*Mg*), and Potassium (*K*) – as a function of pore volume injected for test number [A3]

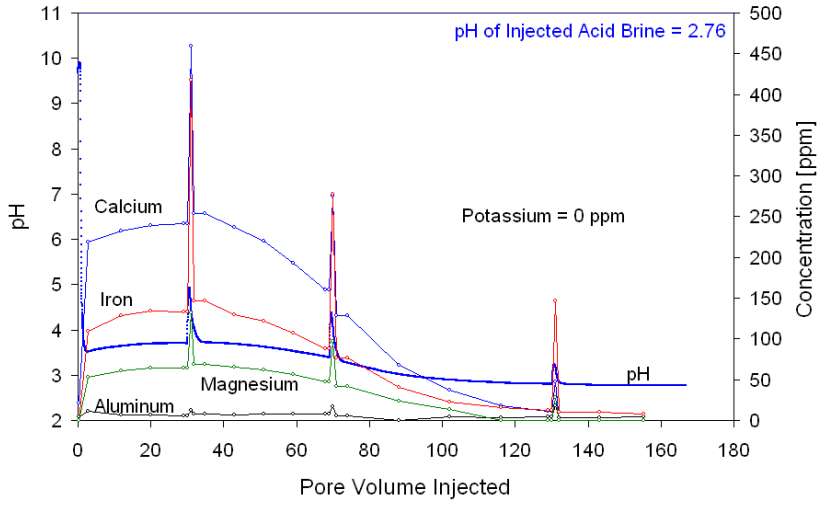

Figure 3.20: Five cations history - Aluminum (*Al*), Calcium (*Ca*), Iron (*Fe*), Magnesium (*Mg*), and Potassium (*K*) – as a function of pore volume injected for test number [A4]

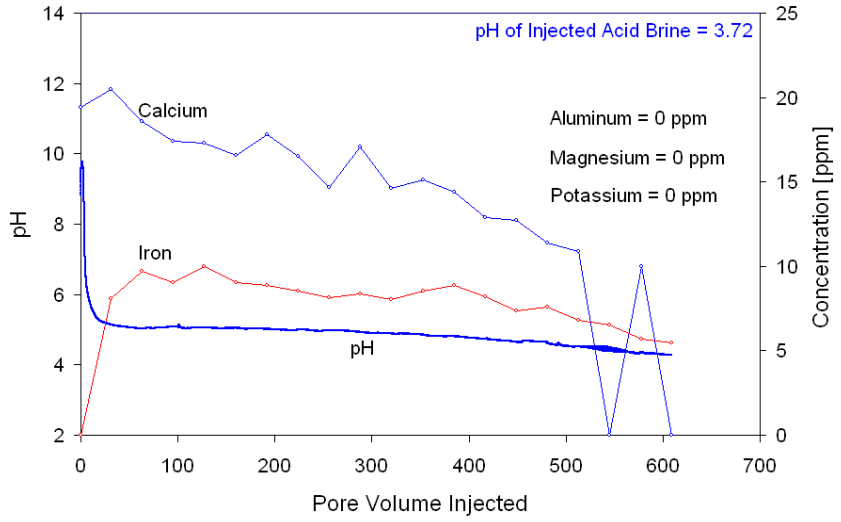

Figure 3.21: Five cations history - Aluminum (*Al*), Calcium (*Ca*), Iron (*Fe*), Magnesium (*Mg*), and Potassium (*K*) – as a function of pore volume injected for test number [A5]

4. Preliminary Reactive Flow and Transport Reservoir Simulations to History-Match the Acid Coreflood Results

4.1 INTRODUCTION

While the main focus of this research is the laboratory characterization of the polymer rheology, and acid and polymer transport in sandstone cores, a preliminary simulation attempt has been made to better interpret the acid coreflood results of **Chapter 3**. These simulations were carried out, as previously done by Benson (2007), employing the GEM-GHG simulator (from Computer Modeling Group), which has a comprehensive geochemical reaction option (Nghiem, 2002-2005). The GEM-GHG simulator employs the PLE (Partial Local Equilibrium) approximation in order to simplify modeling of the large number of geochemical reactions; the PLE approximation states that most chemical reactions in an aqueous phase are in local equilibrium (instantaneous equilibrium is achieved), while others are in kinetically controlled reactions (Sevougian *et al*., 1995).

The objective of this simulation is to history-match a series of citric acid coreflood experiments, described in detail in **Chapter 3**. The effluent pH and cation histories, as functions of pore volume injected (available from the 5 acid coreflood experiments), were matched to identify equilibrium reactions, kinetically controlled reactions, and the corresponding mineral rate constants. The pH histories and the cation histories, as functions of pore volume injected (PVI), are shown in **Figures 3.10** to **3.14**, and **Figures 3.17** to **3.21** in **Chapter 3**, respectively. The case descriptions of 5 acid coreflood experiments and the corresponding petrophysical data are shown in **Tables 3.1** and **3.3**, respectively.

4.2 DESCRIPTION OF GEM-GHG

GEM (Generalized Equation of State) is an equation-of-state (EOS) compositional simulator developed by CMG (Computational Modeling Group), with the purpose of modeling a miscible gas injection process. The GHG (Green House Gas Option) was incorporated with GEM to provide a capability of geochemical reactions, based on Partial Local Equilibrium (PLE), for modeling CO_2 sequestration. The GEM-

GHG simulator uses an adaptive implicit technique to model the transport of components in porous media. The phase equilibrium compositions and the densities of the gas and oil phases can be predicted with a couple of equation-of-states: Peng-Robinson or Soave-Redlich-Kwong. The GEM-GHG simulator's capability for geochemical reactions allows the modeling of intra-aqueous reactions in an aqueous phase, as well as rate-controlled kinetic reactions between the aqueous phase and rock minerals. The GEM-GHG version 2004-19, hereafter referred to as GEM, was used with metric units in this research.

GEM is capable of dealing with reactive fluid flow and transport in reservoir by solving the transport equation and chemical reaction, including intra-aqueous reactions and mineral dissolution/precipitation reactions. The intra-aqueous reactions in an aqueous phase are controlled by the following equation:

$$Q = K_{eq} \tag{4.1}$$

where $Q = \prod_{i=1}^{nct} a_k^{v_i}$

and Q is the activity product; K_{eq} is the chemical equilibrium constant; a_k is the activity of component k; v_α is the stoichiometric coefficients of reaction α, and; nct is the number of components in the aqueous phase.

The rate for the dissolution and precipitation of minerals is calculated as:

$$r_\beta = \mathrm{sgn}\left[1-\left(\frac{Q_\beta}{K_{eq,\beta}}\right)\right]\hat{A}_\beta S_w\left(k_{0,\beta}+\sum_{i=1}^{nct} k_{i,\beta} a_i^{w_{i,\beta}}\right)\left|1-\left(\frac{Q_\beta}{K_{eq,\beta}}\right)^{\xi}\right|^{\zeta} \tag{4.2}$$

where r_β is the rate per unit bulk volume; $\hat{A}_\beta$ is the reactive surface area of mineral β of bulk volume of rock; S_w is the water saturation; $k_{o,\beta}$ is the rate constant of mineral β; $k_{i,\beta}$ is the rate constant of mineral β related to activity of each species; $a_i^{w_{i,\beta}}$ is the activity of ions for mineral β, and; ξ and ζ are the parameters.

The flow equations, along with the above chemical equilibrium reaction equation and rate-dependent mineral dissolution/precipitation equation are solved separately or sequentially, until the systems are converged within a defined error range. In this

simulation, the separate approach was chosen to solve the system in the same way as Benson's work solved it.

4.3 SIMULATION INPUT

The GEM simulator requires 7 different input data groups in the keyword input system: I/O Control; Reservoir Description; Component Properties; Rock-fluid Data; Initial Conditions; Numerical Methods Control; and Well Data and Recurrent Data. Several important input parameters, confined to this simulation, and assumptions are discussed here. Along with the history-matching procedure, the input parameters related to geochemical reactions will be discussed in the next section.

- Reservoir and grid data-

  A Cartesian rectangular grid coordinate, with layers of uniform thickness, was used to describe the core plug. 100 grid blocks in the flow direction were specified to increase the simulation accuracy and to improve the convergence. The grid number of other directions was set as a unity, indicating 1-dimensional simulation. Due to the limitation of the quadrilateral shape of the grid block, the circle cross-section of the core was described as a square shape; this was done by setting the area the same as that of the cross-sectional area of the core. The specified porosity and permeability were assumed to be unchanged by mineral dissolution or precipitation reactions.

- Hydrocarbon species-

  GEM requires hydrocarbon species to be specified, although hydrocarbon species are not involved in this simulation. The C7-16 pseudo-component was specified, as done by Benson (2007). The hydrocarbon property is summarized in **Table 4.1**.

- Aqueous species-

  Aqueous species represent the main ion components that are involved in intra-aqueous and rate controlled reactions. GEM requires specification of the properties of each aqueous species: molecular weight, ion size, and ionic charge. The ion size and ionic charge are used to estimate the ionic strength

of aqueous phases, in case the specific activity model (such as Debye-Huckel or B-dot method) provided in the GEM simulator is chosen. The ideal activity model, which indicates that the activity is the same as the concentration of species, was used in this simulation. Therefore, the properties of the aqueous species do not affect the result. The properties of the aqueous species used in the final match are summarized in **Table 4.2**.

- Elapsed time-

  The *TIME keyword specifies the elapsed time (in days) at which a well is changed. One pore volume injected for each coreflood experiment was set as one elapsed time.

- Minerals involved in reactions-

  It was assumed that the only mineral in Berea sandstone that is involved in the acid reaction is iron-dolomite ($Ca_2FeMg(CO_3)_4$), as discussed in Section 3.6 in **Chapter 3**. The reactive-surface area was defined as 500 m^2/m^3, based on 5.0% composition found in petrographic analysis (in **Chapter 3**); a molecular weight of 400.3448 and mass density of 2850 kg/m^3 were employed.

4.4 FIRST TRIAL FOR HISTORY MATCHING

As the initial attempt, the following reactions were set up and run for Test no. [A1] (which is an injection of pH = 2.5 citric acid in 3% sodium chloride brine into a 5" long Berea core at 1 ml/min, without shut-in). One kinetic controlled reaction with Fe-dolomite was chosen, in addition to five equilibrium reactions, which are considered most important in describing carbonate mineral reactions and citric acid buffering capacity.

Kinetically controlled reaction

$$Fe-Dolomite = 2Ca^{2+} + Fe^{2+} + Mg^{2+} + 4CO_3 \qquad (4.3)$$

Equilibrium Reactions

$$C_6H_8O_7 = H^+ + C_6H_7O_7^- \qquad \text{Log } K_{eq} = -3.128 \qquad (4.4)$$

$$C_6H_7O_7^- = H^+ + C_6H_6O_7^{2-} \qquad \text{Log } K_{eq} = -4.761 \qquad (4.5)$$

$$C_6H_6O_7^{2-} = H^+ + C_6H_5O_7^{3-} \qquad \text{Log } K_{eq} = -6.396 \qquad (4.6)$$

$$H^+ + CO_3^{2-} = HCO_3^- \qquad \text{Log } K_{eq} = 10.329 \qquad (4.7)$$

$$H^+ + HCO_3^- = H_2CO_3 \qquad \text{Log } K_{eq} = 6.352 \qquad (4.8)$$

As an equilibrium constant (25˚C) for Fe-dolomite, $10^{-16.54}$ (which is that of dolomite), was used (Stumm and Morgan, 1996). As a mineral reaction, a zero-order rate with a constant, $10^{-3.19}$ (moles m^{-2} s^{-1}) (which is the same as that of dolomite in U.S.G.S., 2004) was initially assumed, and the constant was changed to $10^{-4.3}$ for a better matching of pH histories. The matching result for this initial attempt is shown in **Figure 4.1**. The overall shape is matched quite well. However, the initial pH's between the simulation and the laboratory data do not match: the initial pH of the experimental measurements is 3.5, while the simulation gives the initial pH as approximately 6.7. Through the case studies, it was found that the initial pH depends on the equilibrium reactions significantly, and the overall shape can be mainly controlled by the rate constant of kinetically controlled reaction.

4.5 SECOND TRIAL FOR MATCHING THE INITIAL PH

As the second trial to match the initial pH's between simulation and the laboratory data, the possible equilibrium reactions were searched and case-studied. **Table 4.3** summarizes all possible combinations of cations and anions in the aqueous phase and the corresponding results. Most acid equilibrium reactions and some salt-solubility reactions were included in the simulations with the corresponding equilibrium reaction constants and solubility products (in the literature) and investigated; however, none of them could decrease the initial pH of simulation.

4.6 THIRD TRIAL FOR MATCHING THE INITIAL PH

The case studies show that one way to decrease the initial pH of simulation is either to change the equilibrium reaction constants of carbonate acid (H_2CO_3) and bicarbonate (HCO_3^-), or to change the equilibrium reaction constants in the reactions

between divalent-ions (Ca^{2+}, Fe^{2+}, and Mg^{2+}) and carbonate ions. The following shows the changed equilibrium constants for carbonate reactions to match the initial pH:

Reactions	*Literature*	*New*	
$H^+ + CO_3^{2-} = HCO_3^-$	Log K_{eq} = 10.329	3.443	(4.9)
$H^+ + HCO_3^- = H_2CO_3$	Log K_{eq} = 6.352	2.117	(4.10)

Figure 4.2 shows the matching result in this case. While the match between laboratory result and simulation looks reasonable overall, the matching in the early PVI (0~30) is not good.

In another attempt to improve the matching, the equilibrium reaction constants in the reactions between divalent-ions and carbonate ions were manipulated as follows:

Reactions	*Literature*	*New*	
$Mg^+ + CO_3^{2-} = MgCO_3$	Log K_{eq} = 2.98	20.0	(4.11)
$Fe^+ + CO_3^{2-} = FeCO_3$	Log K_{eq} = 4.38	20.0	(4.12)
$Ca^+ + CO_3^{2-} = CaCO_3$	Log K_{eq} = 3.224	16.0	(4.13)

Figure 4.3 shows the matching result between laboratory measurements and simulation data. Similar to the previous result, the overall match is reasonable, but the matching in the early PVI (0~60) is still poor.

4.7 FINAL MATCH

The two cases described in Section 4.5 were further evaluated to find the best match between them; this was done through additional matching studies with the laboratory effluent cation concentrations (Mg^{2+}, Ca^{2+}, and Fe^{2+}). It was recognized that the second case (changes of the equilibrium reaction constants in the reactions between divalent-ions and carbonate ion) drastically reduced the concentrations of three cations to several ppms, whereas several hundred ppms were detected in the experimental cation analysis (See Section 3.7.2 in **Chapter 3**). On the other hand, the first case (change of the equilibrium reaction constants of carbonate acid and bicarbonate) produced cation concentrations similar to the laboratory observations (several hundred ppm levels).

The best match for the first case was found through additional tuning of the equilibrium constants in the reactions between divalent-ions and carbonate. **Table 4.4** summarizes the selected equilibrium reactions necessary in the simulation and the

corresponding reaction constants. **Figures 4.4 (a)** and **4.4 (b)** show the final matches of pH and cation histories for Test no. [A1], respectively. The overall trends of both pH and cation histories match very well, and the magnitude of order for the cation concentrations, for both laboratory measurements and simulation data, are also quite similar to one another. However, the reactions in the simulations occur at the very early PVI, in comparison to the laboratory results, shifting the curves to the left. The pressure drops of the laboratory measurements and simulation data are also well-matched, within a reasonable range. **Figures 4.5** through **4.8** show the matching results between laboratory measurements and simulation data, for pH and cation histories of other cases (Test no. [A2], [A3], [A4], and [A5]). All reaction parameters remain the same as those in Test no. [A1]. In Tests no. [A2], [A3], and [A4], the matching results also show reasonable, but still imperfect matching. However, in the case of Test no. [A5], which had a different injection pH (pH = 3.5) than the other tests, the results show the matching of pH and cation histories became very poor. All three minerals were actively consumed at much earlier PVI in this simulation case, compared to the laboratory-measured data. This indicates that the assumed zero-order rate in kinetically controlled reactions may not describe the high pH injection case and it requires a further investigation.

4.8 CONCLUSIONS

The way to decrease the initial pH of simulation is 1) to increase the equilibrium constants in carbonate acid and bicarbonate reactions, or 2) to decrease the equilibrium constants in the reactions between divalent ions and carbonate ions. Both changes increase the concentrations of hydrogen ions (protons) in the solutions, resulting in a decrease of the initial pH. In particular, the case in decreasing the equilibrium constants in carbonate acid and bicarbonate reactions produces good matching of cation histories, as well as pH's, between laboratory measurements and simulation data. However, this modification does not have theoretical basis because the equilibrium constants are well-known values that can be easily found in the literature. It appears that there are missing equilibrium reactions such as complexation of divalent ions or the PLE assumption may not be applicable in this case because the citric acid, a weak acid, is very slowly reacting (instantaneous equilibrium cannot be achieved in chemical reactions while the citric acid is flowing through the porous media). The results also demonstrate that the zero-order rate cannot successfully describe the kinetic geochemical reactions because of poor

matching with higher pH case. More accurate modeling characterization of the geochemical reactions warrants further study.

4.9 APPENDIX 4-A: SIMULATION CODE FOR CMG-GHG

This section gives the simulation code of CMG-GHG for history-matching with Test no. [A1], which is an injection of pH = 2.5 citric acid in 3% sodium chloride brine into a 5" long Berea core at 1 ml/min, without shut-in.

```
------------------------------------------------------------
*FILENAMES *OUTPUT *SRFOUT
*TITLE1 'Acid Coreflood [A1]'
*TITLE2 'Linear 1D Model'
*TITLE3 'Suk Kyoon Choi'
*INUNIT *SI

*RESULTFILE *SR2

*OUTSRF *GRID  *SW  *VISW *POROS *DPORMNR
             *KRW  *VELOCRC *PRES

*MOLALITY 'H+'
*MOLALITY 'Ca++'
*MOLALITY 'Fe++'
*MOLALITY 'Mg++'
*MOLALITY 'Na+'
*MOLALITY 'Cl-'
*MOLALITY 'CO3--'
*MOLALITY 'C6H8O7'
*MOLALITY 'C6H7O7-'
*MOLALITY 'C6H6O7--'
*MOLALITY 'C6H5O7-3'
*MOLALITY 'HCO3-'
*MOLALITY 'H2CO3'
*MOLALITY 'MgHCO3'
*MOLALITY 'FeHCO3'
*MOLALITY 'CaHCO3'
*MOLALITY 'MgCO3'
*MOLALITY 'FeCO3'
*MOLALITY 'CaCO3'
*MOLALITY 'OH-'
*MINERAL  'Dolomite'

*OUTSRF *RES *ALL

*WRST *TIME
*WSRF *WELL 1  **100
*WSRF *GRID *TIME
*WPRN *GRID *TIME
*OUTPRN *RES *ALL
*DIM *MDIMPL 100
**----------------------RESERVOIR & GRID DATA-----------------------
```

```
*GRID *CART 100 1 1
*DI *CON 1.2723E-03
*DJ *CON 2.2308E-02
*DK *CON 2.2308E-02
*KDIR *DOWN
*DEPTH 1 1 1 100
*POR *CON 0.1958
*PERMI  100*664.25
*PERMJ *CON 0.0
*PERMK *CON 0.0
*CPOR 4.5E-7
*PRPOR 101.325
**------------------------FLUID PROPERTY DATA-----------------------
*MODEL   *PR
*NC    1    1
*TRES       25
*COMPNAME
           'C7-16'

*PCRIT      2.0676400E+01
*VCRIT      0.58957324
*TCRIT      611.116
*AC         6.3860000E-01
*MW         1.4718200E+02
*HCFLAG     0
*BIN
*VSHIFT     0.064
*PCHOR      439.1472

*VISCOR     *MODPEDERSEN
*VISCOEFF    1.3040000E-04   2.3030000E+00   7.3780000E-03   1.8470000E+00
5.1730000E-01

*OMEGA   4.5723553E-01
*OMEGB   7.7796074E-02

*DER-CHEM-EQUIL  *ANALYTICAL
*DER-REACT-RATE  *ANALYTICAL

*PERM-VS-POR   0

*ACTIVITY-MODEL  *IDEAL
*AQUEOUS-DENSITY  *LINEAR

*VISW 1
*AQFILL  *OFF

*NC-AQUEOUS    20
*COMPNAME-AQUEOUS
'H+'    'Ca++'    'Fe++'    'Mg++'    'Na+'    'Cl-'    'CO3--'    'C6H8O7'
'C6H7O7-'  'C6H6O7--'  'C6H5O7-3'  'HCO3-'  'H2CO3'  'MgHCO3'  'FeHCO3'
'CaHCO3'  'MgCO3'  'FeCO3'    'CaCO3'    'OH-'

*MW-AQUEOUS
1.00794   40.078   55.847   24.305   22.98977   35.453   60.0092   192.1253
191.11738  190.10944  189.1015  61.01714  62.02508  85.32214  116.86414
101.09514  84.3142  115.8562  100.0872   17.00734
```

```
*ION-SIZE-AQUEOUS
9  6  6  8  4  3  4.5  0  4  4  4  4.5  0  0  0  0  0  0  0  3.5

*CHARGE-AQUEOUS
1  2  2  2  1  -1  -2  0  -1  -2  -3  -1  0  0  0  0  0  0  0  -1

*NC-MINERAL    1
*COMPNAME-MINERAL
'Dolomite'
**Fe-Dolomite is Ca2FeMg(CO3)4(s)

*MW-MINERAL
**Dolomite
  400.3448
*MASSDENSITY-MINERAL
  2850

*N-CHEM-EQUIL    12
*N-RATE-REACT    1

**RXN 1     'C6H8O7' = 'H+'  +  'C6H7O7-'
*STOICHIOMETRY
0     0     1     0     0     0     0     0     0     -1    1     0
      0     0     0     0     0     0     0     0     0     0     0
*LOG-CHEM-EQUIL-CONST
-3.128

**RXN 2     'C6H7O7-'  =  'H+'  +  'C6H6O7--'
*STOICHIOMETRY
0     0     1     0     0     0     0     0     0     0     -1    1
      0     0     0     0     0     0     0     0     0     0     0
*LOG-CHEM-EQUIL-CONST
-4.761

**RXN 3     'C6H6O7--'  =  'H+'   +  'C6H5O7-3'
*STOICHIOMETRY
0     0     1     0     0     0     0     0     0     0     0     -1
      1     0     0     0     0     0     0     0     0     0     0
*LOG-CHEM-EQUIL-CONST
-6.396

**RXN  4    'H+' + 'CO3--'  =  'HCO3-'
*STOICHIOMETRY
0     0     -1    0     0     0     0     0     -1    0     0     0
      0     1     0     0     0     0     0     0     0     0     0
*LOG-CHEM-EQUIL-CONST
3.443

**RXN 5           'H+'  +  'HCO3-'  =  'H2CO3'
*STOICHIOMETRY
0     0     -1    0     0     0     0     0     0     0     0     0
      0     -1    1     0     0     0     0     0     0     0     0
*LOG-CHEM-EQUIL-CONST
2.1173

**RXN 6           'Mg++' + 'HCO3-' = 'MgHCO3'
```

```
*STOICHIOMETRY
0     0     0     0     0     -1    0     0     0     0     0     0
      0     -1    0     1     0     0     0     0     0     0     0
*LOG-CHEM-EQUIL-CONST
1.07

**RXN 7           'Fe++' + 'HCO3-' = 'FeHCO3'
*STOICHIOMETRY
0     0     0     0     -1    0     0     0     0     0     0     0
      0     -1    0     0     1     0     0     0     0     0     0
*LOG-CHEM-EQUIL-CONST
2.0

**RXN 8           'Ca++' + 'HCO3-' = 'CaHCO3'
*STOICHIOMETRY
0     0     0     -1    0     0     0     0     0     0     0     0
      0     -1    0     0     0     1     0     0     0     0     0
*LOG-CHEM-EQUIL-CONST
1.106

**RXN 9           'Mg++' + 'CO3--' = 'MgCO3'
*STOICHIOMETRY
0     0     0     0     0     -1    0     0     -1    0     0     0
      0     0     0     0     0     0     1     0     0     0     0
*LOG-CHEM-EQUIL-CONST
3.22

**RXN 10    'Fe++' + 'CO3--' = 'FeCO3'
*STOICHIOMETRY
0     0     0     0     -1    0     0     0     -1    0     0     0
      0     0     0     0     0     0     0     1     0     0     0
*LOG-CHEM-EQUIL-CONST
3.35

**RXN 11    'Ca++' + 'CO3--' = 'CaCO3'
*STOICHIOMETRY
0     0     0     -1    0     0     0     0     -1    0     0     0
      0     0     0     0     0     0     0     0     1     0     0
*LOG-CHEM-EQUIL-CONST
3.224

**RXN 12    H2O' = 'H+'  +  'OH-'
*STOICHIOMETRY
0     -1    1     0     0     0     0     0     0     0     0     0
      0     0     0     0     0     0     0     0     0     1     0
*LOG-CHEM-EQUIL-CONST
-14

**RXN 13       'Dolomite' = 2'Ca++' + 'Fe++' + 'Mg++' + 4'CO3--'
*STOICHIOMETRY
0     0     0     2     1     1     0     0     4     0     0     0
      0     0     0     0     0     0     0     0     0     0     -1

*REACTIVE-SURFACE-AREA 500.0
*ACTIVATION-ENERGY 52200.0
*LOG-CHEM-EQUIL-CONST
-16.54
```

```
*LOG-TST-RATE-CONSTANT -60
*LOG-TST-RATE-CONSTANT-ACTIV
-60 -60 -4.3 -60 -60 -60 -60 -60 -60 -60 -60 -60 -60 -60 -60 -60 -60 -
60 -60 -60 -60 -60
*TST-ACTIVITY-POWER  0 0 0 0 0 0 0 0 0 0 0 0 0 0 0 0 0 0 0 0 0 0 0
*REF-TEMP-RATE-CONST 25.0

*ANNIH-MATRIX
1     0     0     0     0     0     0     0     0     0     0
      0     0     0     0     0     0     0     0     0     0
0     1     0     0     0     0     0     0     0     0     0
      0     0     0     0     0     0     0     0     0     1
0     0     1     0     0     0     0     0     0     0     -1    -1
      -1    1     1     0     0     0     0     0     0     -1
0     0     0     1     0     0     0     0     0     0     0     0
      0     0     0     0     0     1     0     0     1     0
0     0     0     0     1     0     0     0     0     0     0     0
      0     0     0     0     1     0     0     1     0     0
0     0     0     0     0     1     0     0     0     0     0     0
      0     0     0     1     0     0     1     0     0     0
0     0     0     0     0     0     1     0     0     0     0     0
      0     0     0     0     0     0     0     0     0     0
0     0     0     0     0     0     0     1     0     0     0     0
      0     0     0     0     0     0     0     0     0     0
0     0     0     0     0     0     0     0     1     0     0     0
      0     1     0     0     0     0     1     1     1     0
0     0     0     0     0     0     0     0     0     1     1     0
      0     0     0     0     0     0     0     0     0     0

*PHASEID *OIL
*CW  1E-10
*REFPW 101.325
*OGW_FLASH *NO_H2OVAP
*DERIVATIVE_METHOD *NUMERALL

**--------------------------ROCK FLUID DATA-------------------------
*ROCKFLUID

*RPT
**krw = ((Sw-0.2)/(1-0.2-0.2))^2
**kro = ((1-Sw-0.2)/(1-0.2-0.2))^2
*SWT
0.20000000  0.00000000  1.00000000
0.21250000  0.00043403  0.95876736
0.22500000  0.00173611  0.91840278
0.23750000  0.00390625  0.87890625
0.25000000  0.00694444  0.84027778
0.26250000  0.01085069  0.80251736
0.27500000  0.01562500  0.76562500
0.28750000  0.02126736  0.72960069
0.30000000  0.02777778  0.69444444
0.31250000  0.03515625  0.66015625
0.32500000  0.04340278  0.62673611
0.33750000  0.05251736  0.59418403
0.35000000  0.06250000  0.56250000
0.36250000  0.07335069  0.53168403
0.37500000  0.08506944  0.50173611
```

```
0.38750000  0.09765625  0.47265625
0.40000000  0.11111111  0.44444444
0.41250000  0.12543403  0.41710069
0.42500000  0.14062500  0.39062500
0.43750000  0.15668403  0.36501736
0.45000000  0.17361111  0.34027778
0.46250000  0.19140625  0.31640625
0.47500000  0.21006944  0.29340278
0.48750000  0.22960069  0.27126736
0.50000000  0.25000000  0.25000000
0.51250000  0.27126736  0.22960069
0.52500000  0.29340278  0.21006944
0.53750000  0.31640625  0.19140625
0.55000000  0.34027778  0.17361111
0.56250000  0.36501736  0.15668403
0.57500000  0.39062500  0.14062500
0.58750000  0.41710069  0.12543403
0.60000000  0.44444444  0.11111111
0.61250000  0.47265625  0.09765625
0.62500000  0.50173611  0.08506944
0.63750000  0.53168403  0.07335069
0.65000000  0.56250000  0.06250000
0.66250000  0.59418403  0.05251736
0.67500000  0.62673611  0.04340278
0.68750000  0.66015625  0.03515625
0.70000000  0.69444444  0.02777778
0.71250000  0.72960069  0.02126736
0.72500000  0.76562500  0.01562500
0.73750000  0.80251736  0.01085069
0.75000000  0.84027778  0.00694444
0.76250000  0.87890625  0.00390625
0.77500000  0.91840278  0.00173611
0.78750000  0.95876736  0.00043403
0.80000000  1.00000000  0.00000000

*SGT
  .00000000   .00000000  1.00000000
  .01666667   .00000000   .97222222
  .03333333   .00000000   .94444444
  .05000000   .00000000   .91666667
  .06666667   .00000000   .88888889
  .08333333   .00000000   .86111111
  .10000000   .00000000   .83333333
  .11666667   .00000000   .80555556
  .13333333   .00000000   .77777778
  .15000000   .00000000   .75000000
  .16666667   .00065746   .72222222
  .18333333   .00262985   .69444444
  .20000000   .00591716   .66666667
  .21666667   .01051940   .63888889
  .23333333   .01643655   .61111111
  .25000000   .02366864   .58333333
  .26666667   .03221565   .55555556
  .28333333   .04207758   .52777778
  .30000000   .05325444   .50000000
  .31666667   .06574622   .47222222
  .33333333   .07955293   .44444444
```

```
  .35000000   .09467456   .41666667
  .36666667   .11111111   .38888889
  .38333333   .12886259   .36111111
  .40000000   .14792899   .33333333
  .41666667   .16831032   .30555556
  .43333333   .19000657   .27777778
  .45000000   .21301775   .25000000
  .46666667   .23734385   .22222222
  .48333333   .26298488   .19444444
  .50000000   .28994083   .16666667
  .51666667   .31821170   .13888889
  .53333333   .34779750   .11111111
  .55000000   .37869822   .08333333
  .56666667   .41091387   .05555556
  .58333333   .44444444   .02777778
  .60000000   .47928994   .00000000
  .61666667   .51545036   .00000000
  .63333333   .55292571   .00000000
  .65000000   .59171598   .00000000
  .66666667   .63182117   .00000000
  .68333333   .67324129   .00000000
  .70000000   .71597633   .00000000
  .71666667   .76002630   .00000000
  .73333333   .80539119   .00000000
  .75000000   .85207101   .00000000
  .76666667   .90006575   .00000000
  .78333333   .94937541   .00000000
  .80000000  1.00000000   .00000000
*SIGMA  7. 0. 7.
*ROCKDENR 2650.0
**---------------------INITIAL RESERVOIR CONDITION--------------------
*INITIAL
*SEPARATOR  101.325 15.56
*VERTICAL   *OFF
*PRES       *CON 101.325
*SW         *CON 0.99999
*ZGLOBAL    *CON
            1

*MOLALITY-AQUEOUS-PRIMARY
**'H+'          'Ca++'       'Fe++'     'Mg++'       'Na+'          'Cl-
'        'CO3--'      'C6H8O7'
   5.84269E-11     9.24104E-5     1.00E-60     1.00E-60        5.2920E-01
5.2920E-01   4.11414E-5   1E-25

*VOLUMEFRACTION-MINERAL
** 'Fe-Dolomite'
    0.050
**-------------------------NUMERICAL METHOD-------------------------
*NUMERICAL
*CONVERGE *MAXRES 1.0E-8
*PRECC  1E-8
*MAXSTEPS 399999
*ITERMIN 2
*ITERMAX 200
*AIM OFF
**----------------------------WELL DATA-----------------------------
```

```
*RUN
*DATE 2008 1 1
     *DTMIN 1.0E-16
     *DTMAX 0.01  **0.001
     *DTWELL 0.00000000001
     *AIMSET  *CON 3

**Define Wells
 *WELL 1 'INJ-1'
        *INJECTOR  1
              *INCOMP  *AQUEOUS

**'C7-16'   'H+'          'Ca++'     'Fe++'     'Mg++'     'Na+'      'Cl-'
'CO3--'     'C6H8O7'      'C6H7O7-'     'C6H6O7--'   'C6H5O7-3'   'HCO3-'
'H2CO3'     'MgHCO3'   'FeHCO3'   'CaHCO3'   'MgCO3'    'FeCO3'    'CaCO3'
'OH-'
   0         0.00165959  1.00E-60  1.00E-60  1.00E-60  5.29E-01  5.29E-
01  1.00E-60  2.5458E-03  1.1421E-03  1.1929E-05  2.8880E-09  1.00E-60
1.00E-60    1.00E-60  1.00E-60  1.00E-60  1.00E-60  1.00E-60  1.00E-60
6.0256E-12


*OPERATE  *MAX  *STW 1.44E-3
        *GEOMETRY *K  8.763E-4  2  1.0  0.0
        *PERF *GEO 1
              1 1 1 1.0

*WELL 2 'PROD-2'
        *PRODUCER  2
              *OPERATE *MIN *BHP 101.325

        *GEOMETRY *K  8.763E-4  2  1.0  0.0
        *PERF *GEO 2
              100 1 1 1.0

*TIME 0.008609104
*TIME 0.017218207
*TIME 0.025827311
*TIME 0.034436414
*TIME 0.043045518
      .
      .
      .
*TIME 2.014530243
*TIME 2.023139347
*TIME 2.031748451
*TIME 2.040357554
*TIME 2.048966658
*STOP
----------------------------------------------------------------
```

Table 4.1: Hydrocarbon property

Component	Critical Pressure (atm)	Critical Temperature (K)	Critical Volume (m^3/kg mol)	Accentric Factor	Molecular Weight
C7-16	20.6764	611.116	0.58957	0.6386	147.182

Table 4.2: Properties of aqueous species used in the final match

Species	Molecular Weight	Ion Size (A)	Ionic Charge
H^+	1.00794	9	1
$Ca^{++`}$	40.078	6	2
Fe^{++}	55.847	6	2
Mg^{++}	24.305	8	2
Na^+	22.98977	4	1
Cl^-	35.453	3	-1
CO_3^{--}	60.0092	4.5	-2
$C_6H_8O_7$	192.1253	0	0
$C_6H_7O_7^-$	191.1174	4	-1
$C_6H_6O_7^{--}$	190.1094	4	-2
$C_6H_5O_7^{-3}$	189.1015	4	-3
HCO_3^-	61.01714	4.5	-1
H_2CO_3	62.02508	0	0
$MgHCO_3^+$	85.32214	0	0
$FeHCO_3^+$	116.8641	0	0
$CaHCO_3^+$	101.0951	0	0
$MgCO_3$	84.3142	0	0
$FeCO_3$	115.8562	0	0
$CaCO_3$	100.0872	0	0
OH^-	17.00734	3.5	-1

Table 4.3: Possible combinations of cations and anions in the aqueous phase

Cation	Anion	Influence	Cation	Anion	Influence
Ca^{2+}	Cl^-	Not Considered	Fe^{2+}	Cl^-	Not Considered
Ca^{2+}	CO_3^-	No	Fe^{2+}	CO_3^-	No
Ca^{2+}	HCO_3^-	No	Fe^{2+}	HCO_3^-	No
Ca^{2+}	$C_6H_7O_7^-$	No	Fe^{2+}	$C_6H_7O_7^-$	No
Ca^{2+}	$C_6H_6O_7^{2-}$	No	Fe^{2+}	$C_6H_6O_7^{2-}$	No
Ca^{2+}	$C_6H_5O_7^{3-}$	No	Fe^{2+}	$C_6H_5O_7^{3-}$	No
Ca^{2+}	OH^-	No	Fe^{2+}	OH^-	No
Mg^{2+}	Cl^-	Not Considered	Na^+	Cl^-	Not Considered
Mg^{2+}	CO_3^-	No	Na^+	CO_3^-	No
Mg^{2+}	HCO_3^-	No	Na^+	HCO_3^-	Not Considered
Mg^{2+}	$C_6H_7O_7^-$	No	Na^+	$C_6H_7O_7^-$	Not Considered
Mg^{2+}	$C_6H_6O_7^{2-}$	No	Na^+	$C_6H_6O_7^{2-}$	Not Considered
Mg^{2+}	$C_6H_5O_7^{3-}$	No	Na^+	$C_6H_5O_7^{3-}$	Not Considered
Mg^{2+}	OH^-	No	Na^+	OH^-	Not Considered
H^+	Cl^-	Not Considered			
H^+	CO_3^-	In Simulation			
H^+	HCO_3^-	In Simulation			
H^+	$C_6H_7O_7^-$	In Simulation			
H^+	$C_6H_6O_7^{2-}$	In Simulation			
H^+	$C_6H_5O_7^{3-}$	In Simulation			
H^+	OH^-	In Simulation			

Table 4.4: Equilibrium reactions and the corresponding reaction constants for the best matched simulation

Reactions	Log K_{eq}	
	Literature	New
$C_6H_8O_7 = H^+ + C_6H_7O_7^-$	-3.128	-
$C_6H_7O_7^- = H^+ + C_6H_6O_7^{2-}$	-4.761	-
$C_6H_6O_7^{2-} = H^+ + C_6H_5O_7^{3-}$	-6.396	-
$H^+ + CO_3^{2-} = HCO_3^-$	10.329	3.443
$H^+ + HCO_3^- = H_2CO_3$	6.352	2.117
$Mg^+ + HCO_3^{2-} = MgHCO_3^-$	1.07	-
$Fe^+ + HCO_3^{2-} = FeHCO_3^-$	2.0	-
$Ca^+ + HCO_3^{2-} = CaHCO_3^-$	1.106	-
$Mg^+ + CO_3^{2-} = MgCO_3$	2.98	3.22
$Fe^+ + CO_3^{2-} = FeCO_3$	4.38	3.35
$Ca^+ + CO_3^{2-} = CaCO_3$	3.224	-

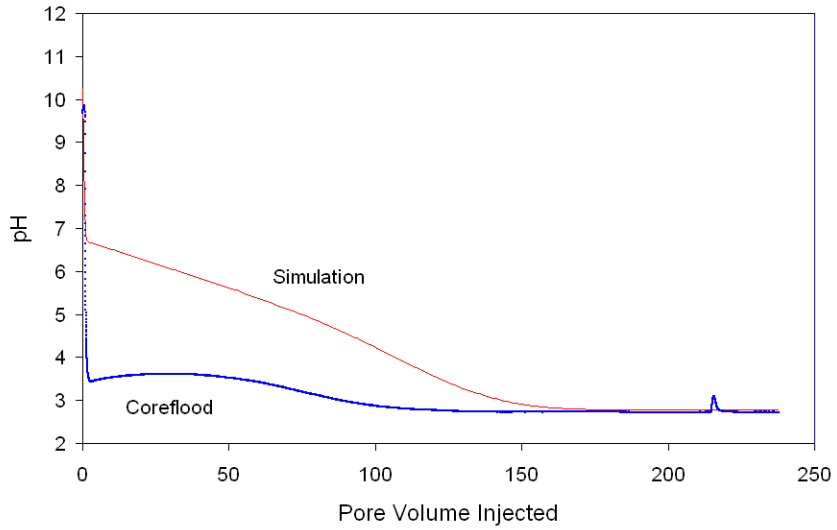

Figure 4.1: Initial pH history matching result for Test no. [A1], which is an injection of pH = 2.5 citric acid in 3% sodium chloride brine into a 5" long Berea core at 1 ml/min, without shut-in

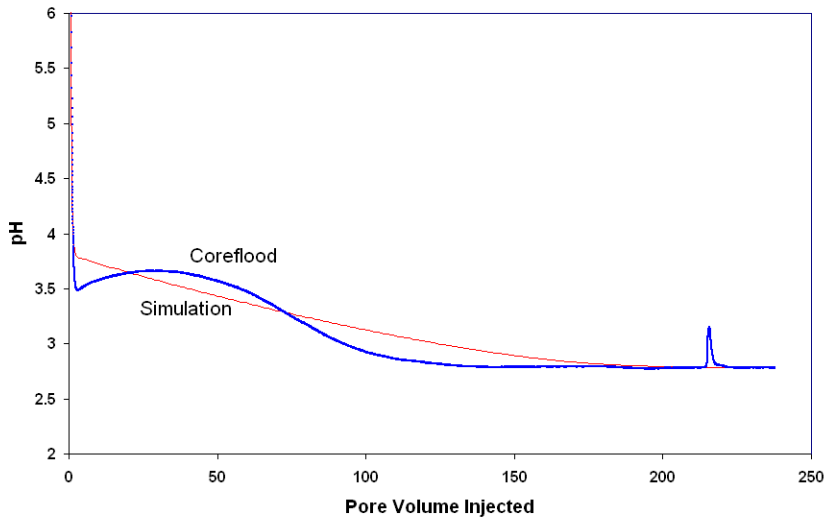

Figure 4.2: pH history matching result by change of the equilibrium reaction constants of carbonate acid and bicarbonate reactions for Test no. [A1], which is an injection of pH = 2.5 citric acid in 3% sodium chloride brine into a 5" long Berea core at 1 ml/min, without shut-in

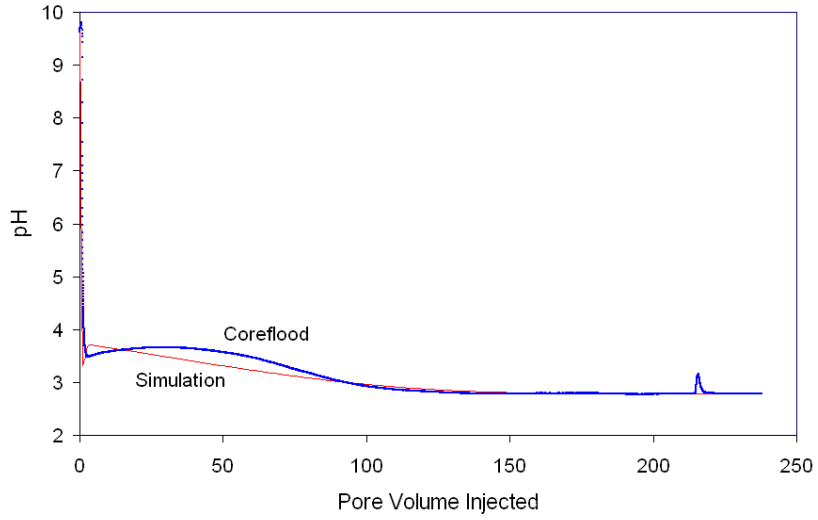

Figure 4.3: pH history matching result by change of the equilibrium reaction constants in the reactions between divalent-ions and carbonate ions for Test no. [A1], which is an injection of pH = 2.5 citric acid in 3% sodium chloride brine into a 5" long Berea core at 1 ml/min, without shut-in

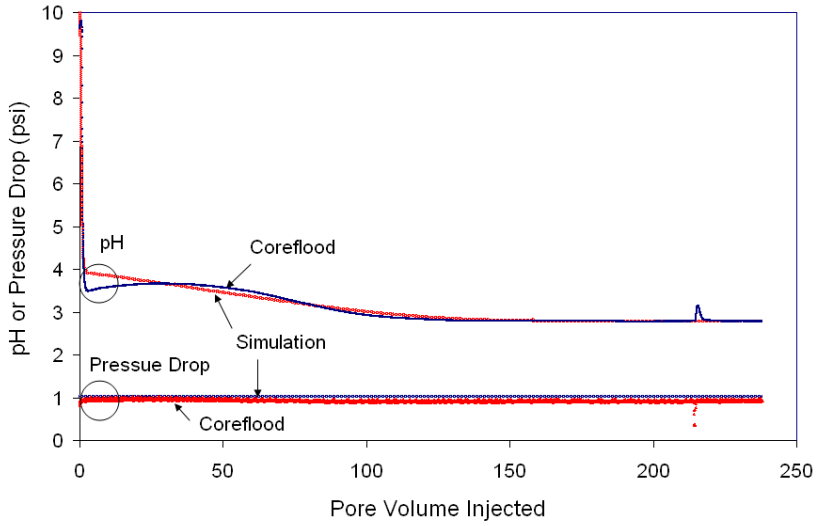

Figure 4.4(a): Final pH history matching result for Test no. [A1], which is an injection of pH = 2.5 citric acid in 3% sodium chloride brine into a 5" long Berea core at 1 ml/min, without shut-in

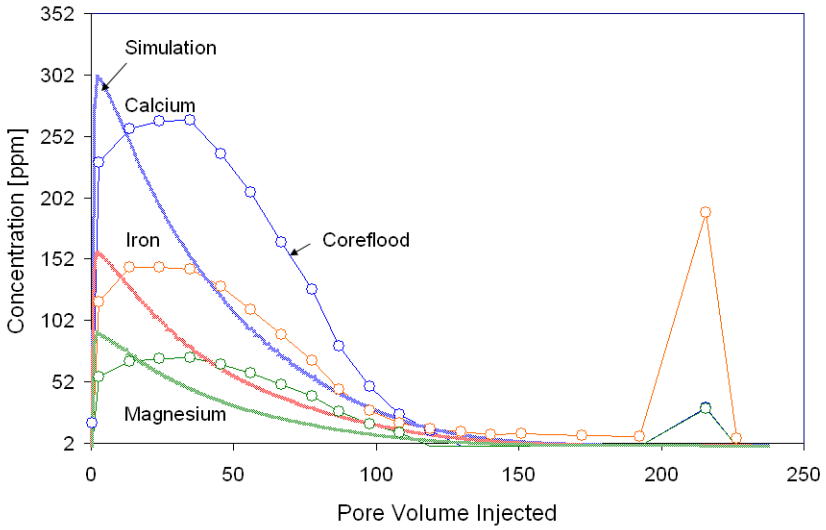

Figure 4.4(b): Final cation history matching result for Test no. [A1], which is an injection of pH = 2.5 citric acid in 3% sodium chloride brine into a 5" long Berea core at 1 ml/min, without shut-in

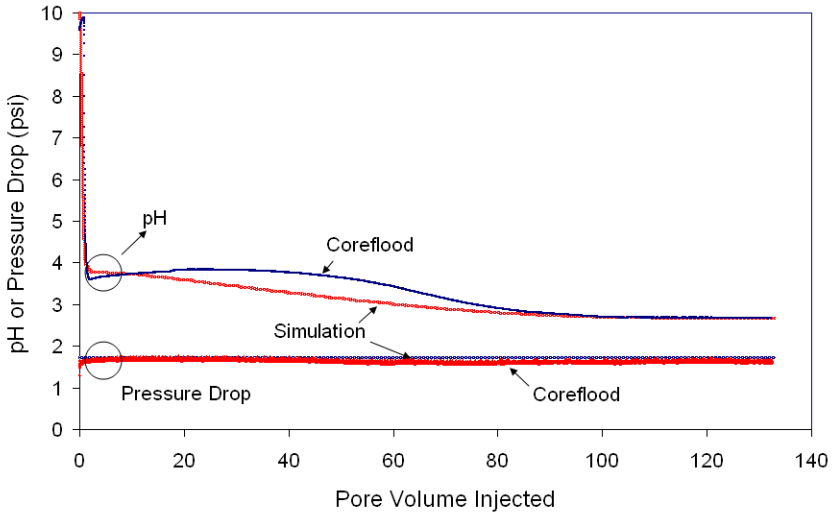

Figure 4.5(a): Final pH history matching result for Test no. [A2], which is an injection of pH = 2.5 citric acid in 3% sodium chloride brine into an 8" long Berea core at 1 ml/min, without shut-in

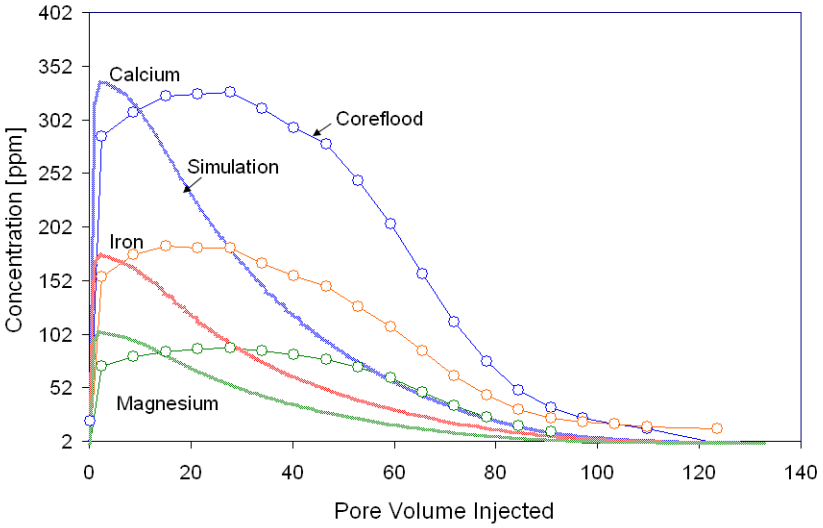

Figure 4.5(b): Final cation history matching result for Test no. [A2], which is an injection of pH = 2.5 citric acid in 3% sodium chloride brine into an 8" long Berea core at 1 ml/min, without shut-in

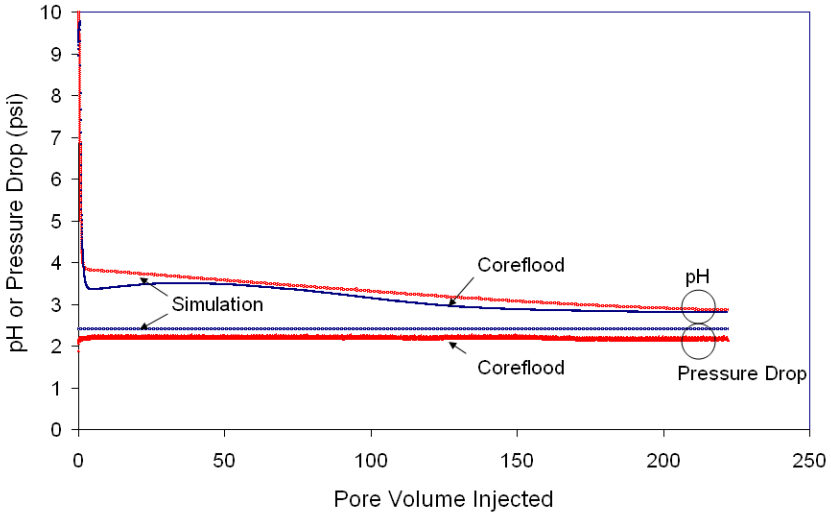

Figure 4.6(a): Final pH history matching result for Test no. [A3], which is an injection of pH = 2.5 citric acid in 3% sodium chloride brine into a 5" long Berea core at 2 ml/min, without shut-in

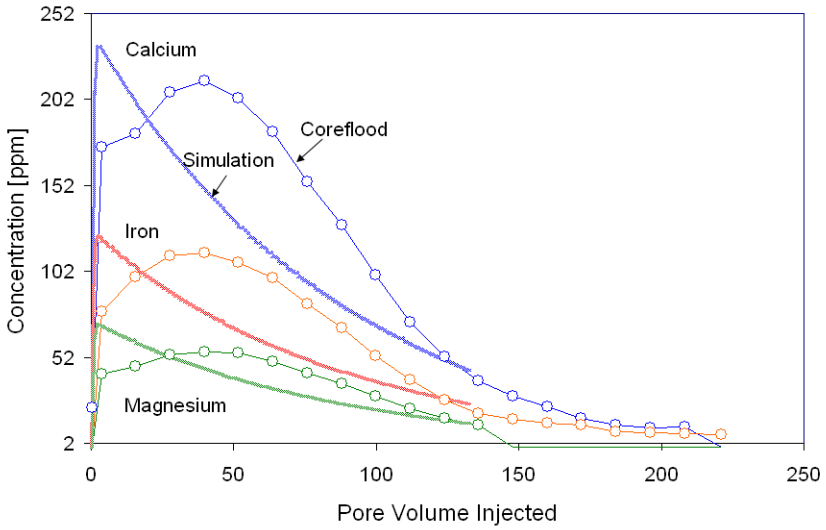

Figure 4.6(b): Final cation history matching result for Test no. [A3], which is an injection of pH = 2.5 citric acid in 3% sodium chloride brine into a 5" long Berea core at 2 ml/min, without shut-in

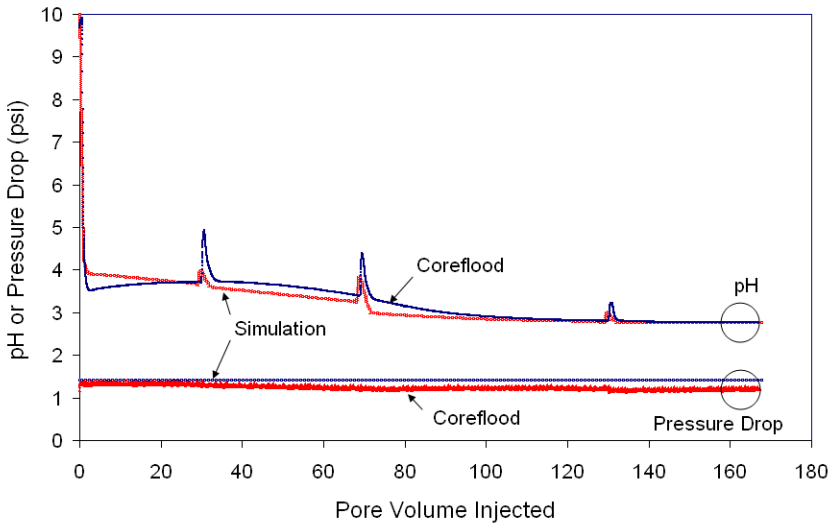

Figure 4.7(a): Final pH history matching result for Test no. [A4], which is an injection of pH = 2.5 citric acid in 3% sodium chloride brine into a 5" long Berea core at 1 ml/min, with shut-ins

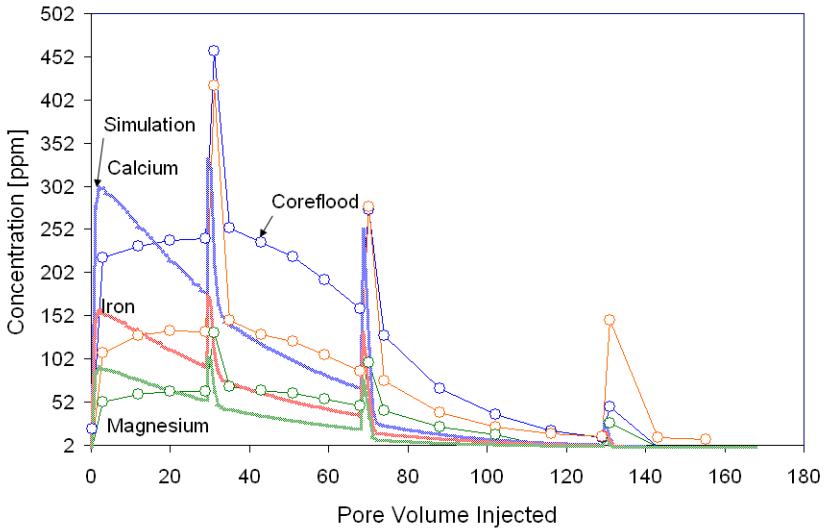

Figure 4.7(b): Final cation history matching result for Test no. [A4], which is an injection of pH = 2.5 citric acid in 3% sodium chloride brine into a 5" long Berea core at 1 ml/min, with shut-ins

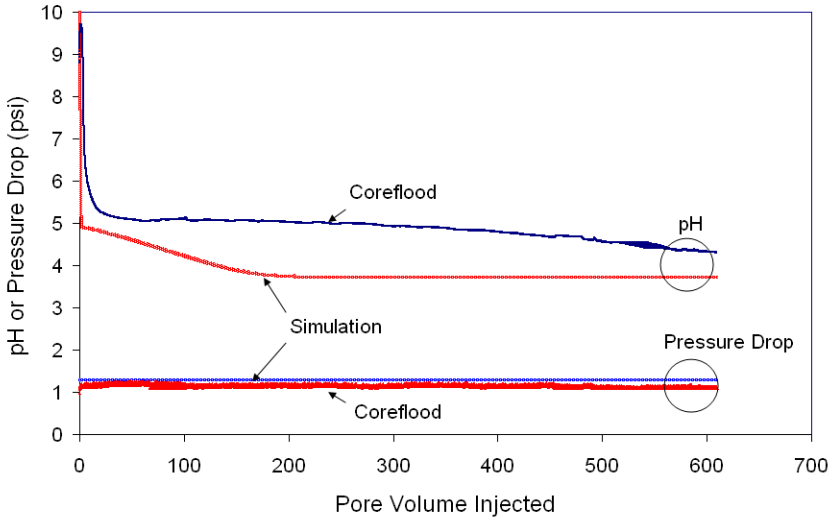

Figure 4.8(a): Final pH history matching result for Test no. [A5] which is an injection of pH = 3.5 citric acid in 3% sodium chloride brine into a 5" long Berea core at 1 ml/min, without shut-in

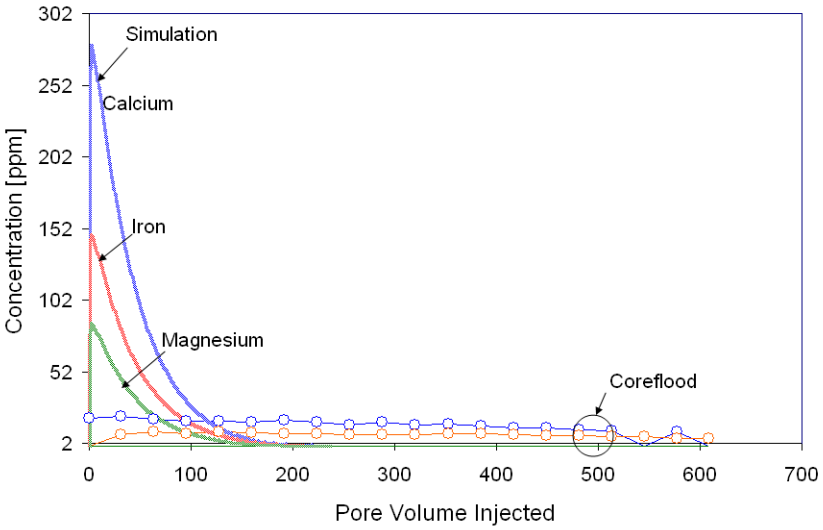

Figure 4.8(b): Final cation history matching result for Test no. [A5], which is an injection of pH = 3.5 citric acid in 3% sodium chloride brine into a 5" long Berea core at 1 ml/min, without shut-in

5. Transport Evaluation of HPAM Solutions

5.1 INTRODUCTION

The main purpose of using polymer in the enhanced oil recovery (EOR) process is to increase solution viscosity and/or reduce rock permeability, both of which help to increase sweep efficiency by reducing the mobility of displacing fluid. The viscosity increase is caused by interactions among polymer molecules in the solution, whereas permeability reduction is the result of interactions between polymer molecules and rock surfaces. For an accurate characterization of polymer flow through porous media, two additional factors should be considered: 1) retention of polymer molecules and 2) inaccessible pore volume and/or surface exclusion/depleted layer phenomenon (Lake, 1989; Sorbie, 1991). Since the viscosity behavior of polymer solutions has been discussed in detail in **Chapter 1** and **2**, other factors (permeability reduction; polymer retention; and inaccessible pore volume and/or surface exclusion/depleted layer phenomenon) will be the focus of this chapter, in order to characterize a low-pH polymer flow through porous media.

Permeability reduction is mainly induced by channel-blocking of polymer molecules (Lake, 1989). It is closely related to, but not always proportional to the amount of, polymer retention. For instance, polyelectrolyte polymers in higher salinity brine show lower permeability reduction than those in lower salinity brine, although polymers are absorbed on rock surfaces to much greater extent in higher salinity conditions. This is because the adsorbed polymer molecules with smaller hydrodynamic radius in higher salinity do not effectively block the rock pore throats. Permeability reduction depends on many factors: polymer type; molecular structure; degree of hydrolysis (in case of partially hydrolyzed polyacrylamide); shear rate, and; pore structure of permeable media (Lake, 1989).

Polymer retention is caused by interactions between polymer molecules and porous media, and it results from three mechanisms: physical adsorption, mechanical entrapment, and hydrodynamic retention (Sorbie, 1991). Mechanical entrapment is a size exclusion phenomenon that occurs when large polymer molecules are trapped at the pore throats of low-permeability rocks (Willhite *et al*., 1977). Hydrodynamic retention is similar to mechanical entrapment, but is a flow rate dependent effect, meaning that

polymer retention increases with the flow rate. However, this mechanism is not well understood and is not believed to be a large contributor in field-scale polymer floods (Sorbie, 1991). Adsorption, the most important mechanism in polymer retention, is caused by physical interactions between polymer chains and rock surfaces, such as: Van der Waals attraction, electrostatic interaction, and hydrogen bonding. Adsorption is known as an irreversible process, depending on the same factors that affect permeability reduction (Lakatos *et al*., 1979; Gramain *et al*., 1981).

Numerous researchers have studied the effects of various process parameters for polymer adsorption and permeability reduction. At low polymer concentrations, polymer adsorption is directly proportional to polymer concentration in the absence of mechanical entrapment, resulting in an increase of permeability reduction (Szabo, 1975; Baijal *et al*., 1981). Higher concentration increases the numbers of polymer molecules per unit volume, thereby increasing the probability of polymer adsorption on rock surfaces. In particular, permeability reduction is greatly increased above a certain polymer concentration, due to collective retention of polymer chains; polymer molecules are adsorbed and form a bridge over pore constrictions (Vela *et al*., 1976). The laboratory data on the effect of molecular weight on polymer adsorption show conflicting results in the literature. Lipatov *et al*. (1974) and Gramain *et al*. (1981) reported higher levels of adsorption with increasing molecular weight. However, other studies noted that polymer adsorption in silica sand is inversely proportional to its molecular weight, albeit with small effects (Lakatos *et al*., 1979; Lakatos *et al*., 1980). The molecular size or coil density was used to explain this inverse proportionality: the larger the polymer molecules, the fewer molecules available to occupy a given unit area of rock surfaces (Lakatos *et al*., 1979). On the other hand, permeability reduction always increases with increasing molecular weight of polymers (Smith, 1970).

The degree of hydrolysis is another important factor that affects adsorption and permeability reduction in case of polyelectrolytes such as HPAM (Lakatos *et al*., 1979; Martin *et al*., 1975; Baijal, 1981). Hydrolysis increases the hydrodynamic radius of polymer molecules because the negative charges on polymer molecules repel one another. The increased negative charge on polymer molecules decreases the adsorption level, due to the repulsion from negatively charged rock surfaces. With the additional reason of size contribution, adsorption level decreases with increasing degree of

hydrolysis. This is a pronounced effect, demonstrated by the fact that the adsorption level of an unhydrolyzed polymer is more than 3 times higher than that of the 30% hydrolyzed polymer (Lakatos *et al*., 1979). It is difficult to predict the dependence of permeability reduction upon hydrolysis, because it depends on both the size and adsorption level of polymer molecules: a higher adsorption level in unhydrolyzed polymers increases permeability reduction (as compared to hydrolyzed polymers), while a smaller hydrodynamic radius decreases permeability reduction. Few cases in the literature have been found to deal with the effect of hydrolysis in terms of permeability reduction.

Salinity is the factor that shows the most significant effect on the adsorption level of polymers: adsorption increases in proportion to salinity (Smith, 1970; Szabo, 1979). Sorbie (1991) provided two reasons for the increase. The first of these reasons is size contribution; the reduced size of polymer molecules under higher salinity sterically fits them onto surface, requiring less conformational entropy when they are absorbed onto surfaces. A second reason is the solvent quality; higher salinity results in bad solvent quality, pushing the polymer molecules further to the solid surface and thereby providing more chances of interactions. However, permeability reduction decreases with increasing salinity, a result opposite from that of adsorption (Denys *et al*., 1998). The shielding effect of cations in salts is said to significantly reduce the hydrodynamic radius of polymer chains, and does not block pore throats effectively, in spite of high adsorption levels. It was reported that hydrolysis and the presence of divalent ions cause the salinity dependence to be more pronounced (Smith, 1970; Lakatos et al., 1979). The pH also shows to be as significant an effect as is the salinity, because protons play the same role as cations of salts. Adsorption increases and permeability reduction decreases with decreasing pH (Lecourtier *et al*., 1990).

Shear rate (Darcy velocity) and rock permeability also affect polymer adsorption and permeability reduction. The resistance factor considers the viscosity contribution, as well as permeability reduction, of polymer flow through porous media; in this case, the resistance factor and the permeability reduction exhibit the same trend, because shear rate and rock permeability do not affect the polymer properties. Vela *et al*. (1976) showed with Berea cores that both adsorption and the corresponding resistance factor are strong functions of rock permeability, decreasing with increasing rock initial permeability. The

influence of shear rate on the resistance factor was systematically studied by Jennings *et al*. (1971). He showed that the resistance factor increases with increasing shear rate, due to the viscoelastic property of polymer molecules. The recent study by Chauveteau *et al*. (2002) showed that above a certain critical shear rate, the polymer adsorption level is slowly increasing with the shear rate. He reasoned that the increase of hydrodynamic forces normal to the pore wall by the increase of shear rate pushed the additional molecules into the already adsorbed layer. The type of rock mineral also has a significant influence on the polymer adsorption level; rock adsorption is higher for clay than silicate and higher for carbonate than sandstone (Smith, 1970). The additional presence of aluminol groups in clay promotes adsorption more than does the presence of silanol groups alone in silicate (Sorbie, 1991). Calcium ions in carbonate strongly bond with polymers, showing higher adsorption than sandstone (Smith, 1970; Lakatos, 1979; Szabo, 1975).

Another characteristic of polymer flow through porous media is that polymers flow faster than tracers. Two mechanisms can explain this phenomenon: 1) **inaccessible pore volume** and 2) **surface exclusion/depleted layer**. The concept of inaccessible pore volume, proposed by Dawson *et al*. in 1972, states that polymer molecules with relatively large size cannot access small pore throats, thereby enhancing the superficial velocity of the polymer molecules. Another mechanism is the surface exclusion layer, in which polymer molecules are excluded from the vicinity of the walls of the porous medium (Chauveteau *et al*., 1981; Lecourtier *et al*., 1984; Chauveteau *et al*., 1984). Both mechanisms are closely related to the hydrodynamic size of polymer molecules. Therefore, HPAM with flexible coil structure shows more pronounced velocity enhancement than rigid biopolymers, such as Xanthan (Sorbie, 1991). Several researchers have shown that IPV dominantly occurs in low-permeability rocks, and the surface exclusion phenomenon is a major contributor for velocity enhancement in higher permeability rocks (Sorbie *et al*., 1987; Sorbie, 1991).

This chapter describes a series of coreflood experiments in order to characterize the transport properties of polymer solutions in low-pH conditions through porous media. Transport efficiency is evaluated in terms of permeability reduction and mobility reduction. Adsorption in dynamic flow conditions and inaccessible/excluded pore volumes are measured by quantitative analyses of the effluent polymer and tracer

concentrations. The effects of various variables, such as polymer concentration, molecular weight, salinity, degree of hydrolysis, and flow rates on polymer transport under a low-pH condition are systematically investigated. The solution densities and viscosities are also measured to estimate the intrinsic viscosity and hydrodynamic radius of various HPAM's employed in this study. This size information is used with the results of coreflood experiments in order to interpret the effect of various process variables on polymer transport.

5.2 THEORY

5.2.1 Solution Properties

A filterability test was carried out in polymer solution for the purpose of quality control. The filtration ratio, which compares the time of initial flow-through volume to that of volume later in filtration, is a preferred method to measure the filterability. If it is close to a unity, it means that the quality of the polymer solution is good, *i.e.*, well-mixed and homogeneous. API RP 63 (1990) recommends a standard method:

$$FR_{500} = \frac{t_{500} - t_{400}}{t_{200} - t_{100}} \tag{5.1}$$

where t_{500}, t_{400}, t_{200}, and t_{100} are the times, in seconds, required to filter 500, 400, 200, and 100 mL of the solution, respectively. Since a filtration instrument with only 250ml capacity was available for our use, the modified filtration ratio was employed as follows:

$$FR_{200} = \frac{t_{200} - t_{180}}{t_{80} - t_{60}} \tag{5.2}$$

The intrinsic viscosity is a property related to the polymer molecular size and polymer chain extension in solution. It is useful in that it allows (with Flory-Fox equation) the estimation of the hydrodynamic radius of polymer molecules at the specific conditions. The Huggins and Kraemer equations described below were used to calculate the intrinsic viscosities of various polymer solutions. The Huggins equation relates the specific viscosity (η_{sp}) to polymer concentration for low-concentration solutions (Huggins, 1942):

$$\frac{\eta_{sp}}{C} = |\eta| + k' |\eta|^2 C \tag{5.3}$$

where $\eta_{sp} = \frac{\eta_o}{\eta_s} - 1$ (5.4)

and η_o is the zero-shear limit viscosity; η_s is the solvent viscosity; C is the polymer concentration; $|\eta|$ is the intrinsic viscosity, and; k' is the Huggins constant. The Kraemer equation relates the relative viscosity (η_r) to polymer concentration for low-concentration solutions (Kraemer, 1938):

$$\frac{\ln \eta_r}{C} = |\eta| + k_L |\eta|^2 C \quad (5.5)$$

where $\eta_r = \frac{\eta}{\eta_s}$ (5.6)

and k_L is the polymer-constant. A plot of (η_{sp}/C) or ($\ln \eta_r/C$) is a straight line with C and the intercept is the intrinsic viscosity. In our measurements with relatively higher polymer concentrations, the intrinsic viscosity was sometimes estimated as the inaccurate value, depending on which equation was used. Both equations were used to estimate the intrinsic viscosity, and the most reasonable one among them was chosen.

The effective hydrodynamic radius of polymer molecules (Ω_r) was then estimated with the Flory-Fox equation (Flory, 1953):

$$\Omega_r = \left[\frac{|\eta| M}{\Phi} \right]^{1/3} \quad (5.7)$$

where M is the molecular weight, and; Φ is the universal constant (2.1×10^{21} dl/g·mol·cm^3).

5.2.2 Petrophysical Properties

The single-phase brine permeability of Berea sandstone cores was obtained by measuring the pressure drops at two different flow rates. The Darcy equation (3.1) was transformed in order to calculate brine permeability from the multi-flow rate tests:

$$k = \frac{\mu L}{mA} \quad (5.8)$$

where m is the slope of line for ΔP (pressure drop) versus q (flow rate).

5.2.3 Flow Efficiency

The apparent polymer viscosity needs to be calculated at the specific effective shear rates to obtain the permeability reduction and the mobility reduction during polymer flow. The ARES LS-1 rheometer (described in **Chapter 1**) was used to measure the steady shear viscosities of the injected solutions at different shear rates. The Carreau model was used and the corresponding four parameters were obtained with data fitting of the measured viscosity data (Sorbie, 1991):

$$\eta = \eta_\infty + (\eta_\infty - \eta_o)\left[1 + (\lambda\dot{\gamma})^2\right]^{(n-1)/2} \tag{5.9}$$

where η_∞ and η_o are the infinite and zero shear-limit viscosities, respectively; λ is the time constant; $\dot{\gamma}$ is the shear rate, and; n is the power-law exponent.

The effective shear rate of polymer flow in a permeable rock (γ_{eff}), which is required for the Carreau Model, was obtained with the following equation (Cannella *et al.*, 1988):

$$\gamma_{eff} = 6.0\left[\frac{3n+1}{4n}\right]^{n/(n-1)}\left[\frac{U_w}{\sqrt{k_w S_w \phi}}\right] \tag{5.10}$$

where U_w is the Darcy velocity of the polymer-containing water phase; k_w is the water-phase permeability; S_w is the water saturation, and; ϕ is the porosity.

Transport efficiency of polymer flow through porous media was quantified in terms of permeability reduction and mobility reduction (resistance factor). Permeability reduction (R_k) was calculated by:

$$R_k = \frac{k_p}{k_w} = \frac{U_w/(\Delta p_w / L_w)}{U_p/(\Delta p_p / L_p)}\frac{\mu_w}{\mu_p} \tag{5.11}$$

where k is the permeability; U is the Darcy velocity; Δp is the pressure drop; μ is the viscosity; L is the core length; subscript p is the polymer flow, and; subscript w is the brine flow.

The mobility reduction (R_m) was calculated by the mobility ratio of water and polymer phase:

$$R_m = \frac{m_{Lw}}{m_{Lp}} = \frac{k_w / \mu_w}{k_p / \mu_p} = \frac{U_w / (\Delta p_w / L_w)}{U_p / (\Delta p_p / L_p)} \tag{5.12}$$

where m_L is the mobility in porous rock.

The length (L) and Darcy velocity (U) are constant through all coreflood experiments. Therefore, equation (5.11) and (5.12) can be reduced to:

$$R_k = \frac{\Delta p_p}{\Delta p_w} \frac{\mu_w}{\mu_p} \tag{5.13}$$

$$R_m = \frac{\Delta p_p}{\Delta p_w} \tag{5.14}$$

5.2.4 Polymer Adsorption

There are two common methods in measuring polymer adsorption in laboratory-scale experiments: 1) bulk static adsorption and 2) adsorption in dynamic flow conditions in cores. In static adsorption measurements, the crushed rock sample is soaked in the polymer solution. The difference of polymer concentrations before and after mixing with rock sample is measured. The dynamic method uses a core or sandpack, in which the polymer solution is injected. In general, a tracer is simultaneously injected, and the material balance calculation for the effluent concentration profiles is performed in order to determine the adsorption level. Typically, the adsorption by bulk static method is much larger than that by dynamic flow conditions (Lakatos *et al*., 1979). The presence of inaccessible pore volume and smaller specific surface area in dynamic methods reduces the actual rock surface area that is exposed to the polymer solution during flow.

Two experimental techniques have been widely used to measure adsorption under dynamic flow condition. The first method is to measure the normalized effluent polymer concentration in the polymer frontal breakthrough as a function of injection pore volume (Willhite *et al*., 1977). Adsorption is then determined by reading off the injection pore volume, where normalized concentration reaches 50%, and subtracting 1 PV (50% normalized point of non-adsorbing tracer); or, it can also be determined by calculating the difference between the areas of polymer and tracer curves, as schematically shown in **Figure 5.1**. This estimation is valid only under the assumption that there are no inaccessible pore volume and surface exclusion layers. The second method is to inject a

polymer slug, followed by a brine of the same salinity in order to wash out the polymer, while leaving the irreversibly-adsorbed polymer. A complete material balance can then be obtained by calculating the difference between the mass of produced polymer and the amount of input polymer, as schematically shown in **Figure 5.2** (Kolodziej, 1988). The balance equation is expressed as:

$$\frac{M_p}{V_p C_{po}} = \left\{ \begin{matrix} AREA\ UNDER \\ NORMALIZED \\ TRACER\ PULSE \end{matrix} \right\} - \left\{ \begin{matrix} AREA\ UNDER \\ NORMALIZED \\ POLYMER\ PULSE \end{matrix} \right\} \qquad (5.15)$$

where M_p is the mass of polymer adsorbed; V_p is the measured pore volume of the core, and; C_{po} is the injected polymer concentration. However, this method is susceptible to error, due to the viscous fingering when the brine displaces the polymer.

In our measurements, the second method under dynamic flow condition was used to estimate the adsorption level of polymers, with the assumption that there is no viscous instability with chase-brine injection, because of the small core diameter (1 inch) and the relatively low polymer viscosity at low-pH conditions. To ensure the accuracy of the measured tracer curve, the amount of the injected polymer solution in pore volume, was also calculated and compared with the area under normalized tracer pulse in pore volume. These two values must be the same because both represent the same meaning.

5.2.5 Inaccessible Pore Volume and Surface Exclusion Layer Phenomenon

Several experimental techniques have been proposed to estimate inaccessible pore volume and surface exclusion layer (hereafter referred as to IPV). The simplest way is to use the leading or trailing edges of the polymer and tracer effluent profiles, after the polymer slug injection, as schematically shown in **Figure 5.2** (Dawson *et al*., 1972; Kolodziej, 1988; Sorbie, 1991). In case of using the leading edge, knowledge of the adsorption level is a pre-requisite. The technique using the trailing edge carries uncertainty because of the potential presence of viscous instabilities. With both techniques, IPV can be calculated by measuring the pore volume corresponding to 50% point of normalized concentration; or, it can be calculated by integrating the area difference between polymer and tracer effluent curves. A technique of successive polymer slug injections, separated by brine injection, was proposed by Zaitoun *et al*. (1987) and Chauveteau *et al*. (1988). The IPV can be estimated from the later slug data

by using the above material balance calculation. In our measurements, the single-slug method using the tailing edge with the area difference calculation was used to estimate IPV, with the same assumption that viscous fingering with the chase-brine injection would be negligible (**Figure 5.2**). For the verification purposes, the result was also compared with that obtained by the area method of the leading edge:

$$\Delta t_p = 1 + D_p - \phi_e \tag{5.16}$$

where Δt_p is the pore volume taken until the polymer solution breakthroughs the core (it can be estimated by the area above the effluent polymer curve during polymer injection in **Figure 5.2**); D_p is the adsorption level in pore volume; and ϕ_e is the inaccessible pore volume in pore volume.

5.2.6 Polymer Effluent Concentration and Tracer Test

There are many techniques to measure the polymer and tracer effluent concentrations. **Tables 5.1** and **5.2** summarize those techniques with brief descriptions. In our tracer tests, bromide anion in the form of sodium bromide was used. It is a water-soluble salt, and is feasible to our application because its presence does not affect the solution pH. Reagent-grade sodium bromide was added to the injection solution during its preparation stage, and a membrane bromide ion electrode, connected to a standard pH/mV meter, was used to measure the bromide concentrations in the effluents. A relatively high concentration of bromide was used to avoid interference with the chloride ions that had disassociated from the sodium chloride. Chloride ions are elements in the same halogen group as bromide ions, interfering with the measurement of bromide concentration. A calibration curve was prepared for each separate coreflood test.

The effluent polymer concentration was measured by an in-line capillary viscometer. A long capillary tube (with a very small volume, as compared to rock pore volume) was set up at the outlet of the core, and the pressure drop across the capillary tube was measured and converted to polymer concentration. This method is quite similar to the concentration-determination method, in which the viscosities of the collected samples are measured in order to back out the polymer concentration that produces the viscosity. However, this method is more attractive, in that the sample collection is not

necessary for the viscosity measurement, and it also provides the continuous data for effluent polymer concentration. Separately, a calibration curve for each test was prepared and used to convert the measured pressure drops to the corresponding effluent polymer concentrations. The procedure details of the polymer and tracer effluent measurements will be provided in Section 5.4 (Experimental Procedure), with a concrete example.

5.3 COREFLOOD EXPERIMENTAL SETUP

Figure 5.3 shows a schematic diagram of an experimental setup for a polymer coreflood. A syringe pump (LC-5000, ISCO Inc.) was used to inject the fluids at a constant rate. It can pump in the range between 0 to 400 ml/hr, with maximum 500 ml storage capacity. A Hassler-type core holder was chosen to safely operate high-pressure polymer flood experiments. Two pressure taps, among the total of 5 available, were connected to the pressure transducers (Model DP15-30, Validyne Engineering Corp.). The pressure drops across three segments were continuously measured for transport performance of polymer solutions. In order to confirm the proper operation of pressure transducers, the pressure drop across the entire core was also measured and compared with the sum of three pressure drops. Two pressure transducers for each section were installed in parallel for a wide range of pressure drop measurements in brine and polymer floods.

A 0.03" diameter and 59" long capillary tube was installed at the end of the core holder to serve as a capillary viscometer. The two pressure transducers for brine and polymer services were set up in parallel, across the capillary tube, to measure the pressure drops on a continuous basis. A calibration curve for each experiment was separately prepared in order to convert the pressure drop to the corresponding effluent polymer concentration for adsorption and IPV calculation. At the end of the capillary tube, a back-pressure regulator (Grove Valve & Regulator co.) was installed to control downstream pressure. An 80 psi back-pressure was applied to suppress CO_2 gas generation that possibly occurs from the reactions between acid and carbonate mineral components. The effluents from the core were collected at regular intervals with a sample collector (Retriever II, ISCO Inc.) for tracer tests, and the effluent pH's were continuously measured with an in-line pH indicator (Cole Parmer Inc.). As with the acid coreflood experiments (**Chapter 3**), the signals from the pressure transducers and pH

indicator were collected and transformed in a data collector (Model MCI-20, Validyne Engineering Corp.) and the data were displayed in the LabVIEW version 8 (National Instrument Co.). All the flow-lines were prepared with stainless steel tubing and all experiments were run at room temperature (25˚C). **Figure 5.4** shows a photograph of the polymer coreflood setup.

5.4 EXPERIMENTAL PROCEDURE

Figure 5.5 shows a schematic diagram of the experimental procedure for polymer corefloods. It consists of two tests: 1) the main test for the polymer coreflood experiment, and; 2) the support tests to prepare the calibration curve for the capillary viscometer, and to measure rheological and physical properties of polymer solutions. The detailed procedure for each is given below.

5.4.1 Solution Preparation

A series of partially-hydrolyzed polyacrylamides (HPAM) and unhydrolyzed non-ionic polyacrylamides (PAM), provided by SNF Inc., were chosen to study the effects of the different process variables on the polymer transport. The specifications for the polymers are the same as those for the rheological measurements, as shown in **Table 1.3** in **Chapter 1**. Only polyacrylic acid (PAA) was excluded in these coreflood experiments, because it is incompatible with citric acid (precipitation occurs). Reagent-grade sodium chloride (NaCl) was used as salts to prepare brine, and sodium bromide (NaBr) was used as the tracer. The pH of the solutions was adjusted by directly adding a powder form of citric acid ($C_6H_8O_7$).

Three polymer solutions for each coreflood experiment were prepared on a mass basis in a beaker: one is at the injection concentration (500 ml), and the other two solutions are at lower concentrations (250 ml). The polymer solution at the injection concentration was used for both the coreflood experiment and the capillary tube test, and the other two solutions in lower concentrations were used to prepare the calibration curve for the capillary viscometer. **Table 5.3** summarizes the compositions and properties of all polymer solutions used in these experiments. The solutions were prepared in the same way as that described in Section 1.3.1 in **Chapter 1**. The only difference is that 2000

ppm sodium bromide was added as tracer during the brine preparation, before adding the polymers. As described earlier, the high concentration of the tracer was to avoid the possible chloride interference in accurately measuring the effluent tracer concentration. If required, the pH of the polymer solutions was then adjusted by adding citric acid into the polymer solution with high speed mixing, while measuring the pH of the solution continuously with a pencil-thin pH meter.

All polymer solutions were filtrated to remove possible microgels or precipitates that might have formed during the preparation stage. The filtration was performed with 1.2 μm Millipore filter paper under 15-psi pressure, applied by a high-purity Argon gas in a cylinder. The filtered volume was measured with a mass cylinder, and the time required to filter the accumulated volume was also measured with a stopwatch, in order to calculate the filtration ratio given in equation (5.2). 10 ml samples were taken before and after filtration, and their steady shear viscosities were measured for shear rates ranging from 1 to 1000 s^{-1}. The viscosity drop after filtration, if any, represents imperfect hydration (mixing) and the presence of gels or precipitates in the solution. Densities of the filtered polymers were measured with a scale and a 10ml mass cylinder. The rheological property and density data were used to estimate intrinsic viscosity and, accordingly, the hydrodynamic radius, described in Section 5.2.1.

5.4.2 Calibration Curve for a Capillary Viscometer

A capillary viscometer was used to measure the effluent polymer concentrations, necessary to quantify the adsorption and IPV from polymer coreflood experiments. This method directly relates the measured pressure drop to the polymer concentration by using a calibration curve. Before each polymer coreflood experiment, a capillary tube-test was performed to prepare the calibration curve. A syringe pump was connected directly to the capillary tube, and then the brine and three different known concentrations of polymer solutions were sequentially injected into the capillary tube, from lowest to highest concentration. In order to prepare the calibration curve, the pressure drops across the capillary tube were measured and correlated with the known polymer concentrations. Because a constant flow rate was maintained for each polymer coreflood experiment, a direct correlation between the pressure drop and the effluent polymer concentration can be obtained without performing the viscosity calculation. A couple of assumptions were

made: no adsorption or mechanical degradation occurs during polymer flow in the capillary tube. The pressure drop across the capillary tube, attached at the exit of the core, can therefore be converted to obtain the effluent polymer concentrations from the coreflood experiment.

To validate the reliability of the capillary tube method, a polymer coreflood experiment was performed separately from those scheduled (described in Section 5.5). The effluent polymer concentrations were measured with both Total Organic Carbon (TOC) and capillary tube methods, and the results were compared. TOC, which represents the amount of total carbon in the sample, is sometimes used to measure the polymer concentrations because polymer consists of carbon elements. As the test polymer solution, 0.5% Flopaam 3330S (8 million MW and 25~30% degree of hydrolysis), prepared in 3.0% sodium chloride brine with pH = 2.5, was used. As shown in **Figure 5.3**, a capillary viscometer was used to obtain the effluent polymer concentrations, and the effluent samples were simultaneously collected for the TOC measurements. The collected samples were diluted by 20 times with brine so that the concentration could be in the detectable range of the TOC instrument (less than 500 ppm). The calibration samples with known concentrations were separately prepared and used to generate a calibration curve, *i.e.*, the relationship between the TOC counts and the polymer concentrations. **Figure 5.6** shows a comparison of the results between the TOC and capillary tube methods. The measurements show a good match, and verify that the capillary tube method gives a reasonable result.

5.4.3 Polymer Coreflood Experiment

The closed system for the core holder was prepared by blocking the valves and the vacuum evacuation was carried out with a vacuum pump (Model 2AAR2, Marvac Scientific Manufacture Co.) for more than 10 hours. The core was saturated with pure CO_2 gas, twice at 30 minute intervals, at the beginning of vacuum evacuation to effectively remove any air trapped in the pores of the Berea core. The core was then saturated with sodium chloride brine with salinity equivalent to that of the injection polymer solution. The porosity was calculated by subtracting the dead volume of the closed system (the amount of brine saturated in unnecessary parts, such as valves or lines) from the total amount of saturated brine. After the back-pressure regulator was set

at 80 psi, the sodium chloride brine, with equivalent salinity to the polymer solution, was injected at 1 and 2 ml/min for approximately 3 pore volumes, respectively, to measure the brine permeability. Subsequently, the citric acid solution, with its pH same as that of the injection polymer solution, was injected for approximately 3 pore volumes, to allow the citric acid to equilibrate with the rock surfaces. The purpose of this acid pre-injection is to maintain a constant citric acid concentration during the injection of low-pH polymer solution. Otherwise, the variation in the citric acid concentration might interfere with the measurement of bromide (tracer) concentration in the effluents.

The prepared polymer solution was then injected into the Berea core for approximately 5 pore volumes, until a steady flow condition was achieved, *i.e.*, stabilization of the pressure drop across the capillary tube. A brine with citric acid, with the same pH as the injection polymer solution, was then injected for more than 5 pore volumes in order to wash out the mobile polymers from the core, leaving only the adsorbed polymers on the rock surfaces. In some tests, brine with neutral pH was further injected to check the possibility of polymer desorption by the high-pH condition. During the polymer and post-acid brine injection period, the effluent samples were collected in plastic tubes by the fraction collector. The pH and the pressure drop were continuously measured and recorded for the entire coreflood experiment period.

5.4.4 Tracer Tests

As the last step, bromide concentrations in the effluent samples were measured with the membrane bromide selective electrode. Four standard solutions – 0, 200, 1000, and 2000 ppm – were prepared, and the voltage for each standard solution was measured to prepare the calibration curve between the voltage and the bromide concentration. All the standard solutions were prepared by adding the equivalent sodium chloride and citric acid to the injected polymer solution in order to minimize the possible interference. Because the electrode response is very sensitive to temperature, all the samples and standards were stored for more than 1 day, at the same temperature. The measurements were made, starting from the standards to the samples. The electrode was rinsed with distilled water and dried between measurements to prevent cross contamination.

5.5 MEASUREMENT PLAN

Table 5.4 shows a measurement plan for the polymer coreflood experiments. As a base case, 0.5% Flopaam 3330S (which has 8M molecular weight and 25~30% degree of hydrolysis), prepared in 3.0% sodium chloride brine with pH = 2.5 at 1 ml/min, was chosen. The effects of various variables on the polymer transport were systematically investigated and compared. The variables studied are: (a) pH = 2.5, 3.5, and 6.0; (b) polymer concentration = 0.5 and 0.8%; (c) molecular weight = 8 and 20 million; (d) salinity = 2.0 and 3.0%; (e) degree of hydrolysis = 0, 20~25, and 25~30%; and (f) flow rate = 1 and 2 ml/min. Relatively high polymer concentration was selected in order to more clearly investigate transport dependence on the variables. Temperature was maintained at 25˚C for all experiments.

5.6 ANALYSIS OF COREFLOOD EXPERIMENTS

5.6.1 Injection Polymer Preparation

Table 5.5 shows the viscosities before and after filtration for all the polymer solutions. Except for the polymer solution in the highest pH condition (pH = 6.0), the viscosities of other polymer solutions drop after filtration with 1.2μm filter paper. The highest viscosity drop is found in the polymer solution with the highest molecular weight (20 million). The viscosity drop may become more pronounced as pH decreases, as the degree of hydrolysis increases, or as the polymer concentration increases. When estimating from the original and dropped viscosities with the rheological model (described in **Chapter 2**), the polymer concentrations were dropped by approximately 10~15% of the original concentration by filtration. At very low pH's, citric acid appears to have some tendency to associate with polymers, thereby aggregating some polymer molecules to be precipitated. Because the filtered polymer solutions were used for the coreflood experiments, the actual injection polymer concentration was slightly lower than that which had been originally prepared.

5.6.2 Base Case

This section describes the experimental results, shown in **Figures 5.7** to **5.15**, for the base case, which has 0.5% Flopaam 3330S (8M molecular weight and 25 ~ 30% degree of hydrolysis), prepared in 3.0% sodium chloride brine with pH = 2.5 at 1 ml/min.

Table 5.6 summarizes the properties of the injected polymer solutions. The filtration ratio was obtained as almost 1, indicating that the solution was homogenous and well mixed. However, the viscosity after filtration was dropped by 24%, as compared to that before filtration, showing that some precipitates formed during the solution preparation and screened by filtration. Hydrodynamic radius was obtained as 0.22 μm with intrinsic viscosity of 279 cm^3/g. In these calculations, the zero-shear rate viscosities, measured at 0.1, 0.3, and 0.5% polymer concentrations, were used with the corresponding densities.

Figure 5.7 shows the results of capillary tube-tests to prepare a calibration curve. Starting from brine, polymer solutions of 0.1, 0.3, and 0.5%, prepared in the same brine as the injected solution, were injected into the capillary tube until the polymer flow reached a steady state. The average pressure drop for each injection was measured, and the calibration curve was prepared, as shown in **Figure 5.8**. The data could be perfectly fitted as a second order polynomial equation. **Figure 5.9** shows the calibration curve for a bromide tracer test. The voltages for 200, 1000, 2000, and 20000 ppm standards were measured and plotted in a semi-log coordinate, which resulted in a straight line.

Figures 5.10 and **5.11** show the pressure drop responses across the core and capillary tube, respectively, as a function of pore volume injected (PVI) during brine and acid injection. The pressure drops responded instantaneously to the change of the flow rate, but the measured total pressure drop deviated slightly from the sum of each of the pressure drops from the core segments. Considering that the low-pressure range transducer has a smaller range of error than a high-pressure one, the total sum of pressure drops from the segments was used to calculate brine permeability, permeability reduction, and mobility reduction. **Figure 5.12** shows the corresponding effluent pH history during brine and acid injection. The pH reaches almost 10 during the brine injection, and drops very quickly when the brine with acid breaks through the core; the pH stabilized at 3.5. From the brine injection, the permeability of 593 md and porosity of 23% were obtained, which is the typical range for Berea sandstone. **Figures 5.13** and **5.14** show the permeability reduction and mobility reduction as functions of PVI during polymer flooding. The curves achieved a plateau value, indicating that there is no sign of mechanical entrapment (filtration) of polymer in the core. In particular, permeability reduction is observed to be between 1.1 ~ 1.3, indicating that the flow efficiency of polymer injection is almost same as that of brine injection. The mobility reduction is, on

the other hand, much higher than the permeability reduction because of the high viscosity of the polymer solution.

Figure 5.15 shows the normalized concentration of effluent polymer and bromide tracer as a function of PVI during the polymer and the chase acid brine injection. The tracer curve passes through the 50% concentration at 1 PV, and the effluent polymer concentration is retarded, indicating the presence of adsorption. The effluent profile for polymer shows that the normalized polymer concentration reaches unity gradually, at almost 5 PVI. This may be due to the non-equilibrium adsorption that occurs due to slow diffusion between the stagnant region and flowing polymer (Sorbie *et al*., 1987). Upon injection of the chase acid brine, the trailing portion of the effluent polymer concentration is ahead of the tracer curve, confirming the presence of inaccessible/excluded pore volume. From the material balance method described earlier, the adsorption is estimated to be 382 μg / g rock. In this case, the areas under normalized tracer and polymer pulses are 5.21 and 4.53 pore volumes, respectively, and the amount of the injected polymer solution is 5.12 pore volume, which is similar to that of the tracer curve, confirming the accuracy of tracer tests. On the other hand, the inaccessible/ excluded pore volume is estimated to be approximately 0.27 PV from the material balance method, which exactly conforms to that calculated by Equation (5.16).

5.6.3 Effect of pH

Table 5.7 summarizes the comparison results of the solution properties and transport efficiencies that were obtained for the polymer solutions with different injection pH's. As the injection pH increases, the intrinsic viscosity and the corresponding hydrodynamic radius of polymer molecules increase. These results conform to the observation made in **Chapter 1**: the low pH triggers the polymer chains to coil and shrink, showing low viscosity, whereas the high pH causes them to be extended, resulting in high viscosity. This size reduction of polymer molecules at low-pH condition substantially improves flow efficiency, in terms of permeability and mobility reductions. It also results in better filtration efficiency (lower filtration ratio), as compared to the polymers in a high-pH condition, confirming that the solution is homogenous and well-mixed. **Figures 5.16 (a)** and **(b)** compare permeability and mobility reductions as functions of PVI for the polymer solutions with different pH's. Permeability reduction in

a low-pH condition is close to that of brine, and it is increased by about 5 times in a high-pH condition. For mobility reduction, there is a difference by about 18 times between low and high pH conditions, due to the large viscosity increase.

The adsorption level increases when the injection pH is decreased, as shown in **Figure 5.16 (c)**. Two reasons for the increase may be given: a) molecular size effect; and b) surface charge effect on polymer molecules and rock minerals. The high pH results in bigger molecular sizes, which require more loss of conformational entropy of polymer chains on adsorption (Sorbie, 1991). As a consequence, the adsorption decreases as the molecular size of polymers is increased. A second reason is related to the effect of pH on the surface charges of polymer molecules and rock minerals. The surface charges of minerals depend on pH, and, in general, as pH increases, the rock surfaces are more negatively charged. On the other hand, a high-pH condition induces the protons to become dissociated from the carboxyl groups on HPAM, which in turn become negatively charged. Therefore, the increased pH causes more repulsion between polymer molecules and rock surfaces, resulting in the decrease of adsorption.

Inaccessible/excluded pore volume is also plotted as a function of the injection pH's, as shown in **Figure 5.16 (c)**. It shows that IPV decreases with increasing the injection pH. These results are opposite to those expected: the smaller molecules in low pH should be able to access smaller pores and a leave thinner layer of excluded volume on the rock surfaces, which corresponds to low IPV. This reverse result may come from viscous instability (fingering), in the case of a high-pH condition. When the chase acid brine displaces high-viscous polymer solutions in the pores, the increased mobility ratio may cause such channeling, resulting in earlier breakthrough of acid brine and, accordingly, the resultant low IPV.

5.6.4 Effect of Polymer Concentration

As the polymer concentration increases, the number of polymer molecules in solution per unit volume increases, thereby increasing interactions between polymer molecules. Theoretically, the change of polymer concentration should not affect the intrinsic molecular size in a very dilute solution. However, in our case, the augmented interactions between molecules apparently increase the intrinsic viscosity and, accordingly, the hydrodynamic radius even in low pH conditions, as shown in **Table 5.8**,

because relatively high polymer concentrations (0.5 and 0.8%) were used in the property measurements. High polymer concentration also causes worse filtration efficiency, but not severely so. **Figures 5.17 (a)** and **(b)** show, respectively, the permeability reduction and mobility reduction as functions of PVI for different polymer concentrations. Permeability reduction slightly increases as the polymer concentration increases, but the increase of mobility reduction is much more pronounced because of the viscosity increase. As expected, the adsorption and IPV increase as the polymer concentration increases, as shown in **Figure 5.17 (c)**. The increased number of polymer molecules per unit volume enhances the probability of contacts between molecules and mineral surfaces, thereby promoting adsorption. Considering the size contribution (no size change for polymer concentration change), the reasons for the increase of IPV are not clear. However, it might be due to the tendency of the higher-viscosity polymer solutions to pass through the wider pore channels (Sorbie, 1991). This reasoning might also be used to explain the tendency of IPV for other variables (pH, molecular weight, and degree of hydrolysis), but it was not mentioned in the corresponding sections due to its uncertainty. The trends of the adsorption and IPV, with changes in polymer concentration in a low-pH condition, conform to that in high-pH condition, as described in Section 5.1 (Introduction).

5.6.5 Effect of Molecular Weight

The molecular weight of polymer is directly related to the size of molecules: the polymer with higher molecular weight has a larger molecular size. **Table 5.9** summarizes the comparison results of the solution properties and transport efficiencies measured for the polymer solutions with different molecular weights in a low-pH condition. As expected, the polymer with 20 million M.W. shows much higher intrinsic viscosity and hydrodynamic radius than the polymer with 8 million. The filtration efficiency also becomes poorer for the polymer solution with 20 million M.W., due to its larger size. As shown in **Figure 5.18 (a)**, the permeability reduction for the polymer with 20 million M.W. is increased by about 30%, as compared to the polymer with 8 million. The mobility reduction in the 20 million M.W. polymer is increased by almost double, compared to the one with 8 million, as shown in **Figure 5.18 (b)**.

The adsorption level of polymer solution in a low-pH condition increases as the polymer molecular weight increases. This observation conforms to those of Lipatov *et al*. (1974) and Gramain *et al*. (1981). Gramain *et al*. (1981) interpreted that the polymers with higher molecular weight occupy a smaller fraction of segments anchored onto the surface, thereby leaving more areas for polymer adsorption. Other researchers (Lakatos *et al*., 1979; Lakatos *et al*., 1980) found a higher adsorption level with increasing molecular weight of polymers, citing the reason of size contributions. The IPV also increases for the polymers with higher molecular weight because of their larger hydrodynamic radius. **Figure 5.18 (c)** shows these observations.

5.6.6 Effect of Salinity

Table 5.10 summarizes the comparison results of solution properties and the transport efficiencies measured for the polymer solutions with different salinities in a low-pH condition. The presence of salts in a low-pH condition does not significantly affect the size of polymer molecules, because the polymer molecules are already coiled and compressed by a low-pH influence. The results prove this fact, showing that the different salinity cases exhibit similar intrinsic viscosities and hydrodynamic radii; minor differences observed may be due to the experimental scatters. The filtration efficiency, again, shows similar values because the hydrodynamic radii of molecules, in both cases, are sufficiently smaller than the pore sizes of filter papers. The permeability reduction is also similar, as shown in **Figure 5.19 (a)**, proving that the hydrodynamic radii and viscosities of both solutions do not exhibit much difference. However, mobility reduction for the 2% salinity case is less than that for the 3% case, as shown in **Figure 5.19 (b)**. This is because the viscosity of the 2% salinity case decreased more, due to the precipitations described earlier. The viscosity data of the injection polymer solutions are available in **Table 5.3**. **Figure 5.19 (c)** shows the adsorption and IPV as functions of the salinity of polymer solutions. It shows that both adsorption and IPV almost remain constant for the salinity change. In fact, the salinity change of HPAM solution in a low-pH condition does little to affect the rheological properties and transport efficiencies.

5.6.7 Effect of Degree of Hydrolysis (DH)

The solution properties and the measured transport efficiencies for three polymers with different degrees of hydrolysis (0%, 25%, and 30% DH) are summarized in **Table 5.11**. The unhydrolyzed polymer shows no sensitivity to pH because of the absence of carboxyl groups, and the higher degree of hydrolysis causes more pronounced viscosity drops in low pH conditions (see **Chapter 1**). Therefore, the 0% DH polymer has the highest intrinsic viscosity among them, showing the largest hydrodynamic radius, while the 30% DH polymer has the smallest hydrodynamic radius. The filtration efficiency also conforms to this fact, showing that the highest DH polymer exhibits the best filtration efficiency. **Figures 5.20 (a)** and **(b)** show the permeability reduction and mobility reduction responses for the polymer solutions with different degrees of hydrolysis; the responses are all in similar range. However, it can be clearly observed that the lower DH polymer shows larger permeability and mobility reductions. The adsorption and IPV follow this trend, showing that the unhydrolyzed polymer has the highest values, as compared to the hydrolyzed polymers, as shown in **Figure 5.20 (c)**. These observations conform to the behaviors of HPAM polymers in high-pH conditions reported in the literature (Lakatos *et al*., 1979).

5.6.8 Effect of Flow Rate

The influences of flow rate on the solution properties and transport efficiencies are summarized in **Table 5.12**. Since the same polymer is used, the solution properties are nearly the same for both cases. **Figures 5.21 (a)** and **(b)** show the permeability and mobility reduction behaviors for different flow rates. Jennings *et al*. (1971) reported that permeability reduction is proportional to the flow rate. However, in low-pH conditions, the rate effect is negligible because the molecular sizes of polymer are small and compact. **Figure 5.21 (c)** shows the adsorption and IPV as functions of PVI. The results show that the adsorption and IPV slightly increase with increasing flow rate. Considering that the flow rate (1 ml/min) is relatively high, the increase of adsorption level with increasing flow rate conforms to the observations of Chauveteau *et al*. (2002). The reasons for IPV increase are not evident, but the increased force parallel in the flow direction by the increase of flow rate might exclude the access of polymer molecules to the small pores that could be reached out in the lower flow rate.

5.6.9 Desorption

In some tests (Test no. 2, 5, 6, 7, and 9 in **Table 5.4**), after the chase acid brine injection, the neutral pH brine was further injected to check whether polymer desorption occurs with the change to high pH conditions. However, all the tests show no desorption of adsorbed polymers, proving that adsorption of polymer onto rock surfaces is irreversible. **Figure 5.22** shows one of the examples, which is for Test no. 6 (0.5% Flopaam 3330S with 8M M.W. and 25~30% degree of hydrolysis, prepared in 2.0% sodium chloride brine with pH = 2.5 at 1 ml/min). There are no observable changes in the polymer effluent concentration during the neutral brine injection.

5.7 CONCLUSIONS

The following conclusions are made:

1. As the solution pH decreases, the hydrodynamic radius of the HPAM polymer decreases and, accordingly, the solution viscosity decreases. The low-pH condition, therefore, substantially improves the efficiency of polymer flow through porous media as measured, in terms of the permeability reduction and mobility reduction. On the other hand, the adsorption increases exponentially as pH decreases. Contrary to our expectation, the inaccessible/excluded pore volume (IPV) decreases with an increase in solution pH. This may be due to viscous instability at the backside of the polymer bank during the polymer coreflood.
2. The salinity change in a low-pH condition does not affect the hydrodynamic size of HPAM molecules because the polymers are already coiled and shrunk by excess proton concentration at low-pH. Accordingly, the transport efficiencies (permeability reduction and mobility reduction), adsorption, and IPV also do not change with salinity.
3. The polymer molecular size in a low-pH condition increases in proportion to both polymer concentration and molecular weight. This effect causes increases in permeability reduction, mobility reduction, and IPV. The adsorption also increases with an increase in polymer concentration and molecular weight.

4. Hydrolysis causes the polymer molecular size to decrease at low-pH, and increase at high-pH. In a low pH condition, as the degree of hydrolysis increases, the hydrodynamic radius of polymer molecules decreases, thereby decreasing mobility reduction and permeability reduction, as well as IPV. Adsorption also decreases with increase in the degree of hydrolysis.
5. The change of flow rate does not significantly affect permeability reduction or mobility reduction in a low pH condition. However, adsorption and IPV increase slightly with increasing flow rate.

Table 5.1: Common methods for measuring effluent polymer concentrations

Methods	Descriptions
Bleach	Spectrophotometric measurements of turbidity by the reaction with sodium hypochlorite and acetic acid
Starch Iodide	Spectrophotometric measurements of a blue starch iodide complex by Hoffmann rearrangement and reaction with bromide and starch
Gravimetry	Measurements of sample weight after water is evaporated
Rheology	Viscometric measurements of the effluent samples with calibration curve
Total Organic Carbon	Measurements of total organic carbon in the effluents with calibration curve
Size Exclusion Chromatography	Measurements by size exclusion chromatography (SEC) with ultraviolet (UV) absorbance detection

Table 5.2: Common methods for tracer tests

Methods	Examples
Radioisotopes	^{14}C, ^{3}H, ^{32}P
Fluorescent dyes	Fluorescein and Rhodamine-WT
Water soluble alcohols	Methanol, Ethanol, Isopropanol and Tertiary Butyl Alcohol
Water Soluble Salts	Nitrate, Bromide, Iodide, Chloride

Table 5.3(a): [Base] 0.5% Flopaam 3330S (8M molecular weight and 25~30 % degree of hydrolysis) in 3.0% sodium chloride brine with pH = 2.5 at 1 ml/min

	0.5%		0.3%		0.1%		0.0% (brine)	
	(g)	(%)	(g)	(%)	(g)	(%)	(g)	(%)
Water	481.5	94.8	240.8	95.0	240.8	95.2	481.5	95.4
NaCl	15.0	3.0	7.5	3.0	7.5	3.0	15.0	3.0
NaBr	1.0	0.2	0.5	0.2	0.5	0.2	0.0	0.0
Polymer	2.5	0.5	0.7	0.3	0.2	0.1	0.0	0.0
Citric Acid	8.0	1.6	4.0	1.6	4.0	1.6	8.0	1.6
Total	508.0	100.0	253.5	100.0	253.0	100.0	504.5	100.0
ρ (g/cm^3)	1.03		1.06		1.10		1.00	
η_o (cP)	8.79		3.33		1.39		1.00	

Table 5.3(b): [pH] 0.5% Flopaam 3330S (8M molecular weight and 25~30 % degree of hydrolysis) in 3.0% sodium chloride brine with pH = 3.5 at 1 ml/min

	0.5%		0.3%		0.1%		0.0% (brine)	
	(g)	(%)	(g)	(%)	(g)	(%)	(g)	(%)
Water	481.5	96.2	240.8	96.4	240.8	96.6	577.80	96.9
NaCl	15.0	3.0	7.5	3.0	7.5	3.0	18.00	3.0
NaBr	1.0	0.2	0.5	0.2	0.5	0.2	0.0	0.0
Polymer	2.5	0.5	0.7	0.3	0.2	0.1	0.0	0.0
Citric Acid	0.4	0.1	0.2	0.1	0.2	0.1	0.48	0.1
Total	500.4	100.0	249.7	100.0	249.2	100.0	596.28	100.00
ρ (g/cm^3)	1.02		1.01		1.03		1.00	
η_o (cP)	9.56		4.36		1.64		1.00	

Table 5.3(c): [pH] 0.5% Flopaam 3330S (8M molecular weight and 25~30 % degree of hydrolysis) in 3.0% sodium chloride brine with pH = 7.0 at 1 ml/min

	0.5%		0.3%		0.1%		0.0% (brine)	
	(g)	(%)	(g)	(%)	(g)	(%)	(g)	(%)
Water	481.5	96.3	240.8	96.5	240.8	96.7	485	97
NaCl	15.0	3	7.5	3.0	7.5	3.0	15	3
NaBr	1.0	0.2	0.5	0.2	0.5	0.2	0.0	0.0
Polymer	2.5	0.5	0.7	0.3	0.2	0.1	0.0	0.0
Citric Acid	0.0	0.0	0.0	0.0	0.0	0.0	0.0	0.0
Total	500.0	100.0	249.5	100.0	249.0	100.0	500.0	100.0
ρ (g/cm^3)	1.03		1.02		1.01		1.00	
η_o (cP)	312.92		50.16		5.64		1.00	

Table 5.3(d): [Polymer Concentration] 0.8% Flopaam 3330S (8M molecular weight and 25~30 % degree of hydrolysis) in 3.0% sodium chloride brine with pH = 2.5 at 1 ml/min

	0.8%		0.5%		0.2%		0.0% (brine)	
	(g)	(%)	(g)	(%)	(g)	(%)	(g)	(%)
Water	480.0	93.8	240.0	94.1	240.0	94.4	240.0	94.7
NaCl	15.0	2.9	7.5	2.9	7.5	2.9	7.5	3.0
NaBr	1.0	0.2	0.5	0.2	0.5	0.2	0.0	0.0
Polymer	4.0	0.8	1.2	0.5	0.5	0.2	0.0	0.0
Citric Acid	11.7	2.3	5.8	2.3	5.8	2.3	5.8	2.3
Total	511.7	100.0	255.1	100.0	254.3	100.0	253.3	100.0
ρ (g/cm^3)	1.05		1.08		1.07		1.00	
η_o (cP)	42.22		12.93		2.43		1.00	

Table 5.3(e): [MW] 0.5% Flopaam 3630S (20M molecular weight and 25~30 % degree of hydrolysis) in 3.0% sodium chloride brine with pH = 2.5 at 1 ml/min

	0.5%		0.3%		0.1%		0.0% (brine)	
	(g)	(%)	(g)	(%)	(g)	(%)	(g)	(%)
Water	481.5	94.8	240.8	95.0	240.8	95.2	240.8	95.4
NaCl	15.0	3.0	7.5	3.0	7.5	3.0	7.5	3.0
NaBr	1.0	0.2	0.5	0.2	0.5	0.2	0.0	0.0
Polymer	2.5	0.5	0.7	0.3	0.2	0.1	0.0	0.0
Citric Acid	8.0	1.6	4.0	1.6	4.0	1.6	4.0	1.6
Total	508.0	100.0	253.5	100.0	253.0	100.0	252.3	0.0
ρ (g/cm^3)	1.05		1.09		1.06		1.00	
η_o (cP)	25.70		7.45		1.94		1.00	

Table 5.3(f): [Salinity] 0.5% Flopaam 3330S (8M molecular weight and 25~30 % degree of hydrolysis) in 2.0% sodium chloride brine with pH = 2.5 at 1 ml/min

	0.5%		0.3%		0.1%		0.0% (brine)	
	(g)	(%)	(g)	(%)	(g)	(%)	(g)	(%)
Water	486.5	95.7	243.3	95.9	243.3	96.0	243.3	96.3
NaCl	10.0	2.0	5.0	2.0	5.0	2.0	5.0	2.0
NaBr	1.0	0.2	0.5	0.2	0.5	0.2	0.0	0.0
Polymer	2.5	0.5	0.7	0.3	0.2	0.1	0.0	0.0
Citric Acid	8.5	1.7	4.3	1.7	4.3	1.7	4.3	1.7
Total	508.5	100.0	253.8	100.0	253.3	100.0	252.5	100.0
ρ (g/cm^3)	1.04		1.05		1.07		1.00	
η_o (cP)	5.77		3.10		1.44		1.00	

Table 5.3(g): [Degree of hydrolysis] 0.5% FA920SH (8M molecular weight and 0 % degree of hydrolysis) in 3.0% sodium chloride brine with pH = 2.5 at 1 ml/min

	0.5%		0.3%		0.1%		0.0% (brine)	
	(g)	(%)	(g)	(%)	(g)	(%)	(g)	(%)
Water	481.5	95.8	240.8	96.0	240.8	96.2	240.8	96.5
NaCl	15.0	3.0	7.5	3.0	7.5	3.0	7.5	3.0
NaBr	1.0	0.2	0.5	0.2	0.5	0.2	0.0	0.0
Polymer	2.5	0.5	0.7	0.3	0.2	0.1	0.0	0.0
Citric Acid	2.5	0.5	1.2	0.5	1.2	0.5	1.2	0.5
Total	502.5	100.0	250.7	100.0	250.2	100.0	249.5	100.0
ρ (g/cm^3)	1.06		1.04		1.05		1.00	
η_o (cP)	65.36		16.45		2.72		1.00	

Table 5.3(h): [Degree of hydrolysis] 0.5% Flopaam 2330S (8M molecular weight and 20~25 % degree of hydrolysis) in 3.0% sodium chloride brine with pH = 2.5 at 1 ml/min

	0.5%		0.3%		0.1%		0.0% (brine)	
	(g)	(%)	(g)	(%)	(g)	(%)	(g)	(%)
Water	481.5	94.6	240.8	94.8	240.8	95.0	240.8	95.3
NaCl	15.0	2.9	7.5	3.0	7.5	3.0	7.5	3.0
NaBr	1.0	0.2	0.5	0.2	0.5	0.2	0.0	0.0
Polymer	2.5	0.5	0.7	0.3	0.2	0.1	0.0	0.0
Citric Acid	8.8	1.7	4.4	1.7	4.4	1.7	4.4	1.7
Total	508.8	100.0	253.9	100.0	253.4	100.0	252.7	100.00
ρ (g/cm^3)	1.03		1.03		1.04		1.00	
η_o (cP)	11.33		5.34		1.74		1.00	

Table 5.3(i): [Flow Rate] 0.5% Flopaam 3330S (8M molecular weight and 25~30 % degree of hydrolysis) in 3.0% sodium chloride brine with pH = 2.5 at 2 ml/min

	0.5%		0.3%		0.1%		0.0% (brine)	
	(g)	(%)	(g)	(%)	(g)	(%)	(g)	(%)
Water	481.5	94.5	240.8	94.7	240.8	94.9	240.8	95.2
NaCl	15.0	2.9	7.5	2.9	7.5	3.0	7.5	3.0
NaBr	1.0	0.2	0.5	0.2	0.5	0.2	0.0	0.0
Polymer	2.5	0.5	0.7	0.3	0.2	0.1	0.0	0.0
Citric Acid	9.5	1.9	4.8	1.9	4.8	1.9	4.8	1.9
Total	509.5	100.0	254.2	100.0	253.8	100.0	253.0	100.0
ρ (g/cm^3)	1.05		1.07		1.09		1.00	
η_o (cP)	6.35		3.35		1.46		1.00	

Table 5.4: Measurement plan for the polymer coreflood experiments

No	Polymer Description			pH	Concentration		Rate
	Polymer	MW	DH(%)		Polymer(%)	Salt (%)	(ml/min)
1	Flopaam 3330S	8M	25-30	2.5	0.5	3.0	1.0
2	Flopaam 3330S	8M	25-30	**3.5**	0.5	3.0	1.0
3	Flopaam 3330S	8M	25-30	**6.0**	0.5	3.0	1.0
4	Flopaam 3330S	8M	25-30	2.5	**0.8**	3.0	1.0
5	**Flopaam 3630S**	**20M**	25-30	2.5	0.5	3.0	1.0
6	Flopaam 3330S	8M	25-30	2.5	0.5	**2.0**	1.0
7	**FA920SH**	8M	**0**	2.5	0.5	3.0	1.0
8	**Flopaam 2330S**	8M	**20-25**	2.5	0.5	3.0	1.0
9	Flopaam 3330S	8M	25-30	2.5	0.5	3.0	**2.0**

Table 5.5: Viscosities before and after filtration for all the polymer solutions (see Table 5.4 for the corresponding polymer information)

No.	Viscosity Before Filtration (cP)	Viscosity After Filtration (cP)	Drop (%)
1	11.6	8.8	-24
2	15.1	9.6	-36
3	294	313	+6
4	66.9	42.2	-37
5	44.3	25.7	-42
6	7.25	5.77	-20
7	74.1	65.4	-12
8	16.5	11.3	-31
9	7.92	6.35	-20

Table 5.6: Properties of the injected polymer solutions for a base case, 0.5% Flopaam 3330S (8M MW and 25~30% degree of hydrolysis), prepared in 0.5% sodium chloride brine with pH = 2.5 at 1 ml/min

Properties	Measured Values
Filtration Ratio, cP	1.04 / 0.95
η_o (Before / After Filtration), cP	11.6 / 8.8
η_o for 0.5% solution, cP	8.79
η_o for 0.3% solution, cP	3.33
η_o for 0.1% solution, cP	1.39
Density, g/cm^3	1.025
Intrinsic Viscosity, cm^3/g	279
Radius of Gyration, μm	0.22

Table 5.7: Comparison results of solution properties and transport efficiencies for the injection polymer solutions with different pH conditions

Case Description

No	Polymer Description			pH	Concentration		Rate
	Polymer	MW	DH(%)		Polymer(%)	Salt (%)	(ml/min)
1	Flopaam 3330S	8M	25-30	**2.5**	0.5	3.0	1.0
2	Flopaam 3330S	8M	25-30	**3.5**	0.5	3.0	1.0
3	Flopaam 3330S	8M	25-30	**6.0**	0.5	3.0	1.0

Results

	(1) pH = 2.5	**(2) pH = 3.5**	**(3) pH = 6.0**
Petrophysical Data			
Porosity (%)	22.5	22.5	22.7
Permeability (md)	593	516	629
Solution Property			
Filtration Ratio	1.04/0.95	1.02/1.05	1.25/1.40
Intrinsic Viscosity (cm^3/g)	279	497	1811
Hydrodynamic Radius (μm)	0.22	0.27	0.41
Flow Characteristics			
Effluent pH	3.4 – 3.5	4.2 - 4.4	9.5 – 9.8
Permeability Reduction	1.1 – 1.3	1.4 – 1.8	5.9 – 7.0
Mobility Reduction	6.6 – 7.6	9.5 – 11.5	119 – 142
Adsorption (μg/g rock)	382	186	76
Inaccessible Pore Volume (PV)	0.27	0.23	0.14

Table 5.8: Comparison results of solution properties and transport efficiencies for the injection polymer solutions with different polymer concentrations

Case Description

No	Polymer Description			pH	Concentration		Rate
	Polymer	MW	DH(%)		Polymer(%)	Salt (%)	(ml/min)
1	Flopaam 3330S	8M	25-30	2.5	**0.5**	3.0	1.0
4	Flopaam 3330S	8M	25-30	2.5	**0.8**	3.0	1.0

Results

	(1) 0.5% Polymer	**(4) 0.8% Polymer**
Petrophysical Data		
Porosity (%)	22.5	22.4
Permeability (md)	593	523
Solution Property		
Filtration Ratio	1.04/0.95	1.08/1.10
Intrinsic Viscosity (cm^3/g)	279	431
Hydrodynamic Radius (μm)	0.22	0.25
Flow Characteristics		
Effluent pH	3.4 – 3.5	3.1 – 3.2
Permeability Reduction	1.1 – 1.3	1.4 – 1.5
Mobility Reduction	6.6 – 7.6	19.1 – 20.7
Adsorption (μg/g rock)	382	819
Inaccessible Pore Volume (PV)	0.27	0.39

Table 5.9: Comparison results of solution properties and transport efficiencies for the polymer solutions with different molecular weights

Case Description

No	Polymer Description			pH	Concentration		Rate
	Polymer	MW	DH(%)		Polymer(%)	Salt (%)	(ml/min)
1	**Flopaam 3330S**	**8M**	25-30	2.5	0.5	3.0	1.0
5	**Flopaam 3630S**	**20M**	25-30	2.5	0.5	3.0	1.0

Results

	(1) 8M MW	**(5) 20M MW**
Petrophysical Data		
Porosity (%)	22.5	22.6
Permeability (md)	593	530
Solution Property		
Filtration Ratio	1.04/0.95	1.12/1.09
Intrinsic Viscosity (cm^3/g)	279	636
Hydrodynamic Radius (μm)	0.22	0.39
Flow Characteristics		
Effluent pH	3.4 – 3.5	3.2 – 3.6
Permeability Reduction	1.1 – 1.3	1.5 – 1.7
Mobility Reduction	6.6 – 7.6	14.9 – 15.8
Adsorption (μg/g rock)	382	558
Inaccessible Pore Volume (PV)	0.27	0.43

Table 5.10: Comparison results of solution properties and transport efficiencies for the polymer solutions with different salinities

Case Description

No	Polymer Description			pH	Concentration		Rate
	Polymer	MW	DH(%)		Polymer(%)	Salt (%)	(ml/min)
1	Flopaam 3330S	8M	25-30	2.5	0.5	**3.0**	1.0
6	Flopaam 3330S	8M	25-30	2.5	0.5	**2.0**	1.0

Results

	(1) 3.0% Salinity	**(6) 2.0% Salinity**
Petrophysical Data		
Porosity (%)	22.5	22.4
Permeability (md)	593	529
Solution Property		
Filtration Ratio	1.04/0.95	1.05/1.00
Intrinsic Viscosity (cm^3/g)	279	290
Hydrodynamic Radius (μm)	0.22	0.22
Flow Characteristics		
Effluent pH	3.4 – 3.5	3.2 – 3.5
Permeability Reduction	1.1 – 1.3	1.0 – 1.2
Mobility Reduction	6.6 – 7.6	5.3 – 5.7
Adsorption (μg/g rock)	382	388
Inaccessible Pore Volume (PV)	0.27	0.26

Table 5.11: Comparison results of solution properties and transport efficiencies for the polymer solutions with different degrees of hydrolyses

Case Description

No	Polymer Description			pH	Concentration		Rate
	Polymer	MW	DH(%)		Polymer(%)	Salt (%)	(ml/min)
1	**Flopaam 3330S**	8M	**25-30**	2.5	0.5	3.0	1.0
7	**FA920SH**	8M	**0**	2.5	0.5	3.0	1.0
8	**Flopaam 2330S**	8M	**20-25**	2.5	0.5	3.0	1.0

Results

	(7) DH = 0%	**(8) DH = 25%**	**(9) DH = 30%**
Petrophysical Data			
Porosity (%)	22.7	22.6	22.5
Permeability (md)	555	610	593
Solution Property			
Filtration Ratio	1.18/1.20	1.05 / 0.99	1.04/0.95
Intrinsic Viscosity (cm^3/g)	1001	567	279
Hydrodynamic Radius (μm)	0.34	0.28	0.22
Flow Characteristics			
Effluent pH	3.9 – 4.0	3.2 – 3.3	3.4 – 3.5
Permeability Reduction	1.2 – 1.5	1.2 – 1.6	1.1 – 1.3
Mobility Reduction	17.8 – 25.4	9.1 – 12.3	6.6 – 7.6
Adsorption (μg/g rock)	438	418	382
Inaccessible Pore Volume (PV)	0.43	0.40	0.27

Table 5.12: Comparison results of solution properties and transport efficiencies for the polymer solutions with different flow rates

Case Description

No	Polymer Description			pH	Concentration		Rate
	Polymer	MW	DH(%)		Polymer(%)	Salt (%)	(ml/min)
1	Flopaam 3330S	8M	25-30	2.5	0.5	3.0	**1.0**
9	Flopaam 3330S	8M	25-30	2.5	0.5	3.0	**2.0**

Results

	(1) 1 ml/min	**(9) 2 ml/min**
Petrophysical Data		
Porosity (%)	22.5	22.6
Permeability (md)	593	560
Solution Property		
Filtration Ratio	1.04/0.95	1.00/1.02
Intrinsic Viscosity (cm^3/g)	279	360
Hydrodynamic Radius (μm)	0.22	0.24
Flow Characteristics		
Effluent pH	3.4 – 3.5	2.9 – 3.1
Permeability Reduction	1.1 – 1.3	1.2 – 1.6
Mobility Reduction	6.6 – 7.6	6.0 – 7.9
Adsorption (μg/g rock)	382	422
Inaccessible Pore Volume (PV)	0.27	0.30

Table 5.13: Trends for adsorption level and IPV of the polymer solutions during dynamic flow conditions in low pH conditions

Trends	Adsorption	IPV
pH (↑)	Increase	Decrease[1]
Polymer concentration (↑)	Increase	Increase
Molecular Weight (↑)	Increase	Increase
Salinity (↑)	No change	No change
Degree of Hydrolysis (↑)	Decrease	Decrease
Flow Rate (↑)	Increase	Increase

1. Due to viscous instability (fingering). The expected trend is "Increase"

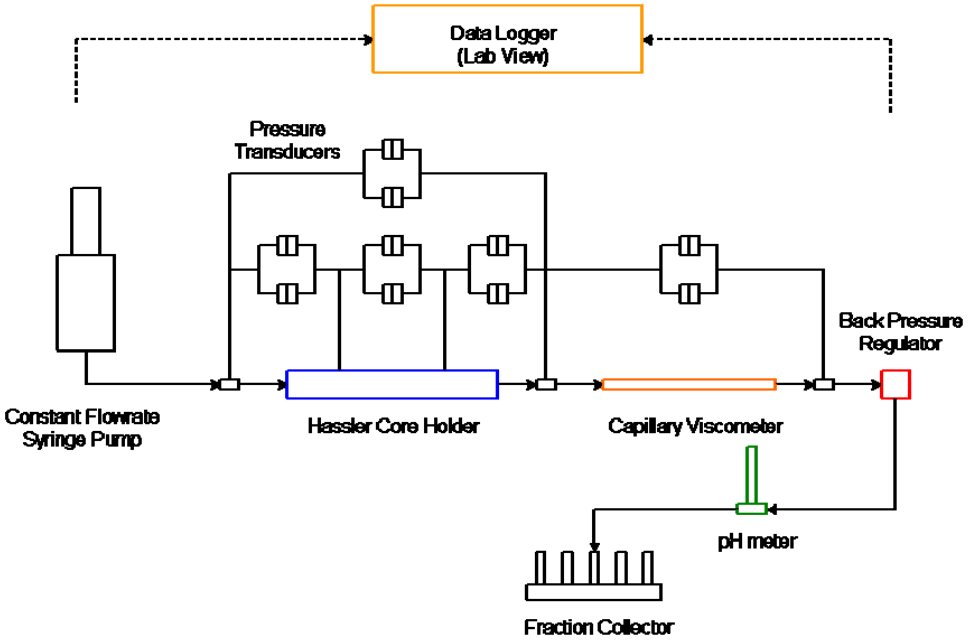

Figure 5.3: Schematic diagram of an experimental setup for polymer coreflood

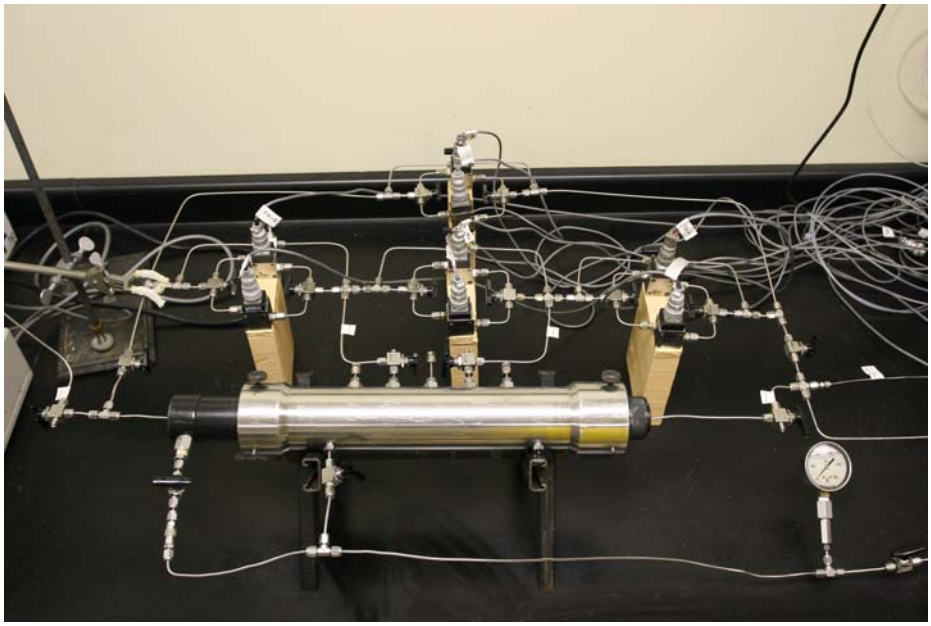

Figure 5.4: Photograph of the polymer coreflood setup

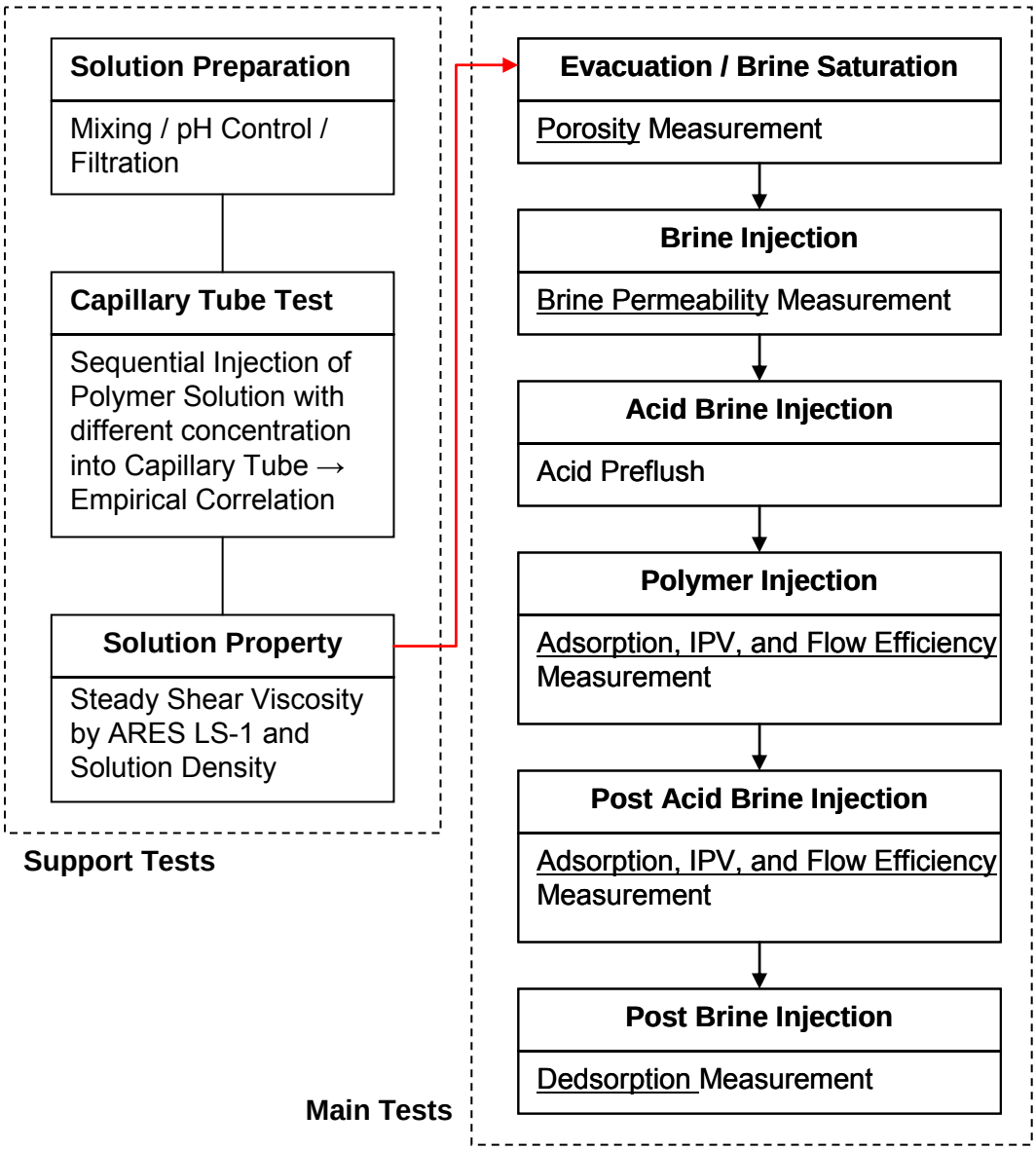

Figure 5.5: Schematic diagram of experimental procedure for polymer corefloods

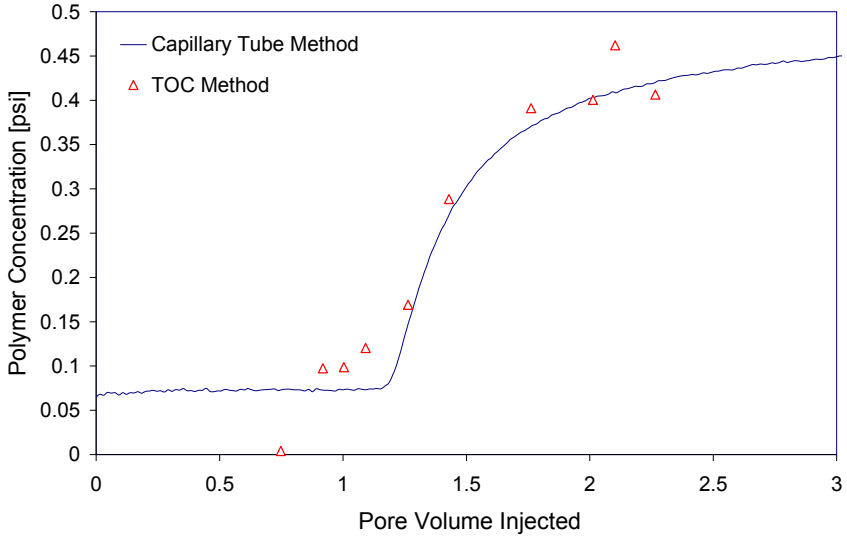

Figure 5.6: Comparison result between TOC and capillary tube methods

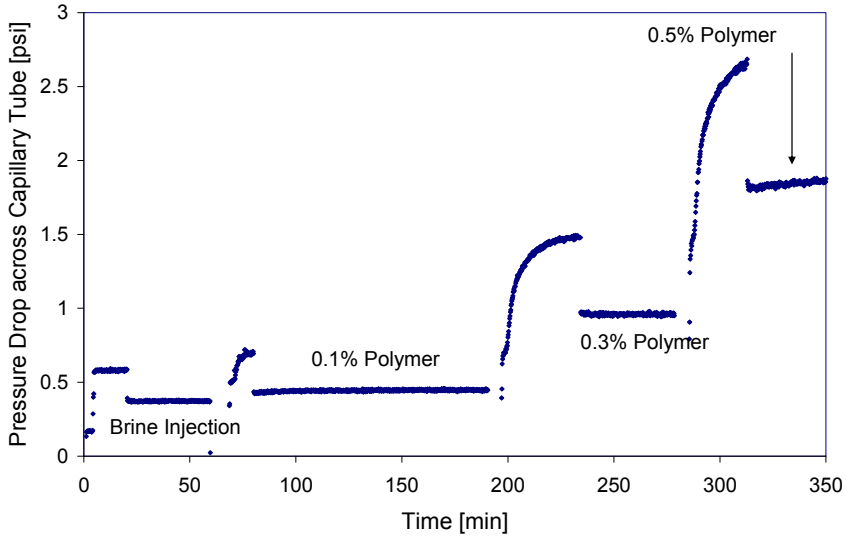

Figure 5.7: Results of capillary tube-tests for a base case, 0.5% Flopaam 3330S (which has 8M molecular weight and 25~30% degree of hydrolysis), prepared in 0.5% sodium chloride brine with pH = 2.5 at 1 ml/min

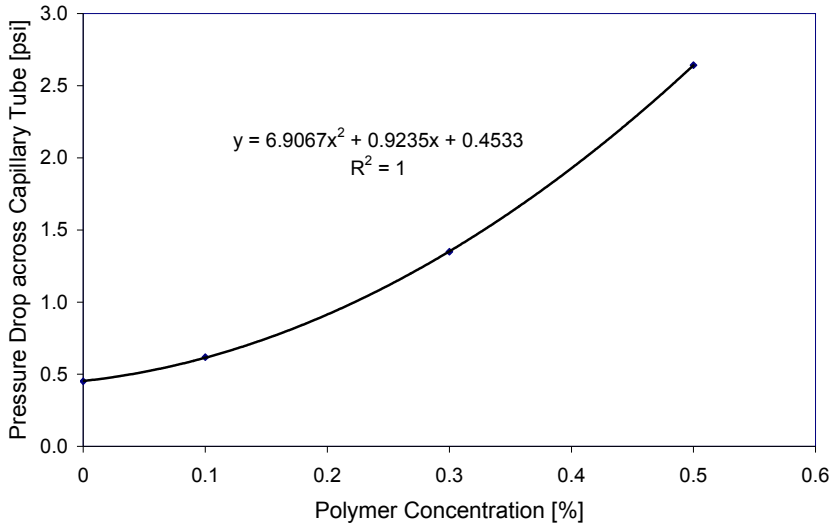

Figure 5.8: Calibration curve for capillary tube-test for a base case

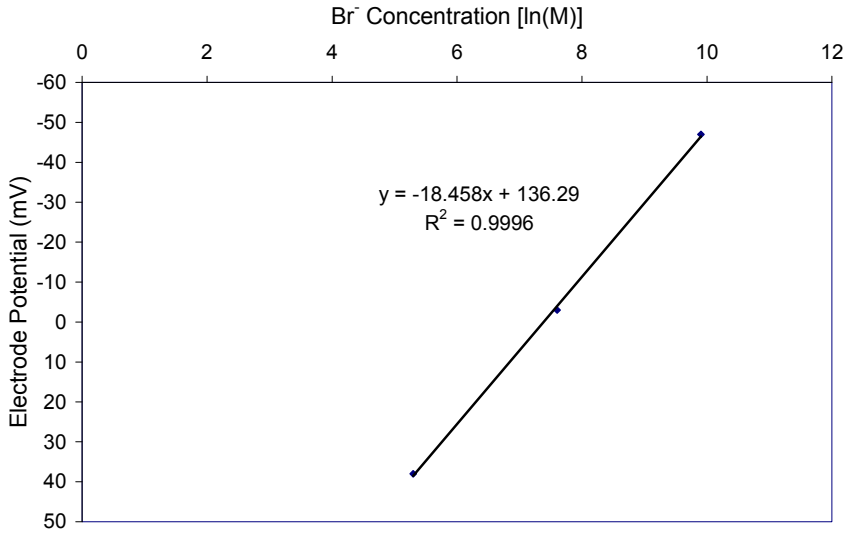

Figure 5.9: Calibration curve for bromide tracer test for a base case

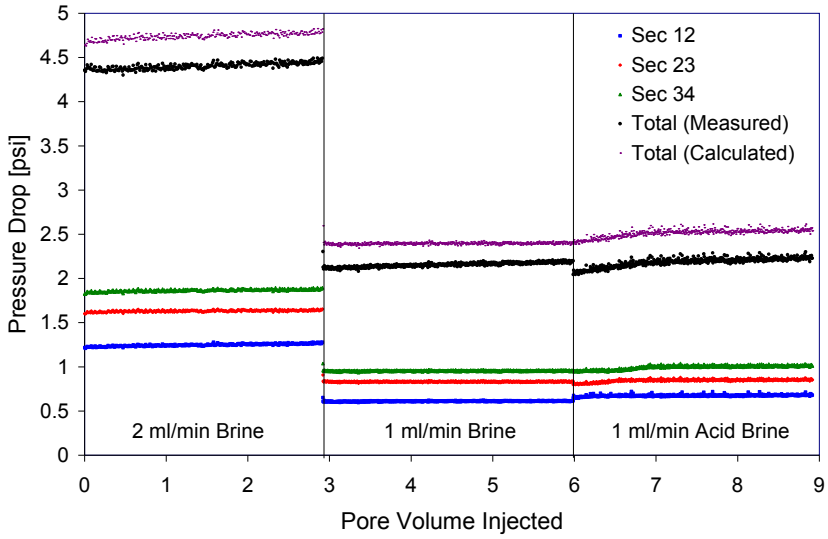

Figure 5.10: Pressure drop responses across the core as a function of pore volume injected (PVI) during brine and acid injection for a base case

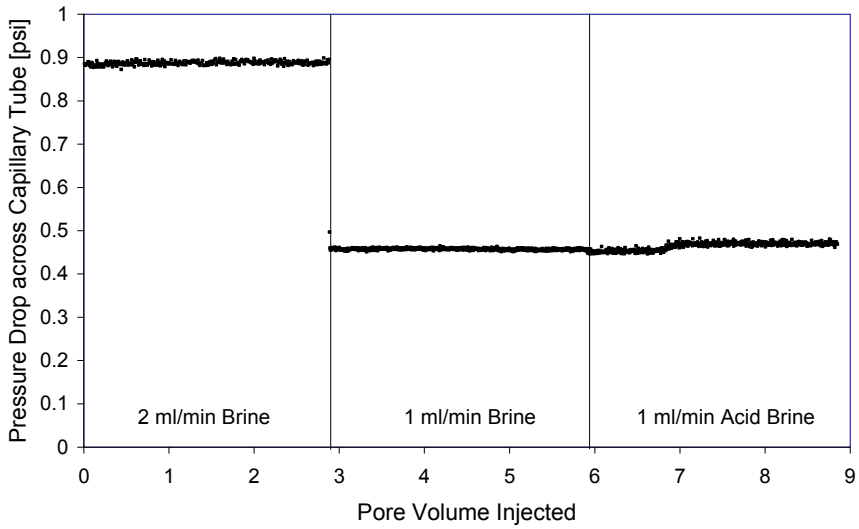

Figure 5.11: Pressure drop responses across the capillary tube as a function of pore volume injected (PVI) during brine and acid injection for a base case

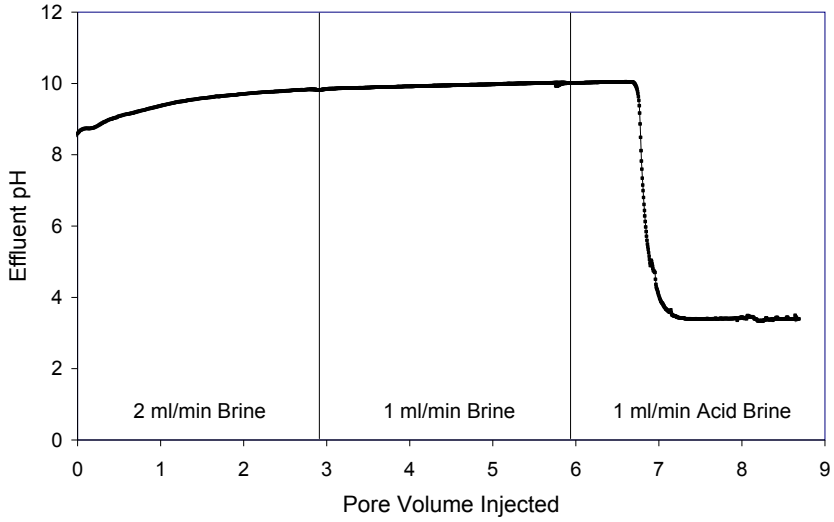

Figure 5.12: Effluent pH history as a function of pore volume injected (PVI) during brine and acid injection for a base case

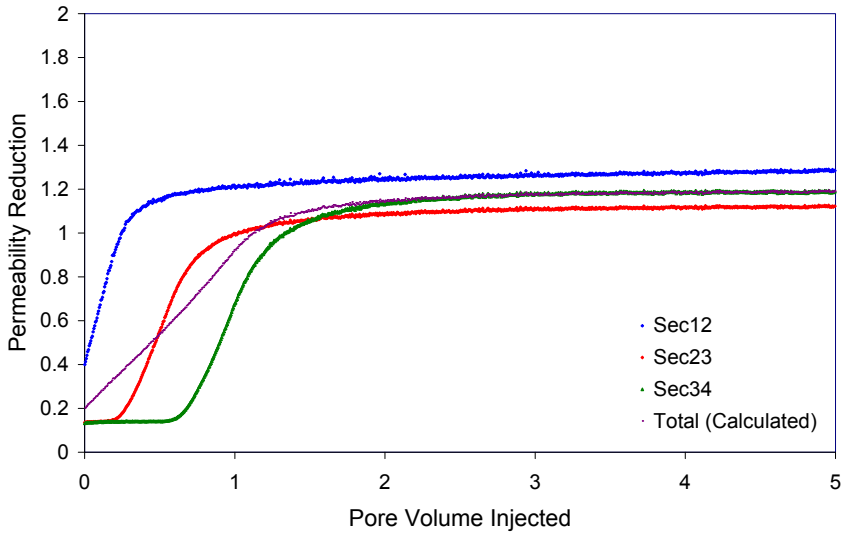

Figure 5.13: Permeability reduction as a function of pore volume injected (PVI) during polymer flooding for a base case

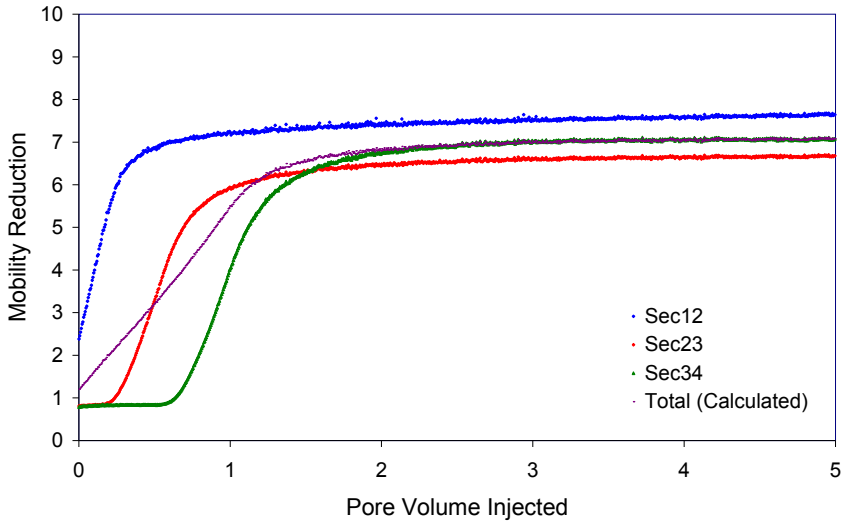

Figure 5.14: Mobility reduction as a function of pore volume injected (PVI) during polymer flooding for a base case

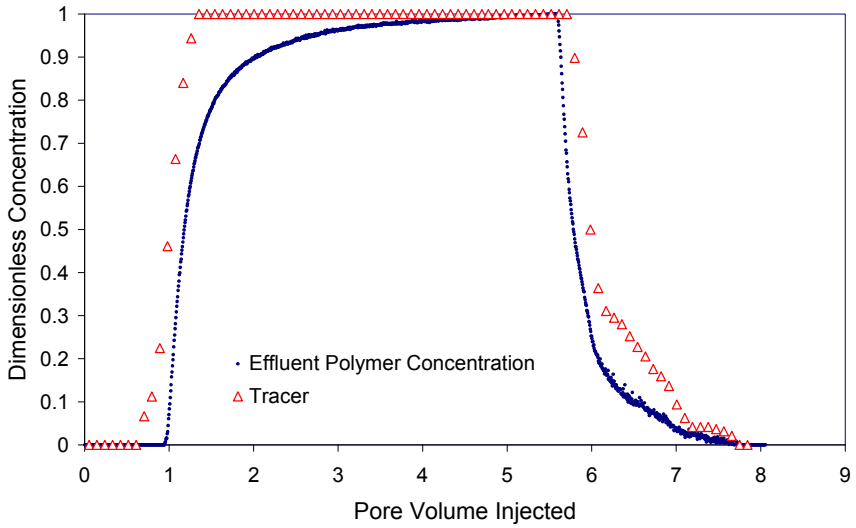

Figure 5.15: Normalized concentration of polymer and bromide tracer as a function of pore volume injected (PVI) during polymer flooding for a base case

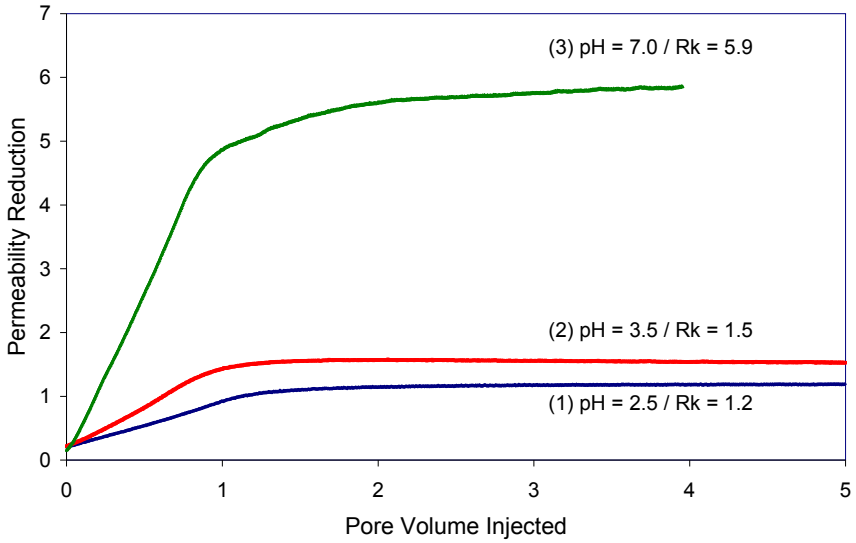

Figure 5.16(a): Permeability reductions as a function of PVI for the injection polymer solutions with different pH conditions

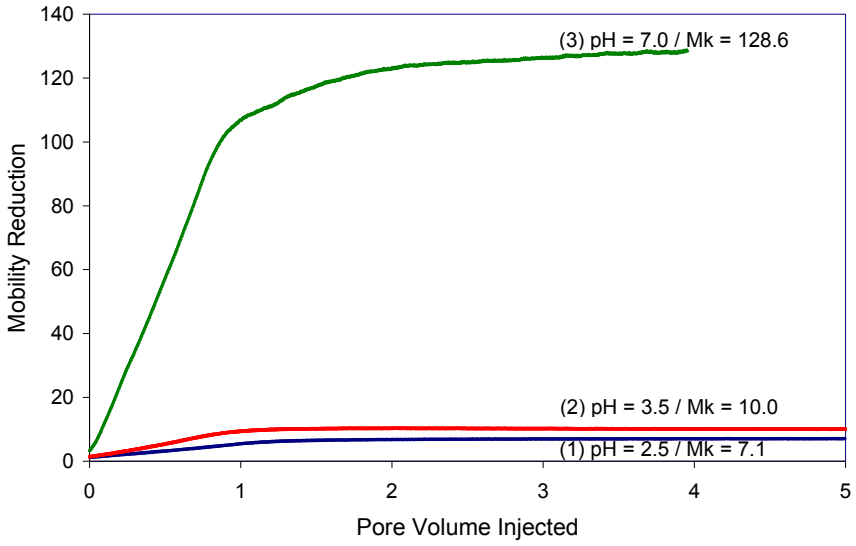

Figure 5.16(b): Mobility reductions as a function of PVI for the injection polymer solutions with different pH conditions

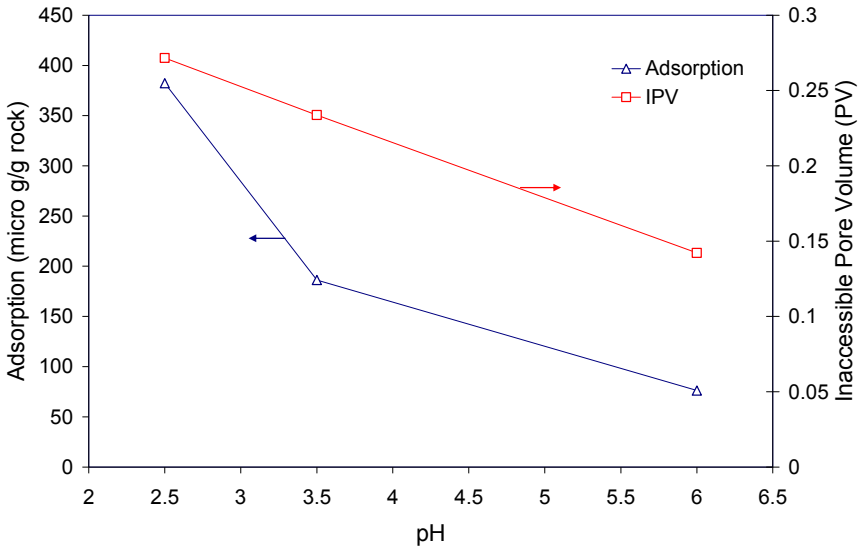

Figure 5.16(c):Adsorption and inaccessible pore volume as a function of PVI for the injection polymer solutions with different pH conditions

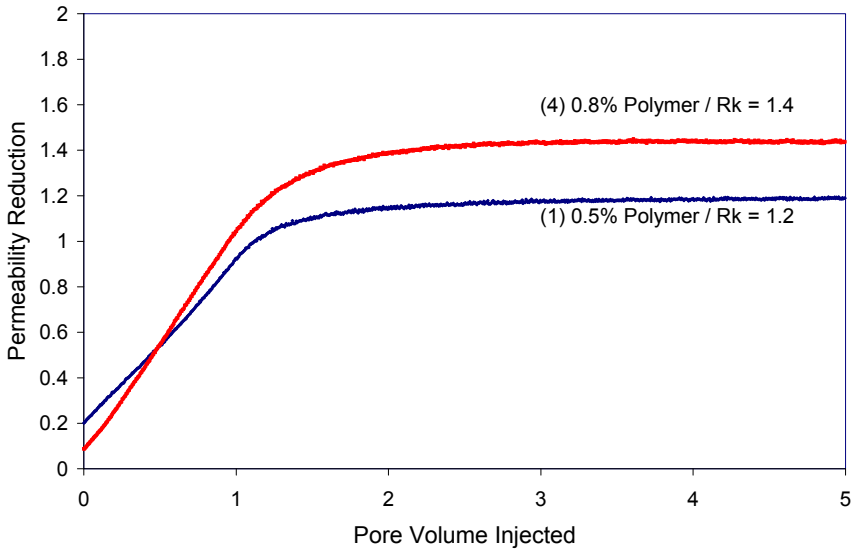

Figure 5.17(a):Permeability reductions as a function of PVI for the injection polymer solutions with different polymer concentrations

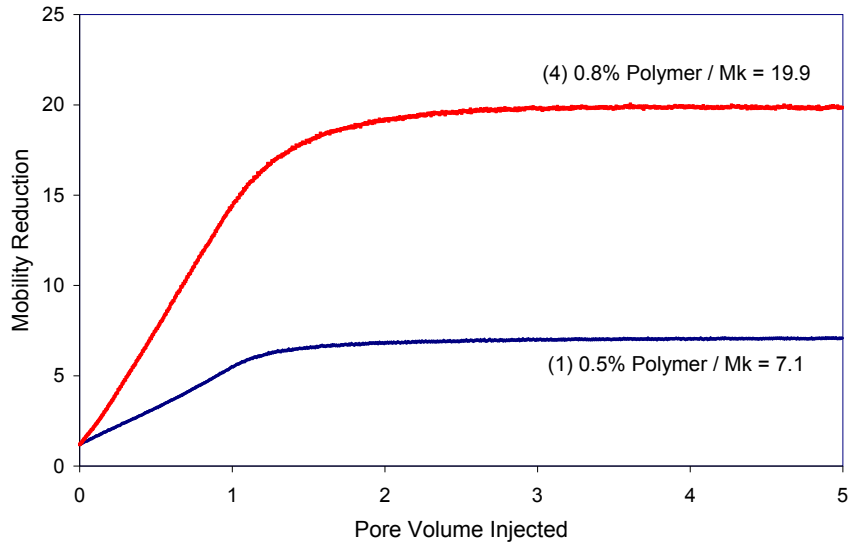

Figure 5.17(b): Mobility reductions as a function of PVI for the injection polymer solutions with different polymer concentrations

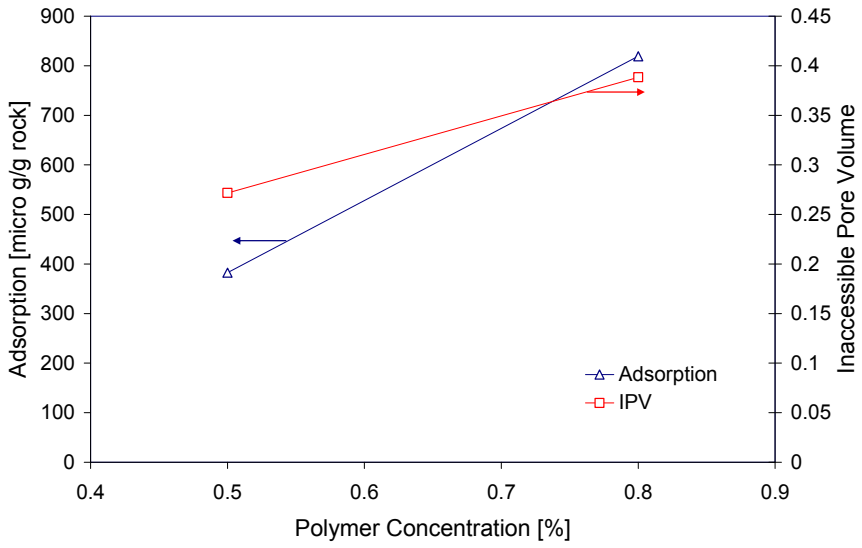

Figure 5.17(c):Adsorption and inaccessible pore volume as a function of PVI for the injection polymer solutions with different polymer concentrations

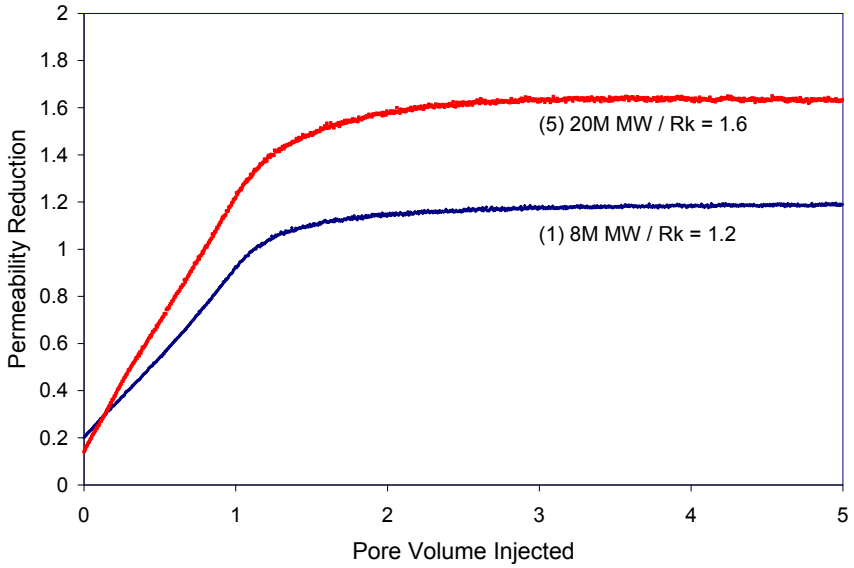

Figure 5.18(a):Permeability reductions as a function of PVI for the injection polymer solutions with different molecular weights

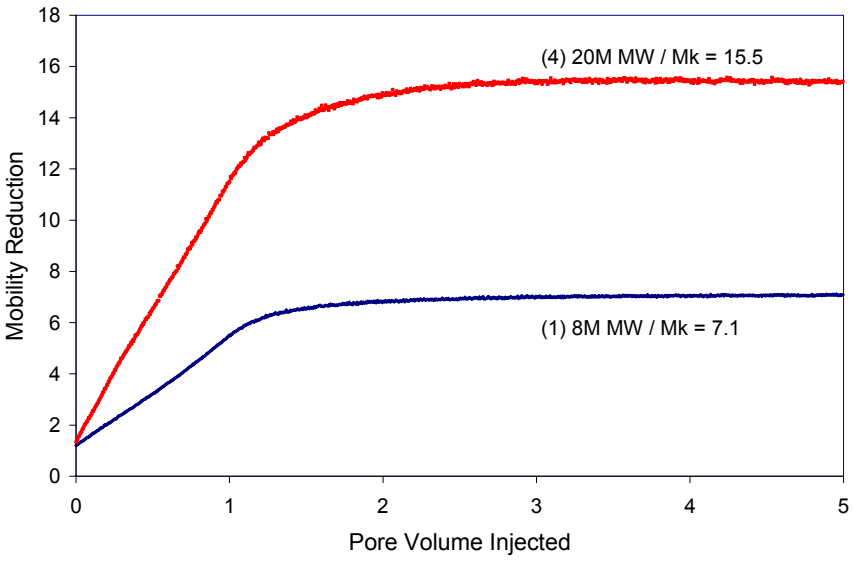

Figure 5.18(b): Mobility reductions as a function of PVI for the injection polymer solutions with different molecular weights

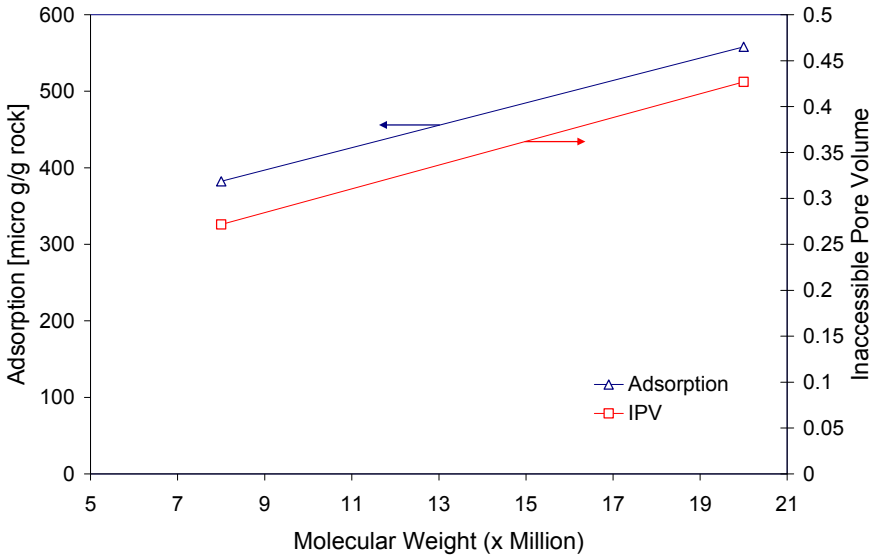

Figure 5.18(c):Adsorption and inaccessible pore volume as a function of PVI for the injection polymer solutions with different molecular weights

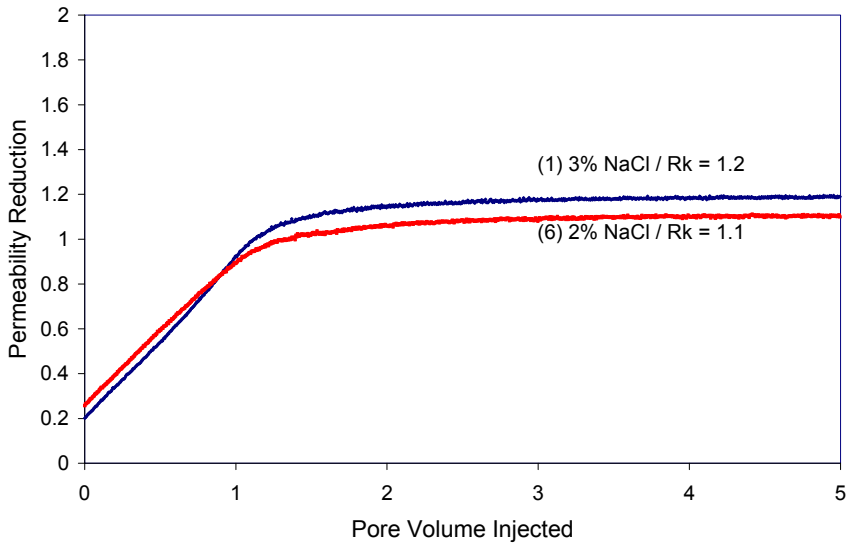

Figure 5.19(a):Permeability reductions as a function of PVI for the injection polymer solutions with different salinities

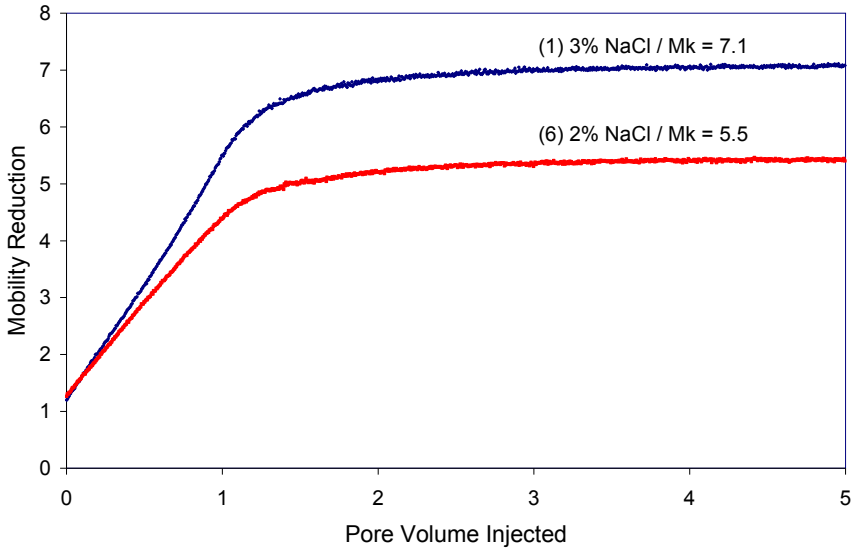

Figure 5.19(b): Mobility reductions as a function of PVI for the injection polymer solutions with different salinities

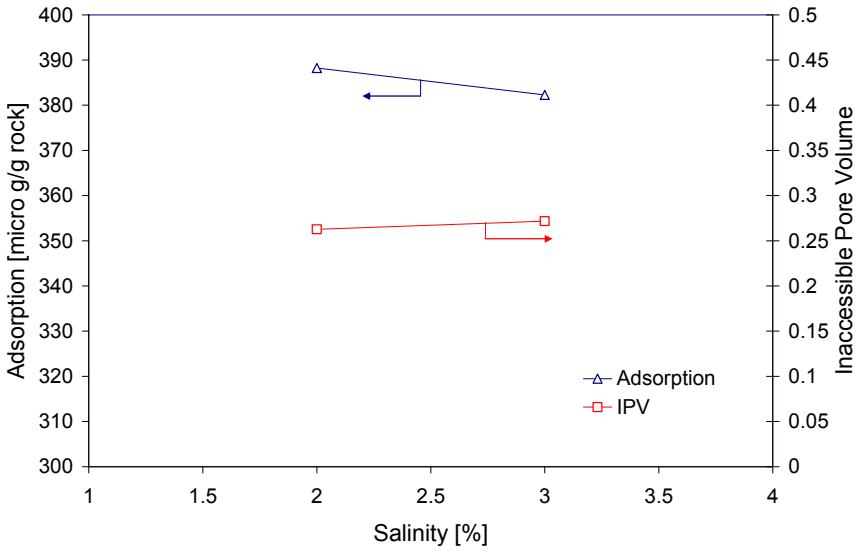

Figure 5.19(c):Adsorption and inaccessible pore volume as a function of PVI for the injection polymer solutions with different salinities

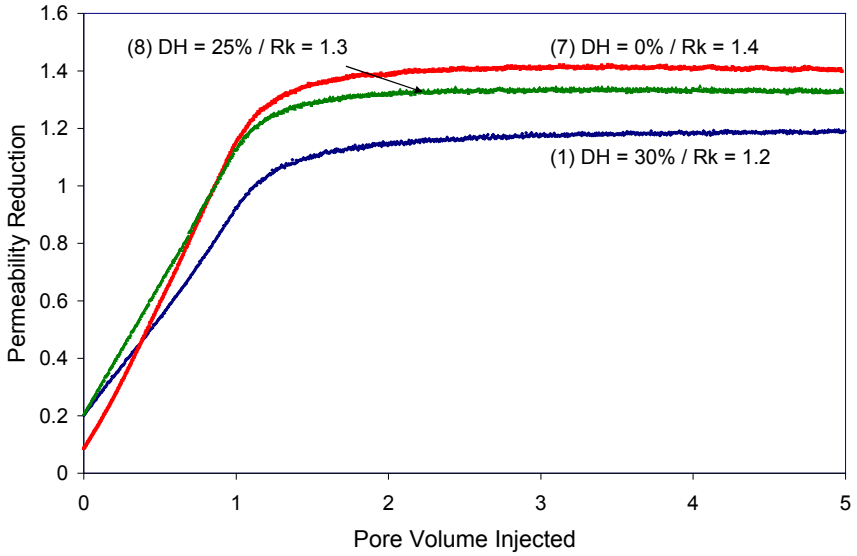

Figure 5.20(a):Permeability reductions as a function of PVI for the injection polymer solutions with different degrees of hydrolysis

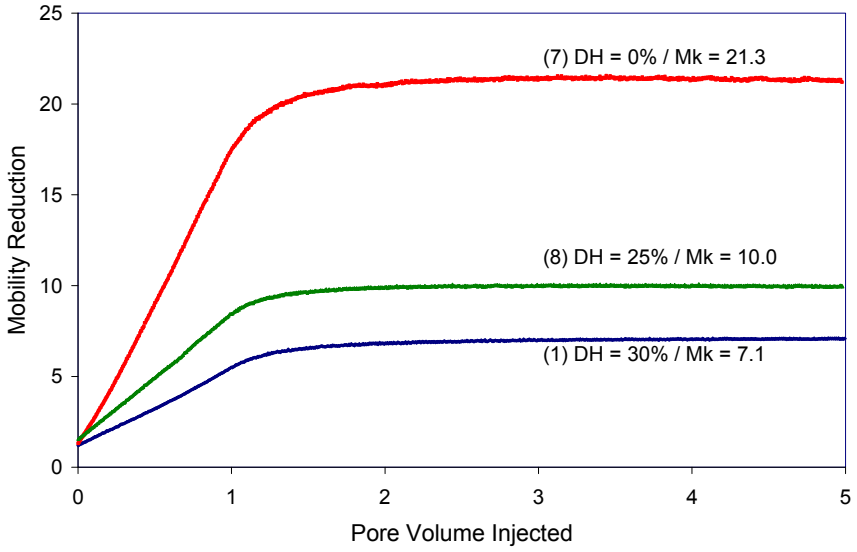

Figure 5.20(b): Mobility reductions as a function of PVI for the injection polymer solutions with different degrees of hydrolysis

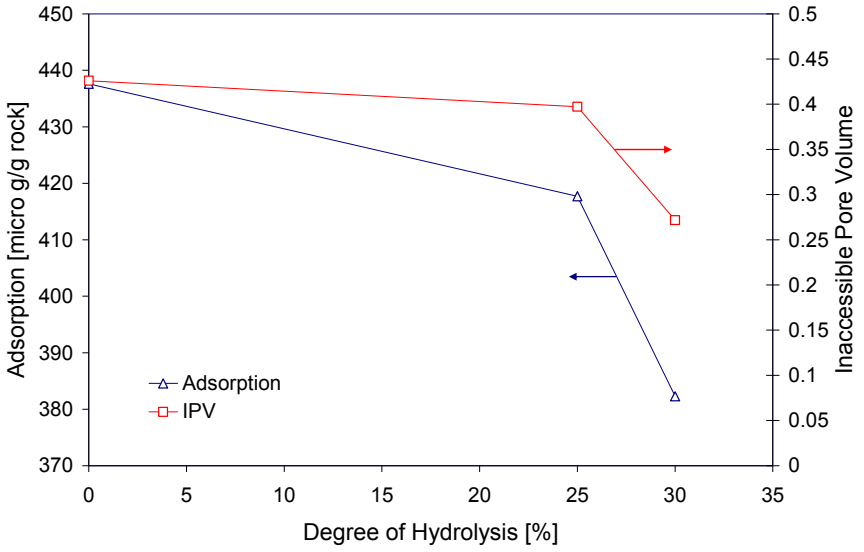

Figure 5.20(c):Adsorption and inaccessible pore volume as a function of PVI for the injection polymer solutions with different degrees of hydrolysis

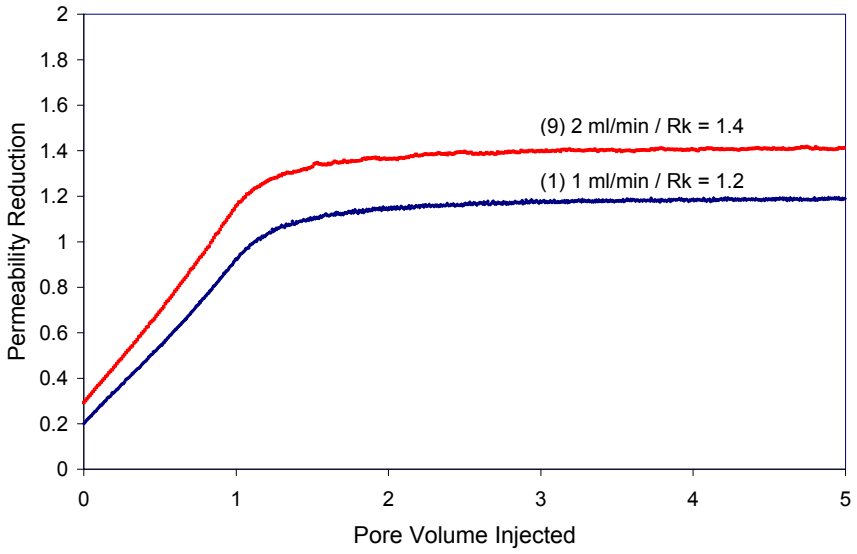

Figure 5.21(a):Permeability reductions as a function of PVI for the injection polymer solutions with different flow rates

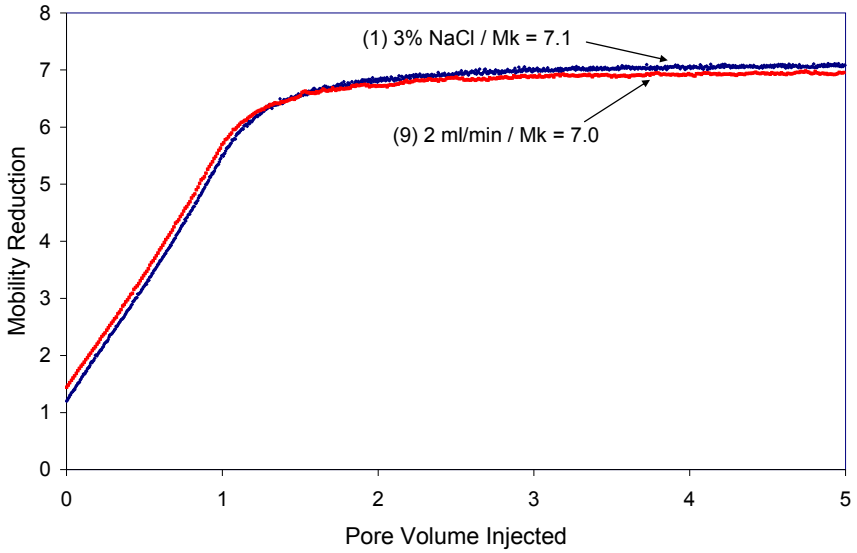

Figure 5.21 (b): Mobility reductions as a function of PVI for the injection polymer solutions with different flow rates

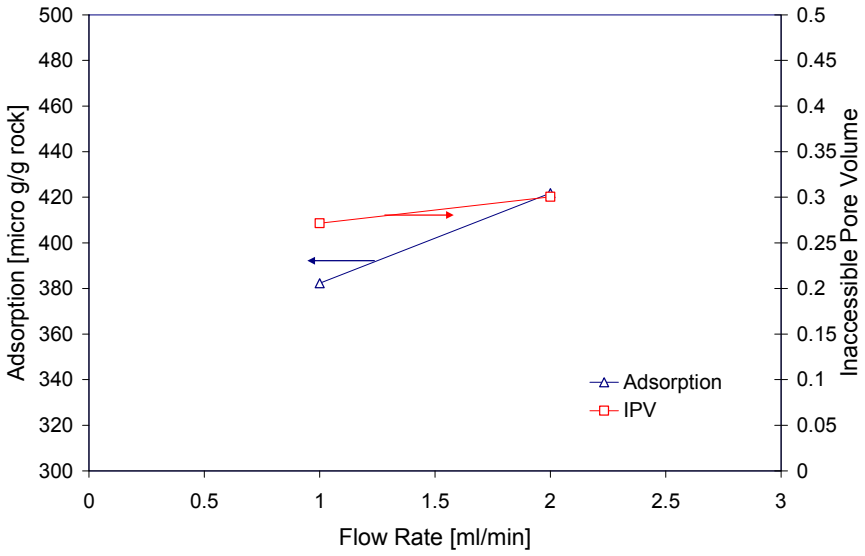

Figure 5.21(c):Adsorption and inaccessible pore volume as a function of PVI for the injection polymer solutions with different flow rates

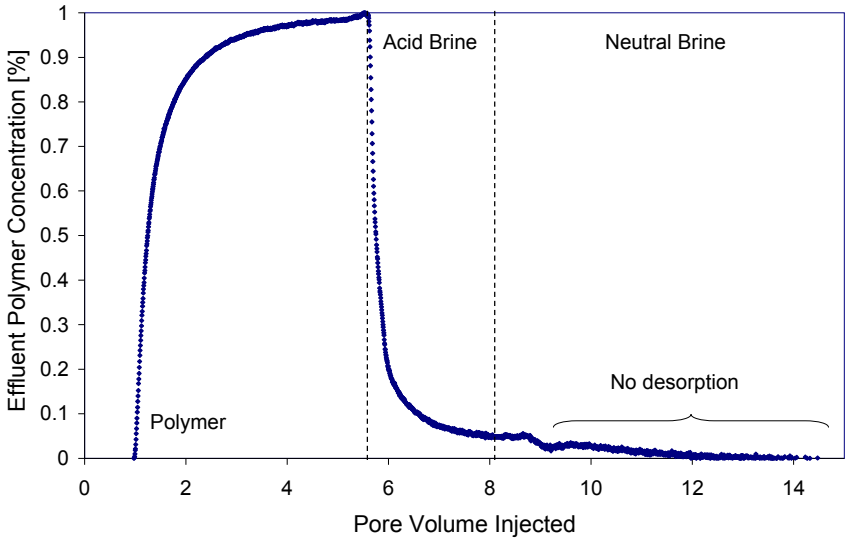

Figure 5.22: Desorption test for Test no. 6 (0.5% Flopaam 3330S (which has 8M molecular weight and 25~30% degree of hydrolysis), prepared in 2.0% sodium chloride brine with pH = 2.5 at 1 ml/min

6. Development and Use of a Simulation Model for Mobility/Conformance Control Using a pH-Sensitive Polymer

6.1 INTRODUCTION

Poor volumetric sweep or poor conformance, due to reservoir heterogeneity, reduces oil recovery and increases operating costs of mature waterfloods. Mobility improvement methods such as polymer flooding, and conformance control methods such as workovers and polymer gel treatments, aim to improve oil recovery by diverting injected fluid from high-permeability zones to low-permeability, unswept areas of a reservoir. Injection of a pH-sensitive polymer as a deep-penetrating mobility control or conformance control method has been developed earlier in our laboratory (Huh *et al*. 2005; Choi *et al*. 2006). A solution of pH-sensitive polymers such as polyacrylic acid hydrogel can exhibit an orders-of-magnitude viscosity increase when its pH increases from acidic condition to above a threshold value. Such polymers are commercially available at low cost in large quantities and are environmentally benign. A major strength of the proposed method is that the pH increase needed to induce the drastic viscosity increase *in situ* can occur naturally by geochemical reactions between acidic polymer solution and the reservoir rock. For the method to be effective, therefore, the ability to model the behavior of pH-sensitive polymer *in situ* in the reservoir environment is essential. Such a capability has been developed in a general-purpose reservoir simulator and is described in this paper.

As discussed in detail earlier (Choi *et al*. 2006), the controlled application of the proposed method requires a good understanding of its three sub-processes:

(1) dependence of polymer viscosity on ionic (pH) conditions in the reservoir;

(2) geochemical characterization of pH change in the rock; and

(3) polymer microgel transport in porous media.

The first of the above has been addressed in detail by Huh *et al*. (2005) and the second and the third by Choi *et al*. (2006). In the latter, history matching was used to estimate the mineral composition and reaction kinetics between hydrochloric acid and Berea sandstone. Estimation of geochemical reactions is critical to modeling the behavior of pH-sensitive polymer since these reactions alter both the pH and ionic

concentration of the polymer solution. The geochemical characterization method employed in Choi *et al*. (2006) is significantly improved in the current effort. The use of the dimensionless Damköhler number (see Section 6.9) was found useful for comparing pH-sensitive polymer flood simulations since it combines the effects of geochemistry, acid concentration, convection rate and geometry into one value.

In the next Section, the new simulation capability to model the deep-penetrating mobility control or conformance control using pH-sensitive polymer is briefly described. History matching of coreflood acid injection experiments to estimate geochemical reactions and reaction rates occurring in Berea cores is then described. Preliminary scale-up simulations employing linear and radial geometry floods in 2-layer reservoir models are given, followed by Conclusions.

6.2 SIMULATION MODEL DESCRIPTION

The key feature of the new simulation capability is the implementation of the pH-sensitive polymer rheological model, developed by Huh, Choi and Sharma (2005), into a 3-D compositional reservoir simulator capable of modeling geochemical reactions (GEM-GHG). The enhanced simulator allows prediction of polymer behavior *in situ*. The rheological model predicts the apparent viscosity of polymer as a function of pH, shear rate, polymer concentration and ionic strength. It is used to calculate water phase viscosity in each grid cell every timestep. The keywords used to enter the rheological model constants are available elsewhere (Benson, 2007). Grid block properties used to calculate aqueous phase viscosity include pH, ion and polymer concentrations, fluid velocity, water saturation, permeability and water phase relative permeability. **Figure 6.1** demonstrates the large effect of pH on polymer viscosity for a 3 wt% EZ-2 polymer solution (ionic strength = 0.5, no flow; Huh *et al*. 2005).

The ability of the simulator to model geochemical reactions occurring between reservoir minerals and the ions in the aqueous phase, coupled with the rheological model, allows the modeling of the desired mobility and conformance control effects. The simulator models reservoir mineral reactions as rate-limited heterogenous reactions. Section 6.8 describes the reaction rate calculation. Mineral reactions cause minerals to dissolve or precipitate in a reservoir and change ion concentrations in reservoir brine. The simulator models intra-aqueous reactions within the water phase as instantaneous

reactions, i.e., reactions that attain chemical equilibrium immediately. Geochemical reactions control the ionic strength and pH of the reservoir brine which are key inputs to the pH-sensitive polymer rheological model.

6.3 CORE FLOOD HISTORY MACTHING

Proper selection of mineral components, chemical reactions among them, mineral reaction rate models and their parameter values, is necessary to model the behavior of pH-sensitive polymer *in situ*. History matching of the effluent composition of laboratory acid corefloods was used to select geochemical modeling parameters. Three corefloods performed by Choi (2005) were used for history matching the reaction rate of hydrochloric acid with Berea sandstone.

Ermel (2005) performed history matches of the same corefloods using the KGEOFLOW simulator (Sevougian *et al.* 1995) and concluded that a 2-mineral model could adequately represent the matrix reactions. The present work focused on a 4-mineral Berea model composed of quartz, calcite, kaolinite, and potassium feldspar minerals. History matching simulations were also performed with a one-mineral model, which demonstrated some advantages over the four-mineral model.

The corefloods were performed on 9" long, 1" diameter cores of Berea sandstone at 24ºC at atmospheric pressure. The core porosities for Experiments 1, 2, and 3 were 0.20, 0.177, and 0.1825, respectively. All three corefloods began with injection of 3 wt% NaCl brine (pH = 7). Hydrochloric acid (pH = 1) was then injected into the cores until the effluent pH approached 1. Fluid injection rates were varied for Experiments 1 and 3. The experiments included shut-in periods ranging from a few minutes to several days. **Figures 6.2**, **6.3**, and **6.4** show the effluent pH and fluid injection rates versus pore volumes of fluid injected, for Experiments 1, 2 and 3, respectively. Effluent concentrations of silicon, aluminum, calcium and potassium were measured for Experiment 2 and are shown elsewhere (Choi, 2005).

As the preliminary step for history matching, initial simulation efforts focused on identifying the key minerals for the simulation model. Berea compositions cited in literature include a large portion of quartz, and lesser amounts of clays, carbonates and feldspars (Ermel, 2005). 1-D domains with 50 gridblocks were employed for simulation, in which various combinations of quartz, calcite, illite, kaolinite, potassium feldspar, and

anorthite are assumed to participate for geochemical reactions. The simulations were run with pH = 1 hydrochloric acid injected, and the maximum pH attained when the acid was fully reacted with the rock was recorded. The experiments showed effluent pH greater than 5, and this preliminary step determined which minerals would allow the pH to exceed 5. All geochemical models tested initially contained mineral reaction and equilibrium constants (at 25ºC) from Stumm and Morgan (1996). High mineral reaction rates were chosen for the simulations to ensure that the acid fully reacted with all the reservoir minerals before exiting the core. Models containing only clay, potassium feldspar, or quartz did not allow the pH to rise above 5. Models containing one clay mineral (illite or kaolinite), potassium feldspar and quartz allowed the acid to form brine with a pH in excess of 5. Models containing calcite allowed the formation of a brine with pH~5.4, or higher if a clay, quartz and potassium feldspar were present.

A Berea mineralogy consisting of kaolinite, calcite, quartz and potassium feldspar was chosen for more detailed history matching of the effluent concentration histories of Experiment 2. The objective here was to determine mineral reaction rate constants and mineral reactive grain fractions (see Section 6.8). Initial estimates of kaolinite, calcite, quartz and potassium feldspar grain fractions were 6%, 3%, 88% and 3%, respectively. The mineral reactions, intra-aqueous reactions, and equilibrium constants shown in **Tables 6.1** and **6.2** were used for these history match runs. Published reaction-rate constants (10^{-13}, $10^{-8.8}$, $10^{-13.9}$, 10^{-12} $mol \cdot m^{-2}s^{-1}$, respectively) compiled by Xu *et al.* (2001) were used for the initial history match runs. The mineral reaction rates were entered as constant values, k_β (see Section 6.8). The published rate constants were too small to allow the pH = 1 acid to produce pH ~5.4 effluent in Experiment 2. The acid injection rate of 2 cm^3/min gave an acid residence time of about 9.7 minutes in the second coreflood experiment. The mineral reaction rates for the four minerals were therefore changed to $10^{-7.2}$, $10^{-4.07}$, $10^{-6.22}$, and $10^{-5.98}$ $mol \cdot m^{-2}s^{-1}$, respectively. These are referred to as the "initial-match parameters" in **Table 6.3**. The mineral concentrations were changed to those given in **Table 6.4** to give a reasonable initial match for the effluent pH and ion concentrations for the second coreflood.

The mineral reaction rates from the initial history match of Experiment 2 were then used in simulations of Experiments 1 and 3. The effluent pH predicted from the "initial match" reaction rate constants did not match observed effluent pH data. It was

necessary to increase the calcite reaction rate by a factor of 5 to prevent the simulated effluent pH from dropping during the high acid injection rates in Experiment 3. The quartz, kaolinite and potassium feldspar reaction rates were decreased by a factor of 2 to match the number of pore volumes of pH=1 acid that had to be injected before the effluent pH from the coreflood dropped from about 5 to about 1.5. The resulting "final-match" reaction parameters and core mineralogy are given in **Table 6.3** and **6.4**, respectively. **Figures 6.2**, **6.3** and **6.4** show, respectively, the simulation matches of Experiments 1, 2 and 3. The simulations agree reasonably well with the laboratory effluent data.

6.3.1 Simulated Mineral Interaction Effects

Mineral interactions in the 4-mineral simulation model created pH = 3 plateaus in the effluent in some runs. The reaction affinity term for each mineral's reaction (see Section 6.8) was plotted versus pore volumes injected to understand mineral behavior in the final simulation of core flood Experiment 2. The reaction affinity is calculated as $\left[1-\left(Q_\beta / K_{eq,\beta}\right)\right]$ for each mineral based on the ion activity product, Q_β, for each mineral reaction in each cell in the 1-D coreflood simulation. Positive reaction affinity values indicate mineral dissolution and negative ones indicate precipitation. **Figure 6.5** shows the dimensionless mineral concentration (fraction of initial concentration), reaction affinity, and selected ion concentrations for the final match simulation after 50 pore volumes of fluid were injected. Coreflood 2 involved injection of 11 pore volumes of pH = 7, 3 wt% brine before injection of pH = 1 hydrochloric acid began.

Figure 6.5 provides valuable insight on the mineral interactions as the acid flows in the core:

- Calcite is dissolving at high rates between the core inlet and a point 3.5 inches from the inlet. Calcite reaction affinity is +1 from the inlet to a point 3 inches in the core, and decreases to a slightly positive value at 3.5 inches. All mineral reaction rates are dependent on the mineral concentration through the surface area value in equation (6.1). Arrival of the calcite dissolution front causes the effluent pH to decrease from ~5.4 in all the models performed in this study.

- Kaolinite reaction behavior is conjectured to be controlled by the calcite reaction through the H^+ concentration. Kaolinite dissolves from the inlet until a point 3 inches into the core. The large decrease in H^+ concentration 3 inches from the core inlet appears to cause strong kaolinite precipitation until a point 6.7 inches from the acid inlet.
- Quartz behavior opposes that of kaolinite. Quartz precipitates where kaolinite is dissolving from the core inlet until a point 3 inches from the inlet. Quartz is strongly dissolving from 3 to 6.7 inches in the core where kaolinite is precipitating. The quartz and kaolinite reactions are strongly coupled by the silica ($H_4SiO_{4(aq)}$) concentration in the model.
- Potassium feldspar (k-feld) dissolves continuously along the core despite changes in H^+ and silica concentrations.

6.3.2 Sensitivity to One-Mineral Model with First-Order Mineral Reaction Rate

The 4-mineral final match coreflood simulation models were altered to create 1-mineral models with a first-order mineral reaction rate. Calcite was chosen as the mineral because it demonstrated a spent-acid effluent pH close to that observed experimentally. The other minerals in the original simulations were removed. Near perfect agreement between the simulated and experimental coreflood effluent pH resulted when a mineral reaction rate first-order in hydrogen concentration was used. The new reaction rate was modeled by setting k_β near zero in the reaction equation (Equation (6.1)), and setting the exponent for the H^+ activity ω_β to 1, and varying reaction constant $k_{i,\beta}$ for the hydrogen activity along with calcite concentration until a match was achieved.

Figures 6.6, **6.7**, and **6.8** show effluent pH from the simulations and the experiments. These matches had a calcite volume fraction of 0.051 (compared to 0.047 in 4-mineral model) and $k_{H+,calcite}$ set to $10^{-1.37}$ mol·m^{-2}·s^{-1}. One drawback of this method was that the final effluent pH was 1, not ~1.3, after all the calcite was dissolved. Another is that although the pH matched well, calcite does not contain aluminum, silicon, or potassium that were also measured in the experiments. It is possible that a mineral or pseudo-mineral that can match those effluent readings could be found or generated. However, the main objective here is to predict the propagation of the pH front, because this controls the transition between small and large viscosity. From this perspective, the 1-mineral model has the advantage of being simpler to apply.

6.3.3 Sensitivity to Weak Acid Injection

Simulations testing the ability of weak acids to propagate low-pH conditions farther into a linear reservoir than a strong acid were performed. Cases were run using both the 4-mineral matrix with fixed reaction rates and the 1-mineral matrix with first-order mineral reaction rates. Both mineralogies yielded similar results. Simulations compared the ability of pH=2 solutions of hydrochloric acid, citric acid and acetic acid to maintain a low-pH away from the injector. It was found that the weak acids (citric acid and acetic acid) propagated a low-pH fluid front farther into the reservoir than the strong acid case (hydrochloric acid). This is true only when the injected acid pHs are similar, not when the injected acid concentrations are similar. The simulations showed drawbacks of using weak acids are that large acid concentrations are required to achieve low-pH, and they achieve a lower equilibrium pH when they are spent.

6.4 CONFORMANCE CONTROL USING PH-SENSITIVE POLYMER: LINEAR GEOMETRY MODEL

Conformance control is a method that improves oil recovery and production rates by diverting injected fluid in a flooding operation into lower permeability unswept regions. 2-layer simulations with linear and radial grid geometries were created to test the ability of pH-sensitive polymer to improve conformance. Comparisons were made between waterflooding, conventional polymerflooding, pH-sensitive polymer flooding and polymer slug treatment cases. All polymer and pH-sensitive polymer cases neglected shear-thinning rheology though this feature exists in the rheological model. Effectively the fluids had Newtonian behavior.

The linear and radial models documented here share many similarities. The injection rate was set at 25 m^3/d, though a 15 MPa pressure limit was applied. The reservoir contained a 0.047 volume fraction of calcite, and the reaction rate constant was varied to provide a range of Damkohler numbers (see Section 6.9) in the pH-sensitive polymer flood cases. Initial oil saturation was 0.8, residual oil saturation was 0.3. The hydrocarbon pore volume (HCPV) was 16,000 m^3, pore volume was 20,000 m^3, and moveable oil was 62.5% HCPV. Oil viscosity was 1.09 cp and brine viscosity was 1 cp. All cases had a producer BHP and initial reservoir pressure of 10 MPa.

Figure 6.9 is a schematic of the linear 2-layer model created for sensitivity runs to investigate the effects of various polymer treatments on oil recovery. While the linear geometry is highly simplistic, it may approximately represent injection from a horizontal well or from a vertical fracture. **Table 6.5** gives the reservoir properties. The linear model has 100 cells in horizontal direction with 10:1 grid refinements near the injection well. Linear cases presented here do not allow crossflow between layers but such cases are documented by Benson (2007).

Water and 10-cp, 100-cp, and 1000-cp viscosity polymers (approximately representing the low-shear limit viscosities in the rheological model; Huh *et al*. 2005) were injected into the linear model. **Figure 6.10** shows the volume of oil produced versus volume of fluid injected. Increasing the viscosity of injected fluid improves recovery (and conformance) until viscosity reaches ~ 100 cp. Injection of high viscosity fluids reduces injectivity greatly.

A pH=1 mixture of hydrochloric acid and pH-sensitive polymer (EZ-2, 3 wt% NaCl; Huh *et al*. 2005) was injected into the model at various Damkohler numbers. A polymer concentration of 1.93×10^{-5} mol/kg gave a polymer viscosity of 2.2 cp at pH = 1 and a final viscosity of 1000 cp *in situ* when the acid reached equilibrium with the calcite reservoir at pH=5.39. Damkohler numbers of 0.01, 0.1, 1, 10 and 100 in the high-permeability zone were modeled by changing the fixed reaction constant of calcite to $10^{-10.447}$, $10^{-9.447}$, $10^{-8.447}$, $10^{-7.447}$ and $10^{-6.447}$ mol·m^{-2}s^{-1}, respectively. The flow rate into the high-permeability zone, estimated by prorating q by the layer kh products, was used in these Damkohler numbers. The actual fluid velocity changes in both zones as the pH-sensitive polymer alters flow distribution between the two zones. The reaction rate constants used here are orders of magnitude smaller than the history matched reaction constants found from the Berea coreflood.

Figure 6.10 shows the volume of oil produced for 1000-cp pH-sensitive polymer floods simulated at various Damkohler numbers (N_{Da}). Predictably, the N_{Da} = 0.01 case behaved more like 1 cp water and the N_{Da} = 10 and N_{Da} = 100 cases behaved as if they were 1000-cp fluids. The N_{Da} = 1 case is remarkable since it greatly improved recovery at early times (before 0.2 pore volumes injected) but ultimately caused recovery to suffer. This important result occurred because at early times the pH-sensitive polymer penetrated the high-permeability zone, increased its flow resistance and automatically diverted

polymer into the low-permeability zone which improved early recovery. Unfortunately, the polymer injected into the low-permeability zone experienced a viscosity increase too and then plugged off the low-permeability zone almost completely. This result occurs when the ratio of the pH-sensitive polymer viscosity at final and initial conditions is greater (say 10 times or more) than the permeability contrast between the two zones.

Polymer slug injection simulations were performed to build on the partial success of the N_{Da}=1 case. The concept is that by injecting a slug of polymer into both zones at low viscosity, the polymer will preferentially penetrate the high-permeability zone. Polymer injection can then be terminated. The polymer will reach maximum viscosity in situ, and water injected afterwards will have an increased preference to invade the low-permeability zone. This is conceptually very similar to conventional gel treatments, except that the viscosity increase is not triggered by environmentally harmful and possibly carcinogenic crosslinkers (Kabir, 2000). In addition other problems such as poor in-situ mixing, chromatographic separation of the cross-linker and possible interference with other metal ions are avoided.

Figure 6.11 shows oil recovery versus volume of fluid injected for some polymer slug treatments. The pH-sensitive polymer treatment was injected at a Damkohler Number of 0.1. Results from slugs of regular polymer are shown although it may prove difficult to inject fluid with viscosities in excess of 10 cp in a real reservoir. All slug volumes were 0.05 HCPV (800m^3) and injected beginning at time zero. Shut-in time was allowed for the pH-sensitive polymer to react, then waterflooding commenced. The improvement in oil recovery dwarfs that observed for continous injection of high viscosity polymer. **Figure 6.12** shows the water phase viscosity immediately after the pH-sensitive polymer slug fully reacted, and the slug position and viscosity after a total of 0.5 pore volumes of fluid were injected. This result does not include the negative effects caused by crossflow and viscous fingering that would occur in a reservoir but qualitatively suggests that slug treatments may improve conformance significantly.

6.5 CONFORMANCE CONTROL USING PH-SENSITIVE POLYMER: RADIAL GEOMETRY MODEL

To test conformance control in a radial geometry (**Figure 6.13**), the linear model described above was converted to a radial model with the injector in the center. The

reservoir and fluid volumes were kept the same. The well radius was 0.1 m, and the drainage radius was 42.4 m. The grid had 61 cells with radial dimensions increasing away from the wellbore. The radial reservoir model has high pressure drops near the injector and is much less sensitive to viscosity changes away from the wellbore. Sorbie and Mackay (2005) discuss the large differences between polymer flood behavior in radial and linear geometry floods.

Water and 10-cp, 100-cp and 1000-cp fluid were injected into the central injector to examine the effect of viscosity on oil recovery. **Figure 6.14** shows oil recovery versus volume of fluid injected. Increasing the viscosity of the injected fluid has a much smaller impact on oil recovery in the radial simulations compared to linear simulations.

Figure 6.15 shows oil recovery versus the volume of fluid injected when a 0.05 HCPV polymer slug was injected to both layers before waterflooding. The 1000-cp pH-sensitive case recovered oil most efficiently in terms of volume of fluid among the slug treatments, and the slug treatments did not improve recovery much compared to the waterflood (1-cp fluid) case. The 100-cp fluid case recovers oil faster than any of the slug cases for the radial simulations without crossflow. The aqueous-phase viscosity distribution in the radial reservoir during the 1000-cp pH-sensitive polymer slug case (not shown here) reveals that the slug reaches high viscosity near the injection well in both layers due to geochemical reactions. However, the slug does not remain stationary in the high-permeability layer but is forced out by waterflooding. According to the viscosity profile after 0.1 PV injected, high-viscosity fluid remains in the low-permeability zone, which explains why slug treatments injected into both layers tend to lower oil recovery.

Figure 6.16 shows oil recovery versus the volume of fluid injected for radial cases with and without vertical crossflow when a 0.05 HCPV polymer slug is injected only into the high-permeability layer before waterflooding. These pH-sensitive polymer treatments significantly improved oil recovery over the cases where polymer was injected into both layers. This suggests the slug treatments can be effective for radial reservoirs when they are applied to the high-permeability thief zones only. The volume of the slug and the final viscosity of the slug will greatly affect the performance of the treatment. Crossflow appears to lower the effectiveness of the high-permeability zone treatments considerably.

6.6 IMPROVED INJECTIVITY USING PH-SENSITIVE POLYMER

A radial simulation was performed to demonstrate improved injectivity of 100-cp pH-sensitive polymer compared to 100-cp fluid. Both cases have a constant injection pressure of 15 MPa, and shear thinning was not incorporated into either model. **Figure 6.17** shows the injected fluid rates versus time. The pH-sensitive polymer injectivity increases with time as the reactive reservoir mineral is consumed near the wellbore. This allows the polymer to penetrate farther away from the well as a low viscosity fluid before its pH reaches it maximum value *in situ*. The wavy flow rate profile for the pH-sensitive polymer case in **Figure 6.17** was observed for many radial simulations but not in any linear simulations.

6.7 CONCLUSION

1. A numerical simulator was successfully used to model the behavior of pH-sensitive polymer in reactive porous media. Preliminary simulations show that pH sensitive polymer slug treatments can improve conformance in 2-layer radial and linear geometry floods.
2. History matching of coreflood experiments allows suitable mineralogy and kinetics to be found for acid-mineral reactions. A 4-mineral model of Berea sandstone matched effluent data well. An approximate 1-mineral model with a first-order in hydrogen reaction rate also matched effluent data reasonably well.
3. pH-sensitive polymer should be positioned in reservoir as a low viscosity fluid before fully reacting with reservoir minerals to form a high viscosity plug. Simulations showed high injection rates and weak acids to be effective in forming such a plug.
4. The use of conventional high-viscosity polymers and pH-sensitive polymer improves vertical conformance in linear reservoirs with and without vertical crossflow. Continuous injection of pH-sensitive polymer in these reservoirs is not recommended since this can plug the low-permeability zones in a reservoir. Simulations suggest that the use of pH-sensitive polymer slug treatments is the preferred way to improve vertical conformance in a linear geometry during waterflooding.

5. Improved injectivity can be achieved using pH-sensitive polymer compared to a conventional polymer. Shear-thinning affects both types of polymer and needs to be considered further.

6.8 APPENDIX 6-A: MINERAL REACTION RATE EQUATION USED IN GEM-GHG SIMULATOR

GEM-GHG uses the following formula to calculate mineral reaction rates for each grid cell:

$$r_\beta = \mathrm{sgn}\left[1-\left(\frac{Q_\beta}{K_{eq,\beta}}\right)\right]\hat{\mathrm{A}}_\beta S_w\left(\mathrm{k}_{o,\beta}+\sum_{i=1}^{n_{aq}} k_{i,\beta}a_i^{\omega,\beta i}\right)\left|1-\left(\frac{Q_\beta}{K_{eq,\beta}}\right)^{\xi_\beta}\right|^{\zeta_\beta} \qquad (6.1)$$

In the above equation:

1) The sign of the reaction affinity term, $\left[1-\left(Q_\beta/K_{eq,\beta}\right)\right]$, determines whether a mineral is dissolving or precipitating.
2) Fixed reaction rate constants ($k_{o,\beta}$), reaction rate dependent on individual ion activity ($k_{i,\beta}$), or combinations thereof can be used. The best history matches were obtained for the hydrochloric acid flood experiments when reaction rates were first-order in hydrogen concentration.
3) The mineral surface area in the reaction equation makes reactions first-order in mineral concentrations in the simulator.
4) Setting the ζ_β exponents to zero removes the ability of the reaction affinity value to control the reaction rate.

6.9 APPENDIX 6-B: CALCULATION OF DAMKÖHLER NUMBER

The Damköhler number, N_{Da}, is a dimensionless number used to compare the acid reaction rate to acid convection rate. This value includes the effects of mineral-acid stoichiometery, kinetics, acid concentration and Darcy velocity.

The Damköhler number is based on hydrogen consumption rate, which is closely related to the mineral reaction rate (r_β) given in equation (6.1). The total hydrogen consumption rate must be used when more than one reactive mineral is present:

$$r_{H^+} = \frac{\nu_{H^+}}{\upsilon_{\min eral}} r_\beta \tag{6.2}$$

The value of N_{Da} depends on the flow layer geometry. For linear or 5-spot geometry the equation is:

$$N_{Da} = \frac{LAr_{H^+}}{\rho_{acid} q \left[H^+\right]} \tag{6.3}$$

where L = length of medium (m), A = area perpendicular to flow (m^2), q = acid flow rate (m^3/s), $[H^+]$ = H^+ molality (mol/kg), r_{H^+} = reaction-rate of H^+ ($mol/m^3 \cdot s$) and ρ_{acid} = density of the aqueous phase (the injected acid), taken to be 1000 kg/m^3 for the purpose of evaluating equation (6.2).

For radial flow layer geometry the equation is:

$$N_{Da} = \frac{\pi \cdot R_e^2 \cdot h \cdot r_{H^+}}{\rho_{acid} q \left[H^+\right]} \tag{6.4}$$

where R_e is the outer radius of the reservoir layer (assuming $R_e >> R_{wellbore}$).

Table 6.1: Mineral Reactions and Equilibrium Constants (at 25°C)

Mineral	Reaction	log K_{eq}
Quartz	$SiO_{2(s)} + 2\ H_2O = H_4SiO_{4(aq)}$	-3.98
Kaolinite	$Al_2Si_2O_5(OH)_{4(s)} + 6\ H^+_{(aq)} = 2\ Al^{3+}_{(aq)} + 2\ H_4SiO_{4(aq)} + H_2O$	7.435
Calcite	$CaCO_{3(s)} = Ca^{2+}_{(aq)} + CO_3^{--}{}_{(aq)}$	-8.42
Potassium feldspar	$KAlSi_3O_{8(s)} + 8\ H_2O = K^+_{(aq)} + Al(OH)_4^-{}_{(aq)} + 3\ H_4SiO_{4(aq)}$	-20.573

Table 6.2: Intra-Aqueous Reactions Equilibrium Constants for Four-Mineral Simulations

Equilibrium Reaction	Log K_{eq} @ 25ºC
$HCO_3^- = H^+ + CO_3^{--}$	-10.329
$Al^{+++} + 4\ H_2O = Al(OH)_4^- + 4\ H^+$	-22.7
$H_2CO_3 = 2\ H^+ + CO_3^{--}$	-16.6
$H_2O = H^+ + OH^-$	-14

Table 6.3: Mineral Reaction Constants (at 25°C) from Literature and History Matching

Mineral Reaction	Rate constant k_β, moles $m^{-2}\ s^{-1}$		
	U.S.G.S. (Palandri and Kharaka, 2004)	Initial-match	Final-match
Quartz	$10^{-13.4}$	$10^{-6.22}$	$10^{-6.52}$
Kaolinite	$10^{-13.2}$	$10^{-7.2}$	$10^{-7.5}$
Calcite	$10^{-0.3}[H^+] + 10^{-5.81}$	$10^{-4.07}$	$10^{-3.37}$
Potassium feldspar	$10^{-12.4}$	$10^{-5.98}$	$10^{-6.28}$

Table 6.4: Mineral Concentrations, Reactive Surface Areas and Activation Energies

Mineral	Grain Fraction	Volume Fraction	Specific Reactive Area (m^2/[m^3 of Bulk Volume])	Activation Energy (J/mol)
Quartz	0.846	0.696	6960	87500
Kaolinite	0.061	0.05	50000	62760
Calcite	0.057	0.047	470	41870
Potassium feldspar	0.036	0.03	300	67830

Table 6.5: Properties of Two-Layer Linear Model

Property	Layer 1 (top)	Layer 2 (bottom)
Porosity	0.177	0.177
Height	18 m	2 m
Length	100 m	100 m
Width	56.497 m	56.497 m
X & Y-direction k	100 md	10000 md
Z-direction k	0 md or 10 md	0 md or 1000 md
k_{rw}	$0.3[(S_w-0.2)/(1-0.2-0.3)]^2$	
k_{ro}	$0.7[(1-S_w-0.3)/(1-0.2-0.3)]^2$	

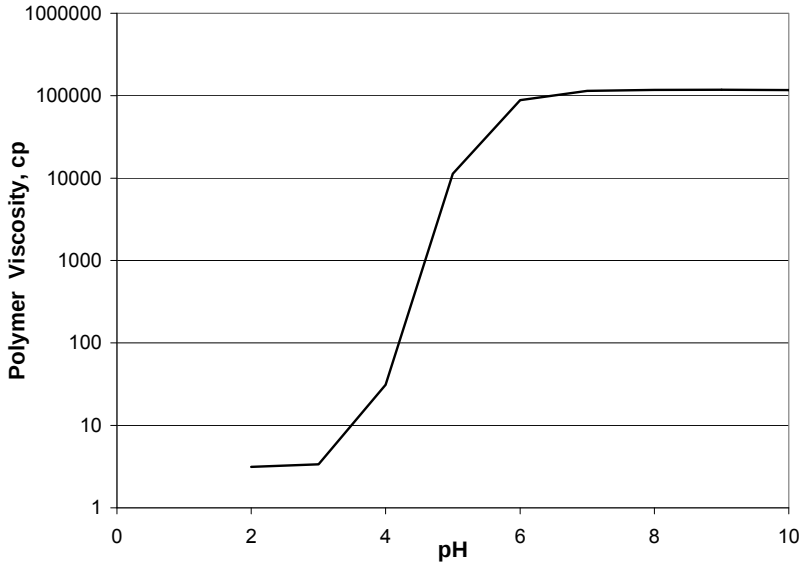

Figure 6.1: Calculated Polymer Viscosity for 3wt% EZ-2 Polymer Solution (Ionic Strength = 0.5, No Flow)

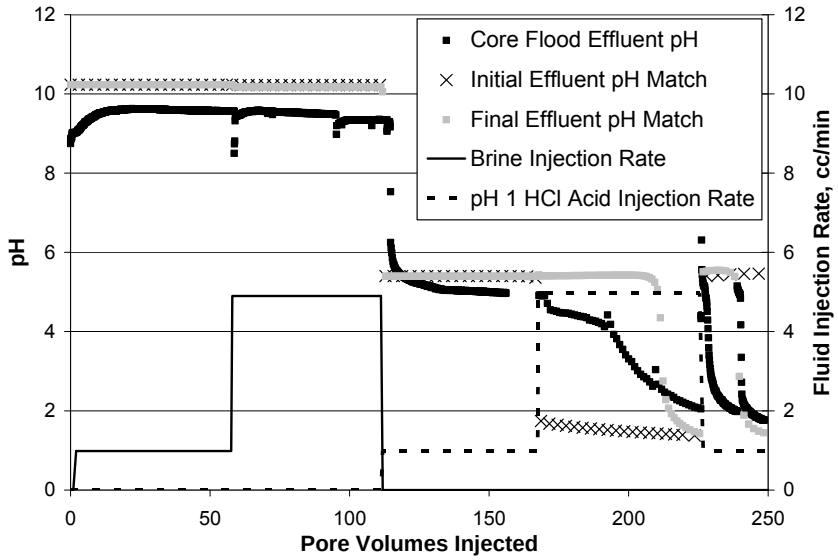

Figure 6.2: pH versus Volume of Acid Injected for Coreflood Experiment 1

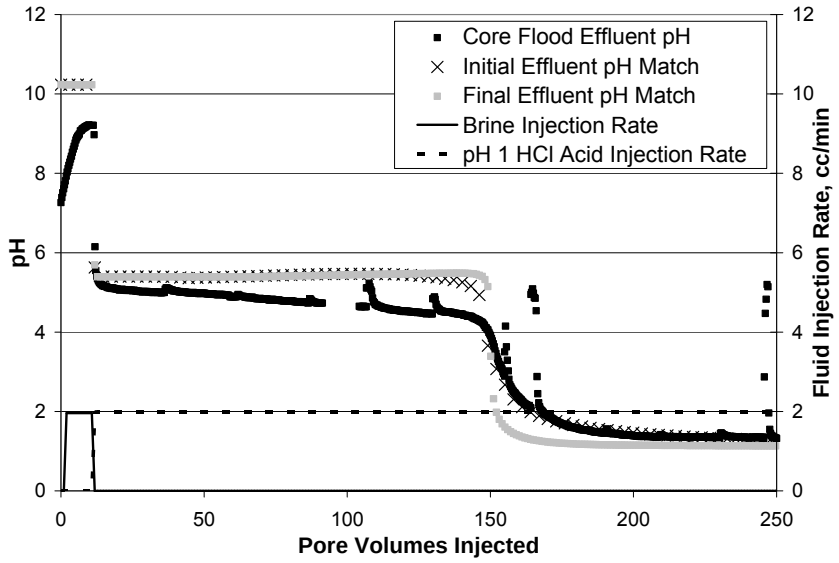

Figure 6.3: pH versus Volume of Acid Injected for Coreflood Experiment 2

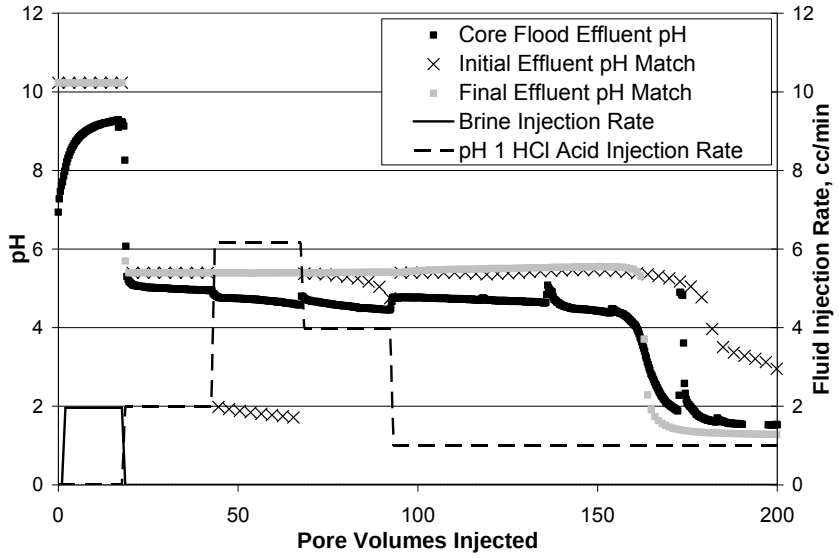

Figure 6.4: pH versus Volume of Acid Injected for Coreflood Experiment 3

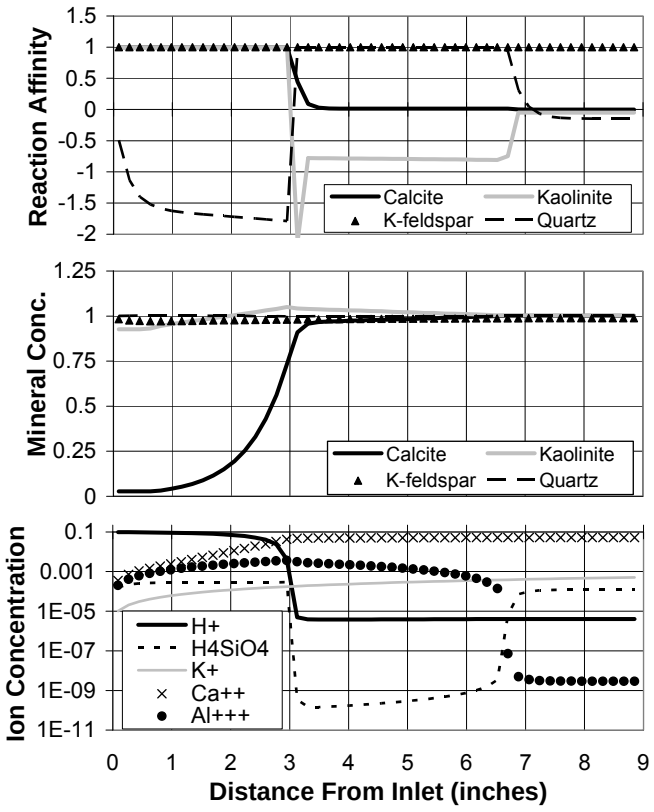

Figure 6.5: Reaction Affinity (for Mineral Reactions), Mineral Concentrations and Select Ion Concentration Profiles for Experiment 2 After 50 Pore Volumes Injected (Using Final-Match Reaction Parameters)

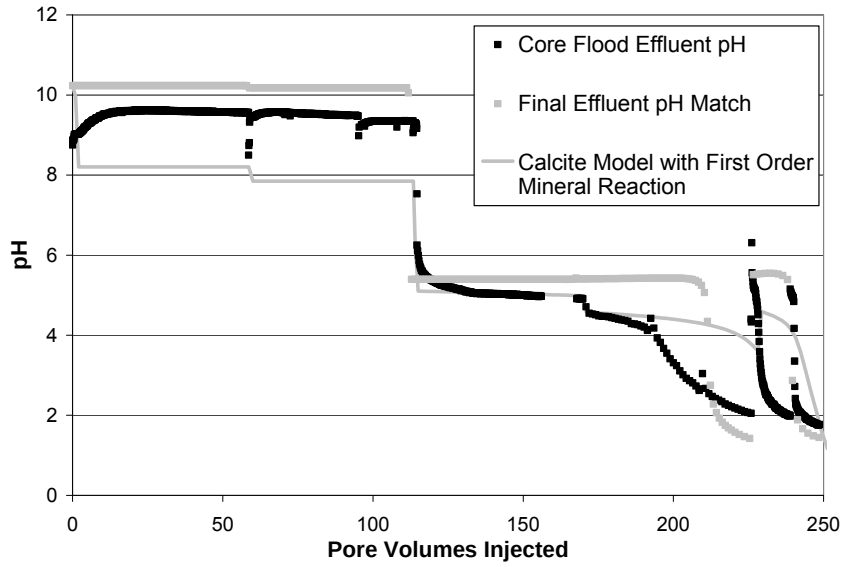

Figure 6.6: Effluent pH for Calcite Model with First-order Calcite Reaction (Experiment 1)

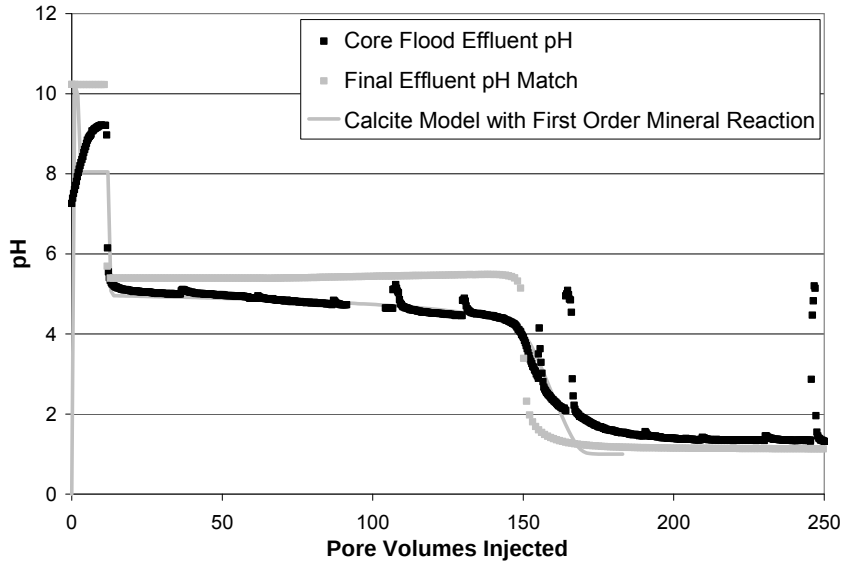

Figure 6.7: Effluent pH for Calcite Model with First-order Calcite Reaction (Experiment 2)

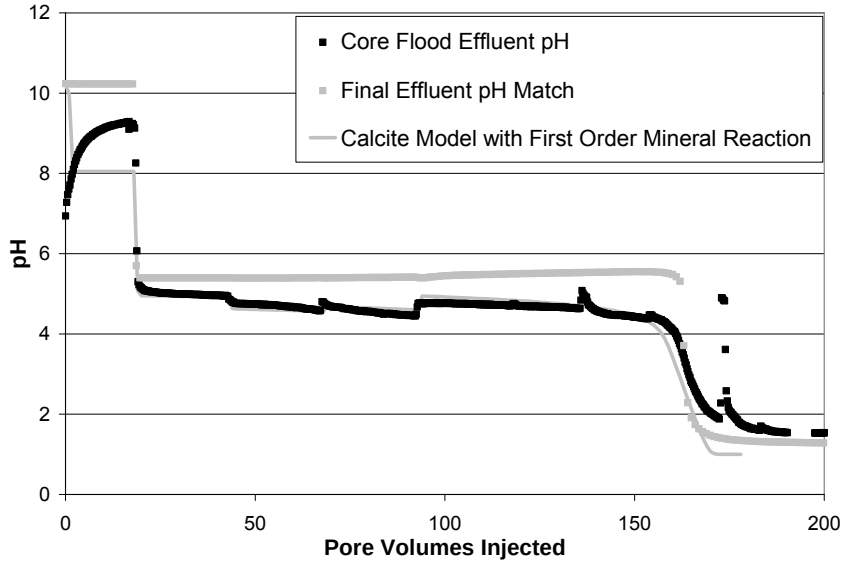

Figure 6.8: Effluent pH for Calcite Model with First-order Calcite Reaction (Experiment 3)

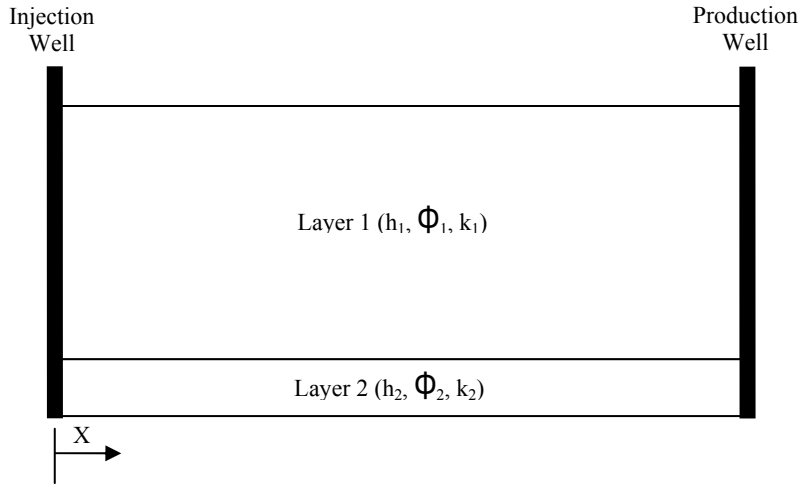

Figure 6.9: Schematic of Two-Layer Linear Oil Reservoir Simulation Grid

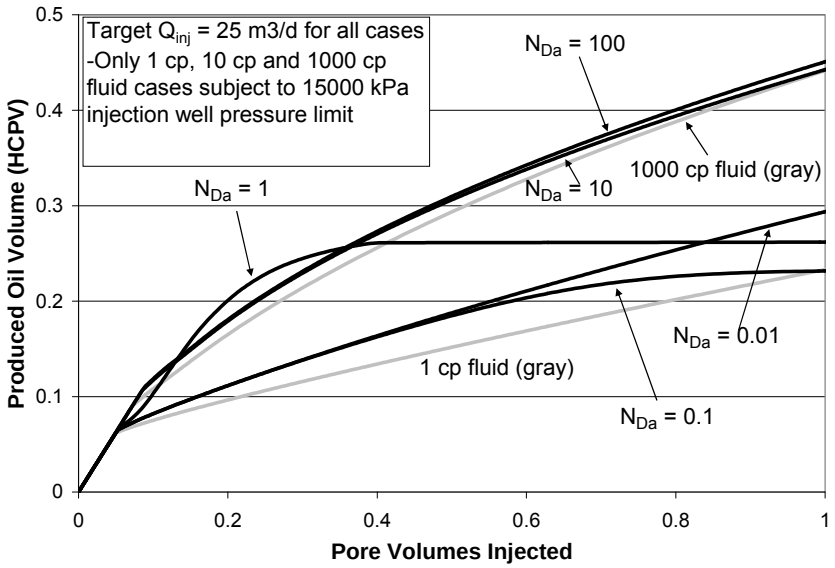

Figure 6.10: Produced Oil Volume versus Volume of Fluid Injected (Linear Case-No Crossflow)

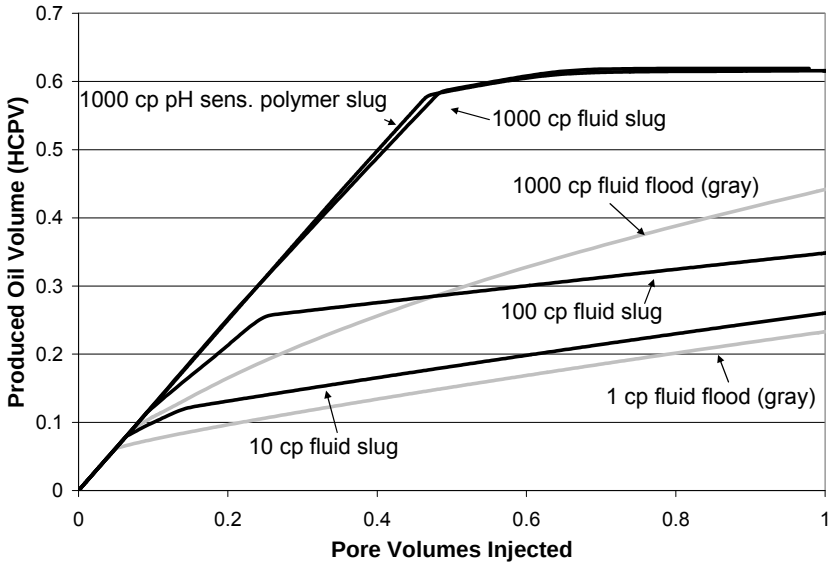

Figure 6.11: Oil Recovery versus Volume of Fluid Injected Using 0.05 HCPV Slug Treatment Followed by Waterflooding (Linear Case, No Crossflow)

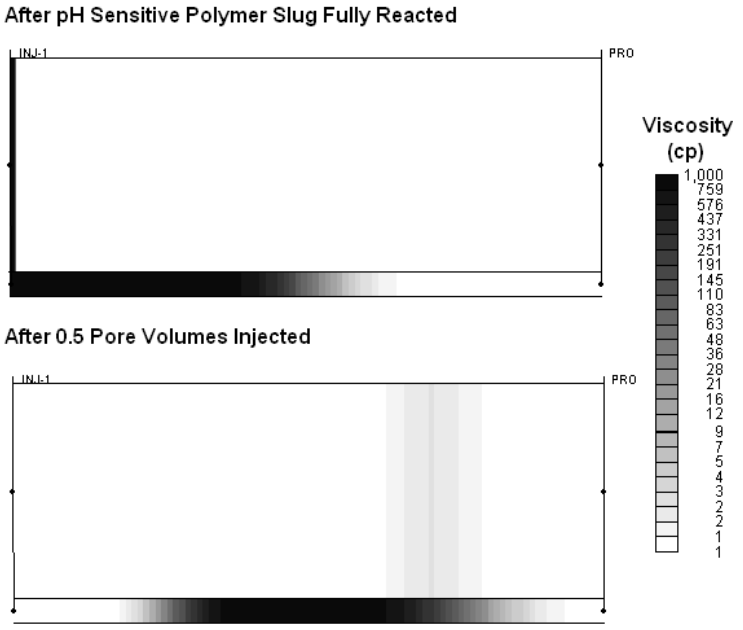

Figure 6.12: Aqueous Phase Viscosity Distribution in Linear Reservoir During 1000-cp pH-Sensitive Polymer Slug Treatment Simulation (Linear Case, No Crossflow)

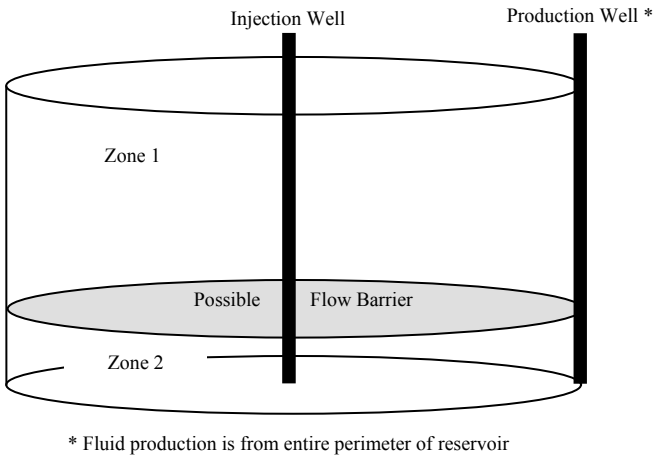

Figure 6.13: Schematic of Two-Layer Radial Oil Reservoir Simulation Grid

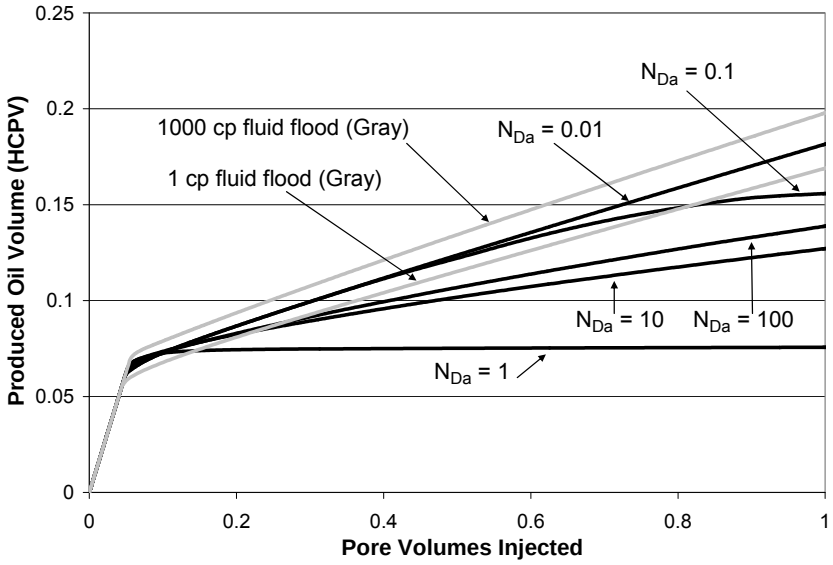

Figure 6.14: Oil Recovery versus Volume of Fluid Injected Using pH-Sensitive Polymer (Radial Case, No Crossflow)

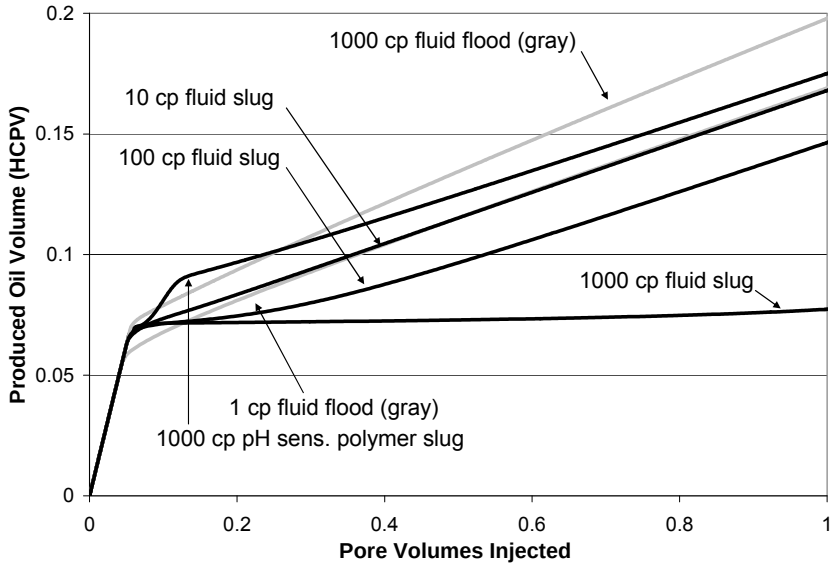

Figure 6.15: Oil Recovery versus Volume of Fluid Injected Using 0.05 HCPV Slug Treatment Followed by Waterflooding (Radial Case, No Crossflow)

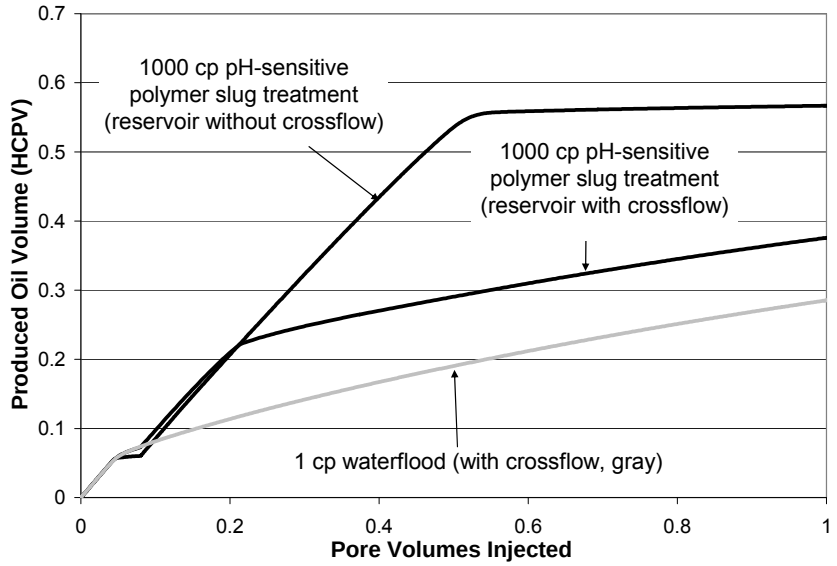

Figure 6.16: Oil Recovery versus Volume of Fluid Injected Using 0.1 HCPV Slug Treatment Followed by Waterflooding (Radial Case)

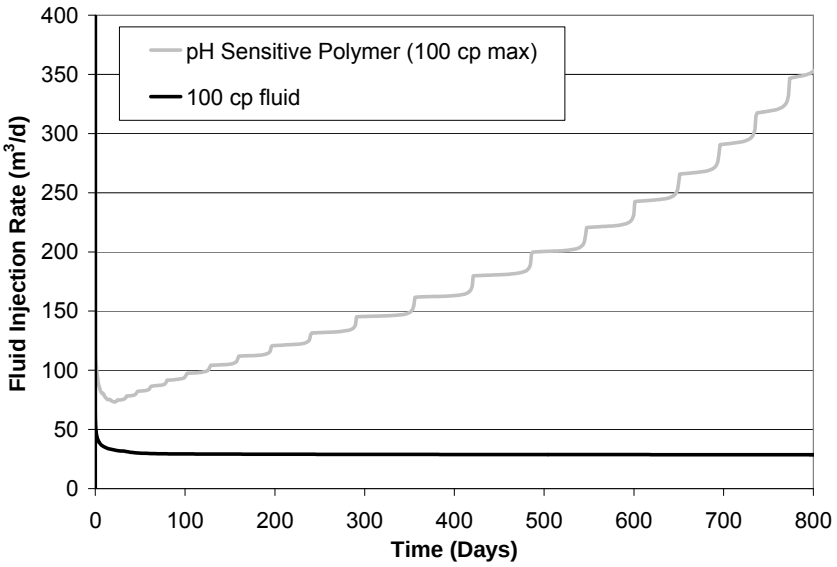

Figure 6.17: Injection Rate versus Time (Constant Injection Pressure, Radial Case, No Crossflow)

7. Application of pH-Triggered Polymers in Fractured Reservoirs to Increase Sweep Efficiency

7.1 INTRODUCTION

There are large reserves of mobile oil in reservoirs around the world that cannot be produced due to problems such as low reservoir pressure and thief zones. Water injection is commonly employed to increase the average reservoir pressure and push out the oil. However, water flooding is not always successful. The most important problem is channeling of the injected water into high permeability zones which occur in heterogeneous reservoirs. In this situation, the water breakthrough time decreases, and significant portions of the reservoir remain untouched by the injected water. This reduces the sweep efficiency and oil recovery. In addition, the water oil ratio (WOR) increase which increases the cost of the water flood process.

One of the methods to overcome the channeling problem is to block the high permeability zones with a specific kind of polymer or gel. By blocking the areas already swept by the water, subsequently injected water can sweep an unswept area of the reservoir and thereby increase the oil recovery. The polymer should be very viscous to be able to block the high permeability zones and ideally, these polymers should be economical and easy to prepare. However, injecting a viscous polymer into the reservoir at reasonable rates requires high injection pressures. The limitation imposed by the local fracture gradient greatly restricts the depth to which such a solution can be placed. Therefore, we are looking for a polymer that can be injected easily to the reservoir, yet offers large resistance to flow once placed in the reservoir.

Several approaches have been proposed to achieve this goal. Chemical cross-linking of polymer molecules is one commonly used method. A solution of polymer and reactive agents such as Cr^{3+} ions has low viscosity. As the polymer cross-links, increasing the hydrodynamic size of the molecules, the viscosity of the solution rises significantly. The challenge in the field application of this method is to control the rate of the cross-linking, especially as reservoir temperature increases. Sydansk and Southwell (2000) discussed their wide experience with Cr (III) - carboxylate/acrylamide-polymer (CC/AP) gel technology for oilfield conformance control, sweep improvement and fluid shutoff treatment. They stated that gel treatments of this technology are

applicable to reservoirs having a broad temperature range (40°F up to 300°F in certain instances). In addition, Sydansk *et al*. (2005) characterized partially formed chromium (III) and high-low molecular weight gels for water shutoff in fractures. Mennella *et al*. (1999) presented an analysis to define several physico-chemical issues to understand the polymer shutoff mechanism and to develop a consistent technology by performing several experimental and simulation studies. In addition to the difficulty in controlling the cross-linking kinetics, the chromatographic separation of the polymer from the cross-linking agent can be an issue in some instances (Garver *et al*. 1989).

Polyacrylic acid microgels can swell a thousand fold as the pH of the surrounding solution changes, with an accompanying large increase in viscosity. This pH trigger is simpler than chemical cross-linking and thus offers operational advantages. Denys *et al*. (1998) studied the effect of pH and salinity on permeability reduction caused by polyacrylate retention in a porous medium. According to them, two mechanisms are involved in such a process: pore plugging and adsorption. On the other hand, microgel particles are typically too large to enter pore throats and thus would be well suited for preferential placement in fractures. We have studied a specific pH triggered polymer (Carbopol® 934) in batch and in reactive transport experiments. This microgel is not viscous in low pH environments but if the pH increases, its viscosity increases by several orders of magnitude, as shown in Fig. 1 (Choi 2006). According to Huh *et al*. (2005), the polymer viscosity can be calculated in porous media using the Peppas equilibrium swelling model, the Carreau model and the Martin equation. We have coded the algorithm and added it to a reservoir simulation model (GEM). Benson *et al*. (2007) modeled and simulated the polymer gelation process and polymer propagation in oil reservoirs using this geochemical simulator. As **Figure 7.1** shows, the transition zone from low viscosity to high viscosity values occurs at a pH around 4.

The application of pH-triggered polymers to matrix treatments requires quantifying the geochemistry and rheology as functions of shear rate, mineralogy, polymer concentration, salinity, etc. Al-anazi and Sharma (2002) studied the permeability reduction and propagation of pH-sensitive polymers in non-fractured Berea cores. They proposed that pH sensitive polymers are excellent candidates for conformance control since the polymer can be placed deep into the reservoir by acid pre-flushing the media designed for that specific rock mineralogy. Based on experimental

results in fractured cores, Seright (2001) developed a model to describe the gel propagation and dehydration into the fractures. He proposed that injecting the polymer gel at the highest practical injection rate will maximize the gel penetration into fractures.

Using pH triggered polymers to seal fractures raises new questions. The rate of pH increase is expected to be slower than in a matrix treatment, because the injected fluid will be contacting only the walls of the natural fractures. The reactive surface area will thus be smaller than for flow through a rock matrix. In principle this should lead to greater depths of penetration. It also raises the possibility that the pH trigger could even be employed in naturally fractured carbonate formations, whose mineralogy rapidly neutralizes acidic solutions. On the other hand, blocking a fracture is more difficult than blocking pore throats. The mechanical strength (yield stress) of the gel may thus be more important than its apparent viscosity. This report describes a series of experiments designed to address these questions.

7.2 EXPERIMENTAL METHOD

7.2.1 Preparation of fractured cores

Homogeneous blocks of sandstone and limestone rocks are used to make the fractured cores in all experiments discussed in this report (**Table 7.1**, **Figure 7.2**). Data in **Table 7.1** were provided by the suppliers. The porosity and permeability measured on the cores agree well with values listed in **Table 7.1**. The diameter of the cores is 1 inch and their lengths vary from 11.3 to 11.6 inches. In order to make fractured cores we saw the cores in half using a very thin blade.

We apply a silicone rubber adhesive sealant on the fracture edges along the length of the cores. This fixes the two halves in place but unlike epoxy adhesive the silicone can be cut after the experiment to allow examination of the gel in the fracture, **Figure 7.3**. All the cores are saturated with brine (3% NaCl) before performing a water/polymer flood.

7.2.2 Polymer preparation

In this research we only use Carbopol® 934 and the word 'polymer' refers to the solution of Carbopol® 934 (3%), NaCl (3%) and water (94%). To make the desired polymer solution, first the brine solution should be prepared and polymer powder should be added to brine very slowly to prevent polymer clogging. The initial polymer solution is stirred continuously for 1 day, yielding a clear milky solution. Vacuuming the polymer solution before injection is recommended to remove any air bubbles trapped in the polymer solution. The pH of fresh polymer is around 2.0 and its viscosity is about 5 to 15 cp.

7.2.3 Coreflood Set up

In all constant rate injection experiments described in this report, we use a dual-piston constametric pump to inject the brine/polymer into a horizontal Hassler core holder. The pressure is monitored at the inlet and outlet of the core holder. The injection pressure varies over a wide range, so we select one of three pressure transducers with different sensitivities to maintain accuracy. The pressure data is recorded in an Excel sheet for post processing. **Figure 7.4** shows the set up for the water/polymer flood experiments.

To measure the polymer yield point, the maximum pressure that the polymer microgel can resist against injected water was measured. We performed the water injection after polymer gelation under a constant pressure constraint and increased the injection pressure gradually. The fractured Berea sandstone cores saturated with brine are used in this set of experiments.

We used a pressure regulator in order to inject water at constant pressure. In these experiments the flowrate is measured at the core outlet. We increased the injection pressure gradually and applied the pressure in each step for 2 minutes. Since we wanted to know the breakthrough point for water flowing through the fracture, we limited each step to 2 minutes of exposure in order to prevent water coming from the matrix. A schematic of the experimental setup is shown in **Figure 7.5**.

To investigate the polymer propagation deep into fractured reservoirs, we conducted a set of experiments in which the polymer solution collected from the core outlet was recycled to the injection beaker (**Figure 7.6**). We continue injection until we

observe polymer gelation in the outlet fluid and a corresponding increase in pressure drop.

A typical procedure for any coreflood begins by measuring the core permeability to 3% NaCl brine. Then 3 to 4 core pore volume of polymer was injected into the core. After this, we shut the pump for a certain amount of time. We then measure the treated core permeability by injecting 3% brine again. In several experiments we pre-flushed the core with HCl before polymer flooding to prevent early gelation of the polymer.

7.2.4 Batch experiments

The key to polymer gelation is the increase in polymer pH due to reaction with rock minerals and mixing with residual water. To confirm that both limestone and sandstone rocks are able to increase the polymer pH and to study the rate of increase in polymer pH with time, we performed several batch experiments, mixing different types of rocks and minerals with polymer solution at ambient conditions of 25^{o}Cand 1 atm.

In this set of experiments, we mixed 50 grams of polymer solution, pH=2, with 50 grams of solids. The solids were crushed Berea sandstone, crushed Texas Cream limestone and pure $CaCl_2$. We monitored the pH of the mixture solution with time. Also, we monitored the gelation time of the mixture by observing the existence of gel particles at the outlet.

7.3 RESULTS AND DISCUSSION

7.3.1 Geochemical reactions – batch experiments

The polymer pH increases faster while is in contact with crushed limestone as might have been expected due to the abundance of carbonate compounds in limestone rocks (**Figure 7.7**). Microgels appeared after 1 hour, 6.5 hours and 1.2 hours in limestone, sandstone and pure $CaCl_2$ containers, respectively. The pH decrease in $CaCl_2$ solution is due to the reaction which is explained later in this section.

The type of microgels that were formed is different in each container. In the sandstone container, a layer of clear microgel is observed and the crushed sandstone is covered with microgel. In the limestone container a colloidal solution is observed.

Microgel and limestone chunks are not distinguishable clearly as they are completely mixed together and form a viscous and sticky material (**Figure 7.8**).

The mixing of the polymer solution and $CaCl_2$ is very exothermic and the temperature rapidly approaches $65^{\circ}C$ due to the following reaction:

$$CaCl_2 + 2H_2O \rightarrow CaCl_2.2H_2O \quad (7.1)$$

However, the increase in temperature is instantaneous and the solution temperature decreases to ambient temperature as time passes. The polymer pH decreases from 2 to 0.9 after mixing with $CaCl_2$ due to acidic compounds formed in the solution. Despite the low pH, a clear polymer gel is observed in this solution. Evidently calcium cations are able to entangle the microgel particles or to precipitate them from solution. This effect is believed to contribute to the behavior of the "long residence time" coreflood experiment in which polymer solution is circulated through the fractured core, discussed below.

7.3.2 Reduction in permeability of fractured sandstone cores

In this set of experiments we used fractured Berea sandstone cores saturated with 3% NaCl brine. The results of seven polymer flood experiments are shown in **Table 7.2**.

The initial core permeability stated in the table is the total core (matrix + fracture) permeability. The matrix permeability is about 100-200 md for Berea Sandstone and the porosity is about 20-25%. Thus the permeability contrast between matrix and fracture is of order 10,000 darcies, ensuring that water goes only through the fracture not the matrix.

In all the experiments, we managed to reduce the permeability of the fractured cores by a factor of 2 to 230. By comparing the PRF of the last three experiments with the rest, we concluded that using an acid pre-flush does not change the PRF significantly, as confirmed by measured effluent pH histories (**Figure 7.9**). This suggests that little increase in pH occurred during flow through the fracture because of the very short residence time (a few seconds). Rather, the pH increased when the polymer solution was stationary. Also, in all experiments which are performed without an acid pre-flush there was no sign of polymer early gelation during the polymer flood process. Therefore, we stopped pre-flushing the cores with HCl.

The PRF depends strongly on the shut-in time, **Figure 7.10**. In Experiments 2 and 5, we injected the water almost immediately after polymer injection. The injected water washed out a majority of the polymer out of the fracture. Even so, we observed a PRF of 1.8 and 5.0 in these cases.

In Experiment #1, the treated core permeability is much lower than the matrix permeability which means that the polymer solution partially invaded the matrix as well as the fracture. To study this case in more detail, we performed Experiment #7. In this experiment we dyed the polymer solution with a trace of blue color to track the polymer invasion. After two days of shut-in and performing the post-treatment water flood, we cut the core in pieces to view the polymer invasion area. As shown in **Figure 7.11**, the blue liquid is all over the matrix area.

The blue liquid in the matrix could only be water extracted from the injected polymer solution. The extent of permeability reduction showed that the matrix was partially invaded by polymer, though there was no sign of the presence of polymer microgel in the matrix. Clearly the gel blocked flow through the fracture due to the large pressure drop (**Figure 7.12**). The x-axis is based on the total core pore volume.

7.3.3 Reduction in permeability of fractured carbonate cores

To study the polymer gelation in carbonate reservoirs, we performed several water/polymer flood experiment in fractured Texas Cream limestone cores. The matrix permeability is about 15-25 md. We repeated exactly the same process described above for fractured Berea cores. One of the factors that should be taken into account is the softness of the carbonates, especially Texas Cream limestones. Due to the low matrix permeability, the pressure drop across the core increases drastically after blocking the fracture using polymer microgels. There is a high chance of core breakage, so confining and axial pressure and injection rate should be set to moderate levels.

We lowered the fractured core permeability in Texas Cream cores. The pressure drop across the core before and after polymer injection is shown in **Figure 7.13**. The pump was shut-in for two hours after polymer injection. In this case, the treatment decreased the core permeability from 630 md down to 354 md which shows that the fracture is partially blocked by polymer microgels.

7.3.4 Constant pressure injection

The results of two cases A and B are represented in **Tables 7.3** and **7.4**. The initial core permeability for Case A was 1475 md and we shut-in the pump for 1 hour after polymer injection to let the microgels form in fracture. The initial core permeability of case B was 1329 md, and the pump was shut-in only for 20 minutes. The polymer held back the water-flow up to 90 and 100 psi in case A and B, respectively. Thus, for pressure gradients less than 9 to 10 psi/ft, the PRF is infinity. After water breakthrough we decreased the pressure to measure the core treated permeability. The PRF is 15.7 and 6.1 in Case A and B respectively, still a significant reduction considering that water had broken through. After finishing the experiment we opened up the core to observe the water path through polymer microgels in fractures. As shown in **Figure 7.14**, the water path is a narrow, tortuous channel through the polymer microgel inside the fracture. The lack of widespread displacement of the gel from the fracture explains the residual PRF values.

7.3.5 Depth of polymer propagation into fractured reservoirs

To study polymer propagation into fractured reservoirs, and to estimate the potential depth of penetration, we recycled the polymer solution into the core. Fractured Berea cores were used in this experiment. The total polymer volume used in this recycling process was 50 cc with pH of 2. The effluent and inlet pH versus time are shown in **Figure 7.15**. The x-axis is based on the total core pore volume. The initial polymer injection rate was 9.6 cc/min which after polymer gelation was reduced to 5 cc/min.

The effluent pH increased gradually from 2 to 3.5 after about 45 pore volumes of polymer injection. Small gas bubbles were observed coming out during the first 4 to 5 pore volumes of polymer injection. No sign of polymer gelation was observed during up to 30 pore volume of polymer injection. The measured permeability of the core is shown in **Figure 7.16**. The initial core permeability in this experiment is 230 md.

It takes a few minutes for pressure to build up and the high initial permeability values are due to this effect. Polymer microgels were observed at the core outlet after about 30 pore volumes of polymer injection. We dyed the polymer solution blue to

distinguish the invaded areas. After polymer gelation, polymer particles were observed in the effluent alternating with brine, **Figure 7.17**.

To estimate the distance to which the polymer will propagate in the field we assume that the polymer only goes into the fracture. The fracture volume is 0.33 ml/ft of core. In polymer injection into reservoirs, the polymer solution sees fresh rock as it propagates. We assume that there are sufficient minerals in Berea rock that the reaction rate remains constant and core acts as a fresh rock even after being contacted with polymer. With these assumptions, the polymer can propagate into fractures for about 2300 ft before it gels. This is an optimistic value. A more realistic value for polymer propagation distance could be about 1000 ft (or lower for higher permeability rocks with more leak-off).

After finishing the experiment we opened the core and we observed the polymer microgels (dark blue) all over the fracture with a uniform distribution as shown in **Figure 7.18**.

To study the polymer propagation distance we repeated the recycling experiment using a fractured Indiana limestone. The reaction rate of polymer with carbonate minerals is much faster than with sandstone minerals due to the abundance of carbonate compounds. The total core permeability is 85 md with a porosity of 9% and it is saturated with brine. As shown in **Figure 7.19**, the change in effluent pH is much faster in carbonates than in sandstones and polymer microgels appeared at the outlet after almost 3.5 pore volumes of polymer injection. Lots of carbon dioxide bubbles were observed at the outlet (formed by reacting the polymer with rock minerals).

According to these results, polymer can propagate into fractures for as much as 130 ft without polymer gelation. A more realistic value for polymer propagation distance could be about 40-50 ft. Acid pre-flushing before polymer flooding is suggested in carbonate cores.

7.4 CONCLUSION

The pH-triggered polymer microgels studied in this work could be effective for conformance control in naturally fractured reservoirs. Polymer treatment reduced the permeability of fractured cores in all experiments. Based on the results of constant

pressure experiments, polymer microgels blocked the fractures completely up to pressure gradients of 90-100 psi/ft. Extrapolation of effluent recycling experiments suggests that the polymer could propagate as much as 1000 feet from an injection well into low-temperature fractured sandstone reservoirs without changing into microgel. Acid pre-flushing the media in carbonate reservoirs is recommended due to the high reaction rate of polymer with carbonate minerals. Even without a preflush, propagation of several tens of feet could be possible. However extensive dissolution of minerals containing divalent cations could trigger polymer precipitation (gelation) even before the pH trigger is activated.

Table 7.1: Properties of rocks used in this research

Berea Sandstone	
Total Intrusion Volume (mL/g)	0.1087
Total Pore Area (m^2/g)	6.182
Median Pore Diameter, Volume(μm)	11.1483
Average Pore Diamater (μm)	0.0703
Bulk Density (g/mL)	1.9969
Apparent Density (g/mL)	2.5503
Porosity (%)	21.7005
Average Permeability (md)	150
Texas Cream Limestone	
Total Intrusion Volume (mL/g)	0.0885
Total Pore Area (m^2/g)	4.747
Median Pore Diameter, Volume(μm)	0.8605
Average Pore Diamater (μm)	0.0746
Bulk Density (g/mL)	2.0403
Apparent Density (g/mL)	2.4898
Porosity (%)	18.0533
Average Permeability (md)	10
Indiana Limestone	
Total Intrusion Volume (mL/g)	0.0701
Total Pore Area (m^2/g)	4.142
Median Pore Diameter, Volume(A)	6318
Average Pore Diamater (A)	677
Bulk Density (g/mL)	2.2817
Apparent Density (g/mL)	2.7162
Average Permeability (md)	60
Porosity (%)	15.9964

Table 7.2: Results obtained from polymer flood on fractured sandstone cores

Experiment #	Initial core permeability, md	Acid pre-flush	Polymer initial pH	Shut-in time, hr	Treated core Permeability, md	PRF
1	4345	Yes	2	48	19	228.7
2	1697	Yes	2.2	0.17	952	1.8
3	2893	Yes	2.1	21	148	19.5
4	2394	Yes	2.1	2	535	4.5
5	2188	No	2	0.25	426	5.1
6	1238	No	2.1	2	181.1	6.8
7	1410	No	2	48	13.4	105.2

Table 7.3: Results of constant pressure tests, Case A

Injecting pressure, psi	Q (cc/min)	Core Permeability (md)
5	Trace	≈0
10	Trace	≈0
20	Trace	≈0
30	Trace	≈0
50	Trace	≈0
70	Trace	≈0
90	4.8	92
50	2.8	96
18	1	95

Table 7.4: Results of constant pressure tests, Case B

Injecting pressure, psi	Q (cc/min)	Core Permeability (md)
10	Trace	≈0
20	Trace	≈0
40	Trace	≈0
70	Trace	≈0
80	Trace	≈0
90	Trace	≈0
100	9.8	213
70	6.8	211
40	4.2	228
20	2.2	239

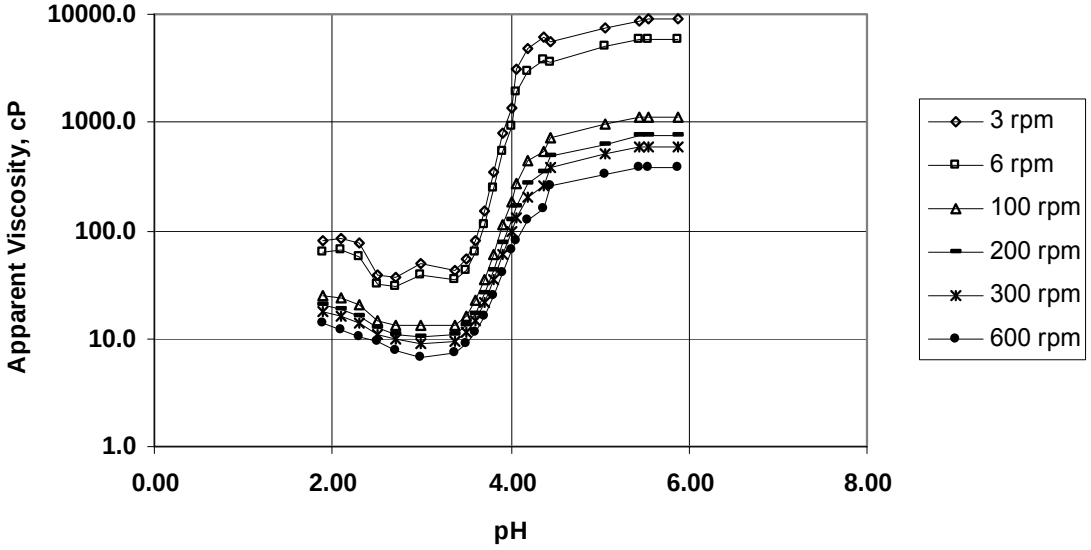

Figure 7.1: Variation of apparent viscosity of Carbopol 934% with pH (Choi, 2006).

Figure 7.2: Left to right: Indiana limestone, Texas Cream limestone and Berea sandstone

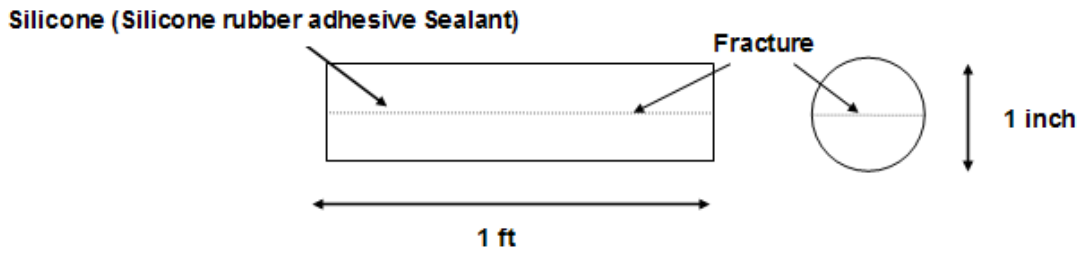

Figure 7.3: Top and side view of fractured cores.

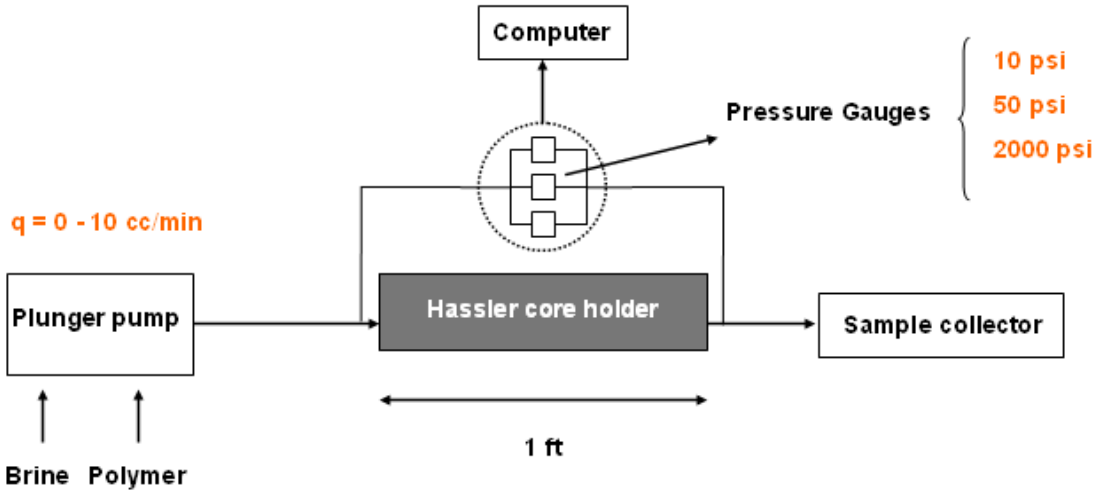

Figure 7.4: Set up of water/polymer flooding experiment at constant injection rate.

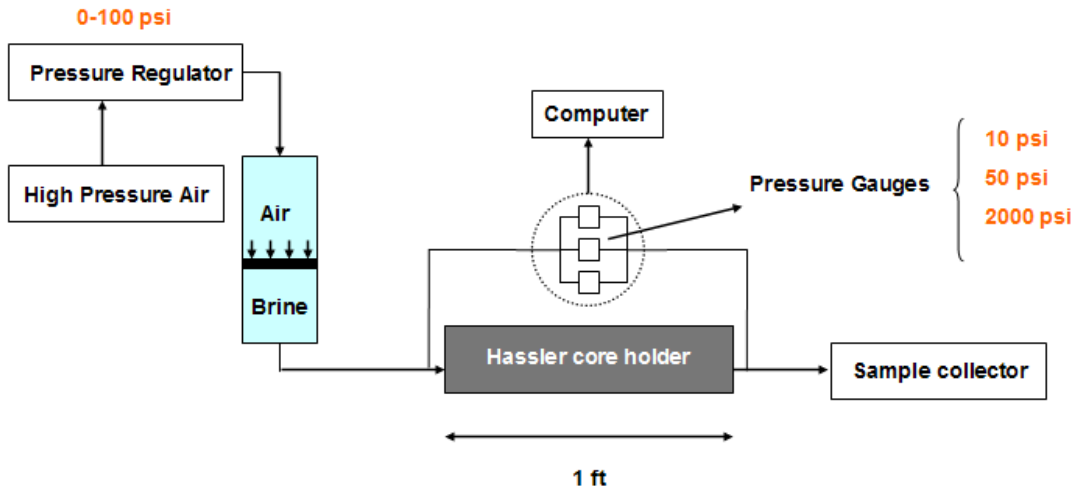

Figure 7.5: Set up of constant pressure water/polymer flooding experiments.

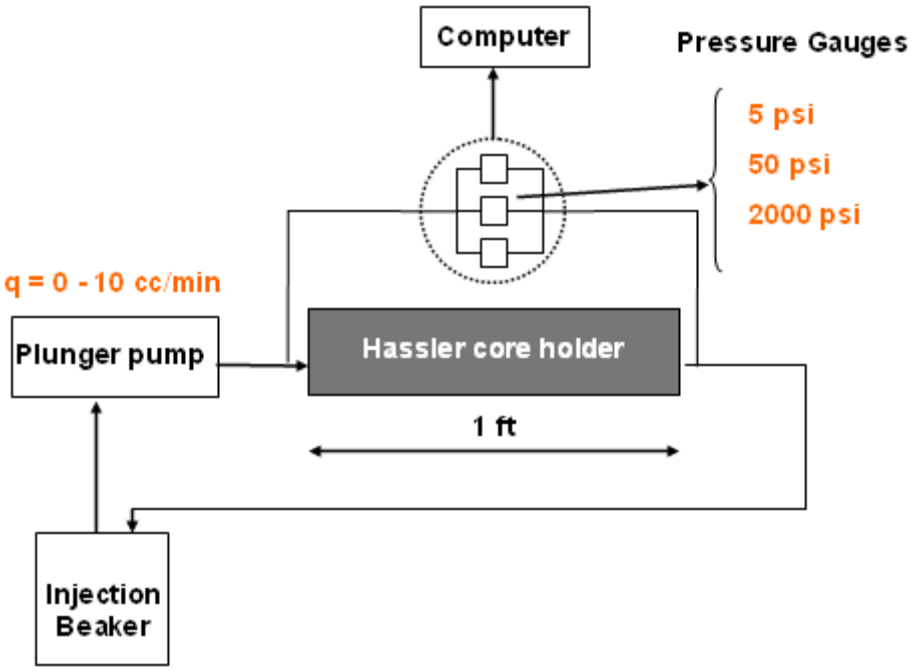

Figure 7.6: Set up of constant pressure polymer recycling experiments.

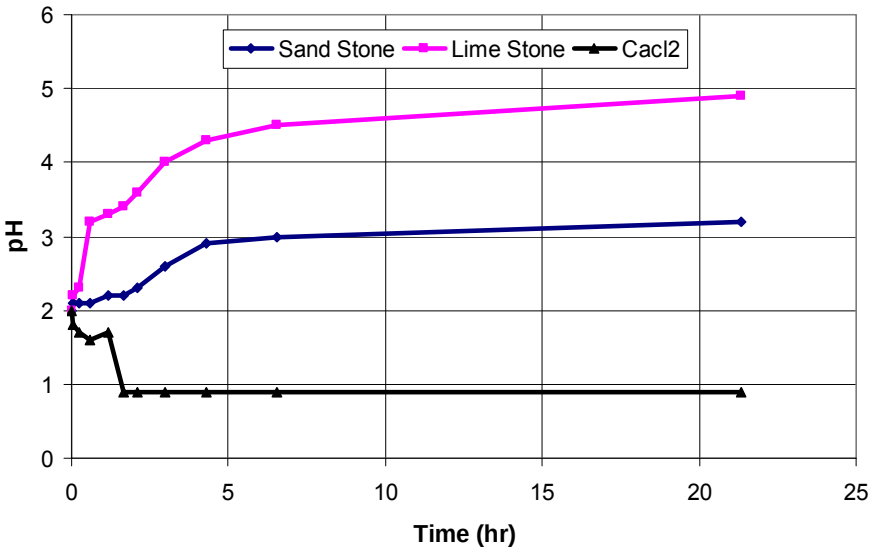

Figure 7.7: Change in polymer solution pH with time of contact with different materials

Figure 7.8: Polymer batch test. From left to right: CaCl2, limestone and sandstone containers

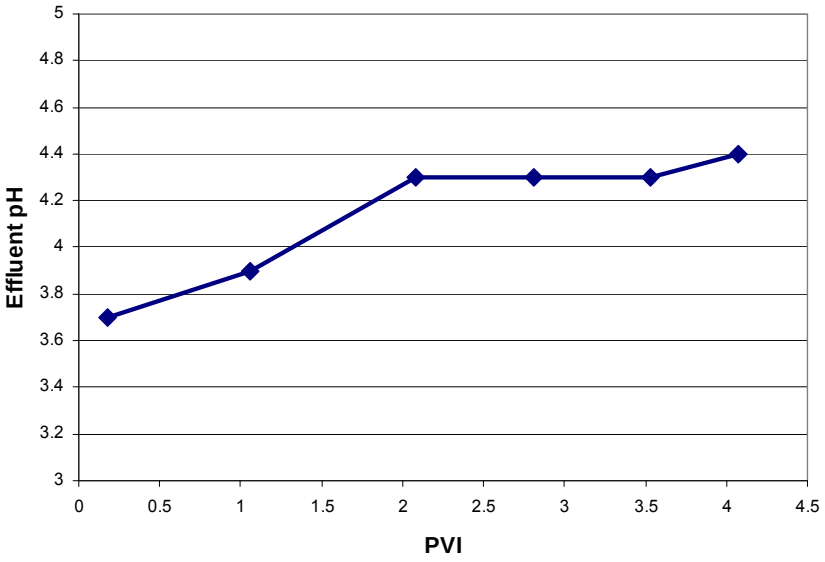

Figure 7.9: Change in polymer pH during polymer injection

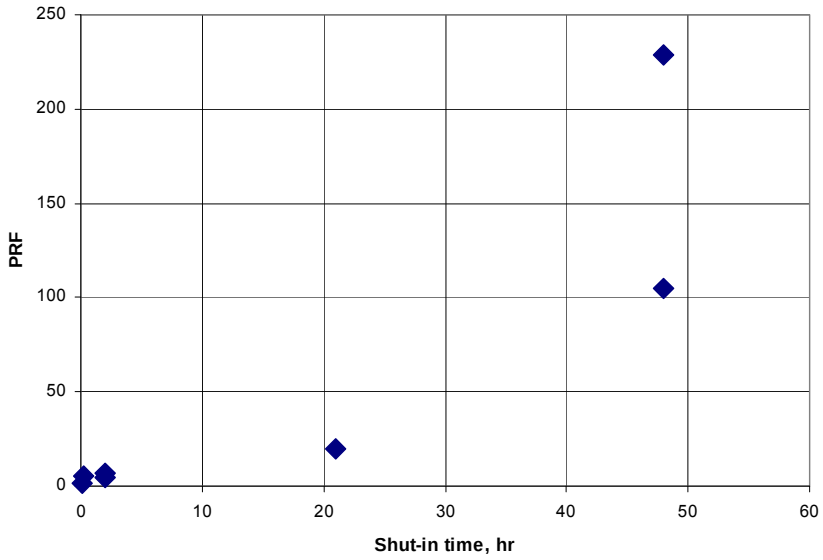

Figure 7.10: PRF vs. Shut-in time

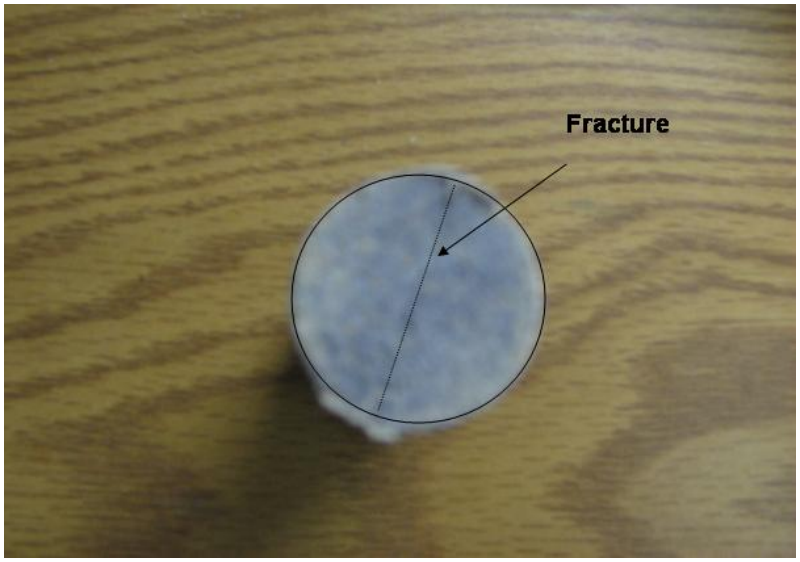

Figure 7.11: Picture of core cross section midway along the core. Blue color indicates invasion of matrix by water from the polymer solution in the fracture.

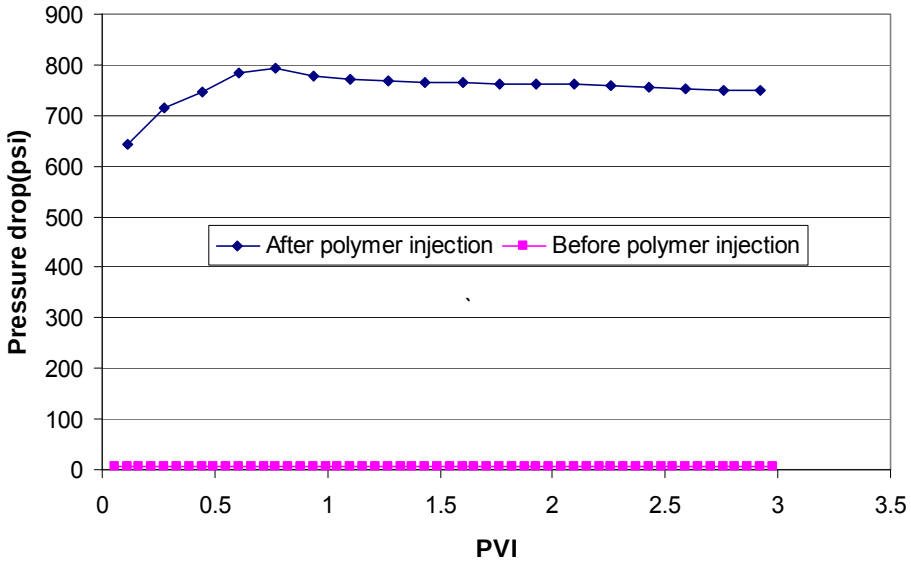

Figure 7.12: Pressure drop after and before polymer injection for experiment #1

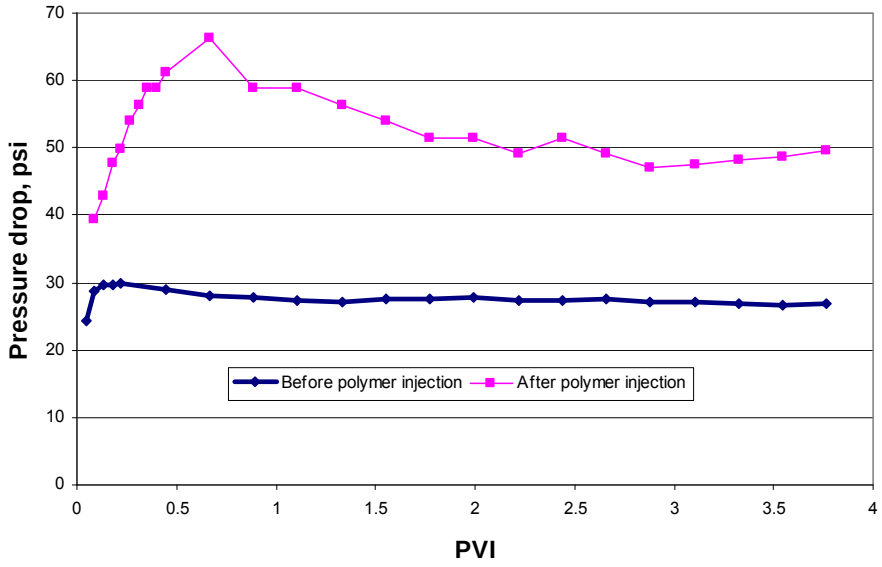

Figure 7.13: Pressure drop across the Texas Cream fractured core after and before polymer injection

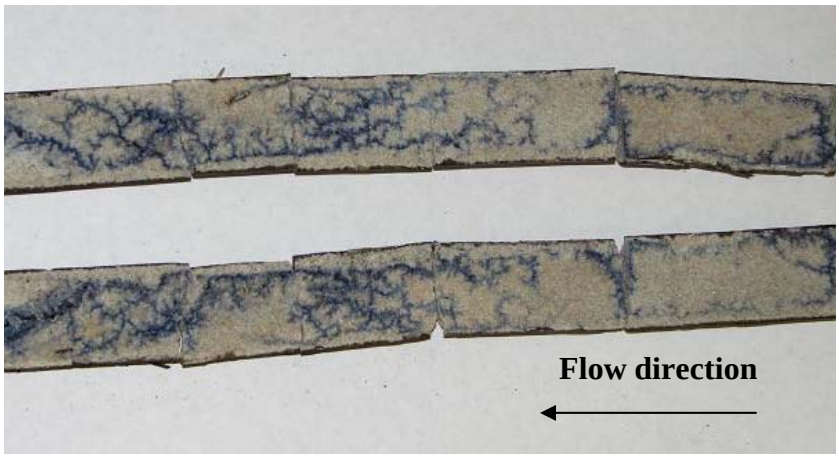

Figure 7.14: Blue regions correspond to channels created by dyed water flowed through the microgel-filled fracture at a sufficiently large pressure.

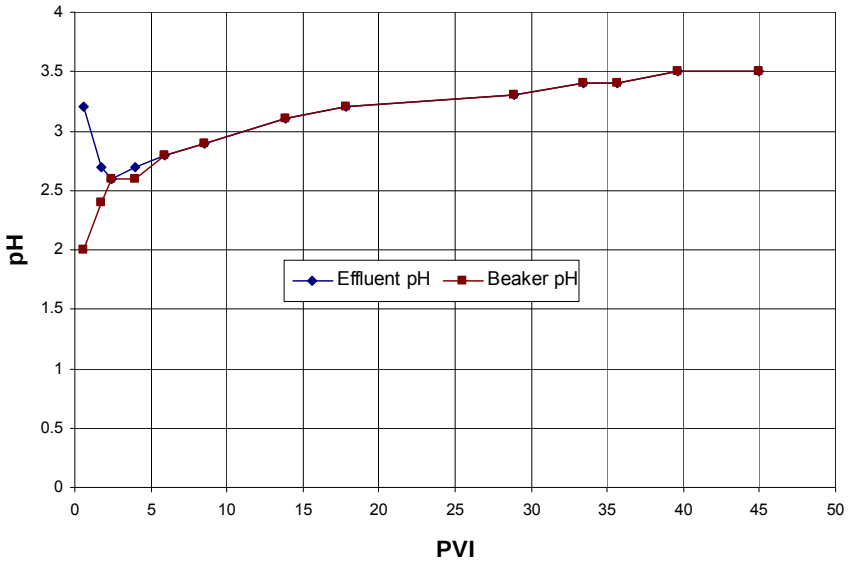

Figure 7.15: Beaker and effluent pH versus pore volume of polymer injected

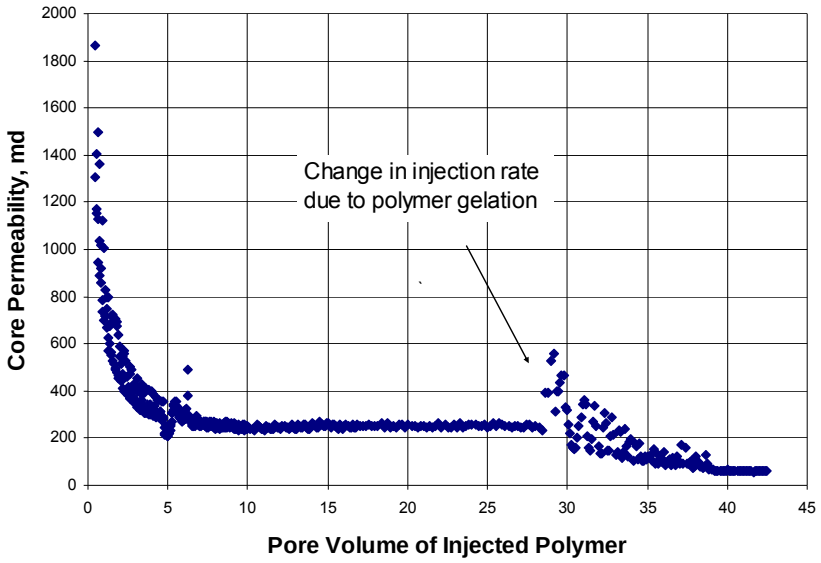

Figure 7.16: Total core permeability in polymer recycling experiment

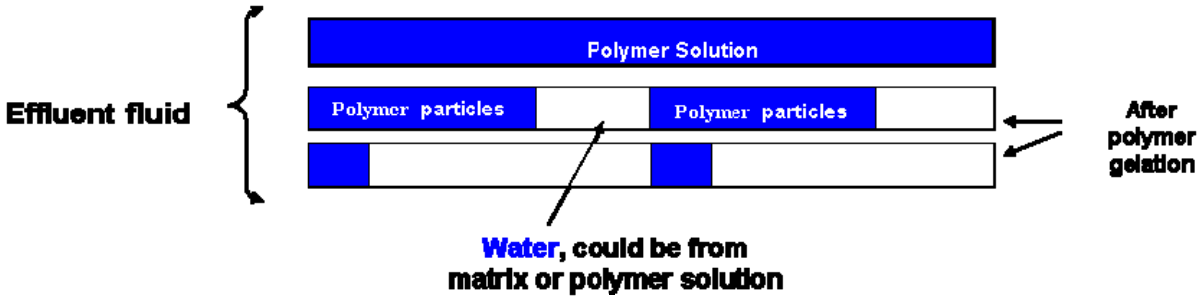

Figure 7.17: Effluent fluid during the polymer recycling experiment

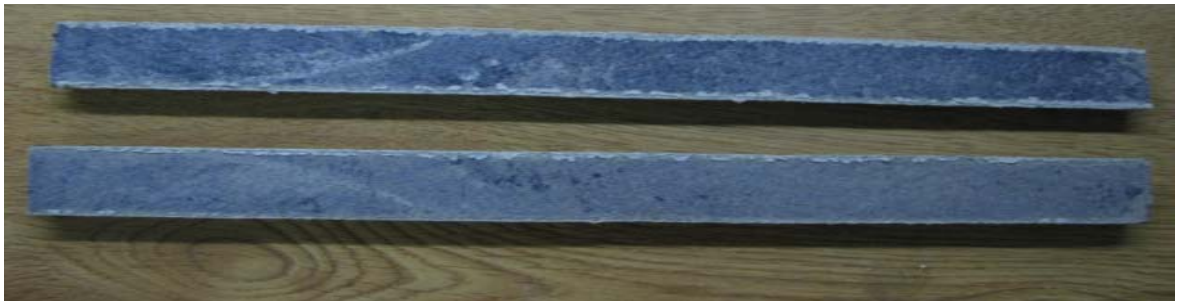

Figure 7.18: Microgel distribution inside the fracture

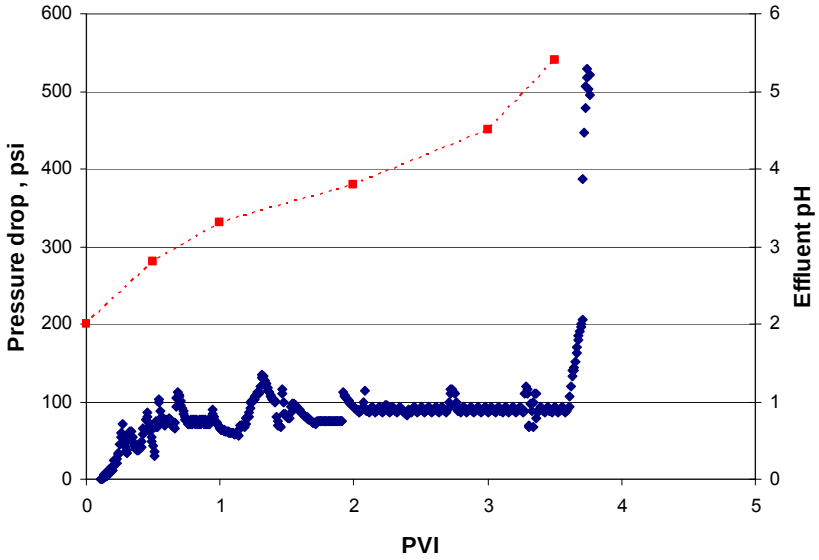

Figure 7.19: Pressure drop across the core and effluent pH versus time, polymer recycling, Indiana limestone

List of Tables

Table 1.1: Examples of rheological properties of HPAM polymers 18

Table 1.2: Dynamic quantities that can be measured in oscillatory test at shear geometry 19

Table 1.3: SNF polymers used in rheological measurements with specifications19

Table 1.4: Test sequence for rheological measurements 20

Table 1.5(a): Viscosity and relaxation time as a function of pH for 0.5% Flopaam 3330S (8M molecular weight and 25~30 % degree of hydrolysis), prepared in 0.5% sodium chloride brine 21

Table 1.5(b): Elastic and loss moduli for 0.5% Flopaam 3330S (8M molecular weight and 25~30 % degree of hydrolysis), prepared in 0.5% sodium chloride brine 21

Table 1.6(a): Viscosity and relaxation time as a function of pH for 0.2% Flopaam 3330S (8M molecular weight and 25~30 % degree of hydrolysis), prepared in 0.5% sodium chloride brine 22

Table 1.6(b): Elastic and loss moduli for 0.2% Flopaam 3330S (8M molecular weight and 25~30 % degree of hydrolysis), prepared in 0.5% sodium chloride brine 22

Table 1.7(a): Viscosity and relaxation time as a function of pH for 0.8% Flopaam 3330S (8M molecular weight and 25~30 % degree of hydrolysis), prepared in 0.5% sodium chloride brine 23

Table 1.7(b): Elastic and loss moduli for 0.8% Flopaam 3330S (8M molecular weight and 25~30 % degree of hydrolysis), prepared in 0.5% sodium chloride brine 23

Table 1.8(a): Viscosity and relaxation time as a function of pH for 0.5% Flopaam 3330S (8M molecular weight and 25~30 % degree of hydrolysis), prepared in 1.0% sodium chloride brine 24

Table 1.8(b): Elastic and loss moduli for 0.5% Flopaam 3330S (8M molecular weight and 25~30 % degree of hydrolysis), prepared in 1.0% sodium chloride brine 24

Table 1.9(a): Viscosity and relaxation time as a function of pH for 0.5% Flopaam 3330S (8M molecular weight and 25~30 % degree of hydrolysis), prepared in 3.0% sodium chloride brine 25

Table 1.9(b): Elastic and loss moduli for 0.5% Flopaam 3330S (8M molecular weight and 25~30 % degree of hydrolysis), prepared in 3.0% sodium chloride brine 25

Table 1.10(a): Viscosity and relaxation time as a function of pH for 0.5% Flopaam 3330S (8M molecular weight and 25~30 % degree of hydrolysis), prepared in 10.0% sodium chloride brine 26

Table 1.10(b): Elastic and loss moduli for 0.5% Flopaam 3330S (8M molecular weight and 25~30 % degree of hydrolysis), prepared in 10.0% sodium chloride brine 26

Table 1.11(a): Viscosity and relaxation time as a function of pH for 0.5% FA920SH (8M molecular weight and 0 % degree of hydrolysis), prepared in 0.5% sodium chloride brine 27

Table 1.11(b): Elastic and loss moduli for 0.5% FA920SH (8M molecular weight and 0 % degree of hydrolysis), prepared in 0.5% sodium chloride brine 27

Table 1.12(a): Viscosity and relaxation time as a function of pH for 0.5% Flopaam 2330S (8M molecular weight and 20~25 % degree of hydrolysis), prepared in 0.5% sodium chloride brine 28

Table 1.12(b): Elastic and loss moduli for 0.5% Flopaam 2330S (8M molecular weight and 20~25 % degree of hydrolysis), prepared in 0.5% sodium chloride brine 28

Table 1.13(a): Viscosity and relaxation time as a function of pH for 0.5% ALP99VHM (8M molecular weight and 100 % degree of hydrolysis), prepared in 0.5% sodium chloride brine 29

Table 1.13(b): Elastic and loss moduli for 0.5% ALP99VHM (8M molecular weight and 100 % degree of hydrolysis), prepared in 0.5% sodium chloride brine 29

Table 1.14(a): Viscosity and relaxation time as a function of pH for 0.5% Flopaam 3630S (20M molecular weight and 25~30 % degree of hydrolysis), prepared in 0.5% sodium chloride brine 30

Table 1.14(b): Elastic and loss moduli for 0.5% Flopaam 3630S (20M molecular weight and 25~30 % degree of hydrolysis), prepared in 0.5% sodium chloride brine 30

Table 1.15(a): Viscosity and relaxation time as a function of pH for 0.5% Flopaam 3330S (8M molecular weight and 25~30 % degree of hydrolysis), prepared in 0.2% sodium chloride and 0.3% calcium chloride brine31

Table 1.15(b): Elastic and loss moduli for 0.5% Flopaam 3330S (8M molecular weight and 25~30 % degree of hydrolysis), prepared in 0.2% sodium chloride and 0.3% calcium chloride brine 31

Table 2.1: Parameters necessary in the viscosity model of HPAM.....74

Table 2.2: 9 model parameters for Flopaam 3330S obtained from literature sources or by simple calculations 75

Table 2.3: Data sets of zero-shear limit viscosity (η_o), time constant (λ), and flow behavior index (n) in the Carreau model evaluated at each pH for three polymer concentrations (0.2, 0.5, and 0.8%) of Flopaam 3330S polymer 76

Table 2.4: Computed and measured zero-shear limit viscosities, η_o, for three different concentrations of Flopaam 3330S polymer.....77

Table 2.5: Summary of the best-fit parameters.....78

Table 3.1: Plan for citric acid coreflood measurements 106

Table 3.2: Mineralogy and composition of Berea sandstone analyzed by Thin Section Method 106

Table 3.3: Petrophysical properties (absolute permeability and porosity) and residence time for five coreflood experiments: Base case is the injection of pH = 2.5 citric acid prepared in 3% sodium chloride brine into a 5" long Berea core at 1 ml/min, without shut-in 107

Table 3.4: Comparison of maximum cation concentration in ppm for five coreflood experiments.....107

Table 3.5: Reaction rate constants calculated with the initial and peak pH values during shut-ins and the corresponding shut-in times in Test [A4]..108

Table 3.6: Experimental Damköhler number for five coreflood experiments..108

Table 4.1: Hydrocarbon property.....135

Table 4.2: Properties of aqueous species used in the final match.....135

Table 4.3: Possible combinations of cations and anions in the aqueous phase 136

Table 4.4: Equilibrium reactions and the corresponding reaction constants for the best matched simulation.....137

Table 5.1: Common methods for measuring effluent polymer concentrations 169

Table 5.2: Common methods for tracer tests.....169

Table 5.3(a): [Base] 0.5% Flopaam 3330S (8M molecular weight and 25~30 % degree of hydrolysis) in 3.0% sodium chloride brine with pH = 2.5 at 1 ml/min 170

Table 5.3(b): [pH] 0.5% Flopaam 3330S (8M molecular weight and 25~30 % degree of hydrolysis) in 3.0% sodium chloride brine with pH = 3.5 at 1 ml/min 170

Table 5.3(c): [pH] 0.5% Flopaam 3330S (8M molecular weight and 25~30 % degree of hydrolysis) in 3.0% sodium chloride brine with pH = 7.0 at 1 ml/min 171

Table 5.3(d): [Polymer Concentration] 0.8% Flopaam 3330S (8M molecular weight and 25~30 % degree of hydrolysis) in 3.0% sodium chloride brine with pH = 2.5 at 1 ml/min 171

Table 5.3(e): [MW] 0.5% Flopaam 3630S (20M molecular weight and 25~30 % degree of hydrolysis) in 3.0% sodium chloride brine with pH = 2.5 at 1 ml/min 172

Table 5.3(f): [Salinity] 0.5% Flopaam 3330S (8M molecular weight and 25~30 % degree of hydrolysis) in 2.0% sodium chloride brine with pH = 2.5 at 1 ml/min 172

Table 5.3(g): [Degree of hydrolysis] 0.5% FA920SH (8M molecular weight and 0 % degree of hydrolysis) in 3.0% sodium chloride brine with pH = 2.5 at 1 ml/min 173

Table 5.3(h): [Degree of hydrolysis] 0.5% Flopaam 2330S (8M molecular weight and 20~25 % degree of hydrolysis) in 3.0% sodium chloride brine with pH = 2.5 at 1 ml/min 173

Table 5.3(i): [Flow Rate] 0.5% Flopaam 3330S (8M molecular weight and 25~30 % degree of hydrolysis) in 3.0% sodium chloride brine with pH = 2.5 at 2 ml/min 174

Table 5.4: Measurement plan for the polymer coreflood experiments.....175

Table 5.5: Viscosities before and after filtration for all the polymer solutions (see Table 5.4 for the corresponding polymer information) 176

Table 5.6: Properties of the injected polymer solutions for a base case, 0.5% Flopaam 3330S (8M MW and 25~30% degree of hydrolysis), prepared in 0.5% sodium chloride brine with pH = 2.5 at 1 ml/min 176

Table 5.7: Comparison results of solution properties and transport efficiencies for the injection polymer solutions with different pH conditions 177

Table 5.8: Comparison results of solution properties and transport efficiencies for the injection polymer solutions with different polymer concentrations 178

Table 5.9: Comparison results of solution properties and transport efficiencies for the polymer solutions with different molecular weights.....179

Table 5.10: Comparison results of solution properties and transport efficiencies for the polymer solutions with different salinities.....180

Table 5.11: Comparison results of solution properties and transport efficiencies for the polymer solutions with different degrees of hydrolyses 181

Table 5.12: Comparison results of solution properties and transport efficiencies for the polymer solutions with different flow rates 182

Table 5.13: Trends for adsorption level and IPV of the polymer solutions during dynamic flow conditions in low pH conditions 183

Table 6.1: Mineral Reactions and Equilibrium Constants (at 25°C) 214

Table 6.2: Intra-Aqueous Reactions Equilibrium Constants for Four-Mineral Simulations 214

Table 6.3: Mineral Reaction Constants (at 25°C) from Literature and History Matching 214

Table 6.4: Mineral Concentrations, Reactive Surface Areas and Activation Energies....215
Table 6.5: Properties of Two-Layer Linear Model....215
Table 7.1: Properties of rocks used in this research....234
Table 7.2: Results obtained from polymer flood on fractured sandstone cores235
Table 7.3: Results of constant pressure tests, Case A....235
Table 7.4: Results of constant pressure tests, Case B....235

List of Figures

Figure 1.1: Typical Maxwell type behavior of elastic and viscous moduli in oscillatory testing (Barnes, 2000) 32

Figure 1.2: ARES LS-1 Rheometer.....32

Figure 1.3: Dynamic strain sweep test for 0.5% Flopaam 3330S prepared in 0.5% sodium chloride brine at pH = 10.2 33

Figure 1.4: Dynamic frequency sweep test for 0.5% Flopaam 3330S prepared in 0.5% sodium chloride brine at pH = 10.2 33

Figure 1.5: Strain-controlled transient test for 0.5% Flopaam 3330S prepared in 0.5% sodium chloride brine at pH = 10.2 at 1000 s^{-1} shear rate.....34

Figure 1.6: Steady rate test for 0.5% Flopaam 3330S prepared in 0.5% sodium chloride brine at pH = 10.2 34

Figure 1.7: Plan for the rheological measurements of HPAM solutions.....35

Figure 1.8: Comparison results of viscosities between the first and second measurements for 0.5% Flopaam 3330S prepared in 0.5% sodium chloride brine as a function of pH.....35

Figure 1.9: Comparison results of dynamic frequencies between the first and second measurements for 0.5% Flopaam 3330S prepared in 0.5% sodium chloride brine at pH = 2 and 10 as a function of frequency.....36

Figure 1.10: Comparison results of measured viscosities between ARES LS-1 rheometer and Fann 35A viscometer for 0.5% Flopaam 3330S prepared in 0.5% sodium chloride brine as a function of shear rate.....36

Figure 1.11: Chemical Structure of Partially Hydrolyzed Polyacrylamide. The left molecule represents amino groups and the right molecule indicates carboxyl functional groups. Hydrolysis level is defined by the mole % of carboxyl functional groups amongst the total functional groups 37

Figure 1.12: Viscosity measurements for 0.5% Flopaam 3330S prepared in 0.5% sodium chloride brine as a function of pH.....37

Figure 1.13: Viscosity measurements for 0.5% Flopaam 3330S prepared in 0.5% sodium chloride brine as a function of shear rate 38

Figure 1.14: Elastic modulus measurements for 0.5% Flopaam 3330S prepared in 0.5% sodium chloride brine as a function of frequency 38

Figure 1.15: Viscous modulus measurements for 0.5% Flopaam 3330S prepared in 0.5% sodium chloride brine as a function of frequency 39

Figure 1.16: pH sensitivity of relaxation time for 0.5% Flopaam 3330S prepared in 0.5% sodium chloride brine 39

Figure 1.17: Loss modulus versus elastic modulus for 0.5% Flopaam 3330S prepared in 0.5% sodium chloride brine 40

Figure 1.18(a): Influence of polymer concentration on measured viscosity as a function of pH for Flopaam 3330S prepared in 0.5% sodium chloride brine 40

Figure 1.18(b): Influence of polymer concentration on measured viscosity as a function of pH for Flopaam 3330S prepared in 0.5% sodium chloride brine at shear rate of 10^{-1} 41

Figure 1.18(c): Measured viscosity as a function of polymer concentration at specific pH's for Flopaam 3330S prepared in 0.5% sodium chloride brine 41

Figure 1.18(d): Influence of polymer concentration on measured viscosity as a function of shear rate at two specific pH's (pH = 2 and 10) for Flopaam 3330S prepared in 0.5% sodium chloride brine.....42

Figure 1.18(e): Influence of polymer concentration on elastic modulus (G') change at two specific pH's (pH = 2 and 10) for Flopaam 3330S prepared in 0.5% sodium chloride brine 42

Figure 1.18(f): Influence of polymer concentration on viscous modulus (G") change at two specific pH's (pH = 2 and 10) for Flopaam 3330S prepared in 0.5% sodium chloride brine 43

Figure 1.18(g): Influence of polymer concentration on elastic and viscous modulus Change at two specific pH's (pH = 2 and 10) for Flopaam 3330S prepared in 0.5% sodium chloride brine 43

Figure 1.18(h): Influence of polymer concentration on approximate relaxation time as a function of pH for Flopaam 3330S prepared in 0.5% sodium chloride brine 44

Figure 1.19(a): Influence of salinity on measured viscosity as a function of pH for 0.5% Flopaam 3330S prepared in sodium chloride brine.....44

Figure 1.19(b): Influence of salinity on measured viscosity as a function of pH for 0.5% Flopaam 3330S prepared in sodium chloride brine at shear rate of 10^{-1} 45

Figure 1.19(c): Measured viscosity as a function of salinity at specific pH's for 0.5% Flopaam 3330S prepared in sodium chloride brine.....45

Figure 1.19(d): Influence of salinity on measured viscosity as a function of shear rate at two specific pH's (pH = 2 and 10) for 0.5% Flopaam 3330S prepared in sodium chloride brine 46

Figure 1.19(e): Influence of salinity on elastic modulus (G') change at two specific pH's (pH = 2 and 10) for 0.5% Flopaam 3330S prepared in sodium chloride brine 46

Figure 1.19(f): Influence of salinity on viscous modulus (G") change at two specific pH's (pH = 2 and 10) for 0.5% Flopaam 3330S prepared in sodium chloride brine 47

Figure 1.19(g): Influence of salinity on elastic and viscous modulus change at two specific pH's (pH = 2 and 10) for 0.5% Flopaam 3330S prepared in sodium chloride brine 47

Figure 1.19(h): Influence of salinity on approximate relaxation time as a function of pH for 0.5% Flopaam 3330S prepared in sodium chloride brine 48

Figure 1.20(a): Influence of degree of hydrolysis on measured viscosity as a function of pH for 0.5% polymer prepared in 0.5% sodium chloride brine 49

Figure 1.20(b): Influence of degree of hydrolysis on measured viscosity as a function of pH for 0.5% polymer prepared in 0.5% sodium chloride brine at shear rate of 10^{-1} 49

Figure 1.20(c): Measured viscosity as a function of degree of hydrolysis at specific pH's for 0.5% polymer prepared in 0.5% sodium chloride brine 50

Figure 1.20(d): Influence of degree of hydrolysis on measured viscosity as a function of shear rate at two specific pH's (pH = 2 and 10) for 0.5% polymer prepared in 0.5% sodium chloride brine.....50

Figure 1.20(e): Influence of degree of hydrolysis on elastic modulus (G') change at two specific pH's (pH = 2 and 10) for 0.5% polymer prepared in 0.5% sodium chloride brine 51

Figure 1.20(f): Influence of degree of hydrolysis on viscous modulus (G") change at two specific pH's (pH = 2 and 10) for 0.5% polymer prepared in 0.5% sodium chloride brine 51

Figure 1.20(g): Influence of degree of hydrolysis on elastic and viscous modulus Change at two specific pH's (pH = 2 and 10) for 0.5% polymer prepared in 0.5% sodium chloride brine.....52

Figure 1.20(h): Influence of degree of hydrolysis on approximate relaxation time as a function of pH for 0.5% polymer prepared in 0.5% sodium chloride brine 52

Figure 1.21(a): Influence of molecular weight on measured viscosity as a function of pH for 0.5% polymer prepared in 0.5% sodium chloride brine ...53

Figure 1.21(b): Influence of molecular weight on measured viscosity as a function of pH for 0.5% polymer prepared in 0.5% sodium chloride brine at shear rate of 10^{-1} 53

Figure 1.21(c): Measured viscosity as a function of molecular weight at specific pH's for 0.5% polymer prepared in 0.5% sodium chloride brine 54

Figure 1.21(d): Influence of molecular weight on measured viscosity as a function of shear rate at two specific pH's (pH = 2 and 10) for 0.5% polymer prepared in 0.5% sodium chloride brine 54

Figure 1.21(e): Influence of molecular weight on elastic modulus (G') change at two specific pH's (pH = 2 and 10) for 0.5% polymer prepared in 0.5% sodium chloride brine 55

Figure 1.21(f): Influence of molecular weight on viscous modulus (G") change at two specific pH's (pH = 2 and 10) for 0.5% polymer prepared in 0.5% sodium chloride brine 55

Figure 1.21(g): Influence of molecular weight on elastic and viscous modulus change at two specific pH's (pH = 2 and 10) for 0.5% polymer prepared in 0.5% sodium chloride brine 56

Figure 1.21(h): Influence of molecular weight on approximate relaxation time as a function of pH for 0.5% polymer prepared in 0.5% sodium chloride brine 56

Figure 1.22(a): Influence of divalent ion on measured viscosity as a function of pH for 0.5% Flopaam 3330S prepared in 0.5% brine.....57

Figure 1.22(b): Influence of divalent ion on measured viscosity as a function of pH for 0.5% Flopaam 3330S prepared in 0.5% brine at shear rate of 10^{-1} ...57

Figure 1.22(c): Measured viscosity as a function of divalent ion at specific pH's for 0.5% Flopaam 3330S prepared in 0.5% brine 58

Figure 1.22(d): Influence of divalent ion on measured viscosity as a function of shear rate at two specific pH's (pH = 2 and 10) for 0.5% Flopaam 3330S prepared in 0.5% brine.....58

Figure 1.22(e): Influence of divalent ion on elastic modulus (G') change at two specific pH's (pH = 2 and 10) for 0.5% Flopaam 3330S prepared in 0.5% brine 59

Figure 1.22(f): Influence of divalent ion on viscous modulus (G") change at two specific pH's (pH = 2 and 10) for 0.5% Flopaam 3330S prepared in 0.5% brine 59

Figure 1.22(g): Influence of divalent ion on elastic and viscous modulus change at two specific pH's (pH = 2 and 10) for 0.5% Flopaam 3330S prepared in 0.5% brine.....60

Figure 1.22(h): Influence of divalent ion on approximate relaxation time as a function of pH for 0.5% Flopaam 3330S prepared in 0.5% brine.....60

Figure 2.1: Typical non-Newtonian shear thinning behavior of polymer solution ...79

Figure 2.2: A comparison of viscosity curves between microgel (1.0% Carbopol EZ-2 in 3.0% sodium chloride brine) and HPAM (0.5% Flopaam 3330S in 0.5% sodium chloride brine) at shear rate = 10 s^{-1} 79

Figure 2.3: A flowchart for the viscosity modeling procedure of HPAM polymer ..80

Figure 2.4: Calculated equilibrium swelling ratio of microgel with $\bar{M}_n$ = 75,000 and $\bar{M}_c$ = 12,000 to calculated equilibrium chain-extension ratio of HPAM with $\bar{M}_n$ = 8,000,000 and $\bar{M}_c$ = 71. Common parameters: $\bar{\upsilon}$ = 0.8 cm^3/g; pK_a = 4.7; $\upsilon_{2,r}$ = 0.5; χ_1 = 0.8; I = 0.09.....81

Figure 2.5: Effect of pK_a on the equilibrium chain-extension ratio (Q) with: (1) pK_a = 2.0; (2) pK_a = 4.0; (3) pK_a = 6.0; (4) pK_a = 8.0; (5) pK_a = 10.0 81

Figure 2.6: Effect of ionic strength (I) on the equilibrium chain-extension ratio (Q) with: (1) I = 0.05; (2) I = 0.25; (3) I = 0.75; (4) I = 1.0; (5) I = 2.0.....82

Figure 2.7: Effect of $\upsilon_{2,r}$ on the equilibrium chain-extension ratio (Q) with: (1) $\upsilon_{2,r}$ = 0.1; (2) $\upsilon_{2,r}$ = 0.2; (3) $\upsilon_{2,r}$ = 0.3; (4) $\upsilon_{2,r}$ = 0.4; (5) $\upsilon_{2,r}$ = 0.5 82

Figure 2.8: Effect of χ_1 on the equilibrium chain extension ratio (Q) with: (1) χ_1 = 0.0; (2) χ_1 = 0.2; (3) χ_1 = 0.4; (4) χ_1 = 0.6; (5) χ_1 = 0.8 83

Figure 2.9: Curve-fitting graphs of measured (n-1) as a function of Clηl.....83

Figure 2.10: Curve-fitting graphs of measured λ as a function of Clηl 84

Figure 2.11: A comparison between laboratory data and model predictions for 0.2% of Flopaam 3330S prepared in 0.5% sodium chloride brine 84

Figure 2.12: A comparison between laboratory data and model predictions for 0.5% of Flopaam 3330S prepared in 0.5% sodium chloride brine 85

Figure 2.13: A comparison between laboratory data and model predictions for 0.8% of Flopaam 3330S prepared in 0.5% sodium chloride brine 85

Figure 2.14: A comparison between laboratory data and model predictions in terms of shear rate for 0.2% of Flopaam 3330S prepared in 0.5% sodium chloride brine 86

Figure 2.15: A comparison between laboratory data and model predictions in terms of shear rate for 0.5% of Flopaam 3330S prepared in 0.5% sodium chloride brine 86

Figure 2.16: A comparison between laboratory data and model predictions in terms of shear rate for 0.8% of Flopaam 3330S prepared in 0.5% sodium chloride brine 87

Figure 2.17: A comparison between laboratory data and model predictions for 0.5% of Flopaam 3330S prepared in 1.0% sodium chloride brine 87

Figure 2.18: A comparison between laboratory data and model predictions for 0.5% of Flopaam 3330S prepared in 3.0% sodium chloride brine 88

Figure 2.19: A comparison between laboratory data and model predictions for 0.5% of Flopaam 3330S prepared in 10.0% sodium chloride brine 88

Figure 2.20: Equilibrium chain extension ratio and measured viscosity as a function of salinity ranging from 0 to 10% for 0.5% Flopaam 3330S in sodium chloride brine at pH = 10.0 89

Figure 2.21: A comparison between laboratory data and model predictions for 0.5% Flopaam 3330S prepared in 0.2% sodium chloride and 0.3% calcium chloride brine 89

Figure 2.22: A comparison between laboratory data and model predictions for 0.2% of Flopaam 3630S prepared in 0.5% sodium chloride brine 90

Figure 2.23: A comparison between laboratory data and model predictions for 0.5% of Flopaam 3630S prepared in 0.5% sodium chloride brine 90

Figure 2.24: A comparison between laboratory data and model predictions for 0.2% of Flopaam 2330S prepared in 0.5% sodium chloride brine 91

Figure 2.25: A comparison between laboratory data and model predictions for 0.5% of Flopaam 2330S prepared in 0.5% sodium chloride brine 91

Figure 2.26: A comparison between laboratory data and model predictions for 0.2% of ALP99VHM prepared in 0.5% sodium chloride brine.....92

Figure 2.27: A comparison between laboratory data and model predictions for 0.5% of ALP99VHM prepared in 0.5% sodium chloride brine.....92

Figure 3.1: Effluent pH history as a function of pore volume injected (PVI) when hydrochloric acid with pH = 1.0 is injected into 1” diameter and 9” long Berea core 109

Figure 3.2: Comparison results of the effluent pH histories as a function of PVI between hydrochloric acid and citric acid in Berea core plug.....109

Figure 3.3: Schematic diagram for the acid coreflood setup.....110
Figure 3.4: Photograph of the acid coreflood setup 110
Figure 3.5: Photomicrograph taken under plain-polarizer for the thin section analysis of Berea sandstone before acidizing (1).....111
Figure 3.6: Photomicrograph taken under plain-polarizer for the thin section analysis of Berea sandstone before acidizing (2).....111
Figure 3.7: Photomicrograph taken under plain-polarizer for the thin section analysis of Berea sandstone after acidizing (1).....112
Figure 3.8: Photomicrograph taken under plain-polarizer for the thin section analysis of Berea sandstone after acidizing (2).....112
Figure 3.9: Results by microprobe equipped with energy-dispersive analysis by x-rays (EDAX) system.....113
Figure 3.10: Effluent pH and pressure drop history as a function of pore volume injected for test number [A1].....113
Figure 3.11: Effluent pH and pressure drop history as a function of pore volume injected for test number [A2].....114
Figure 3.12: Effluent pH and pressure drop history as a function of pore volume injected for test number [A3].....114
Figure 3.13: Effluent pH and pressure drop history as a function of pore volume injected for test number [A4].....115
Figure 3.14: Effluent pH and pressure drop history as a function of pore volume injected for test number [A5].....115
Figure 3.15: Comparison of all the effluent pH responses for the five coreflood experiments.....116
Figure 3.16: Comparison of all the effluent pH responses for the five coreflood experiments with the extended x-axis scale.....116

Figure 3.17: Five cations history - Aluminum (*Al*), Calcium (*Ca*), Iron (*Fe*), Magnesium (*Mg*), and Potassium (*K*) – as a function of pore volume injected for test number [A1].....117

Figure 3.18: Five cations history - Aluminum (*Al*), Calcium (*Ca*), Iron (*Fe*), Magnesium (*Mg*), and Potassium (*K*) – as a function of pore volume injected for test number [A2].....117

Figure 3.19: Five cations history - Aluminum (*Al*), Calcium (*Ca*), Iron (*Fe*), Magnesium (*Mg*), and Potassium (*K*) – as a function of pore volume injected for test number [A3].....118

Figure 3.20: Five cations history - Aluminum (*Al*), Calcium (*Ca*), Iron (*Fe*), Magnesium (*Mg*), and Potassium (*K*) – as a function of pore volume injected for test number [A4].....118

Figure 3.21: Five cations history - Aluminum (*Al*), Calcium (*Ca*), Iron (*Fe*), Magnesium (*Mg*), and Potassium (*K*) – as a function of pore volume injected for test number [A5].....119

Figure 4.1: Initial pH history matching result for Test no. [A1], which is an injection of pH = 2.5 citric acid in 3% sodium chloride brine into a 5" long Berea core at 1 ml/min, without shut-in.....138

Figure 4.2: pH history matching result by change of the equilibrium reaction constants of carbonate acid and bicarbonate reactions for Test no. [A1], which is an injection of pH = 2.5 citric acid in 3% sodium chloride brine into a 5" long Berea core at 1 ml/min, without shut-in.....138

Figure 4.3: pH history matching result by change of the equilibrium reaction constants in the reactions between divalent-ions and carbonate ions for Test no. [A1], which is an injection of pH = 2.5 citric acid in 3% sodium chloride brine into a 5" long Berea core at 1 ml/min, without shut-in .139

Figure 4.4(a): Final pH history matching result for Test no. [A1], which is an injection of pH = 2.5 citric acid in 3% sodium chloride brine into a 5" long Berea core at 1 ml/min, without shut-in 139

Figure 4.4(b): Final cation history matching result for Test no. [A1], which is an injection of pH = 2.5 citric acid in 3% sodium chloride brine into a 5" long Berea core at 1 ml/min, without shut-in 140

Figure 4.5(a): Final pH history matching result for Test no. [A2], which is an injection of pH = 2.5 citric acid in 3% sodium chloride brine into an 8" long Berea core at 1 ml/min, without shut-in 140

Figure 4.5(b): Final cation history matching result for Test no. [A2], which is an injection of pH = 2.5 citric acid in 3% sodium chloride brine into an 8" long Berea core at 1 ml/min, without shut-in 141

Figure 4.6(a): Final pH history matching result for Test no. [A3], which is an injection of pH = 2.5 citric acid in 3% sodium chloride brine into a 5" long Berea core at 2 ml/min, without shut-in 141

Figure 4.6(b): Final cation history matching result for Test no. [A3], which is an injection of pH = 2.5 citric acid in 3% sodium chloride brine into a 5" long Berea core at 2 ml/min, without shut-in 142

Figure 4.7(a): Final pH history matching result for Test no. [A4], which is an injection of pH = 2.5 citric acid in 3% sodium chloride brine into a 5" long Berea core at 1 ml/min, with shut-ins.....142

Figure 4.7(b): Final cation history matching result for Test no. [A4], which is an injection of pH = 2.5 citric acid in 3% sodium chloride brine into a 5" long Berea core at 1 ml/min, with shut-ins.....143

Figure 4.8(a): Final pH history matching result for Test no. [A5] which is an injection of pH = 3.5 citric acid in 3% sodium chloride brine into a 5" long Berea core at 1 ml/min, without shut-in 143

Figure 4.8(b): Final cation history matching result for Test no. [A5], which is an injection of pH = 3.5 citric acid in 3% sodium chloride brine into a 5" long Berea core at 1 ml/min, without shut-in 144

Figure 5.3: Schematic diagram of an experimental setup for polymer coreflood ...184

Figure 5.4: Photograph of the polymer coreflood setup.....184

Figure 5.5: Schematic diagram of experimental procedure for polymer corefloods185

Figure 5.6: Comparison result between TOC and capillary tube methods.....186

Figure 5.7: Results of capillary tube-tests for a base case, 0.5% Flopaam 3330S (which has 8M molecular weight and 25~30% degree of hydrolysis), prepared in 0.5% sodium chloride brine with pH = 2.5 at 1 ml/min 186

Figure 5.8: Calibration curve for capillary tube-test for a base case.....187

Figure 5.9: Calibration curve for bromide tracer test for a base case.....187

Figure 5.10: Pressure drop responses across the core as a function of pore volume injected (PVI) during brine and acid injection for a base case 188

Figure 5.11: Pressure drop responses across the capillary tube as a function of pore volume injected (PVI) during brine and acid injection for a base case 188

Figure 5.12: Effluent pH history as a function of pore volume injected (PVI) during brine and acid injection for a base case 189

Figure 5.13: Permeability reduction as a function of pore volume injected (PVI) during polymer flooding for a base case.....189

Figure 5.14: Mobility reduction as a function of pore volume injected (PVI) during polymer flooding for a base case 190

Figure 5.15: Normalized concentration of polymer and bromide tracer as a function of pore volume injected (PVI) during polymer flooding for a base case190

Figure 5.16(a): Permeability reductions as a function of PVI for the injection polymer solutions with different pH conditions.....191

Figure 5.16(b): Mobility reductions as a function of PVI for the injection polymer solutions with different pH conditions.....191
Figure 5.16(c): Adsorption and inaccessible pore volume as a function of PVI for the injection polymer solutions with different pH conditions 192
Figure 5.17(a): Permeability reductions as a function of PVI for the injection polymer solutions with different polymer concentrations 192
Figure 5.17(b): Mobility reductions as a function of PVI for the injection polymer solutions with different polymer concentrations.....193
Figure 5.17(c): Adsorption and inaccessible pore volume as a function of PVI for the injection polymer solutions with different polymer concentrations193
Figure 5.18(a): Permeability reductions as a function of PVI for the injection polymer solutions with different molecular weights 194
Figure 5.18(b): Mobility reductions as a function of PVI for the injection polymer solutions with different molecular weights.....194
Figure 5.18(c): Adsorption and inaccessible pore volume as a function of PVI for the injection polymer solutions with different molecular weights.....195
Figure 5.19(a): Permeability reductions as a function of PVI for the injection polymer solutions with different salinities.....195
Figure 5.19(b): Mobility reductions as a function of PVI for the injection polymer solutions with different salinities 196
Figure 5.19(c): Adsorption and inaccessible pore volume as a function of PVI for the injection polymer solutions with different salinities.....196
Figure 5.20(a): Permeability reductions as a function of PVI for the injection polymer solutions with different degrees of hydrolysis.....197
Figure 5.20(b): Mobility reductions as a function of PVI for the injection polymer solutions with different degrees of hydrolysis 197

Figure 5.20(c): Adsorption and inaccessible pore volume as a function of PVI for the injection polymer solutions with different degrees of hydrolysis...198

Figure 5.21(a): Permeability reductions as a function of PVI for the injection polymer solutions with different flow rates 198

Figure 5.21 (b): Mobility reductions as a function of PVI for the injection polymer solutions with different flow rates 199

Figure 5.21(c): Adsorption and inaccessible pore volume as a function of PVI for the injection polymer solutions with different flow rates 199

Figure 5.22: Desorption test for Test no. 6 (0.5% Flopaam 3330S (which has 8M molecular weight and 25~30% degree of hydrolysis), prepared in 2.0% sodium chloride brine with pH = 2.5 at 1 ml/min.....200

Figure 6.1: Calculated Polymer Viscosity for 3wt% EZ-2 Polymer Solution (Ionic Strength = 0.5, No Flow) 216

Figure 6.2: pH versus Volume of Acid Injected for Coreflood Experiment 1 216

Figure 6.3: pH versus Volume of Acid Injected for Coreflood Experiment 2 217

Figure 6.4: pH versus Volume of Acid Injected for Coreflood Experiment 3 217

Figure 6.5: Reaction Affinity (for Mineral Reactions), Mineral Concentrations and Select Ion Concentration Profiles for Experiment 2 After 50 Pore Volumes Injected (Using Final-Match Reaction Parameters) 218

Figure 6.6: Effluent pH for Calcite Model with First-order Calcite Reaction (Experiment 1) 218

Figure 6.7: Effluent pH for Calcite Model with First-order Calcite Reaction (Experiment 2) 219

Figure 6.8: Effluent pH for Calcite Model with First-order Calcite Reaction (Experiment 3) 219

Figure 6.9: Schematic of Two-Layer Linear Oil Reservoir Simulation Grid.....220

Figure 6.10: Produced Oil Volume versus Volume of Fluid Injected (Linear Case-No Crossflow).....220
Figure 6.11: Oil Recovery versus Volume of Fluid Injected Using 0.05 HCPV Slug Treatment Followed by Waterflooding (Linear Case, No Crossflow) .221
Figure 6.12: Aqueous Phase Viscosity Distribution in Linear Reservoir During 1000-cp pH-Sensitive Polymer Slug Treatment Simulation (Linear Case, No Crossflow).....221
Figure 6.13: Schematic of Two-Layer Radial Oil Reservoir Simulation Grid.....222
Figure 6.14: Oil Recovery versus Volume of Fluid Injected Using pH-Sensitive Polymer (Radial Case, No Crossflow).....222
Figure 6.15: Oil Recovery versus Volume of Fluid Injected Using 0.05 HCPV Slug Treatment Followed by Waterflooding (Radial Case, No Crossflow) .223
Figure 6.16: Oil Recovery versus Volume of Fluid Injected Using 0.1 HCPV Slug Treatment Followed by Waterflooding (Radial Case).....223
Figure 6.17: Injection Rate versus Time (Constant Injection Pressure, Radial Case, No Crossflow).....224
Figure 7.1: Variation of apparent viscosity of Carbopol 934% with pH (Choi, 2006).236
Figure 7.2: Left to right: Indiana limestone, Texas Cream limestone and Berea sandstone.....236
Figure 7.3: Top and side view of fractured cores.....237
Figure 7.4: Set up of water/polymer flooding experiment at constant injection rate.237
Figure 7.5: Set up of constant pressure water/polymer flooding experiments.....237
Figure 7.6: Set up of constant pressure polymer recycling experiments.....238
Figure 7.7: Change in polymer solution pH with time of contact with different materials.....238
Figure 7.8: Polymer batch test. From left to right: CaCl2, limestone and sandstone containers.....239

Figure 7.9: Change in polymer pH during polymer injection 239
Figure 7.10: PRF vs. Shut-in time 240
Figure 7.11: Picture of core cross section midway along the core. Blue color indicates invasion of matrix by water from the polymer solution in the fracture.240
Figure 7.12: Pressure drop after and before polymer injection for experiment #1 ...241
Figure 7.13: Pressure drop across the Texas Cream fractured core after and before polymer injection 241
Figure 7.14: Blue regions correspond to channels created by dyed water flowed through the microgel-filled fracture at a sufficiently large pressure.....242
Figure 7.15: Beaker and effluent pH versus pore volume of polymer injected 242
Figure 7.16: Total core permeability in polymer recycling experiment.....243
Figure 7.17: Effluent fluid during the polymer recycling experiment 243
Figure 7.18: Microgel distribution inside the fracture.....243
Figure 7.19: Pressure drop across the core and effluent pH versus time, polymer recycling, Indiana limestone 244

Bibliography

Ait-Kadi, A., Carreau, R. J., and Chauveteau, G.: "Rheological Properties of Partially Hydrolyzed Polyacrylamide Solutions", *J. Rheol.*, **31**(7), 537-561, 1987.

Al-Anazi, H. A., and Sharma, M. M.: "Evaluation of a pH-Sensitive Polymer for Gravel-Packing Operations", *SPE Drilling & Completion*, 28-36, March 2001.

Al-Anazi, H. A., and Sharma, M. M.: "Use of pH Sensitive Polymer for Conformance Control", SPE 73782 presented at SPE Intern. Symp. Formation Damage Control, Lafayette, LA, Feb. 20-21, 2002.

Alishaeva, O. M., and Entov, V. M.: "Influence of Inaccessible Pore Volume on the Displacement of Oil by a Polymer Solution", *Fluid Dynamics*, **18**(6), November, 1983.

Al-Moajil, A., Nasr-El-Din, H. A., Al-Yami, A., Al-Aamri, A., and Al-Aqil, A.: "Removal of Filter Cake Formed by Manganese Tetraoxide Based-Drilling Fluids", SPE 112450 presented at 2008 SPE International Symposium and Exhibition on Formation Damage Control, Lafayette, LA, Feb. 13-15, 2008.

Al-Otaibi, M. B., Nasr-El-Din, H. A., Hill, A. D.: "Characteristics and Removal of Filter Cake Formed by Formate-Based Drilling Mud", SPE 112427 presented at 2008 SPE International Symposium and Exhibition on Formation Damage Control, Lafayette, LA, Feb. 13-15, 2008.

Andrew, D. W., Katz, L. E., and Chen, C-C.: "The Impact of Ionic Strength and Background Electrolyte on pH Measurements in Metal Ion Adsorption Experiments", *J. Coll. Int. Sci*., **301**, 329-332, 2006.

API RP 63, Recommended practice for evaluation of polymers used in enhanced oil recovery operations, 1st edition, 1990.

Baijal, S. K.: "Polymer Molecules Interact with Porous Matrix", *Oil and Gas J*., 106-107, March 1981.

Barnes, H. A.: "A Handbook of Elementary Rheology", The University of Wales Institute of Non-Newtonian Fluid Mechanics, Wales, 2000.

Bartelds, A.: "The influence of inaccessible and excluded pore volume on polymer flooding", Dissertation, Technische Universiteit Delft, 1998.

Benson, I. P.: "Numerical Simulation of pH-Sensitive Polymer Injection as a Conformance Control Method", Thesis, The University of Texas at Austin, May 2007.

Bingham, E. C.: "Fluidity and Plasticity", McGraw-Hill, New York, 1962.

Bird, R. B., Stewart, W. E., and Lightfoot, E. N.: "Transport Phenomena", Wiley, New York, 1960.

Bohdanecky, M., and Kovar, J.: "Viscosity of Polymer Solutions", Elsevier Science Ltd, September 1982.

Borling, D., Chan, K., Hughes, T., and Sydansk, R.: "Pushing Out the Oil with Conformance Control", *Oilfield Review*, **6**(2), 44-58, April 1994.

Brannon-Peppas, L., and Peppas, N. A.: "Structural Analysis of Charged Polymeric Networks", *Polymer Bull*., **20**, 285-289, 1988.

Brannon-Peppas, L., "Preparation and Characterization of Crosslinked Hydrophilic Networks", in Absorbent Polymer Technology, Studies in Polymer Sci., 8, Brannon-Peppas, L., and Harland, R. S., eds., 45-66, 1990.

Brannon-Peppas, L., and Peppas, N. A., "The Equilibrium Swelling Behavior of Porous and Non-Porous Hydrogels", in Absorbent Polymer Technology, Studies in Polymer Sci., 8, Brannon-Peppas, L., and Harland, R. S., eds., 67-102, 1990.

Brannon-Peppas, L., and Peppas, N. A., "Equilibrium Swelling Behavior of pH-Sensitive Hydrogels", *Chem. Eng. Sci.*, **46**(3), 715-722, 1991.

Broseta, D., Medjahed, F., Lecourtier, J., and Robin, M.: "Polymer Adsorption/Retention in Porous Media: Effects of Core Wettability and Residual Oil", *SPE Advanced Technology Series*, **3**(1), 103-112, 1995.

Bryant, S. L., and Lockhart, T. P.: "Reservoir Engineering Analysis of Microbial Enhanced Oil Recovery", *SPE Reservoir Evalauaion and Enginnering*, **5**, 365-374, October, 2002.

Butler, J. N., and Cogley, D. R.: "Ionic Equilibrium: Solubility and pH Calculations", Jonh Wiley & Sons, Inc., New York, 1998.

Cannella, W. J., Huh, C., and Seright, R. S.: "Prediction of Xanthan Rheology in Porous Media", SPE 18089 presented at 63rd Annual Tech. Conf. SPE, Houston, TX, Oct. 2-5, 1988.

Carr, M. B., and Christopher, A. P.: "Spatial Analysis of Fabric Elements in the Berea Sandstone through Petrographic Image Analysis", *AAPG Bull*., **82** (13), May 1998.

Chauveteau, G., and Zaitoun, A.: "Basic Rheological Behavior of Xanthan Polysaccharide Solutions in Porous Media: Effects of Pore Size and Polymer Concentration", In: F.J. Fayers, Editor, Proceedings of the First European Symposium on Enhanced Oil Recovery, Bournemouth, England, Society of Petroleum Engineers, Richardson, TX, 197–212, 1981.

Chauveteau, G., Tirrell, M., and Omari, A.: "Concentration Dependence of Effective Viscosity of Polymer Solutions in Small Pores with Repulsive or Attractive Walls", *J. Coll. Int. Sci*., **100**(41), 1984.

Chauveteau, G., and Lecourtier, J.: "Propagation of Polymer Slugs Through Adsorbent Porous Media", in: Water-Soluble Polymers for Petroleum Recovery, eds Stahl, G. A., and Schulz, D. N., Plenum Press, New York, 53-68, 1988.

Chauveteau, G., Omari, A., Tabary, R., Renard, M., Veerapen, J., and Rose, J.: "New Size-Controlled Microgels for Oil Production", SPE 64988 presented at SPE Intern. Symp. Oilfield Chemistry, Houston, TX, Feb. 13-16, 2001.

Chauveteau, G., Denys, K., and Zaitoun, A.: "New Insight on Polymer Adsorption Under High Flow Rates", SPE 75183 presented at SPE/DOE Improved Oil Recovery Symposium, Tulsa, OK, Apr. 13-17, 2002.

Chauveteau, G., Tabary, R., le Bon, C., Renard, M., Feng, Y., and Omari, A.: "In-Depth Permeability Control by Adsorption of Soft Size-Controlled Microgels", SPE 82228 presented at SPE European Formation Damage Conf., The Hague, Netherlands, May 13-14, 2003.

Chauveteau, G., Tabary, R., Blin, N., Renard, M., Rousseau, D., and Faber, R.: "Disproportionate Permeability Reduction by Soft Preformed Microgels", SPE 89390 presented at SPE/DOE 14th Improved Oil Recovery Symp., Tulsa, OK, Apr. 17-21, 2004.

Cheung, S. K., Van Arsdale, and Howard: "Matrix Acid Stimulation Studies Yield New Results With a Multitap Long-Core Permeameter", *J. Pet. Tech.*, **44**(1), Jan., 1992.

Choi, S. K.: "A Study of a pH-Sensitive Polymer for Novel Conformance Control Applications", Thesis, The University of Texas at Austin, December 2005.

Choi, S. K., Ermel, Y. M., Bryant, S. L., Huh, C., and Sharma, M. M.: "Transport of a pH-Sensitive Polymer in Porous Media for Novel Mobility Control Applications", SPE 99656 presented at 2006 SPE/DOE Improved Oil Recovery Symp., Tulsa, OK, Apr. 22-26, 2006.

Churcher, P. L., French, P. R., Shaw, J. C., and Schramm, L. L.: "Rock Properties of Berea Sandstone, Baker Dolomite, and Indiana Limestone", SPE 21044 presented at the SPE International Symposium on Oilfield Chemistry, Anaheim, CA, Feb. 20-22, 1991.

Dawson, R., and Lantz, R. B.: "Inaccessible Pore Volume in Polymer Flooding", *Soc. Petrol. Eng. J*., 448-452, Oct., 1972.

Delshad, M., Kim, D. H., Magbagbeola, O. A., Huh, C., Pope, G. A., and Tarahhom, F.: "Mechanistic Interpretation and utilization of Viscoelastic Behavior of Polymer Solutions for Improved Polymer-Flood Efficiency", SPE 113620 presented at the

2008 SPE Improved Oil Recovery Symposium held in Tulsa, OK, Apr. 19-23, 2008.

Denys, K. F. J., Zitha, P. L. J., Hensens, H. C., and te-Nijenhuis, K.: "Near-wellbore Formation Damage by Polyacrylates: Effects of pH and Salinity", SPE 39465 presented at 1998 SPE International Symposium on Formation Damage Control, Lafayette, LA, Feb. 18-19, 1998.

Dey, N. C., and Baijal, S. K.: "Retention Mechanism During Flow of Polymer Solutions Through Porous Media", SPE 7818, 1978.

Economides, M. J., Hill, A. D., and Ehlig-Economides, C.: "Petroleum Production Systems", Prentice Hall, Upper Saddle River, NJ, 1994.

Ermel, Y. M.: "Application of Geochemical Modeling to Optimize a pH-Sensitive Gel System", Thesis, The University of Texas at Austin, May 2005.

Feng, Y., Tabary, R., Renard, M., le Bon, C., Omari, A., and Chauveteau, G.: "Characteristics of Microgels Designed for Water Shutoff and Profile Control", SPE 80203 presented at SPE Intern. Symp. Oilfield Chemistry, Houston, TX, Feb. 5-7, 2003.

Ferrer, J.: "Some Mechanistic Features of Flow of Polymers Through Porous Media", SPE 4029 presented at the SPE-AIME 47th annual Fall Meeting, San Antonio, Oct. 8-11, 1972.

Flesch, G. A., and Almon, W. R.: "Berea (Mississippian) Sandstone Core from CSO Island Creek Coal C-7, McDowell County, West Virginia", *AAPG Bull.*, **61**(5), 784-785, May 1977.

Fletcher, A. J. P., Flew, S., Forsdyke, I. N., Morgan, J. C., Rogers, C., and Suttles, D.: "Deep Diverting Gels for Very Cost-Effective Waterflood Control", *J. Petrol. Sci. Eng.*, **7**, 33-43, 1992.

Flory, P. J.: "Principles of Polymer Chemistry", Cornell University Press, Ithaca, New York, 1953.

Frampton, H., Morgan, J. C., Cheung, S. K., Munson, L., Chang, K. T., and Williams, D.: "Development of a Novel Waterflood Conformance Control System", SPE 89391 presented at SPE/DOE 14th Improved Oil Recovery Symp., Tulsa, OK, Apr. 17-21, 2004.

Garver, F. J., Sharma, M. M., and Pope, G. A.: "The Competition for Chromium between Xanthan Biopolymer and Resident Clays in Sandstones", SPE 19632, presented at SPE Annual Technical Conference and Exhibition, San Antonio, Texas, October 8-11, 1989.

Ghannam, M. T., and Esmail, M. N.: "Rheological Properties of Aqueous Polyacrylamide Solutions", *J. Appl. Polymer Sci.*, **69**, 1587-1597, 1998.

Gramain, P., and Myard, P.: "Adsorption Studies of Polyacrylamides in Porous Media", *J. Coll. Int. Sci*., **84**(114), 1981.

Heller, H., and Keren, R.: "Anionic Polyacrylamide Polymer Adsorption by Pyrophyllite and Montmorillonite", *Clays and Clay Minerals*, **51**(3), 334-339, 2003.

Hill, J. H., Brew, J. R., Claridge, E. L., Hite, J. R., and Pope, G. A.: "The behavior of Polymers in Porous Media", SPE 4748 presented at Improved Oil recovery Symposium held in Tulsa, OK, Apr. 22-24, 1974.

Hirasaki, G. J., and Pope, G. A.: "Analysis of Factors Influencing Mobility and Adsorption in the Flow of Polymer Solution Through Porous Media", *Soc. Petrol. Eng. J*., 337-345, Aug., 1974.

Huang, T., Ostensen, L., and Hill, A. D.: "Carbonate Matrix Acidizing with Acetic Acid", SPE 58715 presented at the SPE International Symposium on Formation Damage Control, Lafayette, LA, Feb. 23-24, 2000.

Huggins, M. L., *J. Am. Chem. Soc*., **64**, 2716, 1942.

Huh, C., Choi, S. K., Sharma, M. M.: "A Rheological Model for pH Sensitive Ionic Polymer Solutions for Optimal Mobility Control Applications", SPE 96914 presented at 2005 SPE Annual Technical Conference and Exhibition, Dallas, TX, Oct. 9-12, 2005.

Hutchins, R. D., Dovan, H.T., and Sandiford, B. B.: "Aqueous Tracers for Oilfield Applications", SPE 21049 presented at the SPE International Symposium on Oilfield Chemistry, Anaheim, CA, Feb. 20-22, 1991.

Jennings, R. R., Rogers, J. H., and West, T. J.: "Factors Influencing Mobility Control by Polymer Solutions", ", *J. Pet. Tech.*, 391-401, March 1971.

Kabir, A. H.: "Chemical Water & Gas Shutoff Technology", SPE 72119 presented at SPE Asia Pacific Improved Oil Recovery Conf., Kuala Lumpur, Malaysia, October 8-9, 2001.

Kincaid, J. J., Eyring, H., and Stearn, A. E., Chem. Rev. **28**, 301-365, 1941.

Kolodziej, E. J.: "Transport Mechanisms of Xanthan Biopolymer Solutions in Porous Media", SPE 18090 presented at the 63rd Annual Technical Conference and Exhibition, Houston, TX, Oct. 2-5, 1988.

Kraemer, E. O., *Ind. Eng. Chem*., **30**, 1200, 1938.

Lakatos, I., Lakatos-Szabo, J., and Toth, J.: "Factors Influencing Polyacrylamide Adsorption in Porous Media and Their Effect on Flow Behaviour", Plenum Publishing Corp., New York, August 1979.

Lakatos, I., and Lakatos-Szabo, J., *Acta. Chim. Acad. Sci. Hung*. **105**, 57-72, 1980

Lake, L. W.: "Enhanced Oil Recovery", Prentice Hall, Upper Saddle River, New Jersey, 1989.

Lake, L. W., Bryant, S. L., and Araque-Martinez, A. N.: "Geochemistry and Fluid Flow", Elsevier Science B.V., The Netherlands, 2002.

Lange, E. A., and Huh, C.: "A Polymer Thermal Decomposition Model and Its Application in Chemical EOR Process Simulation", SPE/DOE 27822 presented at SPE/DOE Improved Oil Recovery Symp., Tulsa, OK, Apr. 17-20, 1994.

Lecourtier, J., and Chauveteau, G.: "Propagation of Polymer Slugs Through Porous Media", SPE 13034 presented at SPE Annual Technical Conference and Exhibition, Houston, TX, Sep. 16-19, 1984.

Lecourtier, J., Lee, J. T., and Chauveteau, G.: "Adsorption of Polyacryamides on Siliceous Minerals", Colloids and Surfaces, **47**, 219-231, 1990.

Lewandowska, K.: "Comparative Studies of Rheological Properties of Polyacrylamide and Partially Hydrolyzed Polyacrylamide Solutions", *J. Appl. Polymer Sci.*, **103**, 2235-2241, Jun. 2006.

Liang, J., and Seright, R. S.: "Wall-Effect/Gel-Droplet Model of Disproportionate Permeability Reduction", SPE 59344 presented at SPE/DOE Improved Oil Recovery Symp., Tulsa, OK, Apr. 3-5, 2000.

Lipatov, Y. S., and Sergeeva, L. M.: "Adsorption of Polymers", Wiley, New York, 1974.

Lyons, P. F., and Tobolsky, A. V.: "Viscosity of Polypropylene Oxide Solutions over the Entire Concentration Range", *Polym. Eng. Sci*., **10**, 1, 1970.

Mack, J. C., and Smith, J. E.: "In-Depth Colloidal Dispersion Gels Improve Oil Recovery Efficiency", SPE/DOE 27780 presented at SPE/DOE Improved Oil Recovery Symp., Tulsa, OK, Apr. 17-20, 1994.

Maerker, J. M.: "Shear Degradation of Partially Hydrolyzed Polyacrylamide Solutions", *Soc. Petrol. Eng. J*., 311-322, Aug., 1975.

Maerker, J. M., and Sinton, S. W.: "Rheology Resulting from Shear-Induced Structure in Associating Polymer Solutions", *Intl. Congress on Rheology*, Mexico, 393-410, 1984.

Martin, F. D. and Sherwood, N. S.: "The effect of hydrolysis of polyacrylamide on solution viscosity, polymer retention and flow resistance properties", SPE 5339 presented at SPE Rocky Mountain Regional Meeting, Denver, CO, 7-9 April 1975.

Mennella, A., Chiappa, L., Lockhart, T. P., and Burrafato, G.: "Candidate and Chemical Selection Rules for Water Shutoff Polymer Treatments", SPE 54736, presented at SPE European Formation Damage Conference in The Hague, The Netherlands, May 31–June 1, 1999.

Mezzomo, R. F., Moczydlower, P., Sanmartin, A. N., and Araujo, C. H. V.: "A New Approach to the Determination of Polymer Concentration in Reservoir Rock Adsorption Tests", SPE 75204 presented at the SPE/DOE 13th Symposium on Improved Oil Recovery, Tulsa, OK, Apr. 13-17, 2002.

Mungan, N.: "Rheology and adsorption of aqueous polymer solutions", *J. Can. Pet. Tech.*, **8**, April-June, 45, 1969.

Mungan, N.: "Shear Viscosities of Ionic Polyacrylamide Solutions", *SPE J.*, 469-473, Dec., 1972.

Nashawi, I. S.: "Laboratory Investigation of the Effect of Brine Composition on Polymer Solutions – Part 1: Partially Hydrolyzed Polyacrylamide (HPAM) Case", SPE 23533, 1991.

Nasr-El-Din, H. A., Hawkins, B. F., and Green, K. A.: "Viscosity Behavior of Alkaline, Surfactant, Polyacrylamide Solutions Used for Enhanced Oil Recovery", SPE 21028 presented at the SPE International Symposium on Oilfield Chemistry held in Anaheim, CA, February 20-22, 1991.

Needham, R. B., Threlkeld, C. B., and Gall, J. W.: "Control of Water Mobility using Polymers and Multivalent Cations", SPE 4747 presented at the IOR Symposium of the SPE of AIME, Tulsa, OK, 7-9 April 22-24, 1974.

Nghiem, L.: "Component and Reaction Data Input for GEM-GHG (Version 2002.14)", Computer Modeling Group, September 24, 2002.

Nghiem, L.: "Compositional Simulator for Carbon Dioxide Sequestration", Computer Modeling Group, July 2002.

Nghiem, L.: "Component and Reaction Data Input for GEM-GHG (Version 2002.30)", Computer Modeling Group, June 16, 2003.

Nghiem, L.: "Compositional Simulator for Carbon Dioxide Sequestration", Computer Modeling Group, June 2003.

Nghiem, L.: "Component and Reaction Data Input for GEM-GHG (Version 2004.19A), Computer Modeling Group, December 16, 2005.

Nouri, H. H. and Root, P. J.: "A Study of Polymer Solution Rheology, Flow Behavior, and Oil Displacement Processes", SPE 3523 presented at the SPE-AIME 46th Annual Fall Meeting, New Orleans, Oct. 3-6, 1971.

Omari, A., Tabary, R., Renard, M., Veerapen, J., and Rose, J.: "New Size-Controlled Microgels for Oil Production", SPE 64988 presented at SPE Intern. Symp. Oilfield Chemistry, Houston, TX, Feb. 13-16, 2001.

Palandri, J. L., and Kharaka, Y. K.: "A Compilation of Rate Parameters of Water-Mineral Interaction Kinetics for Application to Geochemical Modeling", U.S. Geological Survey, Open File Report 2004-1068, Menlo Park, California, March 2004.

Pritchett, J., Frampton, H., Brinkman, J., Cheung, S. K., Morgan, J. C., Chang, K. T., Williams, D., and Goodgame, J.: "Field Application of a New In-Depth Waterflood Conformance Improvement Tool", SPE 84897 presented at SPE Intern. Improved Oil Recovery Conf., Kuala Lumpur, Malaysia, Oct. 20-21, 2003.

Seright, R. S.: "The Effects of Mechanical Degradation and Viscoelastic Behavior on Injectivity of Polyacrylamide Solutions", *SPE AIME*, 475-485, Jun. 1983.

Seright, R. S., and Liang, J.: "A Survey of Field Applications of Gel Treatments for Water Shutoff", SPE 26991 presented at III Latin Amer./Caribbean Petrol. Eng. Conf., Buenos Aires, Argentina, Apr. 27-29, 1994.

Seright, R. S., "Gel Propagation through Fractures", *SPE Production & Facilities*, **16**, 225-231, November 2001.

Sevougian, S. A., Lake, L. W., and Schechter, R. S.: "KGEOFLOW: A New Reactive Transport Simulator for Sandstone Matrix Acidizing", *SPE Production & Facilities*, 13-19, February 1995.

Smith, F. W.: "The Behavior of Partially Hydrolyzed Polyacrylamide Solutions in Porous Media", *J. Pet. Tech.*, 148-156, February 1970.

Smith, M. J., Clark, G. J., Hendrickson, A. R., and Egbogah, E. O.: "Acidization of Dirty Sandstones With Buffered HF Acid Systems", SPE 14826 presented at the SPE Formation Damage Control Symposium, Lafayette, LA, Feb. 26-27, 1986.

Sorbie, K. S., Parker, A., and Clifford, P. J.: "Experimental and Theoretical Study of Polymer Flow in Porous Media", *SPE Reservoir Engineering*, 281-304, August 1987.

Sorbie, K. S.: "Polymer-Improved Oil Recovery", Blackie and Son Ltd, Glasgow, 1991.

Sorbie, K. S., and Mackay, E. J.: "Scale Inhibitor Placement: Back to Basics – Theory and Examples", SPE 95090 presented at SPE International Symp. Oilfield Scale, Aberdeen, United Kingdom, May 11-12, 2005

Southwick, J. G., and Manke, C. W.: "Molecular Degradation, Injectivity, and Elastic Properties of Polymer Solutions", *SPE Reservoir Engineering*, 1193-1201, November 1988.

Stumm, W., and Morgan, J. J.: "Aquatic Chemistry Chemical Equilibria and Rates in Natural Waters", 3rd Ed., John Wiley & Sons, Inc., New York, 1996.

Sydansk, R. D., and Moore, P. E.: "Production Responses in Wyoming's Big Horn Basin Resulting from Application of Acrylamide-Polymer/CrIII-Carboxylate Gels", SPE 21894, 1990.

Sydansk, R. D., and Southwell, G. P.: "More Than 12 Years of Experience with a Successful Conformance-Control Polymer Gel Technology", SPE 62561,

presented at SPE/AAPG Western Regional Meeting, Long Beach, California, June 19-23, 2000.

Sydansk, R. D., Xiong, Y., Al-Dhafeeri, A. M., and Seright, R .S.: "Polymer gels formulated with a combination of High-and low-molecular-weight polymers provide improved performance for water shut-off treatments of fractured production wells", *SPE Production & Facilities*, **19**, 229-236, November, 2004.

Sydansk, R. D., Xiong, Y., Al-Dhafeeri, A. M., Schrader, R. J., and Seright, R .S.: "Characterization of partially formed polymer gels for application to fracture production wells for water shutoff process.", *SPE Production and Facilities*, **20**, 240-249, August, 2005.

Szabo, M. T.: "Molecular and Microscopic Interpretation of the Flow of Hydrolyzed Polyacrylamide Solution through Porous Media", SPE 4028 presented at the 47th Annual Fall Meeting of the SPE of AIME in San Antonio, Texas, Oct. 8-11, 1972.

Szabo, M. T.: "Some Aspects of Polymer Retention in Porous Media Using a ^{14}C-tagged Hydrolysed Polyacrylamide", *Soc. Pet. Eng. J.*, 323, August 1975.

Szabo, M. T.: "An Evaluation of Water-Soluble Polymers For Secondary Oil Recovery – Part 1", *J. Pet. Tech.*, 553-560, May, 1979.

Szabo, M. T.: "An Evaluation of Water-Soluble Polymers For Secondary Oil Recovery – Part 2", *J. Pet. Tech.*, 561-570, May, 1979.

Tinker, G. E., Bowman, R. W., and Pope, G. A.: "Determination of In-Situ Mobility and Wellbore Impairment From Polymer Injectivity Data", *J. Pet. Tech.*, 586-593, May, 1976.

Vela, S., Peaceman, D. W., and Sandvik, E. I.: "Evaluation of Polymer Flooding in a Layered Reservoir with Crossflow, Retention, and Degradation", *Soc. Petrol. Eng. J.*, 82-96, Apr., 1976.

Wang, D., Xia, H., Liu, Z., and Yang, Q.: "Study of the Mechanism of Polymer Solution with Visco-Elastic Behavior Increasing Microscopic Oil Displacement Efficiency and the Forming of Steady "Oil Thread" Flow Channel", SPE 68723 presented at SPE Asia Pacific Oil Gas Conf., Jakarta, Indonesia, Apr. 17-19, 2001.

Ward, J. S., Martin, F. D.: "Prediction of Viscosity for Partially Hydrolyzed Polyacrylamide Solutions in the Presence of Calcium and Magnesium Ions", *SPE AIME*, 623-631, Oct. 1981.

Whittington, L. E., and Naae, D. G.: "Conformance Control Gels – Formation by Contact with Brine", *J. Petrol. Sci. Eng.*, **7**, 45-51, 1992.

Willhite, G. P. and Dominguez, J. G.: "Mechanisms of Polymer Retention in Porous Media" in: Improved Oil Recovery by Surfactant and Polymer Flooding, eds Shah, D. O., and Schechter, R. S., Academic Press, New York, 511-554, 1977.

Wu, W., Wang, D., and Jiang, H.: "Effect of the Visco-elasticity of Displacing Fluids on the Relationship of Capillary Number and Displacement Efficiency in Weak Oil-Wet Cores", SPE 109228 presented at SPE Asia Pacific Oil & Gas Conference and Exhibition held in Jakarta, Indonesia, Oct. 30-Nov. 1, 2007.

Xu, T., Apps, J. A., and Pruess, K.: "Analysis of Mineral Trapping for CO2 Disposal in Deep Aquifers", Lawrence Berkeley National Laboratory, Paper LBNL-46992, 2001.

Zaitoun, A., and Kohler, N.: "The Role of Adsorption in Polymer Propagation Through Reservoir Rocks", SPE 16274 presented at SPE International Symposium on Oilfield Chemistry, San Antonio, TX, Feb. 4-6, 1987.

Zaitoun, A., and Potie, B.: "Limiting Conditions for the Use of Hydrolyzed Polyacrylamides in Brines Containing Divalent Ions", SPE 11785 presented at the International Symposium on Oilfield and Geothermal Chemistry held in Denver, CO, Jun. 1-3, 1983.

Zaitoun, A., and Kohler, N.: "Two-Phase Flow Through Porous Media: Effect of an Adsorbed Polymer Layer", SPE 18085 presented at the 63rd Annual Technical Conference and Exhibition of the SPE, Houston, TX, Oct. 2-5, 1988.

Zitha, P. L. J., van-Os, K. G. S., and Denys, K. F. J.: "Adsorption of Linear Flexible Polymers During Laminar Flow Through Porous Media: Effect of the Concentration", SPE 39675 presented at 1998 SPE/DOE Improved Oil Recovery Symposium, Tulsa, OK, Apr. 19-22,1998.

Abbreviations and Nomenclature

A	Cross-sectional area
$\hat{A}_\beta$	Reactive surface area of mineral β of bulk volume of rock
a	Polymer constant
a_k	Activity of component k
$a_i^{w_{i,\beta}}$	Activity of ions for mineral β
b	Polymer constant
C	Polymer concentration

C_{po}	Injected polymer concentration
D_p	Adsorption level
$e_1 \sim e_5$	Empirical parameters specific to each polymer
FR	Filtration ratio
G	Elastic modulus
G^*	Complex modulus
G'	Elastic or storage modulus
G''	Viscous or loss modulus
$\{H^+\}$	Activity of hydrogen ions
$[H^+]$	Molality of hydrogen ions
I	Ionic strength of solvent
J^*	Complex Compliance
J'	Elastic or storage compliance
J''	Viscous or loss compliance
K	Consistency index
K_a	Dissociation constant of ionizable groups on polymer
k	Permeability
K_{eq}	Chemical equilibrium constant
k_L	Polymer constant
k_R	Reaction rate
$k_{o,\beta}$	Rate constant of mineral β
$k_{i,\beta}$	Rate constant of mineral β related to activity of each species
k'	Huggins constant
k''	Empirical constant of polymer solution
L	Core length
M	Molecular weight
M_p	Mass of polymer adsorbed
$\bar{M}_c$	Average molecular weight between crosslinks (gel) / average molecular weight between repeating chain units (HPAM)
$\bar{M}_n$	Average molecular weight of polymer before crosslinking (gel) / average molecular weight of polymer (HPAM)

m	Slope of line for ΔP (pressure drop) versus q (flow rate)
m_L	Mobility
m_i	Concentration of i-th ion
N_{Da}	Damköhler number
n	Power-law exponent
nct	Number of components in the aqueous phase
P	Pressure
pK_a	Acid dissociation constant
Q	Equilibrium chain-extension ratio
$Q_{a,\beta}$	Activity product of mineral β dissolution reaction
q	Flow rate
R_k	Permeability reduction
R_m	Mobility reduction or resistance factor
R_{mn}	Number of mineral reactions
r_β	Rate per unit bulk volume
S	Water saturation
t	Time
t_x	Times, in seconds, required to filter "x" mL of the solution in filtration
U	Darcy velocity
V_1	Molar volume of solvent
V_p	Measured pore volume of the core
z_i	Valence factor of i-th ion

Symbols and Greek characters

γ	Shear strain
γ_{eff}	Effective shear rate of polymer flow in a permeable rock
rH	Reaction-rate of H^+
γ^*	Complex strain amplitude
$\dot{\gamma}$	Shear rate
Δ	Difference
δ	Phase shift

ζ	Parameter in general reaction rate expression
η	Viscosity
η_o	Zero shear-limit viscosity
η_s	Solvent viscosity
η_R	Reduced viscosity
η_r	Relative viscosity
η_{sp}	Specific viscosity
η_∞	Infinite shear-limit viscosity
$\lvert\eta\rvert$	Intrinsic viscosity
η^*	Complex viscosity
η'	In phase viscosity
η''	Out of phase viscosity
λ	Time constant
μ	Fluid viscosity
μ_1	Chemical potential of the swelling agent
μ_1^*	Chemical potential of the swelling agent in the solution surrounding the polymer
v_α	Stoichiometric coefficients of reaction α
ξ	Parameter
τ	Shear stress
τ^*	Complex stress amplitude
$\upsilon_{2,r}$	Polymer volume fraction in the relaxed state
$\upsilon_{2,s}$	Polymer volume fraction in the swollen network
$\bar{\upsilon}$	Specific molar volume of dry polymer
Φ	Universal constant (2.1×10^{21} dl/g·mol·cm^3)
ϕ	Porosity
ϕ_e	Inaccessible pore volume
χ_1	Polymer-solvent interaction parameter
Ω_r	Effective hydrodynamic radius of polymer molecules

ω	Frequency

Subscripts

ion	Ionic contribution
mix	Mixing contribution
el	Elastic contribution
w	Water flow
p	Polymer flow

National Energy Technology Laboratory

626 Cochrans Mill Road
P.O. Box 10940
Pittsburgh, PA 15236-0940

3610 Collins Ferry Road
P.O. Box 880
Morgantown, WV 26507-0880

One West Third Street, Suite 1400
Tulsa, OK 74103-3519

1450 Queen Avenue SW
Albany, OR 97321-2198

2175 University Ave. South
Suite 201
Fairbanks, AK 99709

Visit the NETL website at:
www.netl.doe.gov

Customer Service:
1-800-53-7681